Domain-Informed Signal Processing with Application to Analysis of Human Brain Functional MRI Data

Behjat, Hamid

2018

Document Version:
Publisher's PDF, also known as Version of record

Link to publication

Citation for published version (APA):
Behjat, H. (2018). *Domain-Informed Signal Processing with Application to Analysis of Human Brain Functional MRI Data*. Department of Biomedical Engineering, Lund university.

Total number of authors:
1

Domain-Informed Signal Processing

with Application to

Analysis of Human Brain Functional MRI Data

HAMID BEHJAT
DEPARTMENT OF BIOMEDICAL ENGINEERING
FACULTY OF ENGINEERING | LUND UNIVERSITY
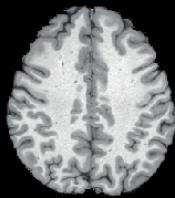
Domain-Informed Signal Processing

with Application to
Analysis of Human Brain Functional MRI Data

Hamid Behjat

LUND
UNIVERSITY

DOCTORAL DISSERTATION
Lund, April 2018

Contents

Popular Science Summary

We have long passed far beyond Aristotle's view that the heart is the feeling and thinking center of the body, and that the brain is a secondary organ serving as a cooling agent for the heart. The human brain is undoubtedly the most complex and unique organ of the human body in terms of both its structure and function. Exquisite techniques have been developed to reveal the topological and microstructural organization of the human brain. Nevertheless, our knowledge on the functioning of the human brain is yet so minute compared to its vast mysteries. To better unveil how the human brain gives rise to cognition and behavior, in both health and disease, advanced data analysis methods are being constantly developed. Yet, the success of these methods significantly varies. One natural key to success, typically taken for granted, is to exploit anatomical knowledge of the brain to enhance the processing of data associated to brain functional activity. In particular, the cerebral cortex, the 2 to 3 millimeter thick outer layer of the brain, exhibits a unique topology in each individual; it is much folded and about two-thirds of it is buried in grooves. The cerebral cortex consists of neuronal cell bodies and is the brain's primary region associated with processing and cognition, basically being the place where ones thoughts, memory, language and behavior are shaped. Advanced algorithms have been developed to extract the delicate structure of this region from conventional magnetic resonance imaging (MRI) brain scans, decoupling it from the surrounding brain white matter tissue, consisting of neuronal axonal connections, and cerebrospinal fluid. The functional activity in the cerebral cortex varies from that in white matter. The hypothesis that has led to the research presented in this dissertation is that taking into account the convoluted structure of the cerebral cortex in relation to its surrounding white matter tissue and cerebrospinal fluid can help to better process functional brain data and to detect the underlying hidden brain activity. Functional MRI (fMRI) is one popular imaging technique used for non-invasive probing of human brain function. Using fMRI, one

seeks to indirectly detect electrical brain activity based on the level of oxygenation present in the blood stream across the brain. In simple terms, when a region of the brain is active, more oxygen-rich blood is pumped to that region, leading to a relative increase in oxygenation. By interpreting the induced activity of the brain captured with fMRI as a signal, signal processing schemes are commonly used to enhance the processing of fMRI data.

In this dissertation, we present a set of novel signal processing schemes that aim to enhance the processing of fMRI data and the detection of brain activity. The fundamental theme of the presented schemes is to exploit knowledge of the intricate anatomy of each individual's brain to enhance the processing of fMRI data. We define models to represent the brain structure as the backbone of the acquired fMRI data. These models are extracted from conventional anatomical MRI scans. In signal processing terms, the anatomy is equivalent to the *domain* of the signal, i.e., the base on which the signal is lying on. We propose four *domain-informed signal processing* schemes with application to analysis of fMRI data. The contributions of this dissertation go beyond neuroimaging since three of the proposed schemes are developed in such way to enable processing not only of fMRI data, but of any data that are defined on an inhomogeneous or irregular domain. Experimental and simulated results on fMRI data show the potential of the proposed schemes in providing an efficient decomposition of the data and revealing fine-grained activity patterns consistent to the anatomy of the brain.

Abstract

Standard signal processing techniques are implicitly based on the assumption that the signal lies on a regular, homogeneous domain. In practice, however, many signals lie on an irregular or inhomogeneous domain. An application area where data are naturally defined on an irregular or inhomogeneous domain is human brain neuroimaging. The goal in neuroimaging is to map the structure and function of the brain using imaging techniques. In particular, functional magnetic resonance imaging (fMRI) is a technique that is conventionally used in non-invasive probing of human brain function.

This doctoral dissertation deals with the development of signal processing schemes that adapt to the *domain* of the signal. It consists of four papers that in different ways deal with exploiting knowledge of the signal domain to enhance the processing of signals. In each paper, special focus is given to the analysis of brain fMRI data, either as the main theme (Paper I) or as proof of practical significance of the proposed schemes (Papers II, III and IV).

Paper I presents a framework for enhanced fMRI activation mapping through exploiting filters that adapt to the brain anatomy. A novel procedure for constructing brain graphs, with subgraphs that separately encode the topology of the cerebral and cerebellar gray matter, is presented. Graph wavelets tailored to the convoluted boundaries of brain gray matter are designed and exploited to implement an anatomically-informed spatial transformation on fMRI data. Compared to conventional brain activation mapping schemes, the proposed approach shows superior type-I error control. Results on real data suggest a higher detection sensitivity as well as capability to capture subtle, connected patterns of brain activity.

Paper II presents a graph-based signal decomposition scheme that adapts to the domain of the data as well as to the spectral content of a given signal set. The construction starts from the design of a prototype Meyer-type system of kernels with uniform subbands. The adaptivity of the approach is introduced by exploiting the ensemble

energy spectral density. Using the ensemble energy spectral density, the prototype design is warped such that the resulting subbands each capture an equal amount of energy for the given signal class. Results on fMRI data and Monte Carlo simulations illustrate the superiority of signal-adapted frames over frames blind to signal characteristics in representing data and in denoising.

Paper III presents a generic interpolation scheme for reconstructing signal samples from an inhomogeneous domain. The interpolation adapts to the inhomogeneity of the domain. The adaptation is incorporated by introducing a domain-similarity metric that characterises the domain in the adjacency of each sample point. The interpolation is shown to satisfy the domain-informed consistency principle, a principle that we define as an extension of the classical consistency principle. As proof of concept, domain-informed linear interpolation is presented as an extension of standard linear interpolation. Results from applying the proposed approach on fMRI data demonstrated its potential to reveal subtle details.

Paper IV extends the theory in Paper III to enable reconstruction of signals with varying degrees of spatial smoothness. In particular, conventional shift-invariant B-spline interpolation is extended to a shift-variant, domain-informed interpolation. This is done by constructing a domain-informed generating basis that satisfies stability properties. The benefit of domain-informed interpolation over standard B-spline interpolation is demonstrated through Monte Carlo simulations across a range of B-spline orders. The practical significance of domain-informed spline interpolation is demonstrated on fMRI data. The results show the benefit of incorporating domain knowledge so that an interpolant consistent to the anatomy of the brain can be recovered by the proposed interpolation.

Preface

This dissertation is divided in to two parts. The first part serves as an introduction to relevant concepts within the field and ends with a brief summary of four papers that are the core of this thesis. The second part consists of the following four papers:

[1] Hamid Behjat, Nora Leonardi, Leif Sörnmo, Dimitri Van De Ville, "Anatomically-Adapted Graph Wavelets for Improved Group-level fMRI Activation Mapping", in *NeuroImage*, vol. 123, pp. 185–199, 2015.

[2] Hamid Behjat, Ulrike Richter, Dimitri Van De Ville, Leif Sörnmo, "Signal-Adapted Tight Frames on Graphs", in *IEEE Trans. Sig. Process.*, vol. 64, no. 22, pp. 6017–6029, 2016.

[3] Hamid Behjat, Zafer Doğan, Dimitri Van De Ville, Leif Sörnmo, "Interpolation in the Presence of Domain Inhomogeneity", manuscript.

[4] Hamid Behjat, Zafer Doğan, Dimitri Van De Ville, Leif Sörnmo, "Domain-Informed Spline Interpolation", submitted for publication.

Author's contribution
For the listed papers, the author of this dissertation is the main contributor who conceived and developed the ideas, implemented the algorithms, performed the experiments and prepared the manuscripts.

Acknowledgments

Introduction

Chapter 1

Motivation

This doctoral dissertation deals with the development of signal processing schemes that adapt to the *domain* of the signal — hence the title "domain-informed signal processing". In particular, two types of signal domains are considered: (i) *irregular* and (ii) *inhomogeneous*. The distinction between the two domains can be conveyed with the aid of simple examples. An example of a discrete signal on an irregular domain consists of a set samples acquired through non-uniform sampling on a 2-D grid, see Figure 1.1(a). The association between sample points is specified based on their Euclidean distance. Samples that fall within a short Euclidean distance to one another are considered as adjacent and connected. These set of connections define an irregular domain different from that of a regular grid. An example of a discrete signal on an inhomogeneous domain consists of a set of samples acquired through uniform sampling on a 1-D grid for which the underlying signal domain is characterized by a set of three different overlapping subdomains, see Figure 1.1(b). In this setting, samples adjacent to each other may be associated to different subdomains. For instance, see the domain associated to the fourth and fifth samples, counting from left.

(a)   (b)
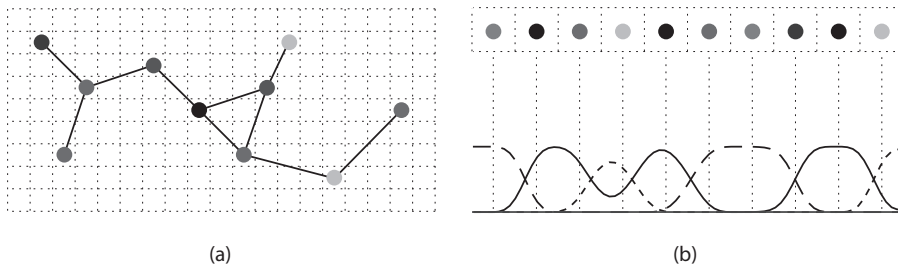
Figure 1.1: (a) A set of signal samples defined on (a) an irregular domain and (b) an inhomogeneous domain. The values of the samples are distinguished by their gray scale contrast.
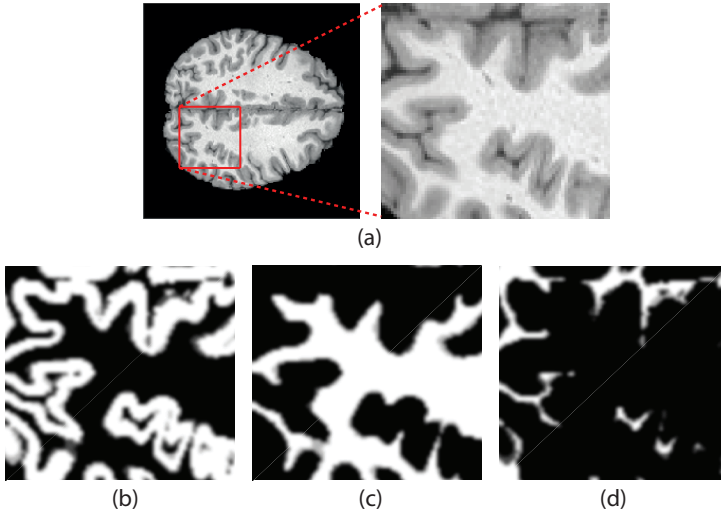
Figure 1.2: (a) A slice of a structural brain MRI scan. (b)–(d) Gray matter, white matter and cerebrospinal fluid segmentations of the ROI shown in (a), respectively.

An application area where data are naturally defined on an irregular or inhomogeneous domain is human brain neuroimaging. The goal in neuroimaging is to map the structure and function of the brain using imaging techniques. Functional magnetic resonance imaging (fMRI) is an imaging technique that has become a convention in non-invasive probing of human brain function. The essence in fMRI lies in detecting changes in blood oxygen level as an indirect measurement of brain activity. The majority of available algorithms for processing fMRI data treat data samples from across brain identically. However, brain activity resides on a topologically convoluted domain, consisting of different tissue types with varying topological and functional characteristics, see Figure 1.2(a). Functional brain activity captured by fMRI is mainly associated to brain's gray matter where nerve cell bodies reside. Gray matter is a topologically convoluted structure that exhibits properties of an irregular domain, see Figure 1.2(b). Thus, it is beneficial to confine the processing of the data to the gray matter and more importantly, to exploit the information on the irregularity of the domain to enhance processing of functional data associated to this tissue. On the other hand, in several fMRI processing applications it is necessary to treat the entire 2-D or 3-D representation of acquired functional data rather than merely considering data associated to gray matter. In this setting, data samples acquired on the 2-D or 3-D grid lie on an inhomogeneous domain consisting of three subdomains: gray matter, white matter and cerebrospinal fluid, see Figures 1.2(b)–(d).

This dissertation consists of four papers that in different ways deal with exploiting

knowledge of the signal domain to enhance the processing of signals. The first two papers address processing of signals defined on irregular domains whereas the second two papers address processing of signals defined on inhomogeneous domains. In each paper, a particular focus has been given to the analysis of brain fMRI data, either as the main theme (Paper I) or as proof of practical significance of the proposed generic schemes (Papers II, III and IV). The central themes of the papers are as follows:

> Paper I presents a framework for enhanced fMRI activation mapping through exploiting filters that adapt to the brain anatomy.

> Paper II presents a generic graph-based signal decomposition scheme that adapts to the domain of the data as well as to the spectral content of a given signal set.

> Paper III presents a generic interpolation scheme for reconstructing signal samples from an inhomogeneous domain.

> Paper IV extends the theory in Paper III to enable reconstruction of signals with varying degrees of spatial smoothness.

The remainder of the dissertation introduction is organized as follows. Chapters 2 and 3 serve as background material, whereas Chapter 4 summarizes the included papers and ends with an outlook to future work. In particular, Chapter 2 presents a brief introduction to graph signal processing, a subfield of signal processing dealing with the processing of data on irregular domains. Chapter 3 reviews the fMRI technique, the conventional methods used for processing fMRI data, and tries to establish the importance of accounting for the anatomy of the brain in mapping brain function.

Chapter 2
Graph Signal Processing

Graphs provide a flexible framework for representing and modeling data that are defined on topologically complicated domains. Examples include data defined on network-like structures, such as sensor [1] or social and biological networks [2], and data defined on manifolds or irregularly shaped domains such as the human brain [3, 4]. The current decade has witnessed a great body of research dedicated to generalizing classical signal processing operations of the Euclidean setting to the graph setting. This has given rise to the emergence of an exciting subfield within signal processing: graph signal processing (GSP) [5], which consists of various extensions of fundamental signal processing concepts, including sampling theory [6, 7], signal stationarity [8, 9], uncertainty principles [10, 11], graph Fourier transforms [12, 13], filter design [14], kernel regression [15, 16], multi-resolution transforms [17, 18] and filter bank designs [19, 20]. To extend these definitions from the classical setting to the GSP setting, the eigenvalues and eigenvectors of a graph associated matrix, the Laplacian matrix, play a central role; this matrix is used to define a spectral space equivalent to that of the Fourier space. The growing interest in developing GSP methods has been coupled with application wise developments spanning various areas such as image processing [21, 22], audio processing [23], speech processing [24], bioinformatics [25, 26] and neuroscience [27, 28, 29, 30].

It is worth noting that there exists an alternative framework for signal processing on graphs: discrete signal processing on graphs (DSP_G) [31, 32, 33]. The fundamental difference between GSP and DSP_G is that the spectral operations in the latter are endowed by the graph adjacency matrix, rather than by graph Laplacian matrix as in the former. For the sake of conciseness as well as relevance to the contents of this dissertation, the presentation in this chapter is dedicated only to GSP.

This chapter starts by formulating the description of a graph, its Laplacian spectrum, followed by a brief introduction to fundamental GSP operations, in particular,

graph Fourier transform, spectral filtering and decomposition of graph signals.

2.1 Graphs

An undirected, weighted graph, denoted $\mathcal{G} = (\mathcal{V}, \mathcal{E}, A)$, consists of a set $\mathcal{V} = \{1, 2, \ldots, N_g\}$ of N_g vertices and a set $\mathcal{E}$ of edges (i.e., pairs (i, j) where $i, j \in \mathcal{V}$). Figure 2.1 illustrates a simple graph. Algebraically, $\mathcal{G}$ can be described by an adjacency matrix A with elements defined as

$$A_{i,j} = \begin{cases} w_{i,j} & \text{if } (i,j) \in \mathcal{E}, \\ 0 & \text{otherwise,} \end{cases} \quad \forall i, j \in \mathcal{V}, \tag{2.1}$$

where $w_{i,j}$ denotes the weight of the edge between vertices i and j. Another matrix associated to $\mathcal{G}$ is the degree matrix D, which is a diagonal matrix with elements

$$D_{i,i} = \sum_j a_{i,j}, \quad \forall i \in \mathcal{V}. \tag{2.2}$$

In many recent GSP applications, the assumption is that the graph is given or can be defined in a reasonable way based on the nature of the application. For instance, in sensor networks, a graph is defined to represents the relative positions of sensors in the environment. The sensor positions are treated as graph vertices and edge weights as a decreasing function of distance between sensors [1, 34]. Figure 2.2 illustrates two example graphs: the Minnesota road graph [35] and the cerebellum gray matter graph [36]. The vertices and edges of the Minnesota graph can be thought of as naturally given by the application; the edges represent major roads in Minnesota state and the
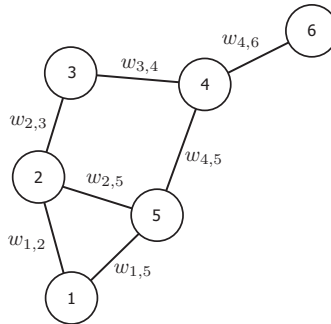
Figure 2.1: A simple undirected graph consisting of 6 vertices and 7 edges. A different weight $w_{i,j}$ can be associated to each edge.

(a)   (b)
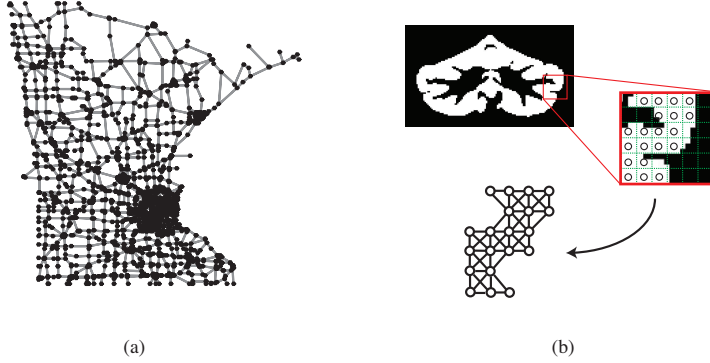
Figure 2.2: (a) The Minnesota road graph [35]. (b) The brain cerebellum gray matter graph [36].

vertices represent their intersection points, which often correspond to towns or cities. On the contrary, the cerebellum gray matter graph is defined based on the application to encode its topological structure. The cerebellum structure and its associated graph are defined in 3-D space, but here only a 2D slice is presented for ease of illustration. The vertices of this graph represent downsampled voxels whose probability of being gray matter exceeds 0.5, and its edges represent neighbourhood connections.

2.2 Signals on graphs

Let $\ell_2(\mathcal{G})$ denote the Hilbert space of all square-summable real-valued vectors $\boldsymbol{f} \in \mathbb{R}^{N_g}$, with the inner product defined as

$$\langle \boldsymbol{f}_1, \boldsymbol{f}_2 \rangle = \sum_{n=1}^{N_g} \boldsymbol{f}_1[n] \boldsymbol{f}_2[n], \quad \forall \boldsymbol{f}_1, \boldsymbol{f}_2 \in \ell_2(\mathcal{G}) \tag{2.3}$$

and the norm as

$$||\boldsymbol{f}||_2^2 = \langle \boldsymbol{f}, \boldsymbol{f} \rangle = \sum_{n=1}^{N_g} |\boldsymbol{f}[n]|^2, \quad \forall \boldsymbol{f} \in \ell_2(\mathcal{G}). \tag{2.4}$$

A real signal defined on the vertices of a graph, $\boldsymbol{f} : \mathcal{V} \to \mathbb{R}$, can be seen as a vector in $\ell_2(\mathcal{G})$, where the n-th element represents the value of the signal on the n-th vertex.

2.3 The graph spectral domain

Another key matrix in the study of graphs is the graph Laplacian matrix, defined as

$$L = D - A, \tag{2.5}$$

with elements given as

$$L_{i,j} = \begin{cases} -w_{i,j} & \text{if} \quad (i,j) \in \mathcal{E} \\ D_{i,i} & \text{if} \quad i = j \\ 0 & \text{otherwise.} \end{cases} \tag{2.6}$$

There exists several variants of the graph Laplacian [37]. Of particular interest, is the normalized Laplacian matrix $\mathcal{L}$ defined as

$$\mathcal{L} = D^{-1/2} L D^{-1/2} \tag{2.7}$$

$$= I - D^{-1/2} A D^{-1/2}, \tag{2.8}$$

with elements given as

$$\mathcal{L}_{i,j} = \begin{cases} \dfrac{-w_{i,j}}{\sqrt{D_{i,i} D_{j,j}}} & \text{if} \quad (i,j) \in \mathcal{E} \\ 1 & \text{if} \quad i = j \\ 0 & \text{otherwise.} \end{cases} \tag{2.9}$$

A comparison of (2.6) and (2.9) shows that the normalization leads to factoring out differences in vertex degrees, and as such, $\mathcal{L}$ only reflects the relative strength of the weights. L and $\mathcal{L}$ are both symmetric positive semi-definite matrices and can therefore be diagonalized. The eigenvalue decomposition of $\mathcal{L}$ is given as

$$\mathcal{L} = \Sigma \Lambda \Sigma^T, \tag{2.10}$$

where $\Sigma = [\boldsymbol{\chi}_1 | \boldsymbol{\chi}_2 | \cdots | \boldsymbol{\chi}_{N_g}]$ is an orthonormal matrix containing N_g eigenvectors $\{\boldsymbol{\chi}_l \in \ell_2(\mathcal{G})\}_{l=1}^{N_g}$ and Λ is a diagonal matrix whose entries equal the associated real, non-negative eigenvalues that define the *graph spectrum*

$$\sigma(\mathcal{G}) = \{0 = \lambda_1 \leq \lambda_2 \cdots \leq \lambda_{N_g} = \lambda_{\max}\}. \tag{2.11}$$

The multiplicity of eigenvalue zero indicates the number of connected components in the graph [37]. The spectral space of a graph shows similarities to the Fourier space in the classical domain, where the eigenvectors associated with higher eigenvalues are
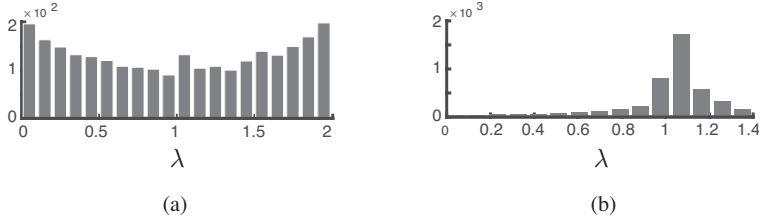
Figure 2.3: Histograms of the eigenvalues of $\mathcal{L}$ for (a) the Minnesota road graph and (b) the cerebellum gray matter graph.

less smooth than those associated to lower eigenvalues, i.e., similar to that complex exponentials associated to higher frequencies represent higher, less smooth harmonics.

The eigenvalue decomposition of L can be similarly expressed, leading to a different set of eigenvalues and eigenvectors. The unique property of $\mathcal{L}$ relative to L is that its eigenvalues, for any given graph, are bounded within the range $[0, 2]$ [37], i.e. $\lambda_{\max} <= 2$. Figure 2.3 illustrates the distribution of the eigenvalues of $\mathcal{L}$ for the two graphs shown in Figure 2.2. The distributions of eigenvalues of the two graphs are very different; the eigenvalues of the Minnesota graph are rather uniformly spread, whereas those of the cerebellum graph are mainly concentrated in the upper end of the spectrum.

2.4 Spectral representation of graph signals

Graph signals, although discrete, cannot be interpreted in the Fourier domain using the classical discrete Fourier transform (DFT). Yet, it is beneficial to derive an equivalent operator that would allow frequency analysis of graph signals — a graph Fourier transform (GFT) operator. In the following, we first briefly review the construction of DFT to establish the required link to subsequently define the GFT.

2.4.1 The discrete Fourier transform (Euclidean domain)

The N-sample DFT of a length-N discrete signal $\boldsymbol{f}$, denoted $\tilde{\boldsymbol{f}}$, is given as

$$\tilde{\boldsymbol{f}}[k] = \sum_{n=0}^{N-1} \boldsymbol{f}[n] e^{-j2\pi kn/N}, \quad k = 0, \ldots, N-1$$
$$= \langle \boldsymbol{f}, \boldsymbol{\xi}_k^* \rangle, \quad k = 0, \ldots, N-1, \tag{2.12}$$

where $\forall p \in \{0, \ldots, N-1\}$

$$\boldsymbol{\xi}_p[q] = e^{j2\pi pq/N}, \quad q = 0, \ldots, N-1. \tag{2.13}$$

The signal can be recovered from the frequency samples using the inverse DFT operation as

$$\boldsymbol{f}[n] = \frac{1}{N} \sum_{k=0}^{N-1} \tilde{\boldsymbol{f}}[k] e^{j2\pi kn/N}, \tag{2.14}$$

$$= \frac{1}{N} \sum_{k=0}^{N-1} \tilde{\boldsymbol{f}}[k] \boldsymbol{\xi}_n[k], \quad n = 0, \ldots, N-1. \tag{2.15}$$

An important property of all variants of the Fourier transform, including the DFT, is energy conservation between the original and transformed domain, known as Parseval's relation. This relation is given as

$$\forall \boldsymbol{f}_1, \boldsymbol{f}_2 \in \mathbb{R}^N, \quad \langle \boldsymbol{f}_1, \boldsymbol{f}_2 \rangle = \langle \tilde{\boldsymbol{f}}_1, \tilde{\boldsymbol{f}}_2 \rangle. \tag{2.16}$$

In essence, the DFT is a linear operator that transforms a given real-valued discrete signal $\boldsymbol{f}$ to a spectral space that has the following two properties:

- indexed by a set of regularly spaced frequency indices

$$f_1 = 0, f_2 = \underbrace{2\pi/N}_{:=\Delta}, f_3 = 2\Delta, \ldots, f_N = (N-1)\Delta, \tag{2.17}$$

- spanned by a set of orthonormal vectors, one associated to each frequency index,

$$\boldsymbol{\xi}_0, \boldsymbol{\xi}_1, \boldsymbol{\xi}_2, \ldots, \boldsymbol{\xi}_{N-1}, \tag{2.18}$$

These two properties show that the Fourier domain has a unique representation within the Euclidean realm, unlike the representation in the graph setting, cf (3). Another key observation is to notice that the corresponding equivalent continuous functions to $\{\boldsymbol{\xi}_n\}_{n=0}^{N-1}$, i.e.,

$$\xi_n(x) = e^{j\Delta nx}, \quad n = 0, \ldots, N-1 \tag{2.19}$$

are the *eigenfunctions* of the one-dimensional Laplacian operator, i.e.,

$$\frac{d^2}{dx^2} \xi_n(x) = -(\Delta n)^2 \xi_n(x), \quad n = 0, \ldots, N-1. \tag{2.20}$$

This observation is essential in paving the way to defining the GFT as described in the following section.

2.4.2 The graph Fourier transform

The elements of the DFT of a signal are obtained through the inner product of the signal and complex exponentials, cf. (2.12), which are themselves eigenfunctions of a Laplacian operator, cf. (2.20). Therefore, in analogy to the classical setting, a natural definition for the GFT is to take the inner product of a graph signal with the eigenvectors of the graph's Laplacian as

$$\forall \boldsymbol{f} \in \ell_2(\mathcal{G}), \quad \widehat{\boldsymbol{f}}[l] = \langle \boldsymbol{f}, \boldsymbol{\chi}_l \rangle, \quad l = 1, \ldots, N_g. \tag{2.21}$$

This spectral representation can be used to express $\boldsymbol{f}$ in terms of the graph Laplacian eigenvectors using the inverse GFT operation as

$$\boldsymbol{f}[n] = \sum_{l=1}^{N_g} \widehat{\boldsymbol{f}}[l] \boldsymbol{\chi}_l[n], \quad n = 1, \ldots, N_g. \tag{2.22}$$

With this definition of the Fourier transform, the Parseval relation holds

$$\forall \boldsymbol{f}_1, \boldsymbol{f}_2 \in \ell_2(\mathcal{G}), \quad \langle \boldsymbol{f}_1, \boldsymbol{f}_2 \rangle = \langle \widehat{\boldsymbol{f}}_1, \widehat{\boldsymbol{f}}_2 \rangle. \tag{2.23}$$

since

$$\langle \widehat{\boldsymbol{f}}_1, \widehat{\boldsymbol{f}}_2 \rangle \overset{(2.3)}{=} \sum_{l=1}^{N_g} \widehat{\boldsymbol{f}}_1[l] \widehat{\boldsymbol{f}}_2[l]$$

$$\overset{(2.21),(2.3)}{=} \sum_{l=1}^{N_g} \sum_{n=1}^{N_g} \boldsymbol{f}_1[n] \boldsymbol{\chi}_l[n] \sum_{m=1}^{N_g} \boldsymbol{f}_2[m] \boldsymbol{\chi}_l[m]$$

$$= \sum_{l=1}^{N_g} \sum_{n=1}^{N_g} \boldsymbol{f}_1[n] \boldsymbol{f}_2[n] \boldsymbol{\chi}_l[n] \boldsymbol{\chi}_l[n],$$

$$= \sum_{n=1}^{N_g} \boldsymbol{f}_1[n] \boldsymbol{f}_2[n] \underbrace{\sum_{l=1}^{N_g} \boldsymbol{\chi}_l[n] \boldsymbol{\chi}_l[n]}_{=\|\boldsymbol{\chi}_l\|_2^2=1},$$

$$\overset{(2.3)}{=} \langle \boldsymbol{f}_1, \boldsymbol{f}_2 \rangle. \tag{2.24}$$

2.5 Graph spectral filtering

In the Euclidean domain, a filter is uniquely defined by its impulse response. Filtering of a signal $\boldsymbol{f} \in \mathbb{R}^N$ with a filter with impulse response $\boldsymbol{g} \in \mathbb{R}^M$ is obtained through

a convolution product as

$$\boldsymbol{f}^{(g)}[n] = \sum_{m=1}^{N} \boldsymbol{f}[m]\boldsymbol{g}[n-m], \quad n = 1, \ldots, N, \tag{2.25}$$

where $\boldsymbol{f}^{(g)}$ denotes the filtered signal. Using tensor products, the convolution product can be readily extended to 2-D and 3-D space for filtering of images and volumes, respectively. The filtering operation can also be expressed as an operation in the spectral domain, i.e.,

$$\forall \boldsymbol{f} \in \mathbb{R}^N, \, \forall \boldsymbol{g} \in \mathbb{R}^M, \quad \tilde{\boldsymbol{f}}^{(g)}[k] = \tilde{\boldsymbol{f}}[k] \cdot \tilde{\boldsymbol{g}}[k], \quad k = 1, \ldots, K, \tag{2.26}$$

where $\tilde{\boldsymbol{f}}, \tilde{\boldsymbol{g}}$ and $\tilde{\boldsymbol{f}}^{(g)}$ denote the K sample DFT of $\boldsymbol{f}, \boldsymbol{g}$ and $\boldsymbol{f}^{(g)}$, respectively.

On the contrary, in the graph setting, the filter impulse response of a given spectral kernel is *shift-variant*, rather than being shift-invariant as in the Euclidean setting. For a given filter with spectral profile $\widehat{\boldsymbol{g}} \in \mathbb{R}^{N_g}$, the graph filter response for an impulse at vertex $i \in \mathbb{R}^{N_g}$, denoted $\boldsymbol{\delta}_i$, is given as

$$\boldsymbol{\delta}_i^{(g)}[n] = \sum_{l=1}^{N_g} \widehat{\boldsymbol{g}}[l] \, \widehat{\boldsymbol{\delta}}_i[l] \, \boldsymbol{\chi}_l[n],$$

$$\stackrel{(1)}{=} \sum_{l=1}^{N_g} \widehat{\boldsymbol{g}}[l] \, \langle \boldsymbol{\delta}_i, \boldsymbol{\chi}_l \rangle \, \boldsymbol{\chi}_l[n], \tag{2.27}$$

$$= \sum_{l=1}^{N_g} \widehat{\boldsymbol{g}}[l] \, \boldsymbol{\chi}_l[i] \, \boldsymbol{\chi}_l[n]. \tag{2.28}$$

This relation shows that the filter impulse response is, in general, shift-variant in the graph setting; i.e., $\forall n \in \{1, \ldots, N_g\}$, $\boldsymbol{\delta}_i^{(g)}[n] \neq \boldsymbol{\delta}_j^{(g)}[n]$, unless: 1) $i = j$, or 2) $i \neq j$ but $\{\boldsymbol{\chi}_l[i] = \boldsymbol{\chi}_l[j]\}_{l=1,\ldots,N_g}$. Due to this shift-variance property, (2.25) cannot be directly extended to the graph setting, since there exist no unique impulse response. The filtering operation can instead be implemented within the graph spectral domain by modulating the spectral content of the signal with a given graph filter spectral profile $\widehat{\boldsymbol{g}}$ as

$$\forall \boldsymbol{f}, \widehat{\boldsymbol{g}} \in \mathbb{R}^{N_g}, \quad \widehat{\boldsymbol{f}}^{(g)}[l] = \widehat{\boldsymbol{g}}[l] \, \widehat{\boldsymbol{f}}[l], \quad l = 1, \ldots, N_g. \tag{2.29}$$

The spectral representation can then be transformed back to the vertex domain as

$$
\begin{aligned}
\forall \boldsymbol{f}, \, \widehat{\boldsymbol{g}} \in \mathbb{R}^{N_g}, \, \boldsymbol{f}^{(g)}[n] \quad &= \mathcal{F}^{-1}\left(\widehat{\boldsymbol{f}}^{(g)}[l]\right), \\
&\overset{(1)}{=} \sum_{l=1}^{N_g} \widehat{\boldsymbol{f}}^{(g)}[l]\,\chi_l[n], \\
&\overset{(2.29)}{=} \sum_{l=1}^{N_g} \widehat{\boldsymbol{g}}[l]\,\widehat{\boldsymbol{f}}[l]\,\chi_l[n], \quad n = 1, \dots, N_g.
\end{aligned}
\tag{2.30}
$$

2.6 Graph spectral decomposition

Many signal processing approaches are based on decomposition schemes that split a signal based on its spectral content. The decomposition transforms the signal into a new space either for representational purposes only or as a first step for further processing. Of particular interest are wavelet transforms [38] that enable decomposition of a signal on an orthonormal basis that allows simultaneous localization in time/space and frequency. Wavelet transforms can provide a better representation of the signal both in the original signal domain as well as in the spectral domain; this is specially true for signals whose primary information content lies in localized singularities [39], such as transients in temporal signals or edges in images. For example, the discrete wavelet transform [40] has found its way in a wide range of applications.

Much attention has been given to generalizing classical spectral decomposition methods to the graph setting. Examples include extensions of wavelet transforms [17, 18, 41] and vertex-frequency analysis [42, 43]. Moreover, various filter bank designs have been proposed which either inherit a graph downsampling [44, 45, 46] or upsampling [19, 47] procedure or do not include graph sampling [48, 20, 49]. There also exists a different family of extensions that are defined within the vertex domain, such as [50, 51, 52, 53]. Here, we focus the presentation for the designs that are defined within the spectral domain, and that do not include a graph sampling step. In such designs, the eigenvalues and eigenvectors of the Laplacian matrix play a central role.

A multi-subband graph signal decomposition essentially requires designing a system spectral kernels within the graph spectrum. For convenience of design as well as implementation, spectral kernels are commonly defined as continuous kernels. In particular, consider a set of J spectral kernels

$$
\mathcal{K}_j(\lambda) : [0, \lambda_{\max}] \to \mathbb{R}^+, \quad j = 1, 2, \dots, J.
\tag{2.31}
$$

If required, the discrete version of the spectral kernels can be obtained through sampling as

$$\widehat{\boldsymbol{k}}_j[l] = \mathcal{K}_j(\lambda_l), \quad l = 1, \ldots, N_g. \tag{2.32}$$

By constructing the impulse response of each spectral kernel $\mathcal{K}_j(\lambda)$ at each vertex k, a dictionary of vertex domain atoms, denoted $\mathcal{D}_{\mathcal{G}}$ is obtained

$$\mathcal{D}_{\mathcal{G}} = \left\{ \left\{ \boldsymbol{\psi}_{j,n} \in \ell_2(\mathcal{G}) \right\}_{j=1}^{J} \right\}_{n=1}^{N_g}, \tag{2.33}$$

where atom $\boldsymbol{\psi}_{j,n}$ is given as

$$\boldsymbol{\psi}_{j,n}[n] = \boldsymbol{\delta}_i^{(\mathcal{K}_j)}[n] \tag{2.34}$$

$$\overset{(2.28)}{=} \sum_{l=1}^{N_g} \widehat{\boldsymbol{k}}_j[l] \, \boldsymbol{\chi}_l[i] \, \boldsymbol{\chi}_l[n]. \tag{2.35}$$

To decompose a graph signal $\boldsymbol{f} \in \ell_2(\mathcal{G})$ onto a set of the atoms in $\mathcal{D}_{\mathcal{G}}$, the coefficients can be obtained as

$$c_{\mathcal{K}_j,m} = \langle \boldsymbol{f}, \boldsymbol{\psi}_{\mathcal{K}_j,m} \rangle \tag{2.36}$$

$$\overset{(5)}{=} \sum_{l=1}^{N_g} \widehat{\boldsymbol{\psi}}_{\mathcal{K}_j,m}[l]\widehat{\boldsymbol{f}}[l], \tag{2.37}$$

$$\overset{(12)}{=} \sum_{l=1}^{N_g} \boldsymbol{k}_j[l]\widehat{\boldsymbol{f}}[l]\boldsymbol{\chi}_l[m]. \tag{2.38}$$

Typically one seeks the coefficient vector associated to each $\boldsymbol{k}_j$

$$\boldsymbol{c}_{\mathcal{K}_j} = [c_{\mathcal{K}_j,1}, c_{\mathcal{K}_j,2}, \ldots, c_{\mathcal{K}_j,N_g}]^T, \tag{2.39}$$

which can be obtained as

$$\boldsymbol{c}_{\mathcal{K}_j} \overset{(20)}{=} \sum_{l=1}^{N_g} \boldsymbol{k}_j[l]\widehat{\boldsymbol{f}}[l]\boldsymbol{\chi}_l. \tag{2.40}$$

However, such a direct decomposition using the explicit definition of the atoms $\boldsymbol{\psi}_{\mathcal{K}_j,m}$ is rather inefficient. Relation (2.40) shows that this decomposition scheme requires a full eigendecomposition of $\mathcal{L}$ since it is explicitly based on i) the Laplacian

eigenvectors $\{\chi_l\}_{l=1}^{N_g}$ and ii) the graph Fourier transform of the signal $\widehat{f}$. For large graphs, it can be cumbersome to compute the full eigendecomposition of $\mathcal{L}$, and in extensively large graphs this can in fact be impossible. Moreover, due to the redundancy of such a transform, it is beneficial to implement the transform using a fast algorithm, rather than using the explicit computation of the coefficients through (20). One solution to overcome this computational burden is to use a polynomial approximation scheme. If $\mathcal{K}_j(\lambda)$ can be approximated as a polynomial, denote $\mathcal{P}_j(\lambda) \in L_2(\mathcal{G})$, the subband decomposition $c_{\mathcal{K}_j}$ can be approximated as

$$c_{\mathcal{K}_j} \stackrel{(\text{11})}{=} \sum_{l=1}^{N_g} \mathcal{K}_j(\lambda_l)\widehat{f}[l]\chi_l \tag{2.41}$$

$$\approx \sum_{l=1}^{N_g} \mathcal{P}_j(\lambda_l)\widehat{f}[l]\chi_l \tag{2.42}$$

$$= \mathcal{P}_j(L) \sum_{l=1}^{N_g} \widehat{f}[l]\chi_l \tag{2.43}$$

$$\stackrel{(\text{1})}{=} \mathcal{P}_j(L)f \tag{2.44}$$

where in (2.43) the property $L\chi_l = \lambda_l\chi_l \Rightarrow \mathcal{P}_j(L)\chi_l = \mathcal{P}_j(\lambda_l)\chi_l$ is exploited.

The spectral graph wavelet transform (SGWT) is one of the first proposals of extending the construction of wavelet transforms to the graph setting [18]. The SGWT system of graph spectral filters consists of a series of spline-based kernels including a lowpass kernel and a sequence of dilated bandpass kernels. Figure 2.4(a) and Figure 2.5(a) illustrate the SGWT system of spectral kernels defined on the normalized spectrum of the Minnesota road graph and the cerebellum gray matter graph, respectively. The SGWT frame is very generic, in the sense that the shape of the spectral kernels are fixed and their maximum support is determined by $\lambda_{\max}$. An extension of the SGWT to form a tight frame was presented in [48]. In particular, Meyer-type wavelet and scaling functions were adopted to obtain spectral kernels that closely resemble the dyadic nature of classical wavelets. Figure 2.4(b) and Figure 2.5(b) illustrate the system of spectral kernels of Meyer-like tight frames defined on the normalized spectrum of the Minnesota road graph and the cerebellum gray matter graph, respectively. Similar to the defining kernels of the SGWT, the characteristics of the Meyer-like tight frame spectral kernels are fixed and independent of the graph, and their maximum support is determined by $\lambda_{\max}$.

One of the difficulties of the graph spectrum is that its construction depends on the graph itself. Consequently, the spectral representation of a graph signal is determined by both the domain and the signal. However, the aforementioned spectral
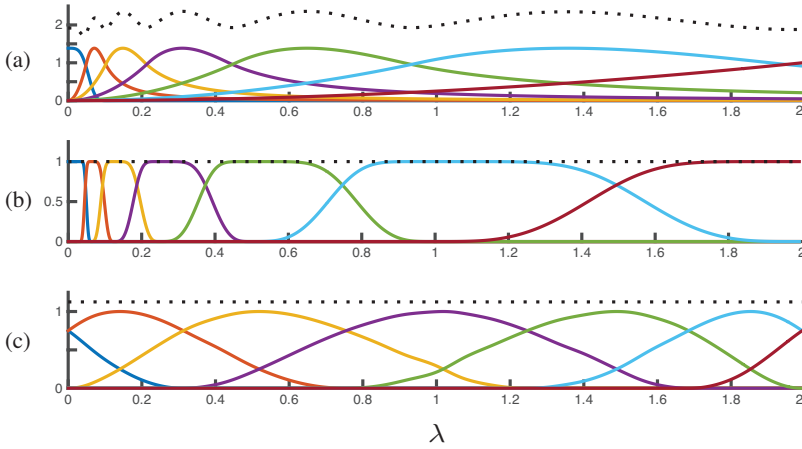
Figure 2.4: System of spectral kernels defined on the spectrum of the Minnesota road graph, with $J = 7$ spectral bands. (a) Spline based system of spectral kernels [18]. (b) Meyer-like system of spectral kernels [48]. (c) Spectrum-adapted system of spectral kernels [49].
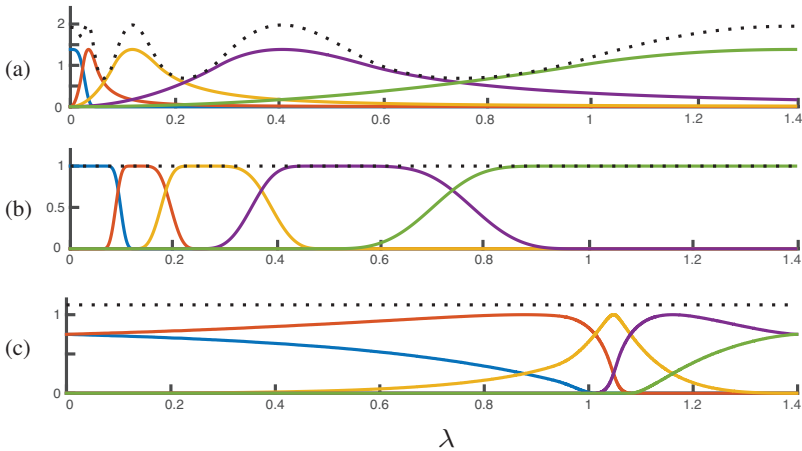
Figure 2.5: System of spectral kernels defined on the spectrum of the cerebellum gray matter graph, with $J = 5$ spectral bands. (a) Spline based system of spectral kernels [18]. (b) Meyer-like system of spectral kernels [48]. (c) Spectrum-adapted system of spectral kernels [49].

designs typically define spectral windows in a way that is independent of the graph and graph signal. One example of adaptation to the spectral properties of the graph domain was recently proposed in [49] for the construction of spectrum-adapted tight graph wavelet and vertex-frequency frames. The spectrum-adapted spectral kernels are adapted to the distribution of eigenvalues of the graph Laplacian matrix such that a similar number of eigenvalues lies in the support of each spectral kernel. Figure 2.4(c) and Figure 2.5(c) illustrate the system of spectral kernels of spectrum-adapted tight frames defined on the normalized spectrum of the Minnesota road graph and the cerebellum gray matter graph, respectively. The spectrum-adapted kernels are centralized to regions of the spectrum where more eigenvalues are concentrated.

Chapter 3

Mapping Human Brain Function

Understanding the functional organization of the human brain has attracted much research attention in the past century. In particular, the advent of non-invasive brain imaging techniques, namely electroencephalography (EEG) [54], positron emission tomography (PET) [55] and functional magnetic resonance imaging (fMRI) [56], have paved the way for convenient probing of brain function across the entire brain in health and disease. Although these three approaches all aim at probing the function of the brain, the nature of the signal they acquire is fundamentally different. The EEG records the electrical field that stems from the joint activity of millions of cortical neurons, and has the benefit of providing a sub-second temporal resolution [57]. The main limitation of the EEG lies in its poor spatial specificity in localizing brain activity since it is measured on the body surface. PET imaging overcomes the lack of spatial specificity in EEG, but it suffers from the limitation of involving radioactive substances. The PET technique tracks changes in cerebral blood flow or cerebral metabolism by scanning a radioactive substance that is injected to the blood stream. The use of PET imaging for studying the brain has significantly declined with the advent of fMRI, due to its higher cost, lower spatial resolution, and need for isotopes compared to fMRI. Compared to the EEG, fMRI provides superior spatial resolution at the cost of a lower temporal accuracy.

This chapter briefly reviews the fMRI technique and the conventional methods used in processing fMRI data for brain activation mapping. It also establishes the importance of accounting for the anatomy of the brain in mapping brain function. The chapter ends by referencing to relevant studies exploiting anatomically-informed approaches for analysis of fMRI data.
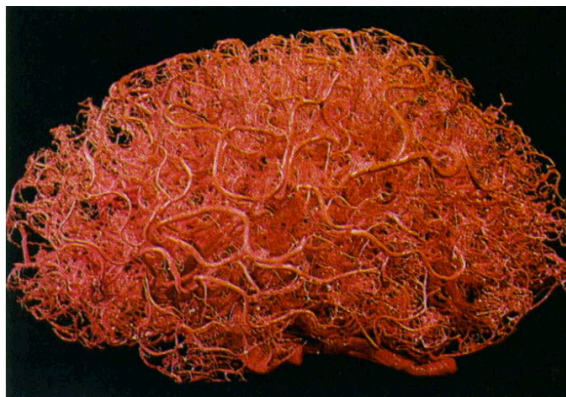
Figure 3.1: Blood vessels in the human brain. Vessels were visualized by filling them with a plastic emulsion and subsequently dissolving the parenchymal tissue. Figure reproduced with permission from [58].

3.1   The fMRI technique

Functional MRI is a key bioimaging modality used for non-invasive studies of the brain. It provides an indirect measurement of brain activity by elucidating changes in cerebral blood flow and oxygenation level, first introduced by Ogawa in 1990 [56]. This relation between neuronal activity and changes in hemodynamic response is known as neurovascular coupling, and several models have been proposed for its origin [59, 60]. As a region of the brain becomes active, the cerebral blood flow increases locally to meet the increased demand from firing neurons. Oxygen is supplied through an extensive and delicate web of vessels, spaced by as little as 20-40 μm in gray matter [58], see Figure 3.1. However, due to a misbalance between the increase in oxygen consumption and the increase in blood flow, more oxygenated blood becomes available in the region than needed for consumption. This slight increase and the difference between the magnetic properties of oxygenated and deoxygenated blood leads to changes in the magnetic resonance signal which is known as the blood-oxygen-level-dependent (BOLD) signal. The exact shape of temporal increase in blood volume evoked by a stimulus varies between different subjects as well as between different brain areas within the same subject [61, 62].

In order to track changes of BOLD signal across time, a series of whole-brain 3-D MRI scans are acquired over a period of time. These scans, commonly called fMRI volumes, are acquired using an echo-planar imaging (EPI) MRI sequence [64]. Compared to conventional MRI sequences adopted to image brain structure, EPI trades spatial resolution for temporal resolution to enable tracking behavior. Figure 3.2

(a)

(b)
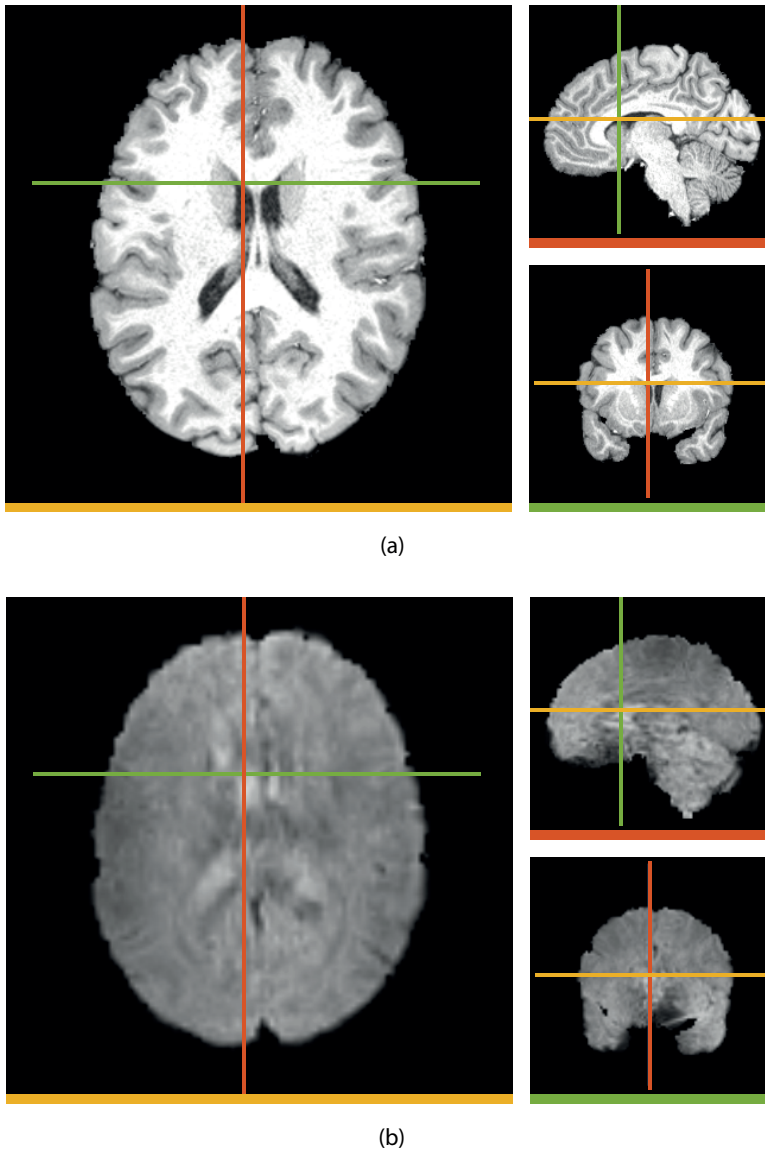
Figure 3.2: (a) A structural MRI scan. (b) An fMRI scan of the same subject in (a). The scans are 3-D; a 2-D extract of data in each dimension is displayed — axial plane (yellow), coronal (green) and sagital (red). The structural and functional scans have been aligned and mapped to a template [63] space.

shows a structural MRI and an fMRI scan of a subject from [65]. The structural volume has been acquired at a spatial resolution of 0.7 mm isotropic over approximately 7.5 minutes, whereas the fMRI volume has been acquired at a spatial resolution of 2 mm isotropic over merely 0.75 seconds.

3.2   Task-based fMRI activation mapping

Functional MRI data are generally acquired in two modalities: task-based and resting-state. The fundamental assumption in task-based fMRI is functional segregation, that is, to identify regions within the brain that are specialized for different behavioral task, such as motor, visual, cognitive, language tasks. An illustrative visual paradigm is shown in Figure 3.3. Using such a paradigm, the aim is to detect regions in the brain that are positively correlated to human face recognition, as that first proposed in the seminal work by Haxby and colleagues [66]. In contrast to task-based fMRI, resting-state fMRI entails imaging subjects while they lie in the scanner idle, without being exposed to any experimental paradigm. By studying spontaneous fluctuations in brain activity across brain regions, the objective is to detect low frequency (< 0.1 Hz) spatially-distributed brain networks[67]. In this dissertation, only analysis of task-based fMRI data is considered.

Different statistical approaches have been proposed for the analysis of task-based fMRI data, known as fMRI activation mapping, including, principal component analysis [68], independent component analysis [69, 70, 71], canonical correlation analysis [72, 73] and sparsity-promoting deconvolution methods [74, 75, 76]. The most widely used approach is a mass univariate hypothesis-driven scheme based on the general linear model (GLM). This parametric method is implemented in many software packages such as statistical parametric mapping (SPM) [77], the FMRIB Software Library (FSL) [78] and AFNI (Analysis of Functional Neuroimages) [79]. It should also be noted that statistical inferences of fMRI data are conventionally made at the level of voxels [77] as well as clusters [80]. In the former, the objective is to determine if a voxel is significantly active, whereas in the latter the aim is to determine whether a cluster of voxels are significantly active. In the following, we present an overview of the conventional GLM technique for voxel level statistical inference of fMRI data.
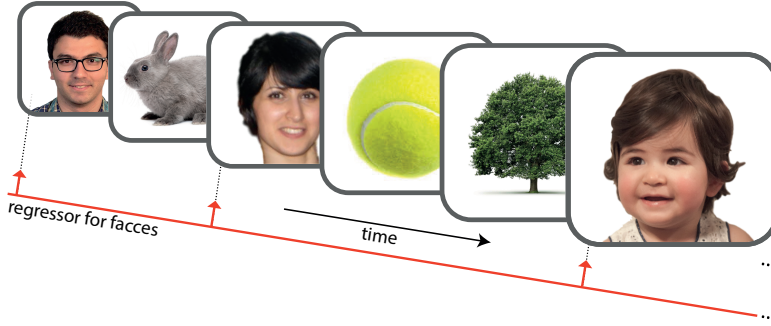
Figure 3.3: An illustrative example of an fMRI paradigm. The subject, while lying in the scanner, is shown a series of images of which some are faces.

3.2.1 GLM fitting of fMRI data

A single subject fMRI dataset consists of a series of N_t functional volumes, each with N_v voxels. By representing each volume as an $N_v \times 1$ vector $\{\boldsymbol{v}^{(t)}\}_{t=1}^{N_t}$, the temporal change in intensity at each voxel k can be expressed as

$$\boldsymbol{y}^{(k)} = [\boldsymbol{v}^{(1)}[k] \ldots \boldsymbol{v}^{(N_t)}[k]]^T. \tag{3.1}$$

A GLM is then fitted independently to the time-series of each of the voxels as

$$\boldsymbol{y}^{(k)} = X\boldsymbol{\beta}^{(k)} + \boldsymbol{\epsilon}^{(k)}, \tag{3.2}$$

where X is the $N_t \times N_r$ design matrix with columns representing a desired set of regressors, $\boldsymbol{\beta}^{(k)}$ is a $N_r \times 1$ vector of regression parameters and $\boldsymbol{\epsilon}^{(k)}$ is a $N_t \times 1$ vector of residual errors. The regressors in the design matrix consists of the a set of experimental paradigms, such as the paradigm shown in Figure 3.3, each convolved with an appropriate hemodynamic response function, as well as a set of pre-computed head movement regressors. The elements of vector $\boldsymbol{\beta}^{(k)}$ are the effect sizes, i.e., the effect that each of the N_r regressors have had on the the BOLD response of the k-th voxel.

Assuming that the design matrix is of full rank, i.e., rank$(X) = N_r$, and that the error component is independently and identically Gaussian distributed, i.e., $\mathcal{N}(0, \sigma^2 I)$, the optimal unbiased estimate of $\boldsymbol{\beta}^{(k)}$ is the least squares estimate given by [77]

$$\boldsymbol{\beta}^{(k)} = (X^T X)^{-1} X^T \boldsymbol{y}^{(k)}. \tag{3.3}$$

The corresponding estimate of the residual errors is obtained as

$$\boldsymbol{\epsilon}^{(k)} = \boldsymbol{y}^{(k)} - X\boldsymbol{\beta}^{(k)}. \tag{3.4}$$

3.2.2   Statistical Inference

Typically, not all components of the estimated $\boldsymbol{\beta}^{(k)}$ are of interest. In particular, to perform a t-test, an appropriate t-test contrast vector $\boldsymbol{c}$ of size $N_r \times 1$ is applied to the estimated parameters as $\boldsymbol{c}^T \boldsymbol{\beta}^{(k)}$. The objective is then to decide between the following two hypothesis

$$\mathcal{H}_0^{(k)} : \boldsymbol{c}^T \boldsymbol{\beta}^{(k)} = 0 \qquad (3.5)$$

$$\mathcal{H}_1^{(k)} : \boldsymbol{c}^T \boldsymbol{\beta}^{(k)} > 0. \qquad (3.6)$$

Using the estimated $\boldsymbol{\beta}^{(k)}$ and $\boldsymbol{\epsilon}^{(k)}$, two scalar values are defined for each voxel k as

$$\mu^{(k)} = \boldsymbol{c}^T \boldsymbol{\beta}^{(k)} \qquad (3.7)$$

$$s^{(k)} = \boldsymbol{\epsilon}^{(k)T} \boldsymbol{\epsilon}^{(k)} \boldsymbol{c}^T (X^T X)^{-1} \boldsymbol{c}, \qquad (3.8)$$

where $\mu^{(k)}$ is the effect size of the contrast of interest and $s^{(k)}$ its uncertainty [81]; $\mu^{(k)}$ is a random variable with Gaussian distribution with mean $\boldsymbol{c}^T \boldsymbol{\beta}$, and $s^{(k)}$ follows a chi-square distributions with $J = (N_t - \text{rank}(X))$ degrees of freedom. A t-value can then be calculated for each voxel k as

$$t^{(k)} = \frac{\mu^{(k)}}{\sqrt{s^{(k)}/J}}. \qquad (3.9)$$

The resulting t-values are tested against a threshold determined by a desired significance level α (e.g. 0.05). The null hypothesis is rejected if the t-value exceeds the threshold, and the associated voxel is declared as active.

3.2.3   The multiple comparison problem

The significance level α of a statistical test indicates the probability p of false positive detection, commonly known as Type I error rate. When multiple statistical tests are implemented on a single data set (N tests), the probability of false positive detection becomes pN, rather than p. This problem is known as the multiple comparison problem. Due to this problem, the significance level needs to be corrected for a correct statistical interpretation.

The standard measure in controlling false positives in multiple testing problems is to control the chance of any Type I error, the familywise error (FWE) rate [82]. One well-known approach to control the FWE rate is to resort to *Bonferroni correction*, i.e., to reduce the significance level by a factor of the number of tests, i.e., from α to α/N_v. The number of tests in a whole-brain fMRI study typically equals the number of voxels

within the brain mask that is a number in the order of 10^4. This strict correction has the drawback of drastically reducing the sensitivity for highly noise-convoluted fMRI datasets, leading to almost no detections.

An aspect that is taken for granted in the Bonferroni correction is the inherent spatial correlation of fMRI data. Gaussian random field theory (GRFT) based methods use estimates of the smoothness of the data to adapt to the severity of the multiple testing problem in controlling the FWE rate. GRFT is adopted in wide range of fMRI statistical analysis packages including SPM [83]. Using GRFT implies adopting the assumption that the functional data lie in a lattice representation of a Gaussian random field [84]. However, since fMRI data typically do not exhibit such smoothness characteristics, it is essential to initially smooth the data before statistical testing. Most conventional analyses schemes use a stationary 3-D spatial lowpass filter, such as a Gaussian kernel of a desired standard deviation. The use of GRFT comes with its own limitations. Firstly, there has been a set of recent studies showing that the approach yields family-wise error rates that are higher than that expected, in particular, for cluster level inference [85, 86], suggesting the use of non-parametric approaches for controlling the FWE rate using permutation testing [87, 88].

3.3   Maintaining spatial specificity of activation maps

Smoothing the data is necessary if GRFT is to be used for statistical inference. However, this is not the only reason to use smoothing. fMRI data have a very low spatial resolution due to the requirement of fast acquisition. Moreover, the BOLD signal itself is a weak signal corrupted by various noise sources of physiological origin, such as cardiac and respiratory signals [89], as well as non-physiological origin, such as scanner noise [90] and head motion, that tends to be spatially and temporally independent [91]. It is therefore necessary to enhance the signal-to-noise ratio to increase the power of consequent statistical tests. To this aim, a denoising step is generally incorporated in fMRI analysis pipelines. Smoothing the data is one such scheme. Conventional schemes rely on isotropic Gaussian smoothing. However, spatially isotropic filters, such as a Gaussian, are optimal only for detecting activations that conform to the size and shape of the filter kernel. Such smoothing leads to loss of information on the spatial extent and shape of activation areas [92, 93], and destroys any non-smooth singularities in the data. With this approach, increased sensitivity is traded for a loss in spatial specificity in detections.

As a step towards maintaining spatial details, approaches have been proposed to replace Gaussian smoothing with more elaborate adaptive spatial filtering schemes, see for example [94, 95, 96]. In such schemes, the adaptation is introduced by exploiting steerable filters [97, 98] constructed using directional derivative operators. The

steerable filters are used as a spatial basis function that can efficiently encode non-spherical activation patterns. Spatial wavelet transforms have also been abundantly exploited as a means to non-linearly denoise functional data within frameworks of both classical [99, 100, 101, 102] and Bayesian [103, 104] inference. As brain activity is highly localized in space [105], it can be efficiently represented using wavelets, which achieve a balance between localization in space and frequency domain. A cluster of active voxels can be encoded with only a few wavelet coefficients [106] whereas the power of white noise remains uniformly spread across the wavelet coefficients. By performing coefficient-wise statistical testing within the wavelet domain [107, 81] a higher sensitivity is achieved than that by voxel-wise testing within the spatial domain [108]. As an example, the discrete-wavelet transform [109] has been used in the wavelet-based SPM (WSPM) framework [81, 110]. WSPM has the unique feature of treating thresholding within the wavelet domain as a denoising step only; statistical testing is deferred to a second thresholding on the reconstructed map within the spatial domain. The statistical analysis is performed by a coefficient-wise t-test. To deal with the multiple comparison problem, WSPM exploits Bonferroni correction for strong type I error control. Adapting the False discovery rate principle [111] to the framework has also been proposed [112].

3.4   The link between brain structure and function

A common characteristic between Gaussian filters, anisotropic filters and wavelets is that they are *stationary* filters; i.e., the same set of filters are used across the brain. Given the extent of spatial variability observed in the underlying neuroanatomy, stationary filters are not ideal in terms of sensitivity to real activations, by virtue of the matched filter argument [113]; i.e. the expected spatial shape of activity patterns varies relative to the variation in the underlying anatomy, and thus, the spatial shape of a stationary filter does not ideally match all expected activity patterns. To better understand this structure-function inter-relation, a brief overview of brain's macro structure is necessary.

The brain consists of two tissue types: gray matter and white matter. Figure 3.4(a) shows a slice of a T1-weighted brain MRI scan of a subject from an open-access database [65]. Figure 3.4(b)–(c) show the gray and white matter probability maps of Figure 3.4(a), obtained through segmentations [114]. The names stem from the color of these two tissues, but their division is rather due to the fundamental difference in their function. Gray matter consists of several billion nerve cell bodies where brain processing takes place. It consists of various functionally specialized regions, including the cerebral cortex, deep nuclei, brain stem, the cerebellum cortex. The cerebral cortex exhibits an exquisite convoluted structure. Its convoluted shape

(a) (b) (c)
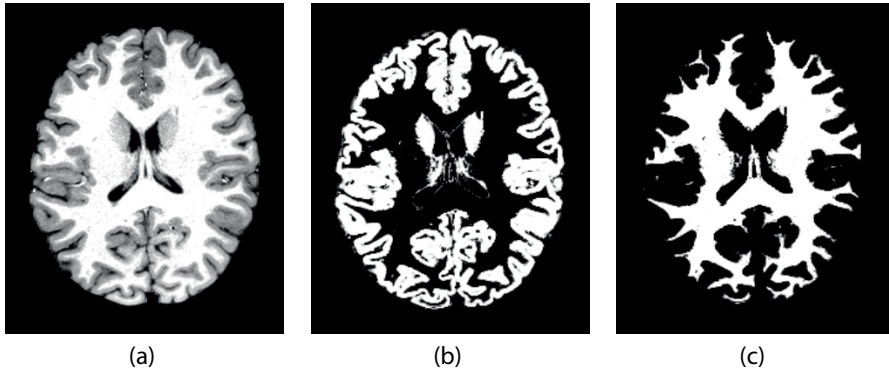
Figure 3.4: (a) An axial slice of a structural T1w MRI scan. Segmented (b) gray matter and (c) white mater probability maps of (a).

is thought to have arouse during evolution as a strategy for packing ever-increasing number of neurons into the limited space of skull [115], since the cortical thickness does not substantially vary across pieces (approximately 2-4 mm thick), but its surface area is significantly larger in higher primates such as humans. Nerve cells lying in gray matter are in contact with each other through their own axons. White matter mostly consists of myelin sheath-covered nerve cells that are responsible for transmitting information between distant neuronal regions across the brain. Myelin sheaths insulate neuronal electrical signals and thus, enable fast transmission of information across the brain at velocities up to 100 m/s [115]. Gray matter and white matter, together with cerebrospinal fluid, make up the whole volume of the brain.

Besides variation in their function, gray matter and white matter exhibit different properties in terms of neurovascular coupling. White matter has a very sparse vascularization compared to gray matter [116], and its energy consumption is one fourth of that of gray matter [117]. White matter also exhibits a differently shaped hemodynamic response function compared to that of gray matter [118]. These differences leads to the white matter being a tissue with very low neurovascular coupling compared to gray matter, which in turn implies the absence or presence of only a weak BOLD signal within white matter [117]. However, it is worth noting that based on current research, the assumption of absence of BOLD activity in white matter has been called into question [119, 120, 121, 122, 123], suggesting the necessity of developing white matter tailored fMRI imaging sequences [124, 125] as well as temporal [126] and spatial [127] analysis schemes. Moreover, fMRI data within gray matter, white matter and cerebrospinal fluid have different noise properties [128]; for example, white matter exhibits smaller between-voxel variation in space than does the gray matter. Due to this difference, filtering a volume of data irrespective of the underly-

ing tissue imposes a nonlinear effect on voxel variances and can lead to a shift of peak significances in the resulting t-maps [129, 130, 131]. This loss in spatial localization is particularly pronounced when Gaussian kernels of large width are used [132].

In summary, understanding these prior knowledge about tissue-function relationship is essential for developing novel methodologies and interpreting obtained results.

3.5   Inter-subject spatial variability in BOLD response

In single-subject fMRI studies, the parameter of interest is the variance observed within each subject, and the variance between subjects is assumed to be fixed or of no interest [133]. On the contrary, in multi-subject fMRI studies, effects observed in a group of subjects are used to make inferences about population responses. Typically a large inconsistency is observed in gray matter foldings across individuals even in standard populations [134, 135]. A fundamental step in group studies is, thus, to account for the inter-subject variability in brain anatomy.

Figure 3.5 illustrates the typical variability observed in the topological structure of the gray matter across six subjects. The challenge lies in deriving a suitable transformation that projects subjects' functional data into a common anatomical space. One of the most commonly used spaces in the Montreal Neurological Institute (MNI) space [63]. The transformation is performed by initially mapping, linearly [136, 137] or nonlinearly [138], the subjects structural scan to a group ensemble anatomical template [139, 140], and then using the resulting transformation to map the associated subjects functional data. Non-linear normalization approaches such as DARTEL [141], which is among the best performing algorithms [142], can be used to further alleviate this problem by defining a common template space for a group of subjects at hand rather than using a population-based template. Using the fast diffeomorphic image registration scheme implemented in DARTEL, the anatomical structure of the set of subjects are iteratively warped to obtain an accurate group-level template gray matter and white matter. Moreover, for sub-regions of the brain such as the cerebellum, there exist methods that provide a normalization of individual subjects' cerebellar region to a population-level, template space [143, 144].

Conventional multi-subject fMRI analysis schemes not only rely on the assumption that functional voxels reside in the same anatomical coordinate system, but also on the assumption that activations are expressed in the same location across subjects. However, it is unlikely that a large set of common voxels evidence activation in all subjects. A spatial discrepancy in the order of a millimeter or two is typically observed in activation patterns across subjects. To alleviate this functional mismatch, first level subject-specific activation patterns are typically smoothed with an isotropic Gaussian kernel to increase their spatial overlap, and in turn to ensure evidence of a common
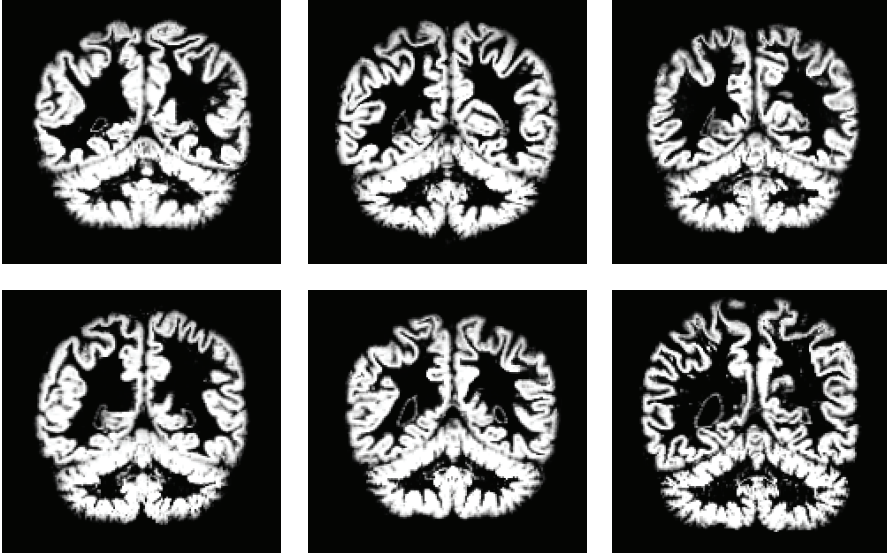
Figure 3.5: The segmented gray matter of six subjects, from the fMRI dataset in [145], showing the inter-subject cortical folding variability.

activation. The significance of the overlap is then typically determined using a one sample t-test [133]. With this approach, the spatial resolution of detected activation patterns is traded for increased statistical power, which in turn leads to an increased detection sensitivity.

3.6   Anatomically-informed approaches for analysis of fMRI data

The use of anatomically-informed methods for analysis of fMRI data is relatively sparse, yet the number of studies is steadily rising. By anatomically-informed methods we refer to schemes that aim to enhance the processing of fMRI data by exploiting in one way or another knowledge about the underlying anatomy of the data. In this line, a rich range of schemes have been proposed for analysis of fMRI data on the cortical surface. Interpolation schemes that exploit anatomical constraints to map volumetric fMRI data on to the cortical surface were proposed in [146, 147]. Various smoothing procedures such as diffusion smoothing [148, 149], heat kernel smoothing [150] and spline smoothing [151] have been proposed to accurately filter fMRI data by taking into account the irregularity of the cortical surface. Construction of cortical geometry encoding spatial basis functions was initially proposed in [152], exploited for multi-

subject fMRI analysis in [153], and further scrutinized in a recent work [154] for characterizing low frequency oscillating neuronal activity. To better describe the dynamics of cortical activity [155], elaborate extensions of the cortical basis have been proposed [156, 157] to encode not only local topology but also distal inter-hemispheric connections [158], the *human connectome* [159]. Aside from surface approaches, a number of volumetric schemes have also been proposed. To minimize blurring of apparent brain activity across anatomic boundaries and to encode local anatomical singularities, bilateral spatial filtering schemes were proposed in [160, 161]. The use anatomical information as spatial priors within a Markov random field regularization framework was proposed [162]. The design of second-generation wavelets [163] adapted to the cortical layer using the wavelet lifting scheme [164] was proposed in [165, 166]. A spatiotemporal fMRI deconvolution method, where the spatial regularization phase is adapted such that it exploits the topological structure of gray matter, was proposed in [167]. In [168], it was shown that fMRI functional networks can be approximated using eigenmodes of brain structural connectome graphs, confirming similar findings on the cortical surface [156]. In [169], fMRI data were decomposed using a similar set of human connectome eigenmodes as that in [156, 168], showing that better alignment between the functional data and the underlying anatomical backbone supports faster cognitive switching. The proposed scheme in [169] was further elaborated in [27] to study the dynamics [170] of cortical activity over time.

Chapter 4 ─────────────────
Summary of the Included Papers

──────────────────────────────

This chapter presents summaries of the four included papers on algorithms for domain-informed signal processing. In Papers I and II, the adaptation to the domain is incorporated by representing the signal domain as a graph. Paper I presents an algorithm developed specifically for the decomposition and denoising of fMRI data. Paper II presents a generic algorithm for domain-informed decomposition of signals; the algorithm can be adopted for the analysis of any set of signals defined on the nodes of a given undirected graph. In particular, the applicability of the approach on an fMRI dataset is presented. In Papers III and IV, the adaptation to the domain is incorporated directly into the conventional signal processing setting; i.e., without the need to represent the domain as a graph. Paper III presents a scheme for extending conventional linear interpolation to an interpolation that adapts to the signal domain. Paper IV further extends the theory in Paper III to obtain higher order domain-informed spline interpolants. In the following, we briefly review the contributions and main results of these four papers.

Paper I: Anatomically-adapted graph wavelets for improved group-level fMRI activation mapping

A graph-based framework for fMRI activation mapping at the group-level is presented. The framework extends WSPM which provides a wavelet-based denoising procedure as an alternative to pre-smoothing the data by a spatial Gaussian kernel, and thus, prevents loss in spatial specificity. The extension is mainly twofold:

Firstly, considering the fact that the BOLD response is mainly expected in gray matter, the convoluted structure of gray matter is considered as the signal domain

rather than the whole brain volume. A novel transformation of fMRI data is then introduced within this domain, using anatomically-adapted wavelets tailored to the convoluted boundaries of gray matter (see Figure 4.1(a)) rather than classical discrete wavelets that have preferential orientations along the Cartesian axes. As part of the framework, the procedure for constructing local-connectivity encoding brain graphs (see Figure 4.1(c)), with subgraphs that separately encode the structural connectivity of the cerebral gray matter and cerebellar gray matter, is also presented.
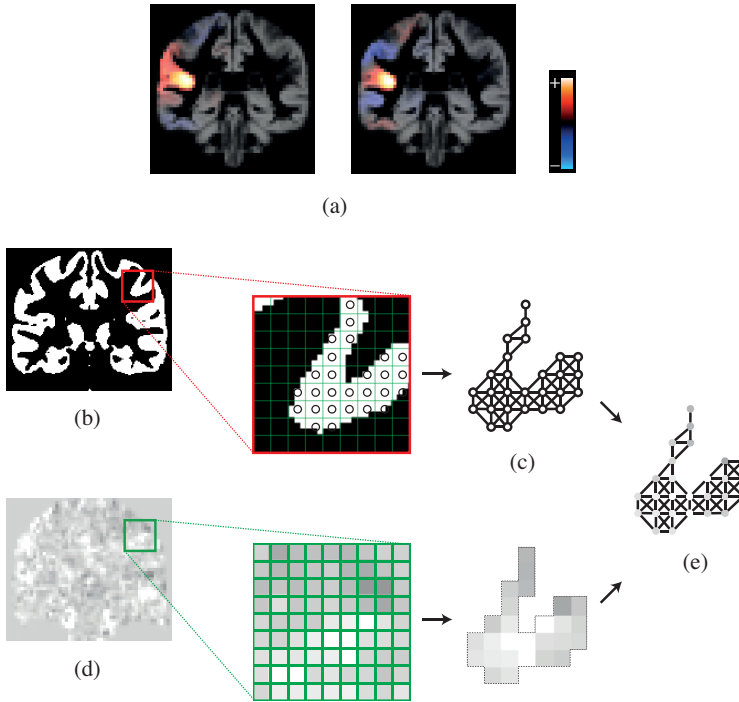
Figure 4.1: (a) Realizations of two gray matter adapted wavelets, at a coarse scale (left) and a fine scale (right), overlaid on the constructed template cerebral gray matter. (b) Template group-level representation of cerebral gray matter obtained using DARTEL. (c) Local-connectivity encoding gray matter graph. (d) First level contrast maps. (e) A graph signals constructed by mapping contrast data on to the designed gray matter graph.

Secondly, the framework is developed in particular for group studies; versions of the scheme for single-subject analysis have been proposed separately [36, 171]. The inter-subject gray matter variability is addressed by the use of template gray matter representations. For the cerebellar region, the SUIT template [143] is used to derive

a population-level, study-independent template gray matter representation. For the cerebral region, DARTEL is used to derive group-level gray matter representation based on the anatomical scans of the set of subjects (see Figure 4.1(b)). The desired graph is then constructed using the derived gray matter representations. First-level contrast maps (see Figure 4.1(d)), derived from GLM fitting of the non-smoothed functional data, are then mapped on the graph (see Figure 4.1(e)), and transformed to the spectral graph domain using the anatomically-adapted wavelets.

In the spectral graph domain, the contrast maps are non-linearly denoised. The processed maps are then reconstructed back to the spatial domain, and statistical inference is performed. The proposed approach is evaluated using semi-synthetic as well as real [145] multi-subject data. Table 4.1 shows the obtained sensitivity and specificity rates obtained on the synthetic data where ground truth is known. Compared to SPM, the proposed approach shows superior type-I error control, which can be observed by comparing the number of false positives. Compared to the use of classical wavelet as exploited in WSPM, the sensitivity of the proposed approach is significantly greater (75% vs. 28%).

Figure 4.2 shows activation maps obtained using SPM and the proposed approach on the real data. Visual comparison of the maps suggests higher detection sensitivity as well as the capability to capture subtle, connected patterns of brain activity using the proposed graph-based approach.

Table 4.1: Detection performance using SPM (with Gaussian filters of $4\ mm$ and $6\ mm$ FWHM), WSPM using classical wavelets and the proposed graph-based framework — TP: true positives, FP: false positive.

Method	SPM^{4mm}	SPM^{6mm}	WSPM	proposed approach
No. of detections	1882	3375	633	1581
No. of TPs	1389	1785	538	1398
Sensitivity	73%	94%	28%	75%
No. of FPs	493	1590	95	183
Specificity	99.2%	97.4%	99.9 %	99.4 %
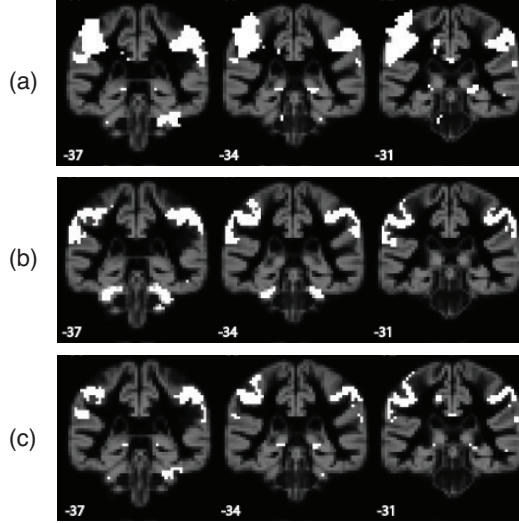
Figure 4.2: Activation maps detected by (a) SPM (Gaussian smoothing, 6 mm FWHM) and (b) the proposed approach, overlaid on group-level gray matter template. (c) Same as in (a) but with activations outside gray matter excluded.

Paper II: Signal-adapted tight frames on graphs

This paper presents an approach to the construction of signal-adapted tight graph frames. Previous graph frame design approaches have been either generic or adapted only to the spectral properties of the graph domain. However, the spectral properties of the signals that lie on the graph can provide insightful information on how to partition and allocate the spectral support of the spectral kernels.

Given a graph, see Figure 4.3(a), the spectrum of the graph can be obtained through eigen-decompostion of its Laplacian matrix, leading to a set of eigenvalues, see Figure 4.3(b), and a set of eigenvectors. For a given set of signals defined on the graph, an ensemble energy spectral density can then be obtained using the graph eigenvectors, see Figure 4.3(c). The essence of designing the proposed frame lies in considering the distribution of the ensemble energy content as a novel means to adaptation. First, a prototype tight, Meyer-type system of kernels with uniform scaling is designed for the given graph, see Figure 4.3(d). Second, an ensemble energy spectral density is defined for a given set of signals defined on the graph. Third, an energy-equalizing transformation function is obtained using the estimated ensemble energy spectral density of the given signal set. Finally, by incorporating this transformation in the prototype design, the desired tight, signal-adapted frame is obtained, see Figure 4.3(e).
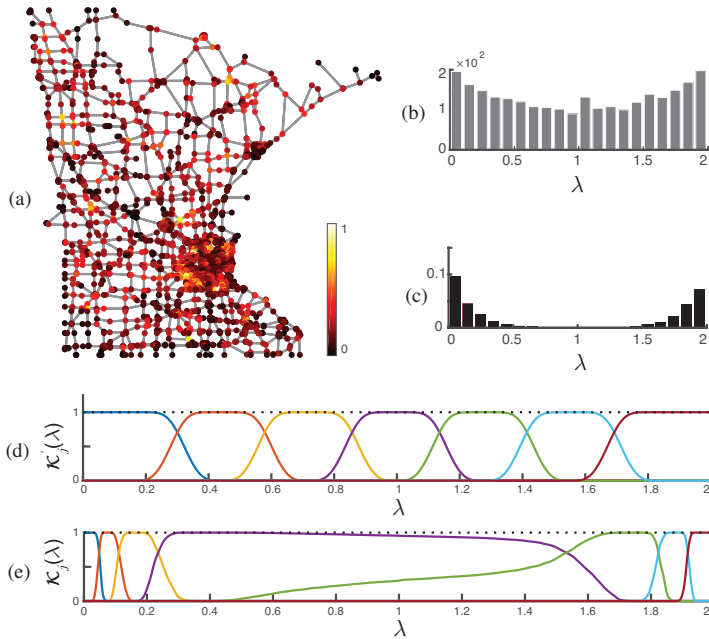
Figure 4.3: (a) A realization of a signal overlaid on the Minnesota road graph. (b) Histogram of the distribution of the eigenvalues of $\mathcal{L}$. (c) Distribution of the ensemble energy spectral density of a set of 20 signals realized on the graph. (d) Uniform Meyer-type system of spectral kernels forming a tight frame. (e) Signal-adapted system of spectral kernel forming a tight frame constructed by warping the uniform Meyer-type system of spectral kernels.

The novelty of the adaptivity lies in considering the energy-wise significance of the graph Laplacian eigenvalues are considered, rather than merely their distribution as previously proposed. The proposed frames are constructed for three different graph signal sets: synthetic signals realized on the Minnesota road graph, real traffic data from Alameda county and brain data from an fMRI study, and compared to non signal-adapted frames. The three graphs and the associated signal sets are chosen such that the independence of the distribution of the graph's eigenvalues and the ensemble energy spectral density is highlighted.

Figure 4.4 shows the mean distribution of the decomposition coefficients of an fMRI signal set consisting of 292 signals using signal-adapted, spectrum-adapted and Meyer-like wavelet frames. The distributions of the coefficients of subband five of all three frames closely resembles a Gaussian, similar to the distributions obtained on a noise dataset, suggesting that the corresponding atoms of this subband have
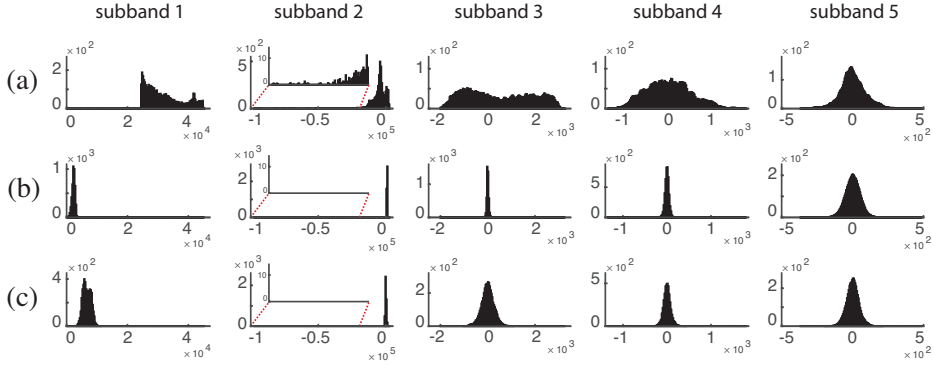
Figure 4.4: The mean distribution of coefficients resulting from decomposing an fMRI signal set using (a) signal-adapted, (b) spectrum-adapted and (c) Meyer-like wavelet system of spectral kernels with five subbands.

captured noise. A similar observation is made for the distributions associated with the third and fourth subbands of the spectrum-adapted [49] and Meyer-like wavelet [48] frame (Figures 4.4(b)-(c)). On the other hand, the coefficients of the first four subbands of the signal-adapted frame significantly deviate from zero and exhibit a broader spread, cf. first four plots in Figure 4.4(a), and have distributions unlike that expected to result from decomposing noise. This suggests the efficiency of using the signal-adapted frame to construct atoms that capture signal components.

The proposed frames have also been tested for signal denoising. Figure 4.5 presents a comparison of performances obtained in denoising the signals using the SGWT frame, the spectrum-adapted frame and the proposed signal-adapted frames, illustrates the superiority of latter frames over frames blind to signal characteristics.
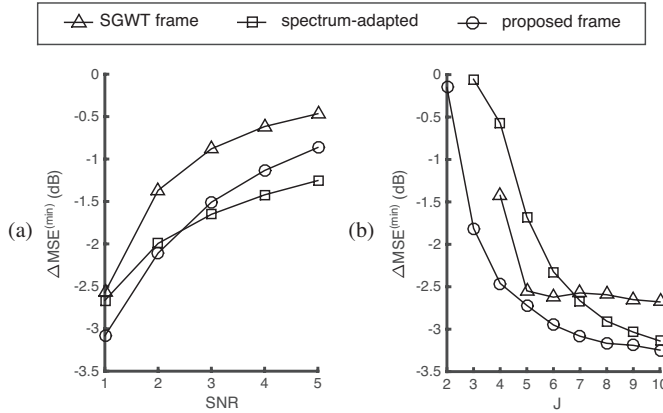
Figure 4.5: Comparison of denoising performance using different frames on a signal set consisting of 20 signals realized on the Minnesota road graph, corrupted with noise. (a) Minimum mean square error reduction $\Delta\text{MSE}^{(\text{min})}$ as a function of $\text{SNR} = \sigma_x^2/\sigma_e^2$, where σ_x^2 and σ_e^2 denote the signal and noise variances, respectively. (b) $\Delta\text{MSE}^{(\text{min})}$ as a function of the number of scales J, where $\sigma_e^2 = \sigma_x^2$ in signal realization for all cases.

Paper III: Interpolation in the presence of domain inhomogeneity

Standard interpolation techniques are implicitly based on the assumption that the signal lies on a homogeneous domain. In this paper, we propose an interpolation scheme which exploits prior information about domain inhomogeneity, characterized by different, potentially overlapping, subdomains. In particular, the interpolation exploits a novel set of modulated generating kernels that adapt to the inhomogeneous domain. The adaptation is incorporated by introducing a domain-similarity metric that characterises the domain in the adjacency of each sample point. The proposed interpolation is shown to satisfy the domain-informed consistency principle — a principle that we define as an extension of the classical consistency principle [172]. This means that the interpolated signal is consistent not only at sample points, with respect to the given samples, but also at intermediate points between samples, with respect to the given domain knowledge. As proof of concept, domain-informed linear interpolation has been presented as an extension of standard linear interpolation.

In the 2-D setting, we denote this interpolation as domain-informed bilinear interpolation (DIBLI). Results from applying DIBLI on fMRI data demonstrated its potential to reveal subtle details. Figures 4.6 and 4.7 illustrates the setting for apply-
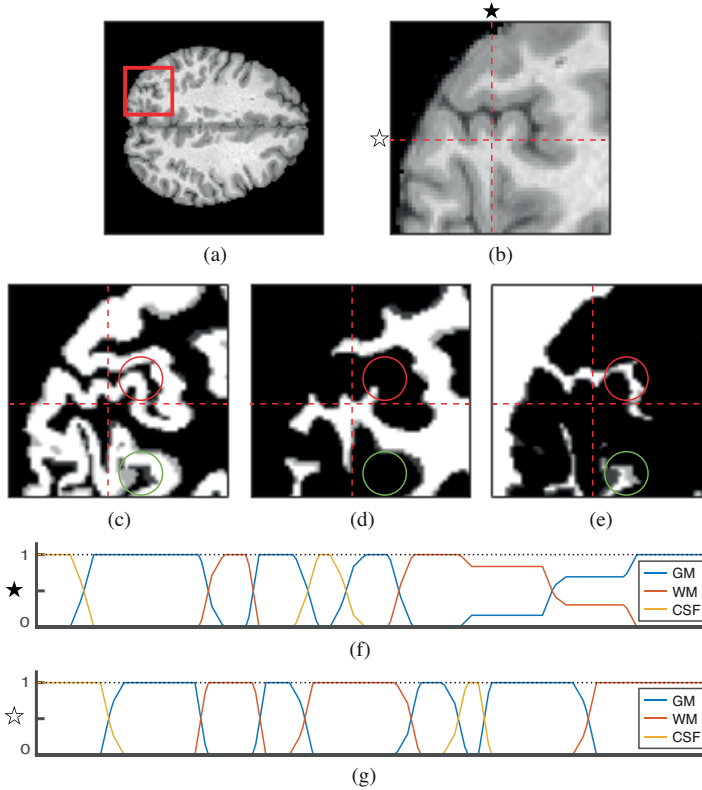
Figure 4.6: The inhomogeneous domain of fMRI data. (a) A slice of a structural brain MRI scan. (b) Close-up of the ROI shown in (a). (c)–(e) GM, WM and CSF of the ROI, respectively. (f)–(g) Domain data associated to the vertical and horizontal marked position in (c), respectively.

ing DIBLI on a 2-D slice of an fMRI volume. We use MRI data of a single subject from the Human Connectome Project [65]. The subject's high resolution structural MRI scan is used as the base for defining a description of the domain of the subjetc's fMRI data. Figure 4.6(b) shows a 2-D slice of the anatomical structure of an individual's brain. A close-up of an ROI marked in Figure 4.6(a) is shown in Figure 4.6(b). Segmenting the structural scan, one obtains gray matter, white matter, and cerebrospinal probability maps, see Figures 4.6(c)–(e); these maps are used to define 1D subdomain functions that fully describe the domain of the fMRI samples. A sample of column and row domain data for the marked position in Figure 4.6(b), is illustrated in Figures 4.6(f) and (g), respectively.

A 2-D slice of an fMRI acquisition of the same subject, registered at the same
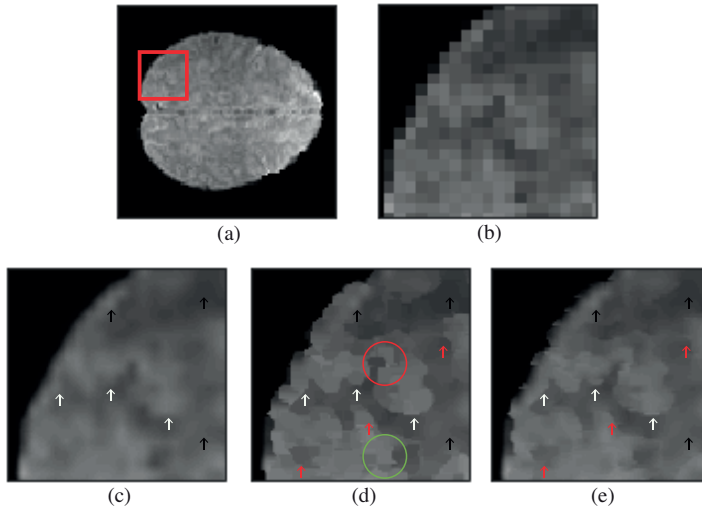
Figure 4.7: Domain-informed bilinear interpolation. (a) A 2-D slice of an fMRI volume. (b) Close-up of the ROI shown in (a). (c) SBLI. (d) DIBLI with maximal domain adaptation. (e) DIBLI with minimal domain adaptation.

anatomical position as the structural image is shown in Figure 4.7(a); the close-up of the marked ROI is shown in Figure 4.7(b). Figure 4.7(c) shows standard bilinear interpolation (SBLI) of the functional pixels shown in Figure 4.7(a). Two versions of DIBLI are shown in Figures 4.7(d) and (e), the former with maximal and the later with minimal adaptation to domain knowledge. SBLI and both version of DIBLI versions are identical at homogeneous parts of the domain (see black arrows), whereas at the inhomogeneous parts (see white arrows), both DIBLI versions present finer details. Sharp signal boundaries at the intersection of subdomains can be recovered by DIBLI; the accuracy is limited by the level of discrepancy observed in the convoluted domain description, see circled regions. DIBLI with maximal adaptation provides further details over the minimal adapted version at some parts (see red arrows). On the other hand, DIBLI with minimal adaptation, cf. Figure 4.7(e), may seem more visually appealing than Figure 4.7(d), and yet, it presents significant subtle details that are missing in SBLI.

Paper IV: Domain-informed spline interpolation

This paper extends the theory and results of Paper III in several respects. Firstly, the theory is extended to enable interpolations using higher order B-spline generating functions [173]. This required modifying the design scheme such that it becomes more robust relative to the extended support of higher order B-splines. In particular, rather than using the domain similarity metric as the basis for defining the domain-informed basis, a construction scheme that directly incorporates the given definition of the subdomains is developed. This is done by constructing a domain-informed generating basis that satisfies stability properties as in the classical, shift-invariant interpolation setting [174] (i) to satisfy the requirements of having a Riesz basis to ensure a stable unambiguous representation model, and (ii) to form a partition of unity across the domain to control the approximation error.

Figure 4.8(a) shows an inhomogeneous domain. Figures 4.8(b) and (c) illustrate domain-informed generating basis constructed for the domain shown in Figure 4.8(a), using B-spline kernels of order one and three, respectively. The constructed kernels respect the inhomogeneity of the domain, and present greater as well as smoother adaptation to the domain when using higher order B-splines.

By advantageously exploiting available domain knowledge, we demonstrate the benefit of domain-informed B-spline interpolation (DIBSI) over B-spline interpolation (BSI) through Monte Carlo simulations across a range of B-spline orders. In particular, we show that the interpolation error of DIBSI is lower than BSI across a range of spline orders ($n = 1$ to 6) and sampling steps, T, see Figure 4.9.

We also demonstrate the feasibility of DIBSI in an fMRI setting where the domain information is available by a complementary anatomical image, see Figure 4.10. In particular, the signal domain is given as a convoluted mixture of three subdomains,
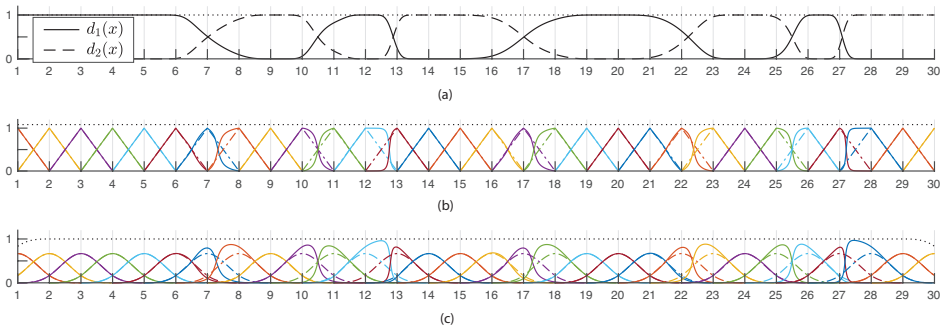
Figure 4.8: (a) A realization of an inhomogeneous domain. (b) Domain-informed B-splines of order 1. (c) Domain-informed B-splines of order 3.
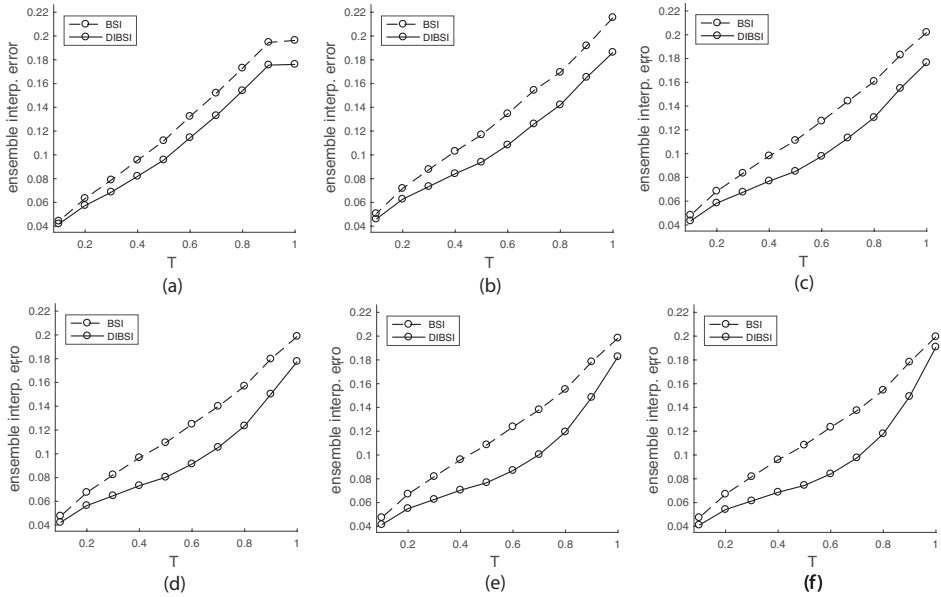
Figure 4.9: (a)-(f) Interpolation errors of DIBSI vs BSI using B-spline basis of orders 1 to 6, respectively.
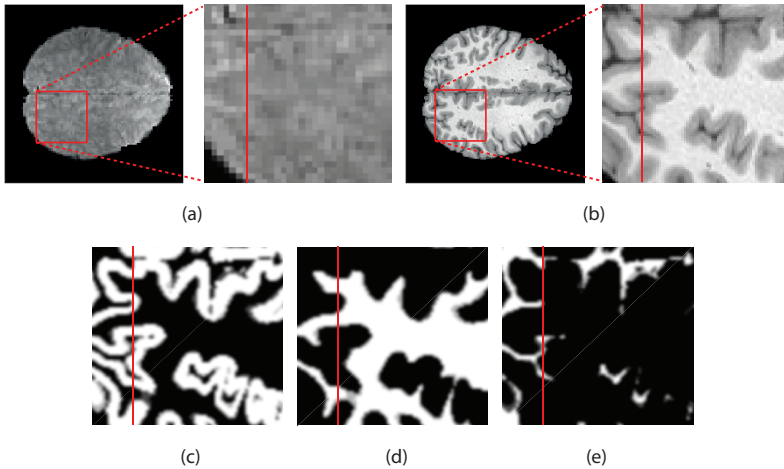
Figure 4.10: (a) A slice of fMRI data of a subject, including a close-up of an ROI. (b) The subject's brain anatomy at the same neurological coordinate as in (a). (c) Gray matter, (d) white matter and (e) cerebrospinal fluid segmented probability maps of the ROI shown in (b).
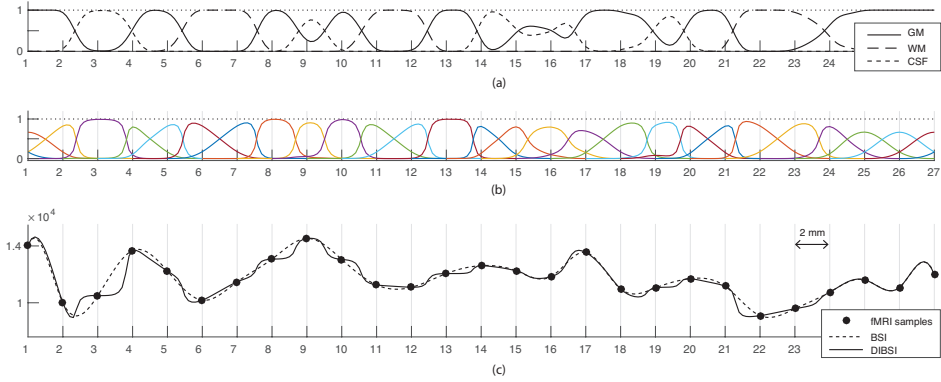
Figure 4.11: (a) Description of the inhomogeneous domain along the marked vertical line within the ROI in Figure 4.10(b). (b) DIBSI basis, of order three, associated to the domain shown in (a). (c) B-spline interpolation and domain-informed B-spline interpolation of the functional samples along the marked line within the ROI in Figure 4.10(a).

namely, gray matter, white matter and cerebrospinal fluid, see Figures 4.10(c)–(e). The description of the domain along one column of the 2-D image is shown in Figure 4.11(a). The constructed domain-informed third order B-splines are shown in Figure 4.11(b). The kernels are adapted to the convoluted description of the domain, and are robust to complex delineation patterns between subdomains, for example see interval 14 to 17. Figure 4.11(c) shows the fMRI samples along the marked line shown in Figure 4.10(a), as well as the resulting BSI and DIBSI interpolants. At any homogeneous parts of the domain DIBSI results in an interpolant that is identical to BSI; for instance see the DIBSI and BSI interpolants within interval 24 to 27 in Figure 4.11(b). At the inhomogeneous parts of the domain, DIBSI presents finer details than the SBLI image. For instance, see the domain description within the interval 7 to 15, cf. Figure 4.11(a). Within this interval samples from gray matter (samples 8 and 10), white matter (samples 7 and 11) and cerebrospinal fluid (sample 9) are given, cf. Figure 4.11(c). On the one hand, both BSI and DIBSI satisfy the consistency principle at the sample points. On the other hand, in between the samples, BSI maintains the smoothness characteristic enforced by using third-order B-splines, whereas DIBSI leads to a signal that is consistent with the anatomy of the brain.

Future work

The methods presented in this thesis can be extended in few respects and be exploited in other application settings. The proposed graph-based activation mapping scheme in Paper I exhibits enhanced sensitivity in detecting subtle weak activations within gray matter. This suggests the potential of exploiting a similar anatomically-adapted scheme for detecting activations within brain white matter; this requires extending the graph definition to encode not only local topology, but also white matter microstructure provided by diffusion MRI data, similar to the design proposed in [175]. Preliminary results based on this idea [127], suggest an enhanced capability to detect functional activity within white matter, which in turn can open up new perspectives on the functional dynamics of the human brain.

As another research avenue, the proposed gray matter encoding graph in Paper I can be adopted in structural studies of the brain, in particular, for characterizing the progression of brain atrophy observed in neurodegenerative disorders such as Alzheimer's disease and its prodromal stage, mild cognitive impairment. Regional morphological alterations in cortical and subcortical structures can be characterized based on variations in the Laplacian spectrum using spectral matching [176] or learning schemes [177, 178]. The characterization can also be done within a multi-scale setting as that implemented using Euclidean wavelets [179, 180]. From a design perspective, the gray matter graph in Paper I can be extended in two respects. Firstly, cortical surface reconstructions [181, 182] can be exploited to prune spurious graph edges across touching banks of sulci. Secondly, the design of graphs associated to localized gray matter regions across the brain can be considered. The latter extension enables obtaining local topology encoding graph eigenmodes [183] or graph Slepian functions [184], which can prove beneficial in providing more efficient representation of functional data as well as cortical athrophy.

The proposed scheme in Paper II can be exploited to design frames that account for dynamics of cortical activity [185, 186]. By constructing the ensemble energy spectral density based on the moment-to-moment functional data defined on a structural back-bone [27, 187], the resulting signal-adapted frame can be used to manifest long-range interactions and fine-scale local organization in the functional data [188]. From a computational perspective, the design in Paper II can be improved to prevent the need for a full eigendecomposition of the graph Laplacian matrix, which can be cumbersome for large and impractical for extensively large graphs. A remedy would be to approximate the ensemble spectral content by either using recently proposed graph spectral estimation techniques [8] or using a polynomial decomposition scheme, cf. Section 2.6, to obtain estimates at the resolution of subbands.

Results from applying the interpolation scheme presented in Paper IV on fMRI data demonstrated the potential of this scheme in obtaining functional patterns con-

sistent to brain anatomy. To account for the 3-D structure of the brain, the interpolation needs to be extended. One approach is to use tensor products to obtain a separable extension to higher order Euclidean spaces, similar to that used in Paper III. A tensor product extension can only incorporate domain knowledge along the Euclidean axis, which may lead to inconsistent interpolation patterns if the domain description is convoluted. Designing a non-separable higher dimensional extension can prove to be more efficient. Moreover, from a design perspective, the definition of the domain can be extended to incorporate cortical surface reconstructions that define white/gray matter boundary and CSF/gray matter boundaries [181, 182]. Such information is necessary to prevent the mixing of samples from (i) touching gray matter on the two banks of a sulci or (ii) opposite sides of gyri that are separated by a narrow band of white matter. This requires extending the problem formulation to allow sharp transients being introduced in the domain definition, and in turn, to account for such singularities when designing the domain-informed B-splines.

References

[1] A. Ciancio, S. Pattem, A. Ortega, and B. Krishnamachari, "Energy-efficient data representation and routing for wireless sensor networks based on a distributed wavelet compression algorithm," in *Proc. Int. Conf. Inf. Process. Sensor Netw.*, pp. 309–316, ACM, 2006.

[2] M. Girvan and M. E. Newman, "Community structure in social and biological networks," *Proc. Natl Acad. Sci.*, vol. 99, no. 12, pp. 7821–7826, 2002.

[3] E. Bullmore and O. Sporns, "Complex brain networks: graph theoretical analysis of structural and functional systems.," *Nat. Rev. Neurosci.*, vol. 10, no. 3, pp. 186–198, 2009.

[4] R. F. Betzel and D. S. Bassett, "Multi-scale brain networks," *NeuroImage*, vol. 160, pp. 73–83, 2017.

[5] A. Ortega, P. Frossard, J. Kovačević, J. M. Moura, and P. Vandergheynst, "Graph signal processing," *arXiv preprint arXiv:1712.00468*, 2017.

[6] A. G. Marques, S. Segarra, G. Leus, and A. Ribeiro, "Sampling of graph signals with successive local aggregations," *IEEE Trans. Signal Process.*, vol. 64, no. 7, pp. 1832–1843, 2016.

[7] A. Hashemi, R. Shafipour, H. Vikalo, and G. Mateos, "Sampling and reconstruction of graph signals via weak submodularity and semidefinite relaxation," *arXiv preprint arXiv:1711.00142*, 2017.

[8] A. G. Marques, S. Segarra, G. Leus, and A. Ribeiro, "Stationary graph processes and spectral estimation," *IEEE Trans. Signal Process.*, vol. 65, no. 22, pp. 5911–5926, 2016.

[9] N. Perraudin and P. Vandergheynst, "Stationary signal processing on graphs," *IEEE Trans. Signal Process.*, vol. 65, no. 13, pp. 3462–3477, 2017.

[10] A. Agaskar and Y. M. Lu, "A spectral graph uncertainty principle," *IEEE Trans. Inf. Theory*, vol. 59, no. 7, pp. 4338–4356, 2013.

[11] M. Tsitsvero, S. Barbarossa, and P. Di Lorenzo, "Signals on graphs: uncertainty principle and sampling," *IEEE Trans. Signal Process.*, 2016. DOI 10.1109/TSP.2016.2573748.

[12] D. I. Shuman, S. K. Narang, P. Frossard, A. Ortega, and P. Vandergheynst, "The emerging field of signal processing on graphs: Extending high-dimensional data analysis to networks and other irregular domains," *IEEE Signal Process. Mag.*, vol. 30, no. 3, pp. 83–98, 2013.

[13] R. Shafipour, A. Khodabakhsh, G. Mateos, and E. Nikolova, "A digraph fourier transform with spread frequency components," *arXiv preprint arXiv:1705.10821*, 2017.

[14] A. Gavili and X.-P. Zhang, "On the shift operator, graph frequency, and optimal filtering in graph signal processing," *IEEE Trans. Signal Process.*, vol. 65, no. 23, pp. 6303–6318, 2017.

[15] D. Romero, M. Ma, and G. B. Giannakis, "Kernel-based reconstruction of graph signals," *IEEE Trans. Signal Process.*, vol. 65, no. 3, pp. 764–778, 2017.

[16] A. Venkitaraman, S. Chatterjee, and P. Händel, "Kernel regression for signals over graphs," *arXiv preprint arXiv:1706.02191*, 2017.

[17] R. R. Coifman and M. Maggioni, "Diffusion wavelets," *Appl. Comput. Harmon. Anal.*, vol. 21, no. 1, pp. 53–94, 2006.

[18] D. Hammond, P. Vandergheynst, and R. Gribonval, "Wavelets on graphs via spectral graph theory," *Appl. Comput. Harmon. Anal.*, vol. 30, no. 2, pp. 129–150, 2011.

[19] Y. Tanaka and A. Sakiyama, "M-channel oversampled graph filter banks," *IEEE Trans. Signal Process.*, vol. 62, no. 14, pp. 3578–3590, 2014.

[20] D. Thanou, D. I. Shuman, and P. Frossard, "Learning parametric dictionaries for signals on graphs," *IEEE Trans. Signal Process.*, vol. 62, no. 15, pp. 3849–3862, 2014.

[21] W. Hu, G. Cheung, A. Ortega, and O. C. Au, "Multiresolution graph fourier transform for compression of piecewise smooth images," *IEEE Trans. Image Process.*, vol. 24, no. 1, pp. 419–433, 2015.

[22] D. Thanou, P. A. Chou, and P. Frossard, "Graph-based compression of dynamic 3D point cloud sequences," *IEEE Trans. Image Process.*, vol. 25, no. 4, pp. 1765–1778, 2016.

[23] N. Perraudin, N. Holighaus, and P. Majdak, "Inpainting of long audio segments with similarity graphs," *IEEE/ACM Trans. Audio Speech Lang.*, 2018. doi:10.1109/TASLP.2018.2809864.

[24] A. Venkitaraman, S. Chatterjee, and P. Händel, "Hilbert transform, analytic signal, and modulation analysis for graph signal processing," *arXiv preprint arXiv:1611.05269*, 2016.

[25] A. Pirayre, C. Couprie, F. Bidard, L. Duval, and J.-C. Pesquet, "BRANE Cut: biologically-related a priori network enhancement with graph cuts for gene regulatory network inference," *BMC bioinformatics*, vol. 16, no. 1, p. 368, 2015.

[26] A. Pirayre, C. Couprie, L. Duval, and J. C. Pesquet, "BRANE Clust: Cluster-assisted gene regulatory network inference refinement," *IEEE/ACM Trans. Comput. Biol. Bioinf.*, 2018.

[27] W. Huang, T. A. W. Bolton, J. D. Medaglia, D. S. Bassett, A. Ribeiro, and D. V. D. Ville, "A graph signal processing perspective on functional brain imaging," *Proc. IEEE*, vol. PP, no. 99, pp. 1–18, 2018.

[28] W. H. Kim, V. Singh, M. K. Chung, C. Hinrichs, D. Pachauri, O. C. Okonkwo, and S. C. Johnson, "Multi-resolutional shape features via non-Euclidean wavelets: Applications to statistical analysis of cortical thickness," *NeuroImage*, vol. 93, pp. 107–123, 2014.

[29] C. Hu, J. Sepulcre, K. A. Johnson, G. E. Fakhri, Y. M. Lu, and Q. Li, "Matched signal detection on graphs: Theory and application to brain imaging data classification," *NeuroImage*, vol. 125, pp. 587–600, 2016.

[30] Y. Guo, H. Nejati, and N.-M. Cheung, "Deep neural networks on graph signals for brain imaging analysis," *arXiv preprint arXiv:1705.04828*, 2017.

[31] A. Sandryhaila and J. Moura, "Discrete signal processing on graphs.," *IEEE Trans. Signal Process.*, vol. 61, pp. 1644–1656, 2013.

[32] A. Sandryhaila and J. M. Moura, "Discrete signal processing on graphs: Frequency analysis," *IEEE Trans. Signal Process.*, vol. 62, no. 12, pp. 3042–3054, 2014.

[33] S. Chen, R. Varma, A. Sandryhaila, and J. Kovačević, "Discrete signal processing on graphs: sampling theory," *IEEE Trans. Signal Process.*, vol. 63, no. 24, pp. 6510–6523, 2015.

[34] K. He, L. Stankovic, J. Liao, and V. Stankovic, "Non-intrusive load disaggregation using graph signal processing," *IEEE Trans. Smart Grid*, 2016.

[35] D. Gleich, "The MatlabBGL matlab library [online]."

[36] H. Behjat, N. Leonardi, L. Sörnmo, and D. Van De Ville, "Canonical cerebellar graph wavelets and their application to fMRI activation mapping," in *Proc. IEEE Int. Conf. Eng. Med. Biol. Soc.*, pp. 1039–1042, 2014.

[37] F. Chung, *Spectral graph theory*. Providence, RI: AMS, 1997.

[38] S. Mallat, *A wavelet tour of signal processing: the sparse way*. Academic press, 2008.

[39] I. Daubechies, *Ten lectures on wavelets*, vol. 61. Siam, 1992.

[40] S. G. Mallat, "A theory for multiresolution signal decomposition: the wavelet representation," *IEEE Trans. Pattern Anal. Mach. Intell.*, vol. 11, no. 7, pp. 674–693, 1989.

[41] S. K. Narang and A. Ortega, "Perfect reconstruction two-channel wavelet filter banks for graph structured data," *IEEE Trans. Signal Process.*, vol. 60, no. 6, pp. 2786–2799, 2012.

[42] D. I. Shuman, B. Ricaud, and P. Vandergheynst, "Vertex-frequency analysis on graphs," *Appl. Comput. Harmon. Anal.*, 2015. doi: 10.1016/j.acha.2015.02.005.

[43] L. Stankovic, E. Sejdic, and M. Dakovic, "Vertex-frequency energy distributions," *IEEE Signal Process. Lett.*, 2017.

[44] S. K. Narang and A. Ortega, "Compact support biorthogonal wavelet filterbanks for arbitrary undirected graphs," *IEEE Trans. Signal Process.*, vol. 61, no. 19, pp. 4673–4685, 2013.

[45] D. B. H. Tay and J. Zhang, "Techniques for constructing biorthogonal bipartite graph filter banks," *IEEE Trans. Signal Process.*, vol. 63, no. 21, pp. 5772–5783, 2015. doi: 10.1109/TSP.2015.2460216.

[46] N. Tremblay and P. Borgnat, "Subgraph-based filterbanks for graph signals," *IEEE Trans. Signal Process.*, vol. 64, no. 15, pp. 3827–3840, 2016.

[47] A. Sakiyama and Y. Tanaka, "Oversampled graph Laplacian matrix for graph filter banks," *IEEE Trans. Signal Process.*, vol. 62, no. 24, pp. 6425–6437, 2014.

[48] N. Leonardi and D. Van De Ville, "Tight wavelet frames on multislice graphs," *IEEE Trans. Signal Process.*, vol. 61, no. 13, pp. 3357–3367, 2013.

[49] D. I. Shuman, C. Wiesmeyr, N. Holighaus, and P. Vandergheynst, "Spectrum-adapted tight graph wavelet and vertex-frequency frames," *IEEE Trans. Signal Process.*, vol. 63, no. 16, pp. 4223–4235, 2015.

[50] M. Jansen, G. P. Nason, and B. W. Silverman, "Multiscale methods for data on graphs and irregular multidimensional situations," *J. Roy. Statistical Soc.: Series B (Statistical Methodology)*, vol. 71, no. 1, pp. 97–125, 2009.

[51] I. Ram, M. Elad, and I. Cohen, "Generalized tree-based wavelet transform," *IEEE Trans. Signal Process.*, vol. 59, no. 9, pp. 4199–4209, 2011.

[52] R. Rustamov and L. Guibas, "Wavelets on graphs via deep learning," in *Proc. Adv. Neural Info. Proces. Syst.*, pp. 998–1006, 2013.

[53] D. I. Shuman, M. J. Faraji, and P. Vandergheynst, "A multiscale pyramid transform for graph signals," *IEEE Trans. Signal Process.*, vol. 64, no. 8, pp. 2119–2134, 2016.

[54] H. Berger, "Über das elektrenkephalogramm des menschen," *Archiv für psychiatrie und nervenkrankheiten*, vol. 87, no. 1, pp. 527–570, 1929.

[55] M. M. Ter-Pogossian, M. E. Phelps, E. J. Hoffman, and N. A. Mullani, "A positron-emission transaxial tomograph for nuclear imaging (pett)," *Radiolog*, vol. 114, no. 1, pp. 89–98, 1975.

[56] S. Ogawa, R. S. Menon, D. W. Tank, S. G. Kim, H. Merkle, J. M. Ellermann, and K. Ugurbil, "Functional brain mapping by blood oxygenation level-dependent contrast magnetic resonance imaging. A comparison of signal characteristics with a biophysical model.," *Biophys. J.*, vol. 64, no. 3, pp. 803–812, 1993.

[57] L. Sörnmo and P. Laguna, *Bioelectrical signal processing in cardiac and neurological applications*, vol. 8. Academic Press, 2005.

[58] B. V. Zlokovic and M. L. Apuzzo, "Strategies to circumvent vascular barriers of the central nervous system," *Neurosurg.*, vol. 43, no. 4, pp. 877–878, 1998.

[59] R. B. Buxton, E. C. Wong, and L. R. Frank, "Dynamics of blood flow and oxygenation changes during brain activation: the balloon model," *Mag. Reson. Med.*, vol. 39, no. 6, pp. 855–864, 1998.

[60] K. J. Friston, A. Mechelli, R. Turner, and C. J. Price, "Nonlinear responses in fMRI: the balloon model, volterra kernels, and other hemodynamics," *NeuroImage*, vol. 12, no. 4, pp. 466–477, 2000.

[61] G. K. Aguirre, E. Zarahn, and M. D'esposito, "The variability of human, bold hemodynamic responses," *NeuroImage*, vol. 8, no. 4, pp. 360–369, 1998.

[62] G. H. Glover, "Deconvolution of impulse response in event-related bold fMRI1," *NeuroImage*, vol. 9, no. 4, pp. 416–429, 1999.

[63] D. L. Collins, P. Neelin, T. M. Peters, and A. C. Evans, "Automatic 3D intersubject registration of mr volumetric data in standardized talairach space.," *J. Comput. Assist. Tomogr.*, vol. 18, no. 2, pp. 192–205, 1994.

[64] M. K. Stehling, R. Turner, and P. Mansfield, "Echo-planar imaging: magnetic resonance imaging in a fraction of a second," *Sci.*, vol. 254, no. 5028, pp. 43–50, 1991.

[65] D. Van Essen, S. Smith, D. Barch, T. Behrens, E. Yacoub, K. Ugurbil, and W.-M. H. Consortium., "The WU-Minn human connectome project: an overview.," *NeuroImage*, vol. 80, pp. 62–79, 2013.

[66] J. V. Haxby, M. I. Gobbini, M. L. Furey, A. Ishai, J. L. Schouten, and P. Pietrini, "Distributed and overlapping representations of faces and objects in ventral temporal cortex," *Sci.*, vol. 293, no. 5539, pp. 2425–2430, 2001.

[67] B. Biswal, F. Zerrin Yetkin, V. M. Haughton, and J. S. Hyde, "Functional connectivity in the motor cortex of resting human brain using echo-planar mri," *Magn. Reson. Med.*, vol. 34, no. 4, pp. 537–541, 1995.

[68] A. H. Andersen, D. M. Gash, and M. J. Avison, "Principal component analysis of the dynamic response measured by fMRI: a generalized linear systems framework," *Magn. Reson. Imaging*, vol. 17, no. 6, pp. 795–815, 1999.

[69] V. D. Calhoun, T. Adali, G. D. Pearlson, and J. J. Pekar, "A method for making group inferences from functional MRI data using independent component analysis," *Hum. Brain Mapp.*, vol. 14, no. 3, pp. 140–151, 2001.

[70] C. F. Beckmann and S. M. Smith, "Probabilistic independent component analysis for functional magnetic resonance imaging," *IEEE Trans. Med. Imag.*, vol. 23, no. 2, pp. 137–152, 2004.

[71] V. D. Calhoun and T. Adali, "Unmixing fMRI with independent component analysis," *IEEE Eng. Med. Biol. Mag.*, vol. 25, no. 2, pp. 79–90, 2006.

[72] O. Friman, P. Borga, M. Lundberg, and H. Knutsson, "Detection of neural activity in fmri using maximum correlation modeling," *NeuroImage*, vol. 15, pp. 386–395, 2002.

[73] O. Friman, M. Borga, P. Lundberg, and H. Knutsson, "Exploratory fMRI analysis by autocorrelation maximization," *NeuroImage*, vol. 16, no. 2, pp. 454–464, 2002.

[74] C. Caballero Gaudes, N. Petridou, S. T. Francis, I. L. Dryden, and P. A. Gowland, "Paradigm free mapping with sparse regression automatically detects single-trial functional magnetic resonance imaging blood oxygenation level dependent responses," *Hum. Brain Mapp.*, vol. 34, no. 3, pp. 501–518, 2013.

[75] F. I. Karahanoğlu, C. Caballero-Gaudes, F. Lazeyras, and D. Van De Ville, "Total activation: fMRI deconvolution through spatio-temporal regularization," *NeuroImage*, vol. 73, pp. 121–134, 2013.

[76] I. Khalidov, J. Fadili, F. Lazeyras, D. Van De Ville, and M. Unser, "Activelets: Wavelets for sparse representation of hemodynamic responses," *Signal Process.*, vol. 91, no. 12, pp. 2810–2821, 2011.

[77] K. J. Friston, A. P. Holmes, K. J. Worsley, J.-P. Poline, C. D. Frith, and R. S. J. Frackowiak, "Statistical parametric maps in functional imaging: a general linear approach," *Hum. Brain Mapp.*, vol. 2, pp. 189–210, 1994.

[78] M. Jenkinson, C. F. Beckmann, T. E. Behrens, M. W. Woolrich, and S. M. Smith, "Fsl," *NeuroImage*, vol. 62, no. 2, pp. 782–790, 2012.

[79] R. W. Cox, "Afni: software for analysis and visualization of functional magnetic resonance neuroimages," *Comput. Biomed. Res.*, vol. 29, no. 3, pp. 162–173, 1996.

[80] S. D. Forman, J. D. Cohen, M. Fitzgerald, W. F. Eddy, M. A. Mintun, and D. C. Noll, "Improved assessment of significant activation in functional magnetic resonance imaging (fMRI): use of a cluster-size threshold," *Magn. Reson. Med.*, vol. 33, no. 5, pp. 636–647, 1995.

[81] D. Van De Ville, T. Blu, and M. Unser, "Integrated wavelet processing and spatial statistical testing of fMRI data," *NeuroImage*, vol. 23, pp. 1472–1485, 2004.

[82] T. Nichols and S. Hayasaka, "Controlling the familywise error rate in functional neuroimaging: a comparative review," *Stat. Methods Med. Res.*, vol. 12, no. 5, pp. 419–446, 2003.

[83] J. B. Poline, K. J. Worsley, A. C. Evans, and K. J. Friston, "Combining spatial extent and peak intensity to test for activations in functional imaging.," *NeuroImage*, vol. 5, pp. 83–96, 1997.

[84] K. J. Worsley, S. Marrett, P. Neelin, A. C. Vandal, K. J. Friston, and A. C. Evans, "A unified statistical approach for determining significant signals in images of cerebral activation," *Hum. Brain Mapp.*, vol. 4, pp. 58–73, 1996.

[85] A. Eklund, M. Andersson, C. Josephson, M. Johannesson, and H. Knutsson, "Does parametric fMRI analysis with SPM yield valid results? - An empirical study of 1484 rest datasets.," *NeuroImage*, vol. 61, no. 3, pp. 565–578, 2012.

[86] A. Eklund, T. Nichols, and H. Knutsson, "Cluster failure: Why fMRI inferences for spatial extent have inflated false-positive rates," *Proc. Natl Acad. Sci.*, vol. 113, no. 28, pp. 7900–7905, 2016.

[87] A. P. Holmes, R. Blair, J. Watson, and I. Ford, "Nonparametric analysis of statistic images from functional mapping experiments," *J. of Cereb. Blood Flow Metab.*, vol. 16, no. 1, pp. 7–22, 1996.

[88] T. E. Nichols and A. P. Holmes, "Nonparametric permutation tests for functional neuroimaging: a primer with examples," *Hum. Brain Mapp.*, vol. 15, no. 1, pp. 1–25, 2002.

[89] T. E. Lund, K. H. Madsen, K. Sidaros, W.-L. Luo, and T. E. Nichols, "Non-white noise in fMRI: does modelling have an impact?," *NeuroImage*, vol. 29, no. 1, pp. 54–66, 2006.

[90] A. M. Smith, B. K. Lewis, U. E. Ruttimann, Q. Y. Frank, T. M. Sinnwell, Y. Yang, J. H. Duyn, and J. A. Frank, "Investigation of low frequency drift in fMRI signal," *NeuroImage*, vol. 9, no. 5, pp. 526–533, 1999.

[91] K. J. Friston, S. Williams, R. Howard, R. S. Frackowiak, and R. Turner, "Movement-related effects in fMRI time-series," *Magn. Reson. Med.*, vol. 35, no. 3, pp. 346–355, 1996.

[92] H. J. Jo, J. M. Lee, J. H. Kim, Y. W. Shin, I. Y. Kim, J. S. Kwon, and S. I. Kim, "Spatial accuracy of fMRI activation influenced by volume- and surface-based spatial smoothing techniques," *NeuroImage*, vol. 34, no. 2, pp. 550–564, 2007.

[93] M. Mikl, R. Mareček, P. Hluštík, M. Pavlicová, A. Drastich, P. Chlebus, M. Brázdil, and P. Krupa, "Effects of spatial smoothing on fmri group inferences," *Magn. Reson. Imaging*, vol. 26, no. 4, pp. 490–503, 2008.

[94] O. Friman, M. Borga, P. Lundberg, and H. Knutsson, "Adaptive analysis of fMRI data," *NeuroImage*, vol. 19, no. 3, pp. 837–845, 2003.

[95] G. A. Hossein-Zadeh, B. A. Ardekani, and H. Soltanian-Zadeh, "Activation detection in fMRI using a maximum energy ratio statistic obtained by adaptive spatial filtering," *IEEE Trans. Med. Imag.*, vol. 22, no. 7, pp. 795–805, 2003.

[96] H. Y. Kim, J. Giacomantone, and Z. H. Cho, "Robust anisotropic diffusion to produce enhanced statistical parametric map from noisy fMRI," *Comput. Vis. Image Underst.*, vol. 99, no. 3, pp. 435–452, 2005.

[97] H. Knutsson, R. Wilson, and G. Granlund, "Anisotropic nonstationary image estimation and its applications: Part i–restoration of noisy images," *IEEE Trans. Commun.*, vol. 31, no. 3, pp. 388–397, 1983.

[98] W. T. Freeman, E. H. Adelson, *et al.*, "The design and use of steerable filters," *IEEE Trans. Pattern Anal. Mach. Intell.*, vol. 13, no. 9, pp. 891–906, 1991.

[99] G.-A. Hossein-Zadeh, H. Soltanian-Zadeh, and B. A. Ardekani, "Multiresolution fmri activation detection using translation invariant wavelet transform and statistical analysis based on resampling," *IEEE Trans. Med. Imag.*, vol. 22, no. 3, pp. 302–314, 2003.

[100] A. M. Wink and J. B. Roerdink, "Denoising functional MR images: a comparison of wavelet denoising and gaussian smoothing," *IEEE Trans. Med. Imag.*, vol. 23, no. 3, pp. 374–387, 2004.

[101] J. Aston, R. Gunn, and F. Hinz, R. Turkheimer, "Wavelet variance components in image space for spatiotemporal neuroimaging data," *NeuroImage*, vol. 25, no. 1, pp. 159–168, 2005.

[102] M. Breakspear, E. T. Bullmore, K. Aquino, P. Das, and L. M. Williams, "The multiscale character of evoked cortical activity," *NeuroImage*, vol. 30, no. 4, pp. 1230–1242, 2006.

[103] G. Flandin and W. D. Penny, "Bayesian fMRI data analysis with sparse spatial basis function priors," *NeuroImage*, vol. 34, no. 3, pp. 1108–1125, 2007.

[104] N. Sanyal and M. A. Ferreira, "Bayesian hierarchical multi-subject multiscale analysis of functional MRI data," *NeuroImage*, vol. 63, no. 3, pp. 1519–1531, 2012.

[105] E. Bullmore, J. Fadili, V. Maxim, L. Sendur, B. Whitcher, J. Suckling, M. Brammer, and M. Breakspear, "Wavelets and functional magnetic resonance imaging of the human brain.," *NeuroImage*, vol. 23 Suppl 1, pp. S234–S249, 2004.

[106] U. E. Ruttimann, M. Unser, R. R. Rawlings, D. Rio, N. F. Ramsey, D. Mattay, V. S. Hommer, J. Frank, and D. R. Weinberger, "Statistical analysis of functional MRI data in the wavelet domain," *IEEE Trans. Med. Imag.*, vol. 17, no. 2, pp. 142–154, 1998.

[107] F. E. Turkheimer, M. Brett, J. A. Aston, A. P. Leff, P. A. Sargent, R. J. Wise, P. M. Grasby, and V. J. Cunningham, "Statistical modeling of positron emission tomography images in wavelet space," *J. of Cereb. Blood Flow Metab.*, vol. 20, no. 11, pp. 1610–1618, 2000.

[108] D. Van De Ville, T. Blu, and M. Unser, "Surfing the brain – An overview of wavelet-based techniques for fMRI data analysis.," *IEEE Eng. Med. Biol. Mag.*, vol. 25, pp. 65–78, 2006.

[109] S. G. Mallat, "A theory for multiresolution signal decomposition: the wavelet representation," *IEEE Trans. Pattern Anal. Mach. Intell.*, vol. 11, no. 3, pp. 674–693, 1989.

[110] D. Van De Ville, M. Seghier, F. Lazeyras, T. Blu, and M. Unser, "WSPM: wavelet-based statistical parametric mapping.," *NeuroImage*, vol. 37, pp. 1205–1217, 2007.

[111] C. R. Genovese, N. A. Lazar, and T. Nichols, "Thresholding of statistical maps in functional neuroimaging using the false discovery rate," *NeuroImage*, vol. 15, no. 4, pp. 870–878, 2002.

[112] D. Van De Ville and M. Unser, "False discovery rate for wavelet-based statistical parametric mapping," *IEEE J. Sel. Top. Signal Process.*, vol. 2, no. 6, pp. 897–906, 2008.

[113] S. M. Kay, "Fundamentals of statistical signal processing, vol. ii: Detection theory," *Signal Processing. Upper Saddle River, NJ: Prentice Hall*, 1998.

[114] J. Ashburner and K. J. Friston, "Unified segmentation," *NeuroImage*, vol. 26, no. 3, pp. 839–851, 2005.

[115] E. R. Kandel, J. H. Schwartz, T. M. Jessell, S. A. Siegelbaum, A. J. Hudspeth, and S. Mack, eds., *Principles of neural science*. McGraw-Hill medical, New York [u.a.]: McGraw-Hill Medical, 5. ed. ed., 2013.

[116] T. H. Jochimsen, D. Ivanov, D. V. Ott, W. Heinke, R. Turner, H. E. Möller, and J. R. Reichenbach, "Whole-brain mapping of venous vessel size in humans using the hypercapnia-induced bold effect," *NeuroImage*, vol. 51, no. 2, pp. 765–774, 2010.

[117] N. Logothetis and B. Wandell, "Interpreting the BOLD signal.," *Annu. Rev. Physiol.*, vol. 66, pp. 735–769, 2004.

[118] T. Yarkoni, D. M. Barch, J. R. Gray, T. E. Conturo, and T. S. Braver, "Bold correlates of trial-by-trial reaction time variability in gray and white matter: a multi-study fMRI analysis," *PLoS One*, vol. 4, no. 1, p. e4257, 2009.

[119] E. L. Mazerolle, S. D. Beyea, J. R. Gawryluk, K. D. Brewer, C. V. Bowen, and R. C. D'arcy, "Confirming white matter fMRI activation in the corpus callosum: co-localization with DTI tractography," *NeuroImage*, vol. 50, no. 2, pp. 616–621, 2010.

[120] J. R. Gawryluk, E. L. Mazerolle, and R. C. D'Arcy, "Does functional mri detect activation in white matter? a review of emerging evidence, issues, and future directions," *Front. Neurosci.*, vol. 8, p. 239, 2014.

[121] L. Marussich, K.-H. Lu, H. Wen, and Z. Liu, "Mapping white-matter functional organization at rest and during naturalistic visual perception," *NeuroImage*, vol. 146, pp. 1128–1141, 2017.

[122] M. Peer, M. Nitzan, A. S. Bick, N. Levin, and S. Arzy, "Evidence for functional networks within the human brain's white matter," *J. Neurosci.*, vol. 37, no. 27, pp. 6394–6407, 2017.

[123] Z. Ding, Y. Huang, S. K. Bailey, Y. Gao, L. E. Cutting, B. P. Rogers, A. T. Newton, and J. C. Gore, "Detection of synchronous brain activity in white matter tracts at rest and under functional loading," *Proc. Natl Acad. Sci.*, vol. 115, no. 3, pp. 595–600, 2018.

[124] J. R. Gawryluk, K. D. Brewer, S. D. Beyea, and R. C. D'arcy, "Optimizing the detection of white matter fMRI using asymmetric spin echo spiral," *NeuroImage*, vol. 45, no. 1, pp. 83–88, 2009.

[125] J. H. Kim and D. Ress, "Reliability of the depth-dependent high-resolution bold hemodynamic response in human visual cortex and vicinity," *Magn. Reson. Imag.*, vol. 39, pp. 53–63, 2017.

[126] M. J. Courtemanche, C. J. Sparrey, X. Song, A. MacKay, and R. C. D'Arcy, "Detecting white matter activity using conventional 3 tesla fMRI: An evaluation of standard field strength and hemodynamic response function," *NeuroImage*, vol. 169, pp. 145–150, 2018.

[127] D. Abramian Petrosian and M. Larsson, "Diffusion-adapted spatial filtering of fMRI data for improved activation mapping in white matter," 2017. Student Paper.

[128] C. C. Chen, C. W. Tyler, and H. A. Baseler, "Statistical properties of BOLD magnetic resonance activity in the human brain," *NeuroImage*, vol. 20, no. 2, pp. 1096–1109, 2003.

[129] M. Reimold, M. Slifstein, A. Heinz, W. Mueller-Schauenburg, and R. Bares, "Effect of spatial smoothing on t-maps: arguments for going back from t-maps to masked contrast images," *J. Cereb. Blood Flow Metab.*, vol. 26, no. 6, pp. 751–759, 2006.

[130] J. Acosta-Cabronero, G. B. Williams, J. M. Pereira, G. Pengas, and P. J. Nestor, "The impact of skull-stripping and radio-frequency bias correction on grey-matter segmentation for voxel-based morphometry," *NeuroImage*, vol. 39, no. 4, pp. 1654–1665, 2008.

[131] G. R. Ridgway, V. Litvak, G. Flandin, K. J. Friston, and W. D. Penny, "The problem of low variance voxels in statistical parametric mapping; a new hat avoids a ?haircut?," *NeuroImage*, vol. 59, no. 3, pp. 2131–2141, 2012.

[132] H. J. Jo, J. M. Lee, J. H. Kim, C. H. Choi, B. M. Gu, D. H. Kang, J. Ku, J. S. Kwon, and S. I. Kim, "Artificial shifting of fMRI activation localized by

volume-and surface-based analyses," *NeuroImage*, vol. 40, no. 3, pp. 1077–1089., 2008.

[133] K. J. Friston, A. P. Holmes, C. Price, C. Büchel, and K. Worsley, "Multisubject fMRI studies and conjunction analyses," *NeuroImage*, vol. 10, no. 4, pp. 385–396, 1999.

[134] J. F. Mangin, D. Riviere, A. Cachia, E. Duchesnay, Y. Cointepas, D. Papadopoulos-Orfanos, P. Scifo, T. Ochiai, F. Brunelle, and J. Regis, "A framework to study the cortical folding patterns.," *NeuroImage*, vol. 23, pp. S129–S138, 2004.

[135] D. Riviere, J. Mangin, P.-O. D., j. M. Martinez, V. Frouin, and J. Regis, "Automatic recognition of cortical sulci of the human brain using a congregation of neural networks," *Med. Image Anal.*, vol. 6, no. 2, pp. 77–92., 2002.

[136] A. Collignon, F. Maes, D. Delaere, D. Vandermeulen, P. Suetens, and G. Marchal, "Automated multi-modality image registration based on information theory," in *Inf. Process. Med. Imag.*, vol. 3, pp. 263–274, 1995.

[137] J. Ashburner and K. Friston, "Multimodal image coregistration and partitioning?a unified framework," *NeuroImage*, vol. 6, no. 3, pp. 209–217, 1997.

[138] J. Ashburner, K. J. Friston, *et al.*, "Nonlinear spatial normalization using basis functions," *Hum. Brain Mapp.*, vol. 7, no. 4, pp. 254–266, 1999.

[139] A. Evans, D. Louis Collins, S. R. Mills, E. D. Brown, R. L. Kelly, and T. M. Peters, "3D statistical neuroanatomical models from 305 MRI volumes," in *Nucl. Sci. Symp. Med. Imag. Conf.*, pp. 1813–1817, 1993.

[140] J. Mazziotta, A. Toga, A. Evans, P. Fox, J. Lancaster, K. Zilles, R. Woods, T. Paus, G. Simpson, B. Pike, *et al.*, "A probabilistic atlas and reference system for the human brain: International consortium for brain mapping (icbm)," *Philosophical Transactions of the Royal Society B: Biological Sciences*, vol. 356, no. 1412, pp. 1293–1322, 2001.

[141] J. Ashburner, "A fast diffeomorphic image registration algorithm," *NeuroImage*, vol. 38, pp. 95–113, 2007.

[142] A. Klein, J. Andersson, B. Ardekani, J. Ashburner, B. Avants, M. Chiang, G. Christensen, and et al, "Evaluation of 14 nonlinear deformation algorithms applied to human brain MRI registration," *NeuroImage*, vol. 46, no. 3, pp. 786–802, 2009.

[143] J. Diedrichsen, "A spatially unbiased atlas template of the human cerebellum," *NeuroImage*, vol. 33, no. 1, pp. 127–138, 2006.

[144] J. Diedrichsen, S. Maderwald, M. Küper, M. Thürling, K. Rabe, E. Gizewski, M. E. Ladd, and D. Timmann, "Imaging the deep cerebellar nuclei: a probabilistic atlas and normalization procedure," *NeuroImage*, vol. 54, no. 3, pp. 1786–1794, 2011.

[145] A. M. C. Kelly, L. Q. Uddin, B. B. Biswal, F. X. Castellanos, and M. P. Milham, "Competition between functional brain networks mediates behavioral variability," *NeuroImage*, vol. 39, no. 1, pp. 527–537, 2008.

[146] C. Grova, S. Makni, G. Flandin, P. Ciuciu, J. Gotman, and J. Poline, "Anatomically informed interpolation of fMRI data on the cortical surface," *NeuroImage*, vol. 31, no. 4, pp. 1475–1486, 2006.

[147] G. Operto, R. Bulot, J. L. Anton, and O. Coulon, "Projection of fMRI data onto the cortical surface using anatomically-informed convolution kernels," *NeuroImage*, vol. 39, no. 1, pp. 127–135, 2008.

[148] A. Andrade, F. Kherif, J. Mangin, K. J. Worsley, O. Paradis, A. Simon, S. Dehaene, D. L. Bihan, and J. Poline, "Detection of fMRI activation using cortical surface mapping," *Hum. Brain Mapp.*, vol. 12, no. 2, pp. 79–93, 2001.

[149] M. K. Chung and J. Taylor, "Diffusion smoothing on brain surface via finite element method," in *Proc. IEEE Int. Symp. Biomed. Imaging*, pp. 432–435, IEEE, 2004.

[150] D. J. Hagler Jr, A. P. Saygin, and M. I. Sereno, "Smoothing and cluster thresholding for cortical surface-based group analysis of fMRI data," *NeuroImage*, vol. 33, no. 4, pp. 1093–1103, 2006.

[151] A. Qiu, D. Bitouk, and M. I. Miller, "Smooth functional and structural maps on the neocortex via orthonormal bases of the Laplace-Beltrami operator," *IEEE Trans. Med. Imag.*, vol. 25, no. 10, pp. 1296–1306, 2006.

[152] S. J. Kiebel, R. Goebel, and K. J. Friston, "Anatomically informed basis functions," *NeuroImage*, vol. 11, no. 6, pp. 656–667, 2000.

[153] S. Kiebel and K. J. Friston, "Anatomically informed basis functions in multi-subject studies," *Hum. Brain Mapp.*, vol. 16, no. 1, pp. 36–46, 2002.

[154] N. C. Gabay and P. Robinson, "Cortical geometry as a determinant of brain activity eigenmodes: Neural field analysis," *Phys. Rev. E*, vol. 96, no. 3, p. 032413, 2017.

[155] M. Breakspear, "Dynamic models of large-scale brain activity," *Nat. Neurosci.*, vol. 20, no. 3, p. 340, 2017.

[156] S. Atasoy, I. Donnelly, and J. Pearson, "Human brain networks function in connectome-specific harmonic waves," *Nat. Commun.*, vol. 7, p. 10340, 2016.

[157] P. A. Robinson, X. Zhao, K. M. Aquino, J. Griffiths, S. Sarkar, and G. Mehta-Pandejee, "Eigenmodes of brain activity: neural field theory predictions and comparison with experiment," *NeuroImage*, vol. 142, pp. 79–98, 2016.

[158] P. Hagmann, L. Cammoun, X. Gigandet, R. Meuli, C. J. Honey, V. J. Wedeen, and O. Sporns, "Mapping the structural core of human cerebral cortex," *PLoS Biol.*, vol. 6, no. 7, p. e159, 2008.

[159] O. Sporns, G. Tononi, and R. Kötter, "The human connectome: a structural description of the human brain," *PLoS Comput. Biol.*, vol. 1, no. 4, p. e42, 2005.

[160] S. A. Walker, D. Miller, and J. Tanabe, "Bilateral spatial filtering: Refining methods for localizing brain activation in the presence of parenchymal abnormalities," *NeuroImage*, vol. 33, no. 2, pp. 564–569, 2006.

[161] J. Rydell, H. Knutsson, and M. Borga, "Bilateral filtering of fMRI data," *IEEE J. Sel. Top. Signal Process.*, vol. 2, no. 6, pp. 891–896, 2008.

[162] W. Ou, W. M. Wells, and P. Golland, "Combining spatial priors and anatomical information for fMRI detection," *Med. Image Anal.*, vol. 14, no. 3, pp. 318–331, 2010.

[163] W. Sweldens, "The lifting scheme: A construction of second generation wavelets," *SIAM J. Math. Anal.*, vol. 29, no. 2, pp. 511–546, 1998.

[164] W. Sweldens, "The lifting scheme: A custom-design construction of biorthogonal wavelets," *Appl. Comput. Harmon. Anal.*, vol. 3, no. 2, pp. 186–200, 1996.

[165] S. Ozkaya and D. Van De Ville, "Anatomically adapted wavelets for integrated statistical analysis of fMRI data," in *Proc. IEEE Int. Symp. Biomed. Imaging*, (Chicago, IL), pp. 469–472, 2011.

[166] S. Ozkaya, *Randomized wavelets on arbitrary domains and applications to functional MRI analysis*. PhD thesis, Princeton University, 2012.

[167] Y. Farouj, F. I. Karahanoğlu, and D. Van De Ville, "Regularized spatiotemporal deconvolution of fMRI data using gray-matter constrained total variation," in *Proc. IEEE Int. Symp. Biomed. Imaging*, pp. 472–475, Ieee, 2017.

[168] F. Abdelnour, M. Dayan, O. Devinsky, T. Thesen, and A. Raj, "Functional brain connectivity is predictable from anatomic network's laplacian eigenstructure," *NeuroImage*, 2018.

[169] J. D. Medaglia, W. Huang, E. A. Karuza, A. Kelkar, S. L. Thompson-Schill, A. Ribeiro, and D. S. Bassett, "Functional alignment with anatomical networks is associated with cognitive flexibility," *Nat. Hum. Behav.*, vol. 2, no. 2, p. 156, 2018.

[170] M. G. Preti, T. A. Bolton, and D. Van De Ville, "The dynamic functional connectome: State-of-the-art and perspectives," *NeuroImage*, vol. 160, pp. 41–54, 2017.

[171] H. Behjat, N. Leonardi, and D. Van De Ville, "Statistical parametric mapping of functional MRI data using wavelets adapted to the cerebral cortex," in *Proc. IEEE Int. Symp. Biomed. Imaging*, pp. 1070–1073, 2013.

[172] M. Unser and A. Aldroubi, "A general sampling theory for nonideal acquisition devices.," *IEEE Trans. Signal Process.*, vol. 42, no. 11, pp. 2915–2925, 1994.

[173] M. Unser, "Splines: A perfect fit for signal and image processing.," *IEEE Signal Process. Mag.*, vol. 16, no. 6, pp. 22–38, 1999.

[174] M. Unser, "Sampling—50 years after Shannon," *Proc. IEEE*, vol. 88, no. 4, pp. 569–587, 2000.

[175] Y. Iturria-Medina, E. Canales-Rodriguez, L. Melie-Garcia, P. Valdes-Hernandez, E. Martinez-Montes, Y. Alemán-Gómez, and J. Sánchez-Bornot, "Characterizing brain anatomical connections using diffusion weighted mri and graph theory," *NeuroImage*, vol. 36, no. 3, pp. 645–660, 2007.

[176] M. Shakeri, H. Lombaert, A. N. Datta, N. Oser, L. Létourneau-Guillon, L. V. Lapointe, F. Martin, D. Malfait, A. Tucholka, S. Lippé, *et al.*, "Statistical shape analysis of subcortical structures using spectral matching," *Comput. Med. Imaging Graph.*, vol. 52, pp. 58–71, 2016.

[177] C. Wachinger, P. Golland, W. Kremen, B. Fischl, M. Reuter, A. D. N. Initiative, *et al.*, "Brainprint: a discriminative characterization of brain morphology," *NeuroImage*, vol. 109, pp. 232–248, 2015.

[178] M. M. Bronstein, J. Bruna, Y. LeCun, A. Szlam, and P. Vandergheynst, "Geometric deep learning: Going beyond euclidean data," *IEEE Signal Process. Mag.*, vol. 34, pp. 18–42, July 2017.

[179] K. Hackmack, F. Paul, M. Weygandt, C. Allefeld, and J. D. Haynes, "Multi-scale classification of disease using structural MRI and wavelet transform," *NeuroImage*, vol. 62, no. 1, pp. 48–58, 2012.

[180] E. J. Canales-Rodriguez, J. Radua, E. Pomarol-Clotet, S. Sarro, Y. Aleman-Gomez, Y. Iturria-Medina, and R. Salvador, "Statistical analysis of brain tissue images in the wavelet domain: Wavelet-based morphometry," *NeuroImage*, vol. 72, pp. 214–226, 2013.

[181] A. M. Dale, B. Fischl, and M. I. Sereno, "Cortical surface-based analysis: I. segmentation and surface reconstruction," *NeuroImage*, vol. 9, no. 2, pp. 179–194, 1999.

[182] B. Fischl, "Freesurfer," *NeuroImage*, vol. 62, no. 2, pp. 774–781, 2012.

[183] S. Melzi, E. Rodolà, U. Castellani, and M. M. Bronstein, "Localized manifold harmonics for spectral shape analysis," in *Comput. Graph. Forum*, Wiley Online Library, 2017.

[184] D. Van De Ville, R. Demesmaeker, and M. G. Preti, "When slepian meets fiedler: Putting a focus on the graph spectrum," *IEEE Signal Process. Lett.*, vol. 24, no. 7, pp. 1001–1004, 2017.

[185] F. I. Karahanoğlu and D. Van De Ville, "Dynamics of large-scale fMRI networks: Deconstruct brain activity to build better models of brain function," *Curr. Opin. Biomed. Eng.*, vol. 3, pp. 28–36, 2017.

[186] A. Ashourvan, S. Gu, M. G. Mattar, J. M. Vettel, and D. S. Bassett, "The energy landscape underpinning module dynamics in the human brain connectome," *NeuroImage*, vol. 157, pp. 364–380, 2017.

[187] A. Griffa, B. Ricaud, K. Benzi, X. Bresson, A. Daducci, P. Vandergheynst, J.-P. Thiran, and P. Hagmann, "Transient networks of spatio-temporal connectivity map communication pathways in brain functional systems," *NeuroImage*, vol. 155, pp. 490–502, 2017.

[188] M. G. Preti and D. Van De Ville, "Dynamics of functional connectivity at high spatial resolution reveal long-range interactions and fine-scale organization," *Sci. Rep.*, vol. 7, no. 1, p. 12773, 2017.

Paper I

Anatomically-adapted Graph Wavelets for Improved Group-level fMRI Activation Mapping

Abstract

A graph based framework for fMRI brain activation mapping is presented. The approach exploits the spectral graph wavelet transform (SGWT) for the purpose of defining an advanced multi-resolutional spatial transformation for fMRI data. The framework extends wavelet based SPM (WSPM), which is an alternative to the conventional approach of statistical parametric mapping (SPM), and is developed specifically for group-level analysis. We present a novel procedure for constructing brain graphs, with subgraphs that separately encode the structural connectivity of the cerebral and cerebellar gray matter (GM), and address the inter-subject GM variability by the use of template GM representations. Graph wavelets tailored to the convoluted boundaries of GM are then constructed as a means to implement a GM-based spatial transformation on fMRI data. The proposed approach is evaluated using real as well as semi-synthetic multi-subject data. Compared to SPM and WSPM using classical wavelets, the proposed approach shows superior type-I error control. The results on real data suggest a higher detection sensitivity as well as the capability to capture subtle, connected patterns of brain activity.

1 Introduction

Functional magnetic resonance imaging (fMRI) is a key modality to localize brain activity based on the blood-oxygen-level-dependent (BOLD) signal [1]. The most widely used approach in fMRI activation mapping is a mass univariate hypothesis-driven method that is implemented in many software packages such as statistical parametric mapping (SPM) [2, 3]. Using regressors defined by the experimental paradigm, a general linear model (GLM) is fitted to the time course of every voxel of the brain, followed by a statistical test of a linear combination of the fitted parameters, leading to a statistical map indicating evidence for stimulus-related brain activity. Since using a Bonferroni correction is too conservative, SPM deals with the multiple comparison problem based on Gaussian random field theory (GRFT) [4]. A key characteristic of GRFT is that it requires initial smoothing of the functional data by a fixed Gaussian filter. This pre-filtering not only is required to control the spatial smoothness of the data to comply with GRFT, but it also serves as a means to improve the signal-to-noise ratio (SNR) by virtue of the matched filter argument. However, such linear isotropic filtering comes at the expense of a loss in fine spatial details of the underlying activity.

As an alternative to GRFT, spatial wavelet transforms have been proposed as a means to non-linearly denoise functional data within frameworks of both classical inference [5, 6, 7, 8, 9, 10] and Bayesian inference [11, 12]. Since brain activity is highly localized in space [13], the property of sparse signal representation in the wavelet domain makes it possible to encode a cluster of active voxels with only a few coefficients. Such representation enhances the SNR as the background noise remains equally distributed among the wavelet coefficients, and thus, coefficient-wise statistical testing provides a higher sensitivity than voxel-wise testing. Wavelet-based SPM (WSPM) [9] has the unique feature of treating thresholding within the wavelet domain as a denoising step only, and the statistical testing is deferred to a second thresholding on the reconstructed map within the spatial domain.

1.1 Accounting for intra-subject gray matter structure

Gaussian filters as well as standard wavelets such as those deployed by WSPM share several basic properties: they are (i) isotropic in structure, (ii) defined within regular Euclidean spaces (either a square in 2-D space or a cube in 3-D space) and (iii) stationary and quasi shift-invariant, meaning that their structure does not vary as applied to different regions within a volume. To various extents, these properties are opposed to the expected geometrical properties of the activation pattern. Since the gray matter (GM), within which the BOLD response is expected, has a convoluted structure, isotropically shaped activation patterns that cross boundaries of GM are unlikely. Moreover, due to the differences in the structure of the sulci and gyri across the brain,

intra-subject variability of GM geometry is widely observed [14, 15]. Thus, it is essential to construct filters that adapt to the intricately convoluted GM domain rather than assuming the spatial characteristics of the underlying signal independent of its location. As a step in this direction, surface-based approaches have been proposed that restrict the analysis to the cortex by using reconstructions of the cortical surface. One such approach is the anatomically-informed basis function (AIBF) method proposed in [16, 17], where a forward model is determined for solving the inverse problem of explaining the distribution of the functional data using circular Gaussian basis functions defined on the cortical surface. In other approaches, here collectively referred to as cortical surface mapping (CSM), an interpolation scheme is used to map the functional data to the extracted cortical surface, followed by iteratively smoothing the data on the surface using different procedures such as diffusion smoothing [18], heat kernel smoothing [19, 20] and spline smoothing [21]. Nevertheless, the problem of loss in spatial accuracy remains in CSM due to the irreversible smoothing. Aside from that, the mapping of volumetric data to a surface is challenging due to the variability in cortical thickness.

In the present paper, we introduce an alternative approach where we define a *volumetric* GM domain with the help of graph theory, where the graph vertices correspond to irregularly sampled points of the 3-D Euclidean space. Numerous neuroimaging applications have benefited from brain data being modeled as graphs and graph signals [22, 23]. Here, we propose constructing brain graphs that encode local structural connectivity of GM *geometry* (irregular domain in 3-D), as opposed to the surface-based approaches which mainly incorporate cortical *topology* (2-D surface that is folded). Functional data can then be modelled as a scalar function (signal) defined on the vertices, and graph filters that diffuse only within the GM volume can be constructed. As such, the performance in fMRI brain activation mapping can be improved by attenuating the effect of non-signal components that originate from outside the GM.

With the increased interest in graph approaches to data analysis, a great amount of research has been devoted to generalizing signal processing operations to the graph setting [24]. This includes wavelet transforms, with the spectral graph wavelet transform (SGWT) proposed in [25] being an example. To prevent linear irreversible smoothing and to perform analysis at multiple scales, we propose the tight-frame SGWT [26] to construct GM-adapted wavelets that are utilized to implement an advanced spatial transformation on fMRI data, integrated within the statistical analysis of the WSPM framework.

1.2   Accounting for inter-subject GM variability

Group-level fMRI activation mapping is further complicated by the *inter-subject* GM variability that is important to address. This variability renders the need for normalization of functional data to a template space, which, in turn, leads to better domain matching across subjects and improved statistical power as activations better overlap. Due to the observed difference in the extent of geometrical GM variety in the cerebrum and the cerebellum across subjects, it is advantageous to define cerebral and cerebellar template spaces separately.

The geometry of the cerebral cortex is not consistent across subjects. Although there are similarities in terms of the main fissures, the GM foldings are very inconsistent across individuals even in standard populations [27, 15], see Figure 1. The most commonly used cortical templates are based on either the anatomy of a single subject [28] or the ensemble average over many subjects, such as the ICBM-152 [29] that defines the Montreal Neurological Institute (MNI) space. Such templates can be viewed as two extremes in GM representation: single subject templates take no account for inter-subject variability, and the group averaged templates, such as the ICBM-152, lack fine anatomical detail of the cerebral GM, which makes both categories unsuitable for our purpose. To address this problem, study specific template construction methods such as DARTEL [30] are of great benefit. The fast diffeomorphic image registration scheme proposed by Ashburner is among the best performing [31] and can produce a detailed group-averaged template GM through iterative, nonlinear warping of the segmented GM of a set of subjects.

The structural variability within the cerebellum is lower than in the cerebral cortex, since the cerebellar structure is relatively consistent across individuals in terms of the number and shape of its fissures (see Figure 1). This observation has made it possible to create atlas templates of the cerebellum that prevent a loss in spatial accuracy of the anatomical detail. The spatially unbiased infra-tentorial (SUIT) cerebellum template [32] is the most accurate cerebellar template available to date. Compared to the ICBM 152 template [29] that is designed through averaging of T1 scans from 152 different subjects, SUIT is constructed from scans of 20 subjects, and at the same time, has the unique feature of being spatially unbiased; that is, the location of each of the structures is equal to its expected location in the MNI space across subjects [32].

Therefore, we propose the use of the SUIT atlas as the basis for defining a canonical cerebellar subgraph and the DARTEL for constructing study-dependent template cerebral subgraphs. A full GM-adapted brain graph is then defined by merging the two subgraphs.
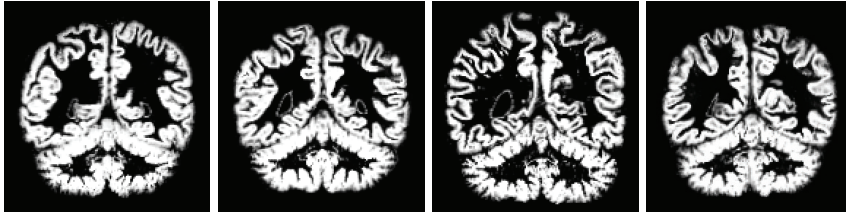
Figure 1: Segmented gray matter of four individuals from an experimental dataset (see Section 3.1) illustrating the inter-subject variability. The variability is less significant in the cerebellum, as opposed to the cerebrum where the pattern of folding varies greatly from one individual to the other.

1.3   Overview

The paper is organised as follows. In Section 2.1, WSPM is reviewed by generalising the framework such that it 1) incorporates any linear spatial transform and 2) is set out for group-level analysis. In Section 2.2, we review the necessary concepts from graph theory and wavelet design. In Section 2.3, we introduce the construction of GM-adapted graphs and wavelets, the required preprocessing steps and contrast mappings. In Section 3, we introduce a real dataset as well as the design of a semi-synthetic multi-subject dataset. In Section 5, we demonstrate the utility of our approach by applying it to the semi-synthetic and experimental datasets, followed by a discussion in Section 5.

2   Methods

For the data structure we assume J subjects, where each subject has a structural scan $\{\mathcal{S}_j\}_{j=1}^J$ and a set of N_t functional volumes (across time), each containing N_v voxels. N_{r1} and N_{r2} regressors are assumed for the first level (subject-level) and second level (group-level) analysis, respectively. $\{X_{1,j}\}_{j=1}^J$ and X_2 denote the corresponding first level and second level design matrices which are of size $N_t \times N_{r1}$ and $J \times N_{r2}$, respectively.

2.1   Transform-Based SPM (tSPM)

We present the WSPM in a more general way as transform-based SPM (tSPM) such that it: 1) incorporates any invertible linear spatial transform, and 2) addresses fMRI activation mapping at the group-level.

The invertible linear spatial transform is a mapping from the voxel space $\mathbb{R}^{N_m}$ to $\mathbb{R}^{N_T}$, where $N_m \leq N_v$ and N_T denotes the dimension of the transform do-

main. $T = [\boldsymbol{\zeta_1}|\boldsymbol{\zeta_2}|\ldots|\boldsymbol{\zeta}_{N_T}]^T$ denotes the corresponding orthogonal transformation matrix, with $\{\boldsymbol{\zeta}_k\}_{k=1}^{N_T}$ being the basis vectors spanning the transform domain. For the classical wavelets such as the discrete wavelet transform (DWT) used in [8, 9], $N_m = N_v = N_T$, where the second equality follows from the DWT being non-redundant. For the graph setting proposed in this paper, N_m is the number of graph vertices, and $N_T = (S+1) \times N_m$, where S denotes the number of wavelet scales of the spectral graph wavelet transform (SGWT) that is a redundant graph transform.

Temporal Modelling at the First Level

Temporal modelling of the data is implemented in the native spatial domain, leading to a parameter map (effect size) for each subject. The approach is mass univariate where a general linear model (GLM) is fitted to the time course of each voxel $i \in \{1, \ldots, N_m\}$ for all subjects $j \in \{1, \ldots, J\}$ as

$$\boldsymbol{v}_{i,j} = X_{1,j}\boldsymbol{\beta}_{i,j} + \boldsymbol{\epsilon}_{i,j}, \tag{1}$$

where $\boldsymbol{v}_{i,j}$ is an $N_t \times 1$ vector representing the time course of the ith voxel of the jth subject, $\boldsymbol{\beta}_{i,j}$ is an $N_{r1} \times 1$ vector of regression parameters and $\boldsymbol{\epsilon}_{i,j}$ is the vector of residual errors. Using the estimated $\boldsymbol{\beta}_{i,j}$, the effect sizes are constructed as

$$p_{i,j} = \boldsymbol{c}_1^T \boldsymbol{\beta}_{i,j} \tag{2}$$

where $\boldsymbol{c}_1$ is an $N_{r1} \times 1$ first level contrast vector that defines how the estimated regression parameters should be combined based on the hypothesis at test. By vectorizing $p_{i,j}$, the fist level parameter maps (contrast maps) of the subjects are obtained as

$$\boldsymbol{p}_j = [p_{1,j}, p_{2,j}, \cdots, p_{N_m,j}]^T. \tag{3}$$

Transform-Domain Spatial Modelling

The first level parameter maps are then taken into the spatial transform domain by applying the transform matrix T as

$$P^{'} = T\,[\boldsymbol{p}_1|\boldsymbol{p}_2|\cdots|\boldsymbol{p}_J], \tag{4}$$

where $P^{'}$ is an $N_T \times J$ matrix, each column representing the transform domain coefficients of one subject.

In order to implement a standard group-level random-effects inference across subjects, a second-level GLM is fitted to the change in value of each coefficient across subjects, i.e., the rows of matrix $P^{'}$ denoted with $P^{'}_{k,:}$, as

$$P^{'}_{k,:} = \mathbf{X}_2\boldsymbol{\beta}_k + \boldsymbol{\epsilon}_k, \tag{5}$$

where $\boldsymbol{\beta}_k$ is an $N_{r2} \times 1$ vector of regression parameters and $\boldsymbol{\epsilon}_k$ is the vector of residual errors. The effect size μ_k and its uncertainty s_k for each coefficient k can then be obtained as

$$\mu_k = \boldsymbol{c}_2^T \boldsymbol{\beta}_k, \tag{6}$$

$$s_k = {\boldsymbol{\epsilon}_k}^T \boldsymbol{\epsilon}_k \, \boldsymbol{c}_2^T (X_2^T X_2)^{-1} \boldsymbol{c}_2, \tag{7}$$

respectively, where $\boldsymbol{c}_2$ is an $N_{r2} \times 1$ second-level contrast vector. In particular, for the one sample t-test that is used for analyzing the datasets in this study, $X_2 = [1, \cdots, 1]^T$, $\boldsymbol{c}_2 = 1$. As such, $\boldsymbol{\beta}_k$ will be a scalar value, and μ_k and s_k will correspond to unbiased estimates of the coefficients' sample mean and variance, respectively.

Transform-Domain Denoising

At this stage, the main idea is to threshold the estimated effect sizes μ_k as a means to denoise the parameter maps. This is done by constructing transform-domain t-values corresponding to the coefficients as

$$t_k = \frac{\mu_k}{\sqrt{\frac{s_k}{J-\mathrm{rank}(X_2)}}}, \tag{8}$$

where $\{t_k\}_{k=1}^{N_T}$ follow a Student's t-distribution with J degrees of freedom under the null hypothesis that stimulus-related activity is driven by noise only.

By subjecting t_k to a transform domain threshold τ_T, the reconstructed, denoised second level parameter map after bias correction is obtained as

$$\hat{u}_i = \min \left(\sum_{k=1}^{N_T} H(|t_k| - \tau_T)\mu_k \boldsymbol{\zeta}_k[i] \, , \, \sum_{k=1}^{N_T} \mu_k \boldsymbol{\zeta}_k[i] \right), \tag{9}$$

where $i = 1, \ldots, N_m$, $H(\cdot)$ is the Heaviside step function and $\sum_{k=1}^{N_T} \mu_k \boldsymbol{\zeta}_k[i]$ denote the elements of the unprocessed map (i.e., the linear estimate). The optimal value of τ_T is obtained in combination with a spatial domain threshold τ_S (see below Eq.(10)) such that the null hypothesis rejection probability in the spatial domain is properly controlled; see [8] for further details and derivations.

Spatial-Domain Statistical Inference

The final detected parameter map is created by constructing spatial domain t-values and performing statistical significance testing by subjecting them to a spatial domain

threshold τ_S as [8]

$$u_i = H\left(\frac{\hat{u}_i}{\sum_{k=1}^{N_T} \mu_k |\boldsymbol{\zeta}_k[i]|} - \tau_S\right)\hat{u}_i. \tag{10}$$

To address the multiple comparison problem, the desired significance level is adjusted using Bonferroni correction when computing the optimal combination of τ_S and τ_T.

2.2 Spectral Graph Wavelet Transform (SGWT)

We now give a brief review of the SGWT on which our framework is based, and refer to [25] for further details.

Classical Wavelets

Classical wavelets defined in the Euclidean domain are constructed by shifting and scaling a mother wavelet $\boldsymbol{\psi}$, as $\boldsymbol{\psi}_{s,l}(x) = \frac{1}{s}\boldsymbol{\psi}\left(\frac{x-l}{s}\right)$, where $\boldsymbol{\psi}_{s,l}(x)$ denotes the wavelet at scale s and location l. To generalize wavelets to graphs, the analogue of the Fourier domain is required for graphs. In the Fourier domain, the classical continuous wavelet is given by

$$\boldsymbol{\psi}_{s,l}(x) = \frac{1}{2\pi}\int_{-\infty}^{\infty}\hat{\boldsymbol{\psi}}(s\omega)e^{-j\omega l}e^{j\omega x}d\omega, \tag{11}$$

where $\hat{\boldsymbol{\psi}}$ denotes the Fourier transform of $\boldsymbol{\psi}$. From Eq. (11), it is clear that the scaling parameter s solely affects the argument of $\hat{\boldsymbol{\psi}}$, and the shifting is represented by multiplication with the complex exponential e^{-jwl}. These two observations are essential when generalizing the wavelet transform to graphs.

Graphs and their Spectra

Turning to spectral graph wavelets, a brief description of some basic notions of graphs and their spectra is in place. An undirected binary graph is described by its set of vertices $\mathcal{V}$ and edges $\mathcal{E}$ as $\mathcal{G} = (\mathcal{V}, \mathcal{E})$, where each edge is defined by a pair of unordered indices (m, n). For a graph with $|\mathcal{V}| = N_g$ vertices and no self-loops, the symmetric adjacency matrix A is given by the off-diagonal elements

$$a_{m,n} = \begin{cases} 1 & \text{if } (m,n) \in \mathcal{E}, \\ 0 & \text{otherwise.} \end{cases} \tag{12}$$

The degree matrix D is diagonal with elements $d_m = \sum_n a_{m,n}$. The normalized graph Laplacian matrix L is given by

$$L = I - D^{-1/2}AD^{-1/2}, \tag{13}$$

where I denotes the identity matrix. Assuming a single connected graph, and noting that L is symmetric and positive semi-definite, the eigendecomposition of L leads to a set of N_g real, non-negative eigenvalues, i.e., $0 = \lambda_1 \leq \lambda_2 \cdots \leq \lambda_{N_g} := \lambda_{max}$. The multiplicity of eigenvalues equal to zero reflects the number of connected components in the graph. The corresponding set of eigenvectors $\{\boldsymbol{\chi}_n\}_{n=1}^{N_g}$ form a complete set of orthonormal vectors, which define the graph spectral domain [33].

Spectral Graph Wavelets

The wavelet shifting and scaling operations are not straightforward to generalize for signals lying on a non-Euclidean domain such as graph signals. Hammond et al. [25] have tackled this issue by taking the design to the graph spectral domain and deriving the equivalence with the Fourier domain of conventional wavelets. Since the complex exponentials $\{e^{j\omega x}\}$ are both the basis functions of the Fourier transform, cf. Eq. (11), and the eigenfunctions of the 1-D Laplacian operator, an analogue spectral design for graphs can be defined based on the graph eigenvectors $\{\boldsymbol{\chi}_n\}_{n=1}^{N_g}$. Thus, the spectral graph wavelet functions $\{\boldsymbol{\psi}_{s,l}\}_{s=1}^{S-1}$ and scaling function ϕ_l localized at each graph vertex l can be defined as

$$\boldsymbol{\psi}_{s,l}(x) = \sum_{n=1}^{N_g} g(\rho_s \lambda_n) \boldsymbol{\chi}_n^*(l) \boldsymbol{\chi}_n(x), \tag{14}$$

$$\phi_l(x) = \sum_{n=1}^{N_g} h(\lambda_n) \boldsymbol{\chi}_n^*(l) \boldsymbol{\chi}_n(x), \tag{15}$$

where $\{\rho_s\}_{s=1}^{S-1}$ denote the scaling parameters, and $g(\cdot)$ and $h(\cdot)$ are wavelet and scaling generating kernels defined as weighted windows on the graph spectrum, respectively. An example of such a frame can be constructed by defining Meyer-like wavelet/scaling generating kernels in the spectral graph domain as shown in 6.

The spectral graph wavelet and scaling coefficients of a graph signal $\boldsymbol{f} \in \mathbb{R}^{N_g}$ at scale s and location l are computed as

$$\boldsymbol{w}_\psi(s, l) = \langle \boldsymbol{f}, \boldsymbol{\psi}_{s,l} \rangle \overset{(14)}{=} \sum_{n=1}^{N_g} g(\rho_s \lambda_n) \hat{\boldsymbol{f}}(n) \boldsymbol{\chi}_n(l), \tag{16}$$

$$\boldsymbol{w}_\phi(l) = \langle \boldsymbol{f}, \boldsymbol{\phi}_l \rangle \overset{(15)}{=} \sum_{n=1}^{N_g} h(\lambda_n) \hat{\boldsymbol{f}}(n) \boldsymbol{\chi}_n(l), \tag{17}$$

respectively, where $\langle \cdot, \cdot \rangle$ denotes the inner product, and $\hat{\boldsymbol{f}}$ is the spectral representation of the graph signal $\boldsymbol{f}$ given by

$$\hat{\boldsymbol{f}}(n) = \langle \boldsymbol{f}, \boldsymbol{\chi}_n \rangle, \quad n = 1, \ldots, N_g.$$

2.3 Spectral Graph Wavelet based SPM (tSPM$^{\text{sgwt}}$)

In what follows, the SGWT is adapted to a GM brain graph and integrated in the tSPM framework for group-level activation mapping, leading to a new graph based fMRI activation mapping referred to as tSPM$^{\text{sgwt}}$. First, the construction of GM-adapted graphs is introduced, followed by the design of the corresponding graph wavelets and a description of the required preprocessing steps and contrast mappings.

GM-adapted Graphs

Defining a graph based on the GM geometry of the brain $\mathcal{G}_{gm}$ is an essential step in our approach. $\mathcal{G}_{gm}$ is constructed as a graph with two subgraph components: a cerebral subgraph $\mathcal{G}_{cbr}$ constructed using the GM information acquired from structural scans of multiple subjects, and a cerebellar subgraph $\mathcal{G}_{cbl}$ constructed based on the SUIT template atlas.

Cerebellar Graph Construction ($\mathcal{G}_{cbl}$)

The cerebellar graph is designed as follows. First, the SUIT cerebellum template $\mathcal{S}_{suit}$ [32], defined in MNI coordinates at 1 mm resolution, is segmented using the unified segmentation algorithm [34] to extract its GM probability map, denoted $\mathcal{M}_{suit}$, with voxel probability values $p_i \in [0, 1]$. Next, a cerebellar GM mask is defined by intersecting the thresholded $\mathcal{M}_{suit}$ (threshold value 0.5) with the SUIT probabilistic atlas of cerebellar lobules $\mathcal{A}_{suit}$ [35]. Intersection of the mask with $\mathcal{A}_{suit}$ ensures that only those voxels which define the cerebellar structure are kept, and that the brainstem is excluded. The resulting map is then morphologically filtered to remove isolated voxels; i.e., a voxel is defined as isolated if it is not adjacent to any other voxel within

its 6-connected neighbourhood in 3-D (see Figure 2). We denote the resulting mask with $\mathcal{M}_{cbl}$ and the binary values of this mask with $\mathrm{v}_i \in \{0, 1\}$.

The resolution of $\mathcal{M}_{cbl}$ is 1 mm isotropic and needs to be downsampled to the functional resolution. Therefore, we propose to first filter the mask weighted with the probability map, using a moving average 3-D box filter with window sizes approximating the functional voxel size in each dimension, followed by thresholding (threshold value 0.5). In particular, the downsampled voxels are obtained as

$$\mathrm{v}_i^{'} = H \left(\frac{1}{M} \sum_{m=1}^{M} \mathrm{v}_m \, p_m \, - 0.5 \right), \tag{18}$$

where $H(\cdot)$ is the Heaviside step function and M denotes the number of nearest neighbour voxels in the 1 mm mask required to interpolate the downsampled voxel. The resulting mask is denoted with $\mathcal{M}_{cbl}^d$. A binary cerebellar graph, denoted $\mathcal{G}_{cbl}$, is then constructed by considering the non-zero voxels in $\mathcal{M}_{cbl}^d$ as vertices and assigning edges by computing connections between adjacent voxels assuming 26-connectivity in 3-D, see Figure 2.
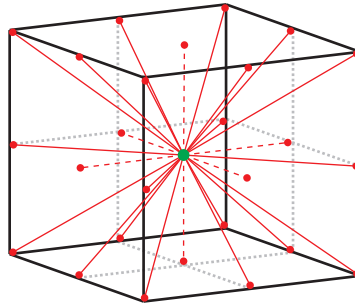
Figure 2: Definition of neighbourhood connectivities. The red dashed lines indicate the directions defining the 6-connectivity neighbourhood with respect to the central green point, whereas the red dashed lines together with the red solid lines define the 26-connectivity neighbourhood.

Cerebral Graph Design ($\mathcal{G}_{cbr}$)

The structural scans $\{\mathcal{S}_j\}_{j=1}^{J}$ are segmented, resulting in a set of GM probability maps, denoted with $\{\mathcal{M}_j\}_{j=1}^{J}$. The DARTEL iterative scheme of averaging and diffeomorphic registration of the probability maps is incorporated to construct a GM template for the group of subjects within the dataset. The algorithm converges after

several iterations, resulting in a detailed GM tissue probability template at 1 mm resolution $\mathcal{M}_{tmp}$, and a set of flow fields $\{\mathcal{T}_j\}_{j=1}^{J}$ describing the deformation required for mapping $\{\mathcal{M}_j\}_{j=1}^{J}$ to this template.

$\mathcal{M}_{tmp}$ is not necessarily aligned to the MNI coordinates, and, therefore, a second level of transformation to the MNI space is required. Thus, $\mathcal{M}_{tmp}$ is updated by subjecting it to an affine transformation $\mathcal{T}_{tmp}$ that registers it to SPM's GM tissue probability map. For reference, we denote the thresholded (threshold value 0.5) and binarized version of $\mathcal{M}_{tmp}$ with $\mathcal{M}_{cbr}$. After downsampling $\mathcal{M}_{tmp}$ to the functional resolution, a binary cerebral GM mask is created by first thresholding the mask (threshold value 0.5), followed by excluding those voxels that lie within its intersection with $\mathcal{M}_{cbl}^{d}$. The mask is then morphologically filtered to remove isolated voxels (6-connectivity in 3-D). The nonzero voxels in the resulting mask are treated as graph vertices, and the edges are defined with the same approach as described for the cerebellar case, leading to a binary cerebral graph that we denote with $\mathcal{G}_{cbr}$.
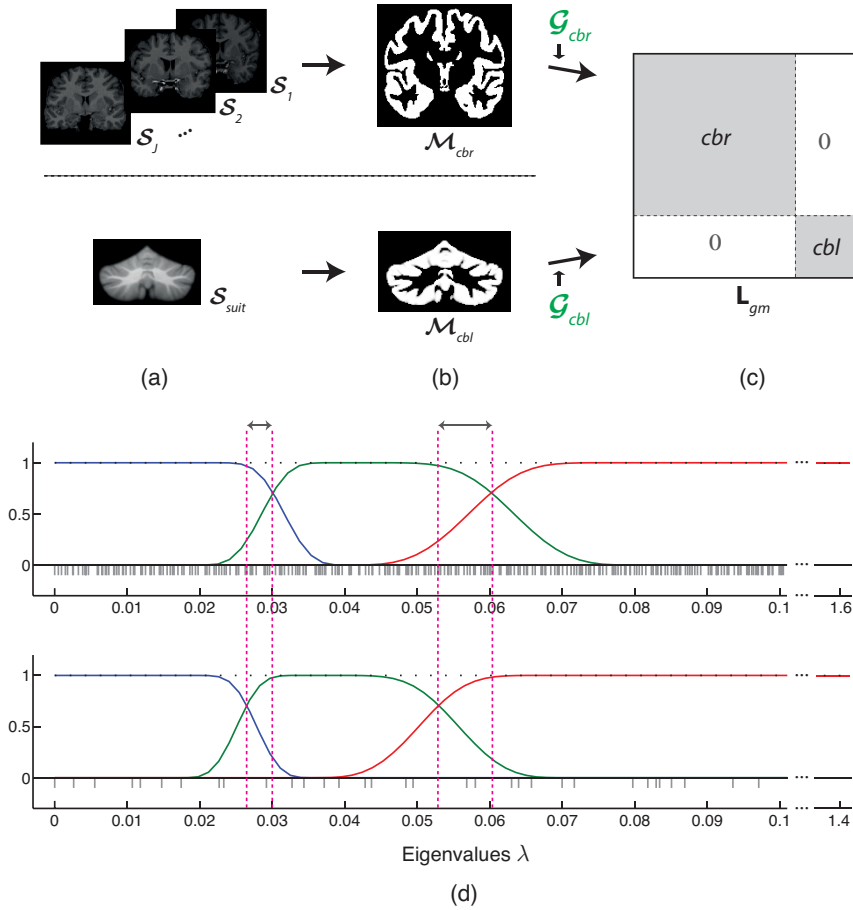
Figure 3: GM-adapted graph and wavelet design. (a) Structural scans of the subjects (top) and the SUIT template atlas (bottom) are used to construct (b) the cerebral (top) and cerebellar (bottom) template GM masks, which are the basis in designing local structural connectivity subgraphs $\mathcal{G}_{cbr}$ and $\mathcal{G}_{cbl}$, respectively. (c) Block diagonal Laplacian matrix defining the spectrum of $\mathcal{G}_{gm}$. (d) Meyer-like windowing functions $h(\rho_S \lambda)$ and $\{g(\rho_s \lambda)\}_{s=1,2}$ at the lower end of the spectra of $\mathcal{G}_{cbr}$ and $\mathcal{G}_{cbl}$. A comparison of the two frames reveals the difference in the support of the corresponding scaling (blue) and wavelet (green and red) kernels of the two subgraphs (indicated by the arrows and dashed lines). The gray coloured vertical parallel bars along the horizontal axis indicate the position of the eigenvalues within the spectral range.

Gray Matter Adapted Wavelet Design

The constructed subgraphs $\mathcal{G}_{cbr}$ and $\mathcal{G}_{cbl}$ are disconnected within $\mathcal{G}_{gm}$. Thus, the corresponding full brain Laplacian matrix L_{gm} is block diagonal (Figure 3(c)). Let N_{cbr} and N_{cbl} denote the number of vertices in each subgraph. As such, the eigenvectors of L_{gm} comprise two sets of distinct basis $\{\boldsymbol{\chi}_n^{cbr}\}_{n=1}^{N_{cbr}}$ and $\{\boldsymbol{\chi}_n^{cbl}\}_{n=1}^{N_{cbl}}$, each separately spanning the cerebral and cerebellar GM domains, respectively. A tight frame design is then used to partition the spectral range of each subgraph and to allocate the support of each wavelet scale. We choose $g(\cdot)$ and $h(\cdot)$ (cf. Section 2.2) such that the set of functions $\{\boldsymbol{\psi}_{s,l}, \boldsymbol{\phi}_l\}_{s\in S, l\in\mathcal{V}}$ forms a tight frame in $\ell_2(\mathcal{V})$ [26]. The tight frame construction is of importance as it leads to energy conservation between the original and transformed domain and enables an efficient inverse transform using the adjoint operator [36]. Also, we prefer the wavelet kernels at different scales to function as scaled bandpass filters and the scaling function as a lowpass filter. Thus, we use the Meyer-like spectral wavelet frame as proposed in [26] (6).

The construction of $\mathcal{G}_{cbl}$ is study-independent, and the resulting $\mathcal{G}_{cbl}$ has 4465 vertices. The size of $\mathcal{G}_{cbr}$ depends on the dataset used. Using the dataset used in this study (see Section 3.1) leads to a $\mathcal{G}_{cbr}$ with 29439 vertices, and thus, a $\mathcal{G}_{gm}$ with 33904 vertices. Due to the large size of $\mathcal{G}_{gm}$, diagonalising L_{gm} is computationally cumbersome. Therefore, we find it advantageous to use a polynomial approximation scheme for estimating the scaled generating kernels $g(\cdot)$ (see Eq. (14)) by low-order polynomials as proposed in [25]. In doing so, the wavelet coefficients at each scale are obtained by applying a polynomial of L_{gm} to the data, and only an estimate of the range of the eigenvalues for each block of L_{gm} is required. L_{gm} has two zero eigenvalues as both $\mathcal{G}_{cbr}$ and $\mathcal{G}_{cbl}$ are constructed such that their single connectivity is ensured and are, at the same time, mutually disconnected. Thus, the lower spectral bound for both $\mathcal{G}_{cbr}$ and $\mathcal{G}_{cbl}$, i.e., λ_1, is 0. However, their upper spectral bounds depend on the complexity present in the GM structure of the respective region, with a higher value expected for $\mathcal{G}_{cbr}$ due to its more intricate geometrical detail. For $\mathcal{G}_{cbl}$ that is constructed to form a template that is canonical in nature, the upper bound is fixed, i.e., $\lambda_{max} = 1.4$, whereas it varies for $\mathcal{G}_{cbr}$ as it is constructed for each dataset separately. For the dataset tested in this study (cf. Section 3.2), $\lambda_{max} = 1.6$. This difference in upper bound, in turn, affects the support of the cerebellar and cerebral frames in terms of the range and width of the kernels, see Figure 3(d).

(a)

(b)
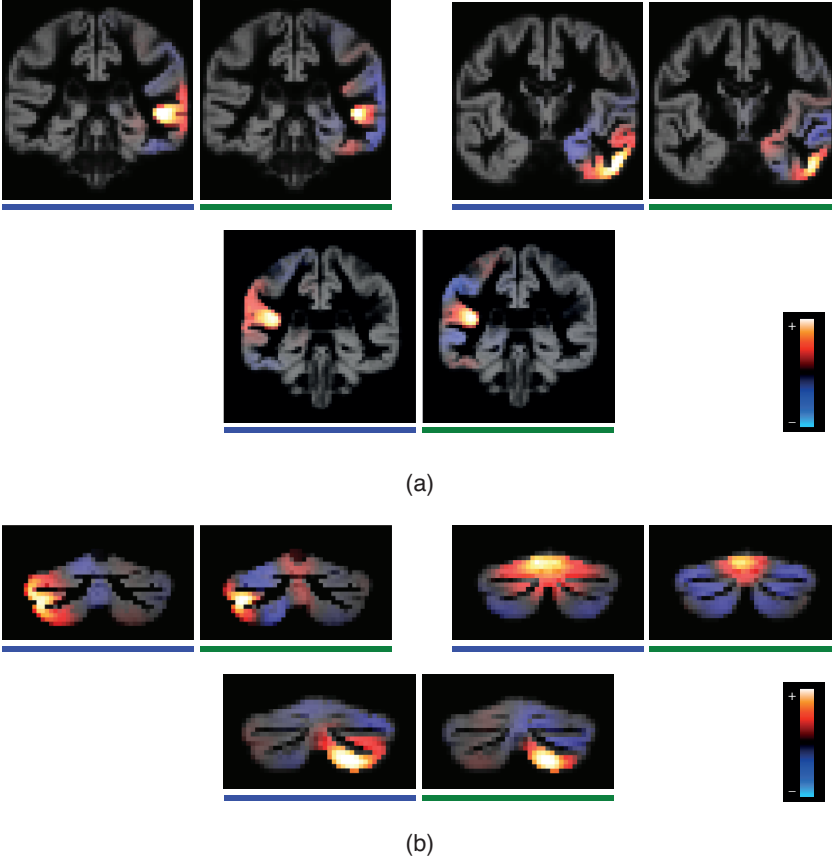
Figure 4: Realizations of the GM-adapted wavelets localized at several different regions of the cerebrum (top row) and the cerebellum (bottom row) overlaid on GM. The figures are color coded (blue and green) corresponding to the spectral designs shown in Figure 3(d); i.e. blue: ϕ_j and green: $\psi_{1,j}$, for six different j denoting the indices of the graph vertices where the wavelets are localized. Note that although the wavelets diffuse within 3-D space, only images of a coronal slice are illustrated.

Functional Data Pre-processing & Contrast Mapping

The functional volumes are corrected for slice-timing and realigned with the first acquired image. The head movement parameters are then estimated and used as covariates in the design matrices $\{X_{1,j}\}$. For each subject, the structural volumes are co-registered with the mean functional volume.

In order to reduce interpolation effects, all computations of the first level analysis are done in the native subject space, thus, no normalization is done on the functional data. Instead, the resulting first level parameter maps $\{\mathcal{P}_j\}_{j=1}^{J}$ [1] are normalized, which leads to normalized cerebral and cerebellar contrast maps denoted with $\{\mathcal{P}_{cbr,j}\}_{j=1}^{J}$ and $\{\mathcal{P}_{cbl,j}\}_{j=1}^{J}$, respectively. The required transformations for this normalization, denoted $\{\mathcal{T}_{cbr,j}\}_{j=1}^{J}$ and $\{\mathcal{T}_{cbl,j}\}_{j=1}^{J}$, respectively, are estimated based on transforming the subjects' structural data to the respective template domains.

Having designed $\mathcal{G}_{cbr}$, the GM of each subject can be constructed through warping $\mathcal{M}_{tmp}$, using the inverse of the estimated flow fields $\{\mathcal{T}_j\}_{j=1}^{J}$. Therefore, as the functional and structural volumes are co-registered, applying the same transformation to the corresponding contrast maps results in their within-subject registration. As such, a better overlap of effects can be gained for second level analysis, which can consequently lead to increased statistical power. The same reasoning holds for the cerebellum. $\{\mathcal{T}_{cbr,j}\}_{j=1}^{J}$ are constructed by combining $\{\mathcal{T}_j\}_{j=1}^{J}$ with $\mathcal{T}_{tmp}$ (cf. Section 2.3). The cerebellar structure of each subject is first annotated using a semi-automatic procedure, and the transformation is determined by mapping it to the SUIT template [32]. The SUIT template is already defined in MNI space and thus no extra transformations are required. Figure 5 illustrates examples of the resulting normalized structural data after applying the normalization transformations, both on the cerebrum and the cerebellum.

The co-registration and normalization procedures are crucial steps in the proposed framework due to the requirement of a one-to-one correspondence between the voxels of the functional and structural data as the constructed graphs are based on anatomical data. Figure 6 illustrates the mapping of an fMRI contrast map to a graph signal. Note that only those voxels of the contrast volumes with a graph vertex counterpart are extracted, and their values are considered as elements of a signal lying on the graph. The extracted contrast voxels from both the cerebrum and cerebellum are vectorized, their SGWT is computed and the resulting set of wavelet coefficients are fed to transform-domain modelling. Figure 7 illustrates an overview of tSPM$^{\text{sgwt}}$.

---

[1] $\mathcal{P}_j$ denotes the same first level parameter maps as $\boldsymbol{p}_j$ given in Eq.(3) but in non-vectorized format.
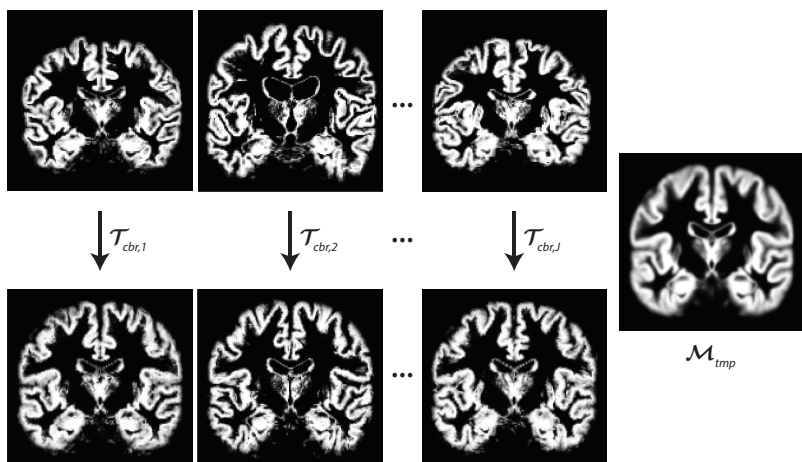
(a)
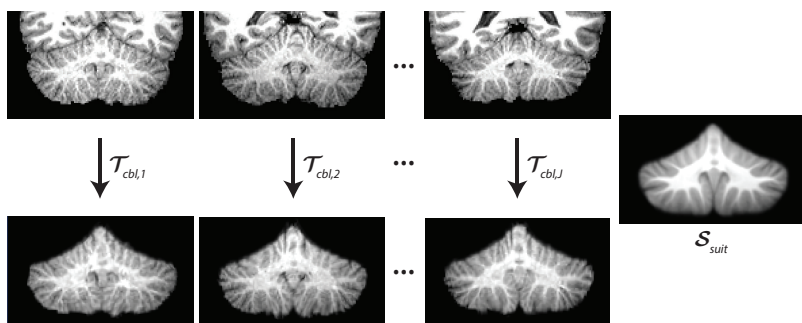
(b)

Figure 5: Addressing inter-subject GM variability. The required transformations for normalizing the first level contrasts to the spaces of $\mathcal{G}_{cbr}$ and $\mathcal{G}_{cbl}$, denoted $\{\mathcal{T}_{cbr,j}\}_{j=1}^{J}$ and $\{\mathcal{T}_{cbl,j}\}_{j=1}^{J}$, respectively, are estimated based on transforming (a) the GM segmentations to $\mathcal{M}_{tmp}$ and (b) the cerebellum structural scans to $\mathcal{S}_{suit}$, respectively. Note that the normalized structural data (bottom row) are not directly used by tSPM$^{\text{sgwt}}$, but rather the estimated transformations.
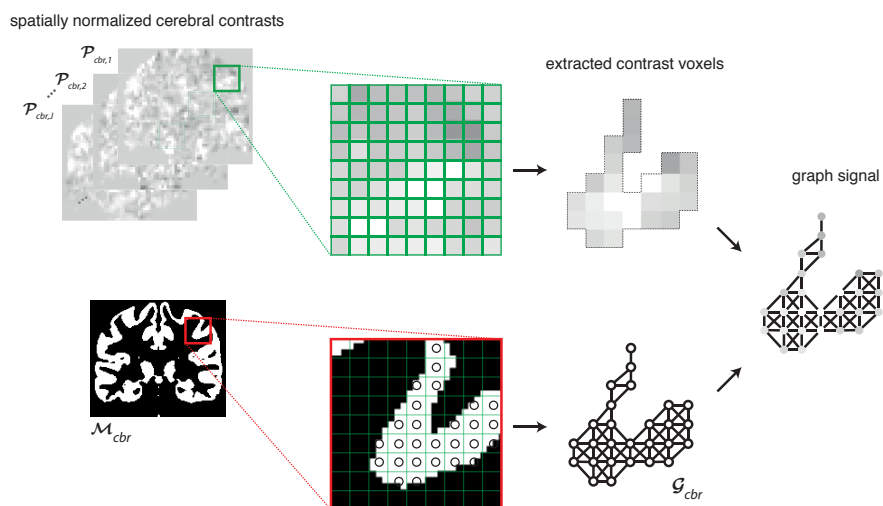
Figure 6: Illustration of mapping an fMRI contrast map to a graph signal. Note that the graph design and mapping procedure is implemented in 3-D space, but for ease of illustration a 2-D example is presented.
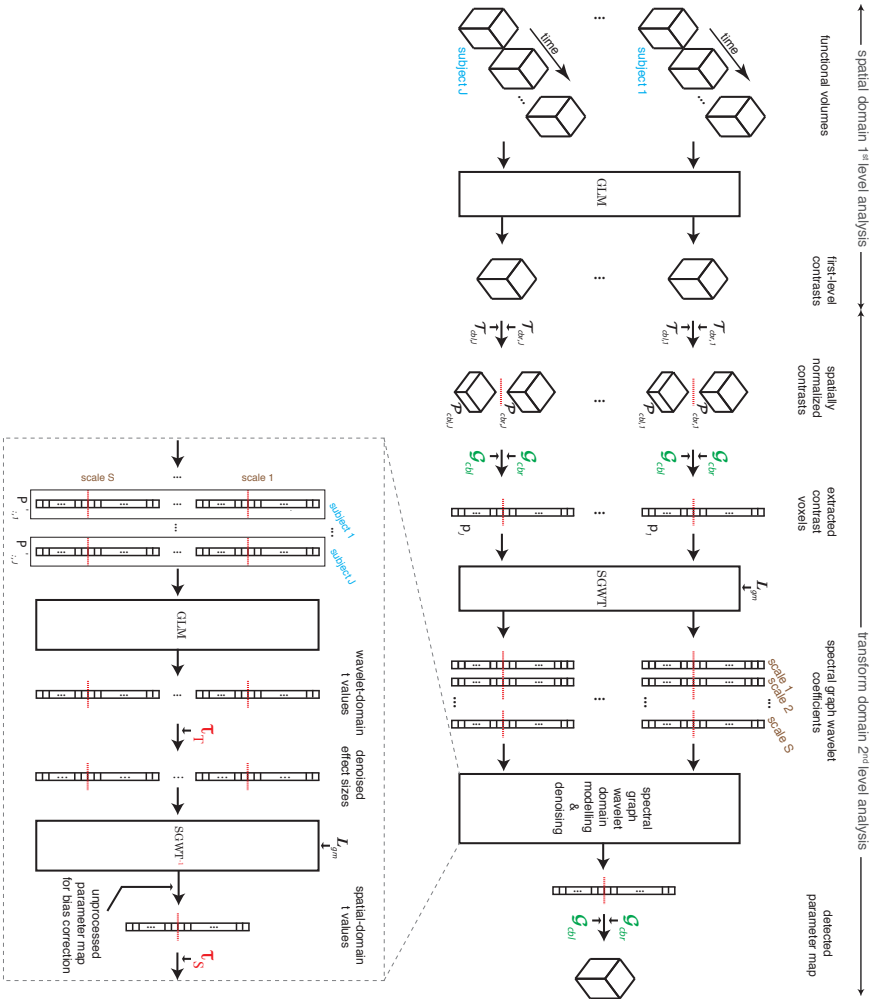
Figure 7: Transform-based SPM using GM-adapted spectral graph wavelets

3 Datasets

3.1 Experimental Dataset

Data from 26 healthy adults performing a slow event-related Eriksen flanker task were studied [37]. In each trial, the subjects used one of two buttons to distinguish between congruent and incongruent trials (inter-trial interval varied between 8 s and 14 s with a mean of 12 s). In congruent trials, the flanking arrows pointed in the same direction as the central arrow (e.g., $<<<<<$), whereas in more demanding incongruent trials the flanking arrows pointed in opposite direction (e.g., $<<><<$).

Functional data were acquired using a 3T scanner, where contiguous whole-brain functional volumes were obtained using echo planar imaging during each of the two flanker task blocks (TE = 30 ms, TR = 2000 ms, flip angle = $8°$, matrix = 64×64, 40 slices, FOV = 192 mm, voxel size = $3 \times 3 \times 4$ mm^3, 146 volumes). T1-weighted anatomical scans were collected using an MPRAGE sequence (TE = 3.93 ms, TR = 2500 ms, flip angle = $8°$, 176 slices, FOV = 256 mm, voxel size = $30 \times 20 \times 10$ mm^3). Using this dataset, a cerebrum graph $\mathcal{G}_{crb}$ with 29439 vertices was created.

3.2 Semi-Synthetic Dataset

To evaluate the proposed algorithm, a semi-synthetic group fMRI dataset with known ground truth underlying simulated brain activity was created, using the anatomical scans of the 26 subjects of the flanker task dataset. The dataset was created to account for inter-subject variability in strength and location of the activity as well as to simulate a realistic activity pattern. Functional contrasts with known subject-specific ground truth activation patterns that diffuse according to the GM of each subject were created as follows.

First, for each subject j, the estimated flow field $\mathcal{T}_{cbr,j}$ (cf. Section 2.3) was applied to its GM probability map, $\mathcal{M}_j$, resulting in a deformed-warped GM in MNI space. The resulting probability maps were then smoothed (FWHM 2 mm), binarized by thresholding at 50%, leading to a set of masks used to construct an unweighted graph for each subject with adjacency matrices $\{A_j\}_{j=1}^{26}$. Three $5 \times 5 \times 5$ mm cubic regions (125 voxels), two in the cerebrum and one in the cerebellum, were then chosen as candidates for three activation centres. The centres were spatially jittered by randomly picking three voxels (one from each region), creating a set of indicator vectors $\{\boldsymbol{x}_j\}_{j=1}^{26}$ defining the voxel location of the three centers for each subject. An activation pattern $\boldsymbol{y}_j$ that diffuses from the three center points along the individual's GM domain was constructed by consecutive application of the corresponding adjacency matrix A_j to $\boldsymbol{x}_j$ and confining the elements of $\boldsymbol{y}_j$ to the range [0, 1] as
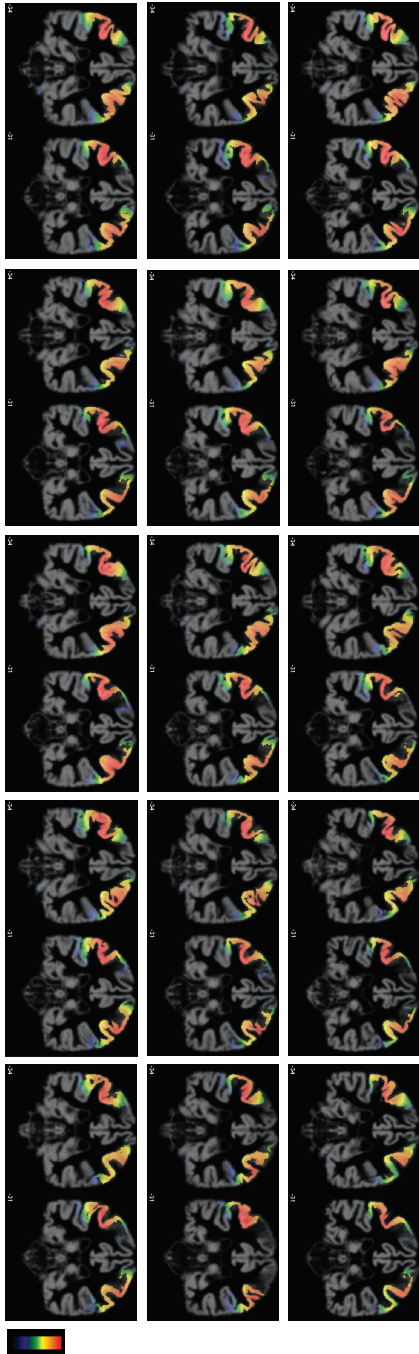
Figure 8: Realizations of synthetic activity patterns y_j for several subjects, overlaid on each subject's GM.
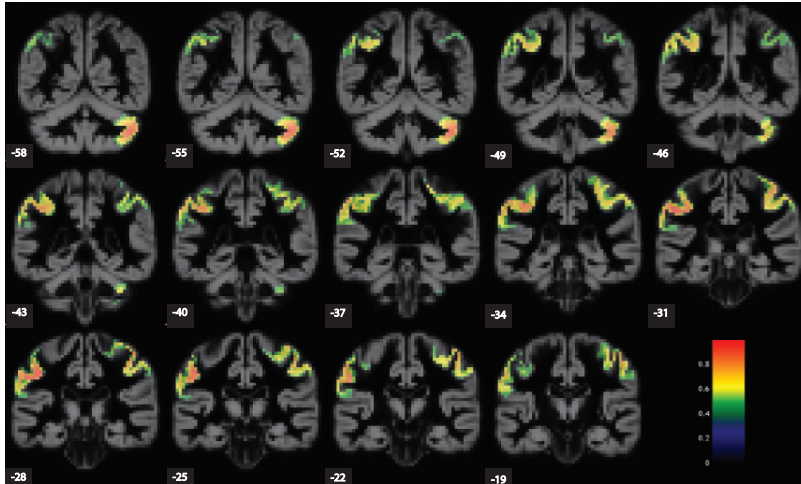
Figure 9: Semi-synthetic Data. Defined ground truth activation map.

$$\boldsymbol{y}_j(i) = \begin{cases} 1 & \text{if } \boldsymbol{x}_j'(i) > 1, \\ \sqrt[n]{\boldsymbol{x}_j'(i)} & \text{otherwise,} \end{cases} \tag{19}$$

where $\boldsymbol{x}_j' = A_j^n \, \boldsymbol{x}_j$ and n defines the extent of the diffusion (Figure 8). With this construction, not only do the patterns vary between subjects, but also the distribution of their values. The resulting patterns were downsampled to 3-mm resolution.

We treat these patterns as the ground truth first level contrasts for the individual subjects (i.e., one pattern per subject). Using the average of all 26 patterns, those voxels whose activity exceeded 0.5 and whose location corresponded to a voxel in $\mathcal{M}_{tmp}$ with at least 50% probability were defined as ground truth (Figure 9). The individual activity patterns were then corrupted with additive white Gaussian noise with variance $\sigma^2 = 1$.

4 Results

4.1 Setup and Performance Measures

For comparative purposes, we implemented SPM (isotropic Gaussian smoothing with FWHM of 4 and 6 mm, denoted SPM^{4mm} and SPM^{6mm}, respectively), and transform-based SPM using standard orthogonal wavelets (2-D+Z, redundant), denoted $tSPM^{dwt}$, and GM-adapted wavelets, denoted $tSPM^{sgwt}$. SPM^{4mm} was performed to illustrate the effect of smoothing on spatial accuracy and detail of detections.

For both datasets, we present the results in terms of the number of detections. For the semi-synthetic data, we also present the number of true positives (TP) and false positives (FP), and the receiver operating characteristic (ROC) curve by varying p-values. Moreover, to indicate the detections that lie outside the expected GM region where a BOLD signal is expected, the detections are also categorised based on their affinity to the underlying tissue; GM50 denotes a mask covering the regions with a GM probability of at least 50%, i.e., greater than that of the probability of being white matter (WM) or cerebrospinal fluid (CSF). This metric provides an intuitive quality measure of activation mapping, especially for real data where the ground truth is not known. As an initial but reasonable approximation, detections that do not intersect with GM50 can be assumed to be FPs.

4.2 Semi-Synthetic Data

Table 1 presents the results in applying the different methods on the semi-synthetic data, when testing at a significance level of $p < 0.05$ familywise error (FWE) corrected. Both wavelet approaches have a significantly better control over FPs (type-I error control) compared to SPM^{6mm} (95 and 183 vs. 1590 FPs). $tSPM^{sgwt}$ shows a significantly higher sensitivity compared to $tSPM^{dwt}$ (1398 vs. 538 TPs). Although SPM^{6mm} also exhibits a higher sensitivity than $tSPM^{sgwt}$ (1785 vs. 1398 TPs), it lacks spatial accuracy (1590 vs. 183 FPs). For example, the lack of spatial accuracy can be observed when comparing SPM^{6mm} and $tSPM^{sgwt}$ detections at coronal slices -34 to -25 in Figures 10(a)–(b), respectively, to the ground truth in Figure 9.

Many SPM^{6mm} detections are outside GM50 (approximately 30%). The classification of FPs with respect to GM50 shows that the specificity of $tSPM^{sgwt}$ is higher than SPM^{6mm} not only in total, but also when only taking detections within GM50 into account (183 vs. 644 FPs). In other words, the fine details detected by $tSPM^{sgwt}$ cannot be obtained by intersecting SPM^{6mm} detections with the GM50 mask. Note that SPM^{6mm} has 387 extra TPs than $tSPM^{sgwt}$ (i.e., $1785 - 1398$), as compared to 461 extra FPs within GM50 (i.e., $644 - 183$), which indicates less than random TP detection. This lack of detail in SPM^{6mm} detections is mainly due to the smoothing
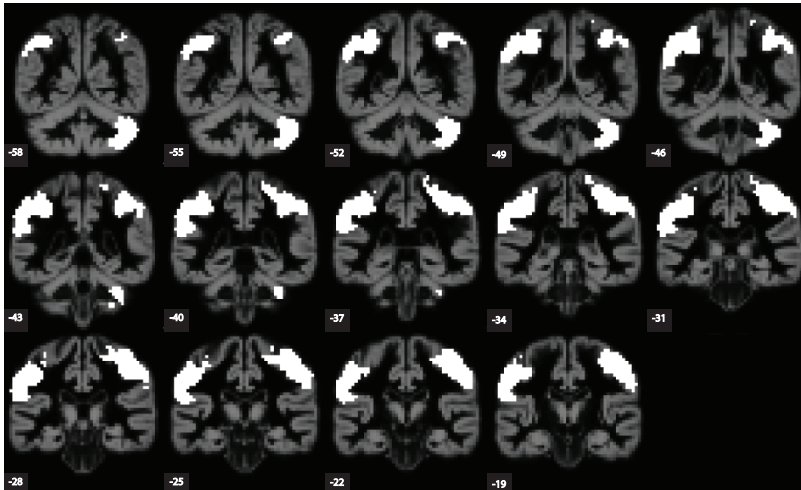
(a)
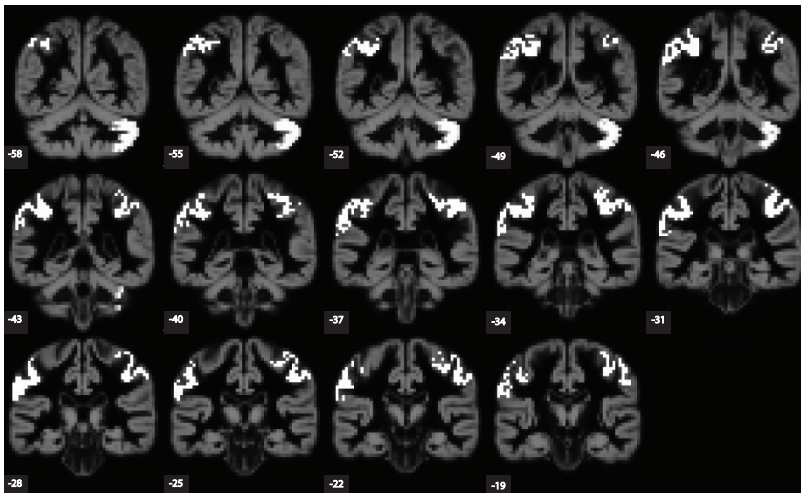
(b)

Figure 10: Semi-synthetic Data. Activation maps detected by (a) SPM^{6mm} and (b) tSPM^{sgwt}, all overlaid on $\mathcal{M}_{tmp}$.

Table 1: Detection performance on the semi-synthetic dataset.

Method	SPM^{4mm}	SPM^{6mm}	tSPM^{dwt}	tSPM^{sgwt}
detections - total	1882	3375	633	1581
detections - in GM50	1587	2429	566	1581
TPs / (sensitivity)	1389 / (73%)	1785 / (94%)	538 / (28 %)	1398 / (75 %)
FPs - total / (specificity)	493 / 99.2%	1590 / (97.4%)	95 / (99.9 %)	183 / (99.4 %)
FPs - in GM50	198	644	28	183

phase, though leading to higher sensitivity. By reducing the amount of smoothing, we observe that the sensitivities of SPM^{4mm} and tSPM^{sgwt} are similar (1389 vs. 1398 TPs) while tSPM^{sgwt} preservs its better specificity (493 vs. 183 FPs).

Figure 11 shows ROC curves illustrating the specificity–sensitivity trade-off of the approaches as a function of the significance level. At the same level of specificity, tSPM^{sgwt} consistently shows superior sensitivity when compared to the other three approaches. Note that specificity of both tSPM^{dwt} and tSPM^{sgwt} is confined to high values due to the inverse inter-relation of the spatial and transform domain thresholds (i.e., τ_S and τ_T) that are inversely proportional [8]; as the significance level input to the algorithm drops below $\alpha = 0.01$, a reasonable low enough limit, τ_T significantly decreases, leading to an excess increase in τ_S, which in turn restricts detections and the sensitivity.
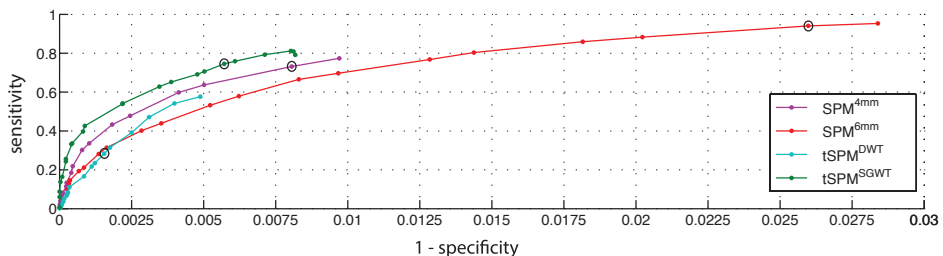
Figure 11: Performance ROC curves for the four approaches. The circled points display the results achieved when testing at a significance level of $p < 0.05$ FWE corrected (i.e., corresponding to Table 1).

4.3 Experimental Data

Table 2 presents the results for the flanker task dataset, where the incongruent active contrast was studied; i.e., detecting activations during incongruent trials. For each subject j,

$$X_{1,j} = [\boldsymbol{x}_{1,j}|\boldsymbol{x}_{2,j}|\boldsymbol{r}_{1,j}|\boldsymbol{r}_{2,j}|\cdots|\boldsymbol{r}_{6,j}, \mathbf{1}],$$

where $\boldsymbol{x}_{1,j}$ and $\boldsymbol{x}_{2,j}$ are binary vectors indicating the onset of congruent and incongruent trials, respectively, $\{\boldsymbol{x}_{k,j}\}_{K=1,\cdots,6}$ are the estimated head movement parameters used as additional regressors, and the last column $\mathbf{1}$ is a constant vector which models the average activity. $\boldsymbol{c}_1$ is set to $[0, 1, 0, \cdots, 0]^T$ for detecting voxels whose activation increase in response to incongruent trials. All tests were performed at a significance level of $p < 0.05$ FWE corrected. A first observation is that both SPM^{6mm} and tSPM^{dwt} result in more detections than tSPM^{sgwt} (9678 and 7707 vs. 7274 detections, respectively). However, restricting the detections to GM50 within which tSPM^{sgwt} functions, we see that tSPM^{sgwt} outperforms both SPM^{6mm} and tSPM^{dwt} by 20% and 50% more detections, respectively (7274 vs. 6165 and 4973 detections, respectively).

Figures 12(a)–(b) show the detection maps using SPM^{6mm} and tSPM^{sgwt}, respectively. tSPM^{sgwt} detections exhibit more spatial details, as evidenced for instance by the subtle patterns observed in the left and right upper cerebrocortical regions in slices -49 to -31. Moreover, tSPM^{sgwt} has better ability to detect connected patterns — a result which is elucidated by re-plotting SPM^{6mm} detections while keeping only those detections that fall within GM50, see Figure 12(c). Examples of this phenomenon can be observed by comparing the detections in the cerebral cortex in slices -61 to -31 in Figures 12(b)–(c). With respect to detection sensitivity within GM50, tSPM^{sgwt} in general performs better with additional activations compared to SPM^{6mm} in several regions, see cerebellar region in slices -55 to -34. It should also be noted that the detections of SPM^{6mm} include deep nuclei regions such as basal ganglia and thalamus, see medial detections in slices -19 to -10 in Figure 12(a), which are not part of the graph definition of tSPM^{sgwt} and thus, remain undetected by tSPM^{sgwt}.

Table 2: Detection performance on the experimental dataset.

Method	SPM^{4mm}	SPM^{6mm}	tSPM^{dwt}	tSPM^{sgwt}
No. of detections - total	5963	9678	7707	7274
No. of detections - in GM50	4182	6165	4973	7274
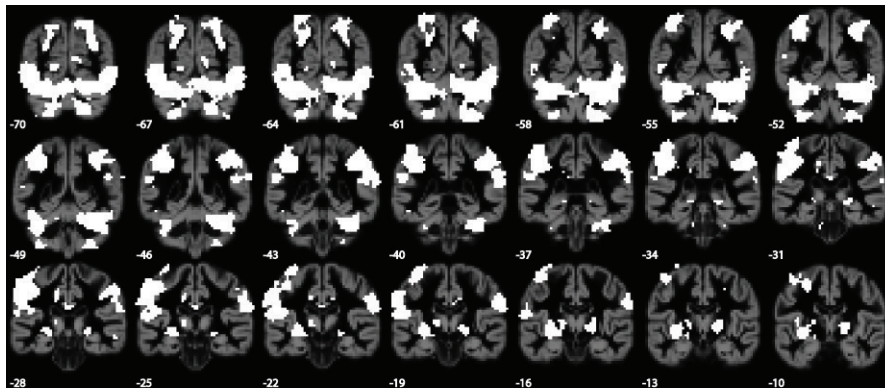
(a)
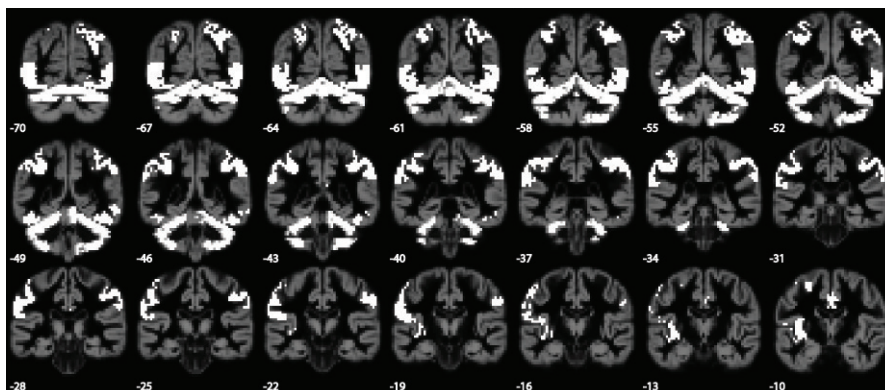
(b)
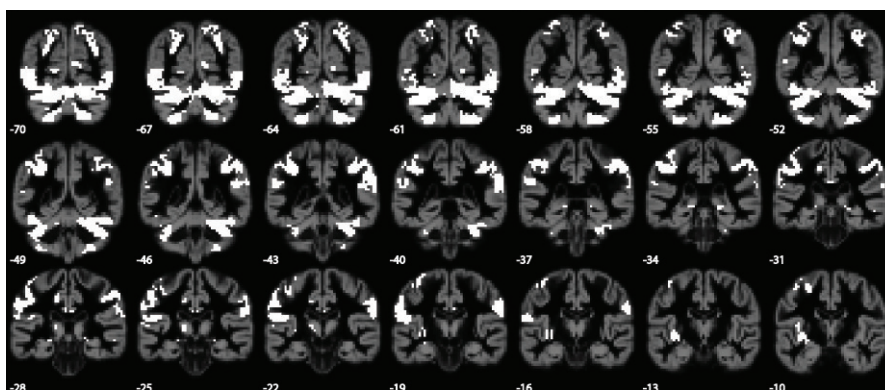
(c)

Figure 12: Experimental Data. Activation maps detected by (a) SPM^{6mm}, (b) tSPM^{sgwt} and (c) SPM^{6mm} (within GM50) — all maps overlaid on $\mathcal{M}_{tmp}$.

5 Discussion

5.1 Improved Spatial Localization and Empirical Sensitivity

The enhanced spatial localization for tSPM$^{\text{sgwt}}$ compared to that of tSPM$^{\text{dwt}}$ and SPM is due to several reasons. First and foremost, prior knowledge about how and where the BOLD signal emerges is taken into account advantageously. WM is an example of a tissue with very low neuro-vascular coupling due to its sparse vascularization, which implies a weak or absent BOLD signal within WM [38]. As such, exploiting this prior knowledge about tissue–function relationship is essential. The prevention of detections in WM or CSF, which would be mainly driven by noise, also prevents these contributions from penetrating and getting mixed with the functional signal in GM. Although even within SPM, statistical analysis can be restricted to a subset of the voxels corresponding to GM, data still needs to be smoothed in order to be sufficiently in line with the Gaussian random field theory [4]. Secondly, compared to SPM, there is no irreversible spatial smoothing of the functional data in wavelet approaches, which in turn results in enhanced spatial accuracy in detecting subtle activity patterns. The conventional approach of spatial smoothing with a non-adaptive Gaussian filter trades increased sensitivity for loss of information on the spatial extent and shape of the activation areas [39, 40]. It has also been shown that isotropic Gaussian smoothing across GM and WM (i.e., without any GM constraint) can lead to displacement of activation peaks in t-value maps towards WM due to the difference in noise variance of the two tissue types [41]. Thirdly, the strong control of FPs using tSPM is linked to the underlying theory in selecting the threshold values through the bound over the null hypothesis rejection probability [8]. On the other hand, SPM yields FWE rates that are higher than the expected one, as recently reported in [42]. This effect is decreased by reducing the amount of smoothing, as was observed when using SPM$^{\text{4mm}}$.

Fixing the desired significance, we observe that tSPM$^{\text{sgwt}}$ outperforms SPM and tSPM$^{\text{dwt}}$ in terms of sensitivity, see Figure 11. Although the use of classical wavelets has shown good sensitivity in single-subject studies [8, 9], it performs worse in group studies due to inter-subject variability that is not countered by smoothing as in SPM, in particular, when there is only partial overlap between activations. Moreover, although the approach is multi-resolution, the wavelets dilate along the axes of the cartesian coordinate system at a scale progression that is too fast. Instead, GM-adapted wavelets lead to much higher sensitivity compared to classical wavelets (i.e., 1398 vs. 483 detections, respectively) thanks to the adaptive scaling of wavelets that respect the GM domain. Moreover, empirical assessment of sensitivity on real data, by considering detections within GM50, reflects the higher sensitivity of tSPM$^{\text{sgwt}}$ compared to both tSPM$^{\text{dwt}}$ and SPM (see Table 2 and Figure 12). Designing basis functions that dilate only within GM, not only prevents high noise data from WM or CSF to be

"mixed" with GM data, but also leads to a more significant overlap of pure activations that follow GM foldings, which in turn, results in higher sensitivity.

5.2   Graph Design for the Brain

A binary graph design is adopted in the proposed framework. Our preliminary tests showed that weighting the edges based on the Euclidean distance does not improve the results, as the Euclidean distances between connected vertices in an isotropic 3-D grid are in the same range (1, $\sqrt{2}$ or $\sqrt{3}$ voxels, see Figure 2). Also, defining weights based on GM probabilities did not improve the results [43]. Thus, the binary design was favoured over an edge weighting scheme due to its simplicity. This construction resembles an $\mathcal{E}$-neighbourhood graph commonly used in spectral clustering [44], with $\mathcal{E}$ equal to a distance of $\sqrt{3}$ voxels.

There are two main reasons why the design of a graph with region-specific subgraphs was preferred over the design of a single connected brain graph. First, the importance of separating the cerebrum from the cerebellum is to prevent activations from the ventral occipital lobe "bleeding" into the cerebellum, and vice versa. Examples of this phenomenon can be observed in SPM detections, see slices $-70 : -49$ in Figure 12(a). Second, the geometrical properties of the GM are different for the cerebrum and the cerebellum. At the resolution of currently available structural MRI scans and segmentation algorithms, there are more fine details observed within the whole range of the cerebral structure than within the more coarse geometry of the cerebellum. As such, constructing subgraphs specific to the cerebrum and cerebellum leads to wavelets specifically designed for each region, as the wavelet frame is based on their corresponding spectra.

By comparing the cerebellar mask $\mathcal{M}_{suit}$ to the cerebellar region of the average GM map $\mathcal{T}_{tmp}$, it can be observed that more spatial detail is preserved within the former, see Figure 13. Moreover, the use of such a template mask leads to a study-independent canonical GM graph, with advantages similar to those of the SUIT atlas itself. The GM template constructed from SUIT was therefore preferred over the cerebellar region of $\mathcal{M}_{tmp}$.
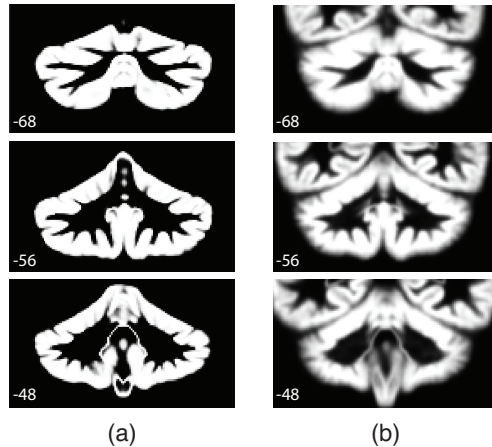
Figure 13: Template cerebellar GM. Three sagital slices of (a) $\mathcal{M}_{suit}$ constructed using SUIT template and (b) the cerebellar region of $\mathcal{M}_{tmp}$ constructed using DARTEL. Finer spatial detail is observed in $\mathcal{M}_{suit}$ than in $\mathcal{M}_{tmp}$.

5.3 Comparison with other Anatomically Constrained Methods

Previous studies following CSM approaches [18, 19, 20, 21], which anatomically constrain the activation mapping, suffer from a few shortcomings. First, the interpolation effects related to the projection of 3-D volumes onto the cortical surface is a major challenge [45, 46]. Second, smoothing leads to spatial inaccuracy and artificial shift of activations, be it using conventional volume-based approaches (e.g., SPM) or CSM [47, 39, 40]. Although the cortical 2-D diffusion smoothing of CSM approaches, rather than 3-D isotropic Gaussian smoothing of conventional volume-based approaches, prevents overlap of activation centres that are geodesically distant but close in a Euclidean sense (e.g., two points, at the opposite sides of a sulcus) [18], the resulting smoothed signal can still be influenced by sources that are geodesically adjacent. tSPM$^{\text{sgwt}}$ overcomes these two limitations by not smoothing the data in the first place and keeping the analysis within the native voxel-space. By modelling the GM as a graph based on the local neighborhood structure, we implicitly define a manifold (with non-zero thickness) on which wavelets dilate with respect to geodesic distances on this structure. In this sense, the design allows upscaling of local properties to a global scale. At the coarse scale, although tSPM$^{\text{sgwt}}$ also implicitly inherits smoothing in applying the lowpass scaling function $h(\cdot)$ that can be interpreted as equivalent to Gaussian pre-filtering [48], this is fundamentally different from pre-smoothing the

data. First, the scaling coefficients are thresholded leading to *non-linear* denoising as opposed to the *linear* filtering done in pre-smoothing where all fine details of the data, be it noise or signal, are removed[2], which in turn, leads to a loss in spatial detail of the underlying activity patterns. Second, the wavelet coefficients that survive thresholding are then used, together with the scaling coefficients, to reconstruct the de-noised signal, unlike the *irreversible* pre-smoothing as in CSM or SPM.

It is interesting to compare tSPM^{sgwt} with the AIBF approach [16, 17]. First, both approaches keep modelling in the spatial and temporal domain separated. However, temporal modelling precedes spatial modelling in tSPM^{sgwt}, i.e., spatial modelling is deferred to the second level analysis (cf. Section 2.1), whereas the opposite is performed in AIBF. If single subject analysis similar to the current graph-based proposal is desired; i.e., only first level analysis, the original joint spatio-temporal model of WSPM as proposed in [8] can be used [49]. Second, tSPM^{sgwt} shares similarities with AIBF in the sense that smoothing of the data is prevented. They both project the data into a transform domain: AIBF to the space spanned by circular, user-specified wide Gaussian basis functions with local support defined on the flattened cortical surface, and tSPM^{sgwt} to a multi-scale GM domain spanned by GM-adapted wavelets defined within the voxel-space. The basis set are then used to represent, by a linear combination, the functional observations (BOLD volumes in AIBF and first level contrast maps in tSPM^{sgwt}). In tSPM^{sgwt}, the modelling is done within the wavelet domain, whereas in AIBF it is done in the voxel-space by back-projecting the constructed basis to the voxel-space. As such, AIBF is also prone to interpolation effects in back-projecting the basis from the cortical surface to the voxel-space, similar to that explained earlier with respect to mapping functional data from the voxel-space to the surface. Third, in tSPM^{sgwt} denoising is performed by subjecting the wavelet coefficients to a threshold (cf. Section 2.1) and applying the inverse transform to project the data back to the native space, whereas in AIBF noise reduction is inherent in the anatomically constraint least-squares modelling. Fourth, in multi-subject AIBF [17], a single subject's cortical surface is used as a canonical surface to construct the basis set and to normalize functional data from all subjects. Here, we made use of recent population-level template atlas constructions as well as deformation algorithms to construct a group-level template of GM, in an attempt to address the observed inter-subject variability of GM structure more elegantly (See Figure 5).

Another limitation of surface-based approaches is their inability to analyse non-cortical regions, such as the cerebellum and the deep nuclei (e.g., thalamus and basal ganglia), as they require a surface reconstruction, which would necessitate additional and tailored representation steps. As such, volumetric techniques, such as the present

---

[2]Note that the Fourier transform of a Gaussian is also a Gaussian, and thus, applying such a Gaussian filter to the data corresponds to multiplying the spectrum of the data with a Gaussian.

proposal, allow more easily to include non-cortical structures.

We also mention an alternative design of anatomically adaptive wavelets proposed in [50, 51]. The design is based on the lifting scheme [52] where an irregular domain can be iteratively sectioned into a nested family of partitions at different spatial scales. As such, the basis construction in [51] becomes shift variant (due to subsampling), while the wavelet basis in SGWT spans the space of eigenfunctions of L that are defined on the GM domain. Moreover, our approach has been directly devised for multi-subject analysis and as such addresses inter-subject GM variability. As both proposals use the segmented GM as the starting point for their construction, the lifting-based anatomically adapted wavelets can also benefit from the GM template as proposed in the present study.

5.4   Limitations

Although we have shown the applicability of tSPM^{sgwt} in enhancing fMRI activation mapping, there are still aspects that can be improved. The present framework lacks a systematic approach in determining the spectral coverage for each wavelet scale; this is a limitations for the SGWT design in general, as also reported in other applications than fMRI [53, 54]. The adopted spectral partitioning in the design has been found empirically by visual assessment of the wavelets and their characteristic scale. The current setting should nevertheless reasonably generalize to other datasets due to the general similarity in the extent and nature of the resulting group-level template GM domains.

Another limitation is that sub-cortical regions, such as the basal ganglia and thalamus, are currently not part of the graph. As such, several detections by SPM in the sub-cortical area were missed by tSPM^{sgwt} (cf. Section 4.3). Although there is a precise atlas of deep cerebellar nuclei available [55], there does not seem to exist a detailed population-level atlas (mask) for the sub-cortical nuclei such as the thalamus and palidum. Available atlases such as the AAL atlas [28] are based on a single subject anatomy, and, when incorporated within our GM template, regions for the sub-cortical nuclei were too coarse and collapsed with the nearby delicate GM structure as defined by G_{cbr}. Therefore, these regions were decided not to be included in the current graph design. Provided a suitable atlas becomes available, it should be possible to include these regions as extra subgraphs to $\mathcal{G}_b$. Another option is to incorporate tractography information provided by diffusion tensor imaging data [56]. A similar idea in constructing such hybrid connectivity graphs has been recently proposed to improve electroencephalography-based source estimation [57].

The computational burden of the proposed approach is another potentially limiting factor. The most costly part of the implementation is the absolute-value wavelet reconstruction needed for the spatial thresholding (cf. denominator of Eq. 10). Since

the graph wavelets are unique, they need to be computed explicitly at each and every vertex and scale. Although this computational burden can be reduced by precomputing and storing the absolute-value-wavelets $\{\{|\boldsymbol{\psi}_{s,l}|, |\boldsymbol{\phi}_l|\}_{s=1}^{S}\}_{l=1}^{N_{cbl}}$ for $\mathcal{G}_{cbl}$, this should still be done for each study-dependent $\mathcal{G}_{cbr}$. Another possibility would be to perform the reconstructions in parallel on the computer's graphic card, as such applicability has been shown for other fMRI analysis procedures [58].

5.5   Extension to Structural Studies

Another research avenue that can directly benefit from the proposed GM-adapted wavelet construction are structural studies. Euclidean wavelet approaches have been used to classify structural brain data [59, 60] as a means to assess structural morphometric differences between different population of subjects. They have also been used to discriminate between healthy and pathological tissue by characterising subtle changes in brain structure in a variety of diseases such as Alzheimer's disease, mild cognitive impairment and multiple sclerosis [61, 62]. Interestingly, the recent proposal in [53], also uses the SGWT to derive multi-scale shape descriptors that can be used to detect group-level effects. However, the approach uses cortical surface reconstructions, and as such, it comes with benefits and limitations of interpolation between the surface and volume as we discussed earlier. Nevertheless, the approach can be easily extended using the proposed volumetric GM graph and wavelet design.

6   Conclusion

We have extended fMRI activation mapping based on spatial multi-scale transforms to exploit the geometrical structure of the GM. We leveraged recent advances in graph-based wavelet design to incorporate this prior knowledge in the transformation. The procedure included the construction of a GM-adapted graph, including different subgraphs for cerebral and cerebellar regions. The wavelet-based SPM framework was presented to incorporate any linear spatial transform, including the spectral graph wavelet transform. Experimental and simulated results showed the potential of the proposed approach in terms of improved specificity and sensitivity for multi-subject studies, and to reveal fine-grained activity patterns.

Software

The source code of the proposed method is made available to the community at bme.lth.se/staff/behjat-hamid/software/ and miplab.epfl.ch/software/.

Acknowledgements

Appendix A. Tight Spectral Graph Meyer-Like Wavelet Frame

An example of tight graph wavelet frame can be constructed by defining Meyer-like wavelet and scaling kernels in the spectral graph domain as [26]

$$
g(\lambda) = \begin{cases} \sin(\frac{\pi}{2}\nu(q(\frac{\lambda}{a} - 1))) & \forall \lambda \in]a, Ma] \\ \cos(\frac{\pi}{2}\nu(q(\frac{\lambda}{Ma} - 1))) & \forall \lambda \in]Ma, M^2 a] \\ 0 & \text{elsewhere} \end{cases} \tag{20}
$$

$$
h(\lambda) = \begin{cases} 1 & \forall \lambda \in [0, a] \\ \cos(\frac{\pi}{2}\nu(q(\frac{\lambda}{a} - 1))) & \forall \lambda \in]a, Ma] \\ 0 & \text{elsewhere} \end{cases} \tag{21}
$$

respectively, where M denotes the dilation factor and is set by $q \in \mathbb{Z}$ as $M = \frac{q+1}{q}$, $a = (q - \epsilon)b$, $\epsilon \in]0, (1 + M)^{-1}]$ and $a, b \in \mathbb{R}^+$. The classical dyadic dilation corresponds to $M = 2$. The J wavelet scales are defined as

$$
t_j = \frac{a}{\lambda_{max}} M^j, \quad j = 1, \dots, J.
$$

The resulting construction leads to a set of kernels where the support of each kernels is a strict subset of the eigenvectors of $\mathcal{L}$ (i.e., bandpass filters), and the union of the functions $|g(t_j\lambda)|^2$ and $|h(t_J\lambda)|^2$ forms a partition of unity, i.e.,

$$
\sum_{j=1}^{J} |g(t_j\lambda)|^2 + |h(t_J\lambda)|^2 = 1.
$$

References

[1] S. Ogawa, R. S. Menon, D. W. Tank, S. G. Kim, H. Merkle, J. M. Ellermann, and K. Ugurbil, "Functional brain mapping by blood oxygenation level-

dependent contrast magnetic resonance imaging. A comparison of signal characteristics with a biophysical model.," *Biophys. J.*, vol. 64, no. 3, pp. 803–812, 1993.

[2] R. S. Frackowiak, K. Friston, C. Frith, R. Dolan, and J. Mazziotta, *Human Brain Function*. Academic Press, 1997.

[3] K. J. Friston, A. P. Holmes, K. J. Worsley, J.-P. Poline, C. D. Frith, and R. S. J. Frackowiak, "Statistical parametric maps in functional imaging: a general linear approach," *Hum. Brain Mapp.*, vol. 2, pp. 189–210, 1994.

[4] J. B. Poline, K. J. Worsley, A. C. Evans, and K. J. Friston, "Combining spatial extent and peak intensity to test for activations in functional imaging.," *NeuroImage*, vol. 5, pp. 83–96, 1997.

[5] J. Aston, R. Gunn, and F. Hinz, R. Turkheimer, "Wavelet variance components in image space for spatiotemporal neuroimaging data," *NeuroImage*, vol. 25, no. 1, pp. 159–168, 2005.

[6] U. E. Ruttimann, M. Unser, R. R. Rawlings, D. Rio, N. F. Ramsey, D. Mattay, V. S. Hommer, J. Frank, and D. R. Weinberger, "Statistical analysis of functional MRI data in the wavelet domain," *IEEE Trans. Med. Imag.*, vol. 17, no. 2, pp. 142–154, 1998.

[7] M. Soleymani, G. Hossein-Zadeh, and H. Soltanian-Zadeh, "Fixed and random effect analysis of multi-subject fMRI data using wavelet transform," *J. Neurosci. Methods*, vol. 176, no. 2, pp. 237–245, 2009.

[8] D. Van De Ville, T. Blu, and M. Unser, "Integrated wavelet processing and spatial statistical testing of fMRI data," *NeuroImage*, vol. 23, pp. 1472–1485, 2004.

[9] D. Van De Ville, M. Seghier, F. Lazeyras, T. Blu, and M. Unser, "WSPM: wavelet-based statistical parametric mapping.," *NeuroImage*, vol. 37, pp. 1205–1217, 2007.

[10] A. M. Wink and J. B. Roerdink, "Denoising functional MR images: a comparison of wavelet denoising and gaussian smoothing," *IEEE Trans. Med. Imag.*, vol. 23, no. 3, pp. 374–387, 2004.

[11] G. Flandin and W. D. Penny, "Bayesian fMRI data analysis with sparse spatial basis function priors," *NeuroImage*, vol. 34, no. 3, pp. 1108–1125, 2007.

[12] N. Sanyal and M. A. Ferreira, "Bayesian hierarchical multi-subject multiscale analysis of functional MRI data," *NeuroImage*, vol. 63, no. 3, pp. 1519–1531, 2012.

[13] E. Bullmore, J. Fadili, V. Maxim, L. Sendur, B. Whitcher, J. Suckling, M. Brammer, and M. Breakspear, "Wavelets and functional magnetic resonance imaging of the human brain.," *NeuroImage*, vol. 23 Suppl 1, pp. S234–S249, 2004.

[14] B. Fischl, D. H. Salat, E. Busa, M. Albert, M. Dieterich, C. Haselgrove, and A. M. Dale, "Whole brain segmentation: automated labeling of neuroanatomical structures in the human brain.," *Neuron*, vol. 33, no. 3, pp. 341–355, 2002.

[15] D. Riviere, J. Mangin, P.-O. D., j. M. Martinez, V. Frouin, and J. Regis, "Automatic recognition of cortical sulci of the human brain using a congregation of neural networks," *Med. Image Anal.*, vol. 6, no. 2, pp. 77–92., 2002.

[16] S. J. Kiebel, R. Goebel, and K. J. Friston, "Anatomically informed basis functions," *NeuroImage*, vol. 11, no. 6, pp. 656–667, 2000.

[17] S. Kiebel and K. J. Friston, "Anatomically informed basis functions in multi-subject studies," *Hum. Brain Mapp.*, vol. 16, no. 1, pp. 36–46, 2002.

[18] A. Andrade, F. Kherif, J. Mangin, K. J. Worsley, O. Paradis, A. Simon, S. Dehaene, D. L. Bihan, and J. Poline, "Detection of fMRI activation using cortical surface mapping," *Hum. Brain Mapp.*, vol. 12, no. 2, pp. 79–93, 2001.

[19] M. K. Chung, S. M. Robbins, K. M. Dalton, R. J. Davidson, A. L. Alexander, and A. C. Evans, "Cortical thickness analysis in autism with heat kernel smoothing," *NeuroImage*, vol. 25, no. 4, pp. 1256–1265, 2005.

[20] D. J. Hagler Jr, A. P. Saygin, and M. I. Sereno, "Smoothing and cluster thresholding for cortical surface-based group analysis of fMRI data," *NeuroImage*, vol. 33, no. 4, pp. 1093–1103, 2006.

[21] A. Qiu, D. Bitouk, and M. I. Miller, "Smooth functional and structural maps on the neocortex via orthonormal bases of the Laplace-Beltrami operator," *IEEE Trans. Med. Imag.*, vol. 25, no. 10, pp. 1296–1306, 2006.

[22] E. Bullmore and O. Sporns, "Complex brain networks: graph theoretical analysis of structural and functional systems.," *Nat. Rev. Neurosci.*, vol. 10, no. 3, pp. 186–198, 2009.

[23] J. Richiardi, S. Achard, H. Bunke, and D. Van De Ville, "Machine learning with brain graphs: predictive modeling approaches for functional imaging in systems neuroscience," *IEEE Signal Process. Mag.*, vol. 30, no. 3, pp. 58–70, 2013.

[24] D. I. Shuman, S. K. Narang, P. Frossard, A. Ortega, and P. Vandergheynst, "The emerging field of signal processing on graphs: Extending high-dimensional data analysis to networks and other irregular domains," *IEEE Signal Process. Mag.*, vol. 30, no. 3, pp. 83–98, 2013.

[25] D. Hammond, P. Vandergheynst, and R. Gribonval, "Wavelets on graphs via spectral graph theory," *Appl. Comput. Harmon. Anal.*, vol. 30, no. 2, pp. 129–150, 2011.

[26] N. Leonardi and D. Van De Ville, "Tight wavelet frames on multislice graphs," *IEEE Trans. Signal Process.*, vol. 61, no. 13, pp. 3357–3367, 2013.

[27] J. F. Mangin, D. Riviere, A. Cachia, E. Duchesnay, Y. Cointepas, D. Papadopoulos-Orfanos, P. Scifo, T. Ochiai, F. Brunelle, and J. Regis, "A framework to study the cortical folding patterns.," *NeuroImage*, vol. 23, pp. S129–S138, 2004.

[28] N. Tzourio-Mazoyer, B. Landeau, D. Papathanassiou, F. Crivello, O. Etard, N. Delcroix, B. Mazoyer, and M. Joliot, "Automated anatomical labeling of activations in SPM using a macroscopic anatomical parcellation of the MNI MRI Single-Subject Brain," *NeuroImage*, vol. 15, pp. 273–289, 2002.

[29] A. Evans, D. Louis Collins, S. R. Mills, E. D. Brown, R. L. Kelly, and T. M. Peters, "3D statistical neuroanatomical models from 305 MRI volumes," in *Nucl. Sci. Symp. Med. Imag. Conf.*, pp. 1813–1817, 1993.

[30] J. Ashburner, "A fast diffeomorphic image registration algorithm," *NeuroImage*, vol. 38, pp. 95–113, 2007.

[31] A. Klein, J. Andersson, B. Ardekani, J. Ashburner, B. Avants, M. Chiang, G. Christensen, and et al, "Evaluation of 14 nonlinear deformation algorithms applied to human brain MRI registration," *NeuroImage*, vol. 46, no. 3, pp. 786–802, 2009.

[32] J. Diedrichsen, "A spatially unbiased atlas template of the human cerebellum," *NeuroImage*, vol. 33, no. 1, pp. 127–138, 2006.

[33] F. Chung, *Spectral graph theory*. Providence, RI: AMS, 1997.

[34] J. Ashburner and K. J. Friston, "Unified segmentation," *NeuroImage*, vol. 26, no. 3, pp. 839–851, 2005.

[35] J. Diedrichsen, J. H. Balsters, J. Flavell, E. Cussans, and N. Ramnani, "A probabilistic MR atlas of the human cerebellum," *NeuroImage*, vol. 46, no. 1, pp. 39–46, 2009.

[36] J. Benedetto and M. Fickus, "Finite normalized tight frames," *Adv. Comput. Math.*, vol. 18, no. 2, pp. 357–385, 2003.

[37] A. M. C. Kelly, L. Q. Uddin, B. B. Biswal, F. X. Castellanos, and M. P. Milham, "Competition between functional brain networks mediates behavioral variability," *NeuroImage*, vol. 39, no. 1, pp. 527–537, 2008.

[38] N. Logothetis and B. Wandell, "Interpreting the BOLD signal.," *Annu. Rev. Physiol.*, vol. 66, pp. 735–769, 2004.

[39] H. J. Jo, J. M. Lee, J. H. Kim, C. H. Choi, B. M. Gu, D. H. Kang, J. Ku, J. S. Kwon, and S. I. Kim, "Artificial shifting of fMRI activation localized by volume- and surface-based analyses," *NeuroImage*, vol. 40, no. 3, pp. 1077–1089., 2008.

[40] M. Mikl, R. Mareček, P. Hluštík, M. Pavlicová, A. Drastich, P. Chlebus, M. Brázdil, and P. Krupa, "Effects of spatial smoothing on fmri group inferences," *Magn. Reson. Imaging*, vol. 26, no. 4, pp. 490–503, 2008.

[41] M. Reimold, M. Slifstein, A. Heinz, W. Mueller-Schauenburg, and R. Bares, "Effect of spatial smoothing on t-maps: arguments for going back from t-maps to masked contrast images," *J. Cereb. Blood Flow Metab.*, vol. 26, no. 6, pp. 751–759, 2006.

[42] A. Eklund, M. Andersson, C. Josephson, M. Johannesson, and H. Knutsson, "Does parametric fMRI analysis with SPM yield valid results? - An empirical study of 1484 rest datasets.," *NeuroImage*, vol. 61, no. 3, pp. 565–578, 2012.

[43] H. Behjat, N. Leonardi, L. Sörnmo, and D. Van De Ville, "Canonical cerebellar graph wavelets and their application to fMRI activation mapping," in *Proc. IEEE Int. Conf. Eng. Med. Biol. Soc.*, pp. 1039–1042, 2014.

[44] U. Von Luxburg, "A tutorial on spectral clustering," *Stat. Comput.*, vol. 17, no. 4, pp. 395–416, 2007.

[45] C. Grova, S. Makni, G. Flandin, P. Ciuciu, J. Gotman, and J. B. Poline, "Anatomically informed interpolation of fMRI data on the cortical surface," *NeuroImage*, vol. 31, no. 4, pp. 1475–1486, 2006.

[46] G. Operto, R. Bulot, J. L. Anton, and O. Coulon, "Projection of fMRI data onto the cortical surface using anatomically-informed convolution kernels," *NeuroImage*, vol. 39, no. 1, pp. 127–135, 2008.

[47] H. J. Jo, J. M. Lee, J. H. Kim, Y. W. Shin, I. Y. Kim, J. S. Kwon, and S. I. Kim, "Spatial accuracy of fMRI activation influenced by volume- and surface-based spatial smoothing techniques," *NeuroImage*, vol. 34, no. 2, pp. 550–564, 2007.

[48] D. Van De Ville, T. Blu, and M. A. & Unser, "Wavelets versus resels in the context of fMRI: establishing the link with SPM," in *SPIE's Symposium on Optical Science and Technology: Wavelets X, vol. 5207*, vol. 5207, pp. 417–425, 2003.

[49] H. Behjat, N. Leonardi, and D. Van De Ville, "Statistical parametric mapping of functional MRI data using wavelets adapted to the cerebral cortex," in *Proc. IEEE Int. Symp. Biomed. Imaging*, pp. 1070–1073, 2013.

[50] S. Ozkaya and D. Van De Ville, "Anatomically adapted wavelets for integrated statistical analysis of fMRI data," in *Proc. IEEE Int. Symp. Biomed. Imaging*, (Chicago, IL), pp. 469–472, 2011.

[51] S. Ozkaya, *Randomized wavelets on arbitrary domains and applications to functional MRI analysis*. PhD thesis, Princeton University, 2012.

[52] W. Sweldens, "The lifting scheme: A custom-design construction of biorthogonal wavelets," *Appl. Comput. Harmon. Anal.*, vol. 3, no. 2, pp. 186–200, 1996.

[53] W. H. Kim, V. Singh, M. K. Chung, C. Hinrichs, D. Pachauri, O. C. Okonkwo, and S. C. Johnson, "Multi-resolutional shape features via non-Euclidean wavelets: Applications to statistical analysis of cortical thickness," *NeuroImage*, vol. 93, pp. 107–123, 2014.

[54] C. Li and A. B. Hamza, "A multiresolution descriptor for deformable 3D shape retrieval," *Vis. Comput.*, vol. 29, no. 6, pp. 513–524, 2013.

[55] J. Diedrichsen, S. Maderwald, M. Küper, M. Thürling, K. Rabe, E. Gizewski, M. E. Ladd, and D. Timmann, "Imaging the deep cerebellar nuclei: a probabilistic atlas and normalization procedure," *NeuroImage*, vol. 54, no. 3, pp. 1786–1794, 2011.

[56] D. Le Bihan, J. F. Mangin, C. Poupon, C. A. Clark, S. Pappata, N. Molko, and H. Chabriat, "Diffusion tensor imaging: concepts and applications," *J. Magn. Reson. Imaging*, vol. 13, no. 4, pp. 534–546, 2001.

[57] D. K. Hammond, B. Scherrer, and S. K. Warfield, "Cortical graph smoothing: a novel method for exploiting DWI-derived anatomical brain connectivity to improve EEG source estimation," *IEEE Trans. Med. Imag.*, vol. 32, no. 10, pp. 1952–1963, 2013.

[58] A. Eklund, P. Dufort, D. Forsberg, and S. M. LaConte, "Medical image processing on the GPU - past, present and future," *Med. Image Anal.*, vol. 17, no. 8, pp. 1073–1094, 2013.

[59] E. J. Canales-Rodriguez, J. Radua, E. Pomarol-Clotet, S. Sarro, Y. Aleman-Gomez, Y. Iturria-Medina, and R. Salvador, "Statistical analysis of brain tissue images in the wavelet domain: Wavelet-based morphometry," *NeuroImage*, vol. 72, pp. 214–226, 2013.

[60] Z. Lao, D. Shen, Z. Xue, B. Karacali, S. M. Resnick, and C. Davatzikos, "Morphological classification of brains via high-dimensional shape transformations and machine learning methods," *NeuroImage*, vol. 21, no. 1, pp. 46–57, 2004.

[61] K. Hackmack, F. Paul, M. Weygandt, C. Allefeld, and J. D. Haynes, "Multiscale classification of disease using structural MRI and wavelet transform," *NeuroImage*, vol. 62, no. 1, pp. 48–58, 2012.

[62] L. C. Harrison, M. Raunio, K. K. Holli, T. Luukkaala, S. Savio, I. Elovaara, S. Soimakallio, H. J. Eskola, and P. Dastidar, "MRI texture analysis in multiple sclerosis: toward a clinical analysis protocol," *Acad. Radiol.*, vol. 17, no. 6, pp. 696–707, 2010.

Paper II

Signal-Adapted Tight Frames on Graphs

Abstract

The analysis of signals on complex topologies modeled by graphs is a topic of increasing importance. Decompositions play a crucial role in representation and processing of such information. Here we propose a new tight frame design that is adapted to a class of signals on a graph. The construction starts from a prototype Meyer-type system of kernels with uniform subbands. The ensemble energy spectral density is then defined for a given set of signals defined on the graph. The prototype design is then warped such that the resulting subbands capture the same amount of energy for the signal class. This approach accounts at the same time for graph topology and signal features. The proposed frames are constructed for three different graph signal sets and are compared to non signal-adapted frames. Vertex localization of a set of resulting atoms is studied. The frames are then used to decompose a set of real graph signals, and are also used in a setting of signal denoising. The results illustrate the superiority of the designed signal-adapted frames, over frames blind to signal characteristics, in representing data and in denoising.

1   Introduction

Graphs provide a flexible framework for representing data that lie on topologically complex domains. Thus, much attention has been given to generalizing fundamental signal processing operations to the graph setting [1, 2, 3]. In particular, many proposals relate to extending multi-resolution transforms, filter bank designs and dictionary constructions for signals on graphs [4, 5, 6, 7, 8, 9, 10, 11, 12, 13, 14, 15, 16, 17, 18, 19, 20, 21, 22, 23, 24, 25, 26, 27]. These studies fall essentially within two regimes: spatial (vertex) and spectral (frequency) designs. Constructions that fall within the former regime include methods based on lifting schemes [4, 5, 6] and methods in designing wavelets for hierarchical trees [7, 8, 9]. The latter regime can be viewed as defining dictionaries comprised of atoms that are constructed by translating smooth graph spectral filters to different vertices of the graph. The graph spectrum is defined as the eigenspace of a graph Laplacian matrix. One of the first proposals of such a dictionary is the spectral graph wavelet transform (SGWT) frame [10] that is constructed based on a system of spline-based spectral kernels, including a lowpass kernel and a sequence of dilated bandpass kernels. Constructions of systems of spectral graph kernels leading to tight frames were proposed in [11, 12, 13]. Tight frames are particularly interesting because of their property of energy conservation between the original and transformed domain [28]. Other approaches to spectral domain design include diffusion wavelets [14], vertex-frequency frames [23] and approaches to graph filter-bank design using bipartite graph decompositions [15, 16, 17, 18, 19, 20], graph coloring [25] and connected sub-graph decomposition [21].

The aforementioned spectral designs are blind to the fact that the eigenvalues of the Laplacian matrix that define the graph spectrum are typically irregularly spaced, unlike the definition of discrete frequencies for regular signals. As a step towards adaptation to the spectral properties of the graph domain, the construction of spectrum-adapted tight graph wavelet and vertex-frequency frames was recently proposed in [24]. The spectrum-adapted spectral kernels are adapted to the distribution of eigenvalues of the graph Laplacian matrix such that a similar number of eigenvalues lies in the support of each spectral kernel.

Besides considering the structural characteristics of the graph, a major improvement to the frame design would be to also consider the properties of the signals realized on the graph. To this aim, Thanou et al. [26, 27] have pursued a structured, numerical dictionary learning approach in which wavelet dictionaries are learnt based on a set of training signals. Since the graph structure is incorporated into the learning process, the learned kernels are indirectly adapted to the graph Laplacian spectrum as well as to the training data. This approach is effective in providing a sparse representation of graph signals that can be described as combinations of overlapping local patterns. In a more empirical approach [29, 30, 31], the Meyer-like frame design [11] has been

tailored to fMRI signals by defining a spectral partitioning such that a small number of narrow-support filters, covering the lower end of the spectrum, are constructed.

In this paper, we propose an approach for constructing tight graph frames that account not only for the intrinsic topological structure of the underlying graph as proposed in [24], but also for the characteristics of a given set of signals. This is accomplished by considering a graph-based energy spectral density notion that includes signal and topology properties and encodes the energy-wise significance of the graph eigenvalues. A system of spectral kernels tailored to the energy spectral density is constructed by starting from the design of a prototype Meyer-type tight frame with uniform spectral coverage, followed by a warping step which incorporates the energy spectral density information to the prototype design, resulting in a tight frame with equi-energy subbands.

The paper is organized as follows. In Section 2, definitions related to spectral graph theory, tight frames and graph signal decomposition are briefly reviewed. In Section 3, the procedure for constructing signal-adapted tight frames is introduced. In Section 4, insight on vertex localization of the resulting atoms is provided. In Section 5, constructions of the proposed frame for three different graph signal sets are presented, vertex localization of a set of resulting atoms is quantified, the coefficients resulting from decomposing a real graph dataset are studied, and finally, the proposed frames are used in the setting of signal denoising.

2 Preliminaries

2.1 Graphs and Spectral Graph Theory

An undirected, weighted graph $\mathcal{G} = (\mathcal{V}, \mathcal{E}, A)$ consists of a set $\mathcal{V}$ of N_g vertices, a set $\mathcal{E}$ of edges (i.e., pairs (i, j) where $i, j \in \mathcal{V}$) and a weighted adjacency matrix $A = [a_{i,j}]$, where $a_{i,j}$ denotes the weight of the edge between vertices i and j. The degree matrix D is diagonal with elements $d_{i,i} = \sum_j a_{i,j}$. The Laplacian matrices of $\mathcal{G}$ in combinatorial form L and normalized form $\mathcal{L}$ are defined as

$$L = D - A, \tag{1}$$

$$\mathcal{L} = D^{-1/2} L D^{-1/2}, \tag{2}$$

respectively. Since both L and $\mathcal{L}$ are symmetric and positive semi-definite, their eigendecompositions lead to a set of N_g real, non-negative eigenvalues that define the graph spectrum

$$\Lambda(\mathcal{G}) = \{0 = \lambda_1 \leq \lambda_2 \cdots \leq \lambda_{N_g} = \lambda_{\max}\}. \tag{3}$$

The corresponding set of eigenvectors $\{\chi_l\}_{l=1}^{N_g}$ forms a complete set of orthonormal vectors that span the graph spectral domain [32]. When necessary, we use the notations $\Lambda_L(\mathcal{G})$ and $\Lambda_{\mathcal{L}}(\mathcal{G})$ to distinguish between the two definitions of the graph Laplacian. As the eigenvalues may be repetitive, for each λ_l, we denote its algebraic multiplicity by m_{λ_l} and the index of its first occurrence by i_{λ_l}. That is, if λ_l is singular, i.e. $m_{\lambda_l} = 1$, then $i_{\lambda_l} = l$, and if λ_l is repetitive, then $i_{\lambda_l} \leq l$. The multiplicity of eigenvalues equal to zero reflects the number of connected components in the graph. In this paper, only connected graphs are considered, and thus, $m_{\lambda_1} = 1$.

2.2 Graph Signals

Let $\mathbb{R}(\mathcal{V})$ denote a Hilbert space of real-valued signals defined on the vertices of the graph, with the inner product defined as $\forall \boldsymbol{f}_1, \boldsymbol{f}_2 \in \mathbb{R}(\mathcal{V}), \langle \boldsymbol{f}_1, \boldsymbol{f}_2 \rangle = \sum_{n=1}^{N_g} \boldsymbol{f}_1[n]\boldsymbol{f}_2[n]$, and the norm as $\forall \boldsymbol{f} \in \mathbb{R}(\mathcal{V}), ||\boldsymbol{f}||_2^2 = \langle \boldsymbol{f}, \boldsymbol{f} \rangle = \sum_{n=1}^{N_g} |\boldsymbol{f}[n]|^2$.

Graph Fourier Transform

For any $\boldsymbol{f} \in \mathbb{R}(\mathcal{V})$, its spectral representation $\widehat{\boldsymbol{f}} \in \mathbb{R}(\mathcal{V})$, known as the graph Fourier transform of $\boldsymbol{f}$, can be used to express $\boldsymbol{f}$ in terms of the graph Laplacian eigenvectors

$$\boldsymbol{f}[n] = \sum_{l=1}^{N_g} \underbrace{\langle \boldsymbol{f}, \chi_l \rangle}_{=\widehat{\boldsymbol{f}}[l]} \chi_l[n]. \tag{4}$$

Parseval Relation

With this definition of the Fourier transform, it can be shown that the Parseval relation holds [23]

$$\forall \boldsymbol{f}_1, \boldsymbol{f}_2 \in \mathbb{R}(\mathcal{V}), \quad \langle \boldsymbol{f}_1, \boldsymbol{f}_2 \rangle = \langle \widehat{\boldsymbol{f}}_1, \widehat{\boldsymbol{f}}_2 \rangle. \tag{5}$$

Generalized Convolution Product

For any two graph signals $\boldsymbol{f}_1, \boldsymbol{f}_2 \in \mathbb{R}(\mathcal{V})$, the generalized convolution product is defined as

$$(\boldsymbol{f}_1 * \boldsymbol{f}_2)[n] = \sum_{l=1}^{N_g} \widehat{\boldsymbol{f}}_1[l]\widehat{\boldsymbol{f}}_2[l]\chi_l[n]. \tag{6}$$

Graph Signal Filtering

In analogy with conventional signal processing, filtering of graph signals can be viewed as an operation in the spectral domain. For a given graph signal $\boldsymbol{f} \in \mathbb{R}(\mathcal{V})$ and graph filter $\boldsymbol{g} \in \mathbb{R}(\mathcal{V})$, defined through its Fourier transform $\widehat{\boldsymbol{g}}$, the filtered signal, denoted by $(F_{\boldsymbol{g}} \boldsymbol{f})$, can be obtained as

$$(F_{\boldsymbol{g}} \boldsymbol{f})[n] = (\boldsymbol{g} * \boldsymbol{f})[n] \tag{7}$$

$$\overset{(6)}{=} \sum_{l=1}^{N_g} \widehat{\boldsymbol{g}}[l] \widehat{\boldsymbol{f}}[l] \boldsymbol{\chi}_l[n]. \tag{8}$$

The filter response of an impulse at vertex m

$$\boldsymbol{f} = \boldsymbol{\delta}_m \leftrightarrow \widehat{\boldsymbol{\delta}}_m[l] = \langle \boldsymbol{\delta}_m, \boldsymbol{\chi}_l \rangle = \boldsymbol{\chi}_l[m], \tag{9}$$

can then be obtained as

$$(F_{\boldsymbol{g}} \boldsymbol{\delta}_m)[n] = \sum_{l=1}^{N_g} \widehat{\boldsymbol{g}}[l] \boldsymbol{\chi}_l[m] \boldsymbol{\chi}_l[n], \tag{10}$$

which, in general, is shift-variant; i.e, in the vertex domain, it is not a shifted version of the same graph signal. Therefore, for convenience, a graph filter can be defined by its spectral kernel $\widehat{\boldsymbol{g}}$.

To design spectral kernels, it is often more elegant to define an underlying smooth continuous kernel. For instance, we consider $\mathcal{K}(\lambda) : [0, \lambda_{\max}] \to \mathbb{R}^+$, from which we derive a discrete version through sampling as

$$\boldsymbol{k}[l] = \mathcal{K}(\lambda_l), \quad l = 1, \ldots, N_g. \tag{11}$$

Note that although spectral kernels (i.e., $\mathcal{K}(\lambda)$ and $\boldsymbol{k}$) are defined in the spectral domain, they are not linked to any explicit vertex representation, and thus, the Fourier symbol $\widehat{}$ is not used for their denotation. This notation convention will be used throughout the paper.

2.3 Dictionary of Graph Atoms

As noted before, for a given kernel $\boldsymbol{k}$ associated with $\mathcal{K}$, the vertex-domain impulse responses are obtained as

$$\boldsymbol{\psi}_{\mathcal{K},m} = (F_{\boldsymbol{k}} \boldsymbol{\delta}_m) \leftrightarrow \widehat{\boldsymbol{\psi}}_{\mathcal{K},m}[l] = \boldsymbol{k}[l] \boldsymbol{\chi}_l[m]. \tag{12}$$

The collection of impulse responses $\{\boldsymbol{\psi}_{\mathcal{K},m}\}_{m=1}^{N_g}$ are considered graph atoms associated with the spectral kernel $\mathcal{K}(\lambda)$. Given a set of J spectral kernels $\{\boldsymbol{k}_j\}_{j=1}^{J} \in \mathbb{R}(\mathcal{V})$, a dictionary $\mathcal{D}_{\mathcal{G}}$ containing JN_g atoms is obtained as

$$\mathcal{D}_{\mathcal{G}} = \left\{ \{\boldsymbol{\psi}_{\mathcal{K}_j,m}\}_{j=1}^{J} \right\}_{m=1}^{N_g}. \tag{13}$$

The atoms of $\mathcal{D}_{\mathcal{G}}$ form a frame in $\ell_2(\mathcal{V})$ if there exist bounds $B_2 \geq B_1 > 0$ such that [28]

$$\forall \boldsymbol{f} \in \mathbb{R}(\mathcal{V}), \quad B_1 ||\boldsymbol{f}||_2^2 \leq \sum_{j,m} |\langle \boldsymbol{f}, \boldsymbol{\psi}_{\mathcal{K}_j,m} \rangle|^2 \leq B_2 ||\boldsymbol{f}||_2^2, \tag{14}$$

where the frame bounds are given by

$$B_1 = \min_{\lambda \in [0,\lambda_{\max}]} G(\lambda), \quad B_2 = \max_{\lambda \in [0,\lambda_{\max}]} G(\lambda), \tag{15}$$

and $G(\lambda)$ is defined as

$$G(\lambda) = \sum_{j=1}^{J} |\mathcal{K}_j(\lambda)|^2. \tag{16}$$

In particular, $\mathcal{D}_{\mathcal{G}}$ forms a tight frame if

$$\forall \lambda \in [0, \lambda_{\max}], \quad G(\lambda) = C, \tag{17}$$

and a Parseval frame if $C = 1$.

2.4 Decomposition of Graph Signals

Direct Decomposition

To decompose a graph signal $\boldsymbol{f}$ onto a set of the atoms in $\mathcal{D}_{\mathcal{G}}$, the coefficients can be obtained as

$$c_{\mathcal{K}_j,m} = \langle \boldsymbol{f}, \boldsymbol{\psi}_{\mathcal{K}_j,m} \rangle \tag{18}$$

$$\overset{(6)}{=} \sum_{l=1}^{N_g} \widehat{\boldsymbol{\psi}}_{\mathcal{K}_j,m}[l]\widehat{\boldsymbol{f}}[l], \tag{19}$$

$$\overset{(12)}{=} \sum_{l=1}^{N_g} \boldsymbol{k}_j[l]\widehat{\boldsymbol{f}}[l]\boldsymbol{\chi}_l[m]. \tag{20}$$

If $\mathcal{D_G}$ forms a Parseval frame, the original signal can be recovered as

$$
\begin{aligned}
\boldsymbol{f}[n] &= \sum_j \sum_m c_{\mathcal{K}_j,m} \boldsymbol{\psi}_{\mathcal{K}_j,m} \\
&= \sum_j \sum_m \sum_l \boldsymbol{k}_j[l]\widehat{\boldsymbol{f}}[l]\boldsymbol{\chi}_l[m] \sum_{l'} \boldsymbol{k}_j[l']\boldsymbol{\chi}_{l'}[m]\boldsymbol{\chi}_{l'}[n] \\
&= \sum_l \sum_{l'} \sum_j \boldsymbol{k}_j[l]\boldsymbol{k}_j[l']\widehat{\boldsymbol{f}}[l]\boldsymbol{\chi}_{l'}[n] \underbrace{\sum_m \boldsymbol{\chi}_l[m]\boldsymbol{\chi}_{l'}[m]}_{\delta_{l-l'}} \\
&= \sum_l \underbrace{\sum_j \boldsymbol{k}_j^2[l]}_{=1}\,\widehat{\boldsymbol{f}}[l]\boldsymbol{\chi}_l[n].
\end{aligned}
\tag{21}
$$

Decomposition Through Polynomial Approximation

The decomposition of $\boldsymbol{f}$ on $\mathcal{D_G}$ leads to the coefficients

$$
\boldsymbol{c}_{\mathcal{K}_j} = [c_{\mathcal{K}_j,1}, c_{\mathcal{K}_j,2}, \ldots, c_{\mathcal{K}_j,N_g}]^T \quad j = 1, \ldots, J,
$$

that can be interpreted as filtered versions of $\boldsymbol{f}$ with different spectral kernels $\{\boldsymbol{k}_j\}_{j=1}^J$. Due to the redundancy of such a transform, it is beneficial to implement the transform using a fast algorithm, rather than using the explicit compution of the coefficients through (20). This becomes even more crucial when large graphs are considered. One such algorithm is the Chebyshev polynomial approximation method [10], which is based on considering the expansion of the continuous spectral window functions $\{\mathcal{K}_j(\lambda)\}_{j=1}^J$ with the Chebyshev polynomials $\mathcal{C}_p(x) = \cos(p\arccos(x))$ as

$$
\mathcal{K}_j(x) = \frac{1}{2}d_{\mathcal{K}_j,0} + \sum_{p=1}^{\infty} d_{\mathcal{K}_j,p}\,\bar{\mathcal{C}}_p(x),
\tag{22}
$$

where $\bar{\mathcal{C}}_p(x) = \mathcal{C}_p(\frac{x-b}{b})$, $b = \lambda_{\max}/2$ and $d_{\mathcal{K}_j,p}$ denote the Chebyshev coefficients obtained as

$$
d_{\mathcal{K}_j,p} = \frac{2}{\pi}\int_0^\pi \cos(p\theta)\mathcal{K}_j(b(\cos(\theta)+1)).
\tag{23}
$$

By truncating (22) to M terms, $\boldsymbol{c}_{\mathcal{K}_j}$ can then be approximated as

$$
\tilde{\boldsymbol{c}}_{\mathcal{K}_j} = \frac{1}{2}d_{\mathcal{K}_j,0}\boldsymbol{f} + \sum_{p=1}^{M} d_{\mathcal{K}_j,p}\bar{\mathcal{C}}_p(L)\boldsymbol{f}.
\tag{24}
$$

We refer to [10] for further details.

3 Signal-Adapted Frame Construction

The objective is to construct a signal-adapted tight frame where the adaptivity is introduced by exploiting the spectral energy content of a given graph signal set. This approach is motivated by two observations: (i) the eigenvalues of the graph Laplacian that define the graph's spectrum are irregularly spaced, and depend in a complex way on the graph topology; (ii) the distribution of graph signals' energy is generally non-uniform across the spectrum. Based on these observations, the idea is to construct an 'adapted' frame, such that the energy-wise significance of the eigenvalues is taken into account, rather than only adapting based on the distribution of the eigenvalues as proposed in [24]. In this way, also the topological information of the graph is implicitly incorporated in the design, since the energy content is given in the graph spectral domain that is in turn defined by the eigenvalues. To formulate the problem, we first introduce a notion of energy for a given graph and a given signal set.

Definition (ensemble energy spectral density)

For a given graph $\mathcal{G}$, with spectrum $\Lambda(\mathcal{G})$, and graph signal set $\mathcal{F} = \{\boldsymbol{f}_s\}_{s=1}^{N_s}$, the ensemble energy spectral density of $\mathcal{F}$ can be obtained as

$$\bar{e}_{\mathcal{F}}[l] = \frac{1}{N_s} \sum_{s=1}^{N_s} \left| \left\langle \frac{\boldsymbol{f}_s}{||\boldsymbol{f}_s||_2}, \boldsymbol{\chi}_l \right\rangle \right|^2, \quad l = 1, \ldots, N_g, \tag{25}$$

where the normalization term ensures that each signal contributes equally to the ensemble energy and $\sum_l \bar{e}_{\mathcal{F}}[l] = 1$.

Using $\bar{e}_{\mathcal{F}}$, the desired system of spectral kernels $\{\boldsymbol{k}_j\}_{j=1}^{J}$ needs to be constructed such that each kernel captures an equal amount of ensemble energy, i.e.,

$$\sum_{l=2}^{N_g} \boldsymbol{k}_j[l] \bar{e}_{\mathcal{F}}[l] = \frac{1 - \bar{e}_{\mathcal{F}}[1]}{J}, \quad j = 1, \ldots, J \tag{26}$$

subject to the Parseval frame constraint, i.e.,

$$\sum_{j=1}^{J} |\boldsymbol{k}_j[l]|^2 = 1, \quad l = 1, \cdots, N_g. \tag{27}$$

The energy contribution from λ_1 is excluded from the design as it merely reflects the ensemble mean of the signal set.

We propose a two-step procedure to obtain such a design. First, a prototype system of continuous spectral kernels, $\{\mathcal{K}'_j(\lambda)\}_{j=1}^J$, is obtained such that they satisfy the following uniformity constraint

$$\exists\, C \in \mathbb{R}^+, \quad \int_0^{\lambda_{\max}} \mathcal{K}'_j(\lambda)\, \mathrm{d}\lambda = C, \quad j = 1, \ldots, J, \tag{28}$$

subject to the tight Parseval frame constraint,

$$\sum_{j=1}^J |\mathcal{K}'_j(\lambda)|^2 = 1, \quad \forall \lambda \in [0, \lambda_{\max}]. \tag{29}$$

Second, an energy-equalizing transformation $T_{\mathcal{F}}(\lambda)$ is constructed and incorporated in $\{\mathcal{K}'_j(\lambda)\}_{j=1}^J$, leading to a warped version of the prototype design

$$\mathcal{K}_j(\lambda) = \mathcal{K}'_j(T_{\mathcal{F}}(\lambda)), \quad j = 1, \ldots, J. \tag{30}$$

Provided that $T_{\mathcal{F}}(\lambda)$ is designed such that it is monotonically increasing and satisfies

$$\sum_{l=a_j}^{b_j} \bar{e}_{\mathcal{F}}[l] = \frac{1 - \bar{e}_{\mathcal{F}}[1]}{J}, \quad j = 1, \ldots, J, \tag{31}$$

where

$$a_j = \underset{l \in \{1, \ldots, N_g\}}{\arg\min} \left\{ \left| T_{\mathcal{F}}(\lambda_l) - \frac{j-1}{J}\lambda_{\max} \right| \right\} \tag{32}$$

$$b_j = \underset{l \in \{1, \ldots, N_g\}}{\arg\min} \left\{ \left| T_{\mathcal{F}}(\lambda_l) - \frac{j}{J}\lambda_{\max} \right| \right\}, \tag{33}$$

the resulting $\{\mathcal{K}_j(\lambda)\}_{j=1}^J$ corresponds to the desired signal-adapted system of spectral kernels in the continuous domain. If a discrete representation is needed for direct decomposition as in (20), $\{\boldsymbol{k}_j\}_{j=1}^J$ can be obtained through sampling. In the following, these two steps are explained in detail.

3.1   Step 1: Prototype System of Spectral Kernels Construction

While there is no unique solution that satisfies (28), prototype systems of spectral kernels satisfying this constraint subject to (29) can be designed. In this paper, we aim at designing spectral kernels similar to those of the Meyer-like graph wavelet
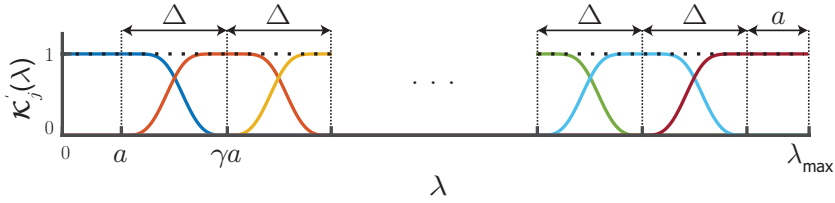
Figure 1: Construction of UMT system of spectral kernels.

frame [11] since they have (i) a finite support of the bandpass type, and (ii) smooth transition bands that have an advantageous effect on localization in the vertex domain [23, 10]. The following proposition introduces the design of a uniform Meyer-type system of spectral kernels.

Proposition 1. *(uniform Meyer-type (UMT) system of spectral kernels) Using the auxiliary function of the Meyer wavelet, given by [33]*

$$\nu(x) = x^4(35 - 84x + 70x^2 - 20x^3),\tag{34}$$

a set of $J \geq 2$ spectral kernels defined as

$$\mathcal{K}'_1(\lambda) = \begin{cases} 1 & \forall \lambda \in [0, a] \\ \cos(\frac{\pi}{2}\nu(\frac{1}{\gamma-1}(\frac{\lambda}{a} - 1))) & \forall \lambda \in]a, \gamma a] \\ 0 & \text{elsewhere} \end{cases}\tag{35a}$$

$$\mathcal{K}'_j(\lambda) = \begin{cases} \sin(\frac{\pi}{2}\nu(\frac{1}{\gamma-1}(\frac{\lambda-(j-2)\Delta}{a} - 1))) & \forall \lambda \in]\lambda_I, \lambda_{II}] \\ \cos(\frac{\pi}{2}\nu(\frac{1}{\gamma-1}(\frac{\lambda-(j-1)\Delta}{a} - 1))) & \forall \lambda \in]\lambda_{II}, \lambda_{II} + \Delta] \\ 0 & \text{elsewhere} \end{cases}\tag{35b}$$

$$\mathcal{K}'_J(\lambda) = \begin{cases} \sin(\frac{\pi}{2}\nu(\frac{1}{\gamma-1}(\frac{\lambda-(J-2)\Delta}{a} - 1))) & \forall \lambda \in]\lambda_I, \lambda_{II}] \\ 1 & \forall \lambda \in]\lambda_{II}, \lambda_{II} + a] \\ 0 & \text{elsewhere} \end{cases}\tag{35c}$$

can be constructed, where

$$\Delta = \gamma a - a,\tag{36a}$$

$$\lambda_I = a + (j-2)\Delta,\tag{36b}$$

$$\lambda_{II} = \gamma a + (j-2)\Delta,\tag{36c}$$

$$a = \frac{\lambda_{max}}{J\gamma - J - \gamma + 3}.\tag{36d}$$
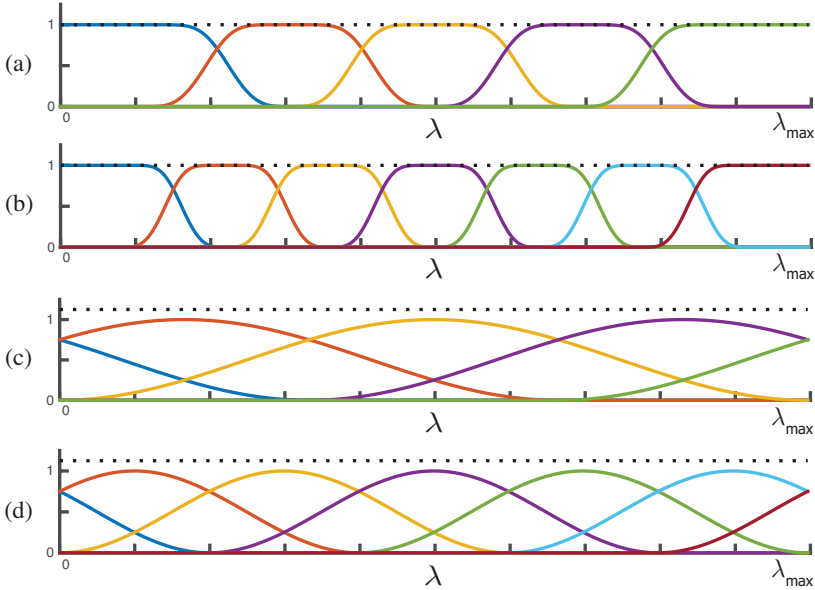
Figure 2: UMT system of spectral kernels as given in Proposition 1 displayed for (a) $J = 5$ and (b) $J = 7$ spectral scales. The HCUT system of spectral kernels [24] displayed for (c) $J = 5$ and (d) $J = 7$ spectral scales.

Fig. 1 illustrates the notations used. By setting $\gamma = 2.73$, the set of kernels defined in (48) satisfies the uniformity constraint given in (28). The atoms of a dictionary constructed using this set of spectral kernels form a Parseval frame on $\mathbb{R}(\mathcal{V})$.

Proof. see Appendix A.   □

Figs. 2(a) and (b) show realizations of the resulting UMT system of spectral kernels for a fixed $\lambda_{\max}$ and two different J. For comparison, the half-cosine uniform translate (HCUT) system of spectral kernels [24] are shown in Fig. 2(c) and (d). There are three main differences when comparing these two designs. First, the atoms of a dictionary constructed using the UMT system of spectral kernels not only form a tight frame but also a Parseval frame. Second, the UMT system of spectral kernels has better passband characteristics compared to HCUT system of spectral kernels as the support of each kernel is a more strict subset of the spectrum, with less overlap of adjacent kernels. Third, the UMT system of spectral kernels satisfies (28). The latter two differences are in favour of the proposed UMT design for our purpose.

3.2 Step 2: Energy-Equalizing Spectral Warping

Although the UMT system of filters satisfy the uniformity constraint (28), they satisfy the equi-energy constraint (26) only if 1) the graph's eigenvalues are uniformly distributed across the spectrum and 2) the ensemble energy contribution at each eigenvalue is equal. In fact, for a given graph and signal set, these two conditions do not hold in general. Using $\bar{e}_{\mathcal{F}}$, the desired continuous energy-equalizing transformation function $T_{\mathcal{F}}(\lambda) : [0, \lambda_{\max}] \to [0, \lambda_{\max}]$, can then be obtained through monotonic cubic interpolation [34] of the pair of points

$$\left\{ \left(\lambda_l \, , \, \frac{\lambda_{\max}}{m_{\lambda_l}(1 - \bar{e}_{\mathcal{F}}[1])} \sum_{r=i_{\lambda_l}}^{i_{\lambda_l}+m_{\lambda_l}} \sum_{k=2}^{r} \bar{e}_{\mathcal{F}}[k] \right) \right\}_{l=2}^{N_g}, \tag{37}$$

together with $(\lambda_1, 0)$. The resulting $T_{\mathcal{F}}(\lambda)$ satisfies (31). Thus, the set of spectral kernels obtained by warping the UMT system of kernels using $T_{\mathcal{F}}(\lambda)$, cf. (30), correspond to the desired signal-adapted system of spectral kernels.

3.3 Generalization

The proposed procedure for the design of signal-adapted frames can be generalised in two aspects. First, prototype designs other than the UMT can be designed and used as the base for the proposed frames, with a general case formulation given in Appendix B. Second, rather than the proposed ensemble energy spectral density measure given in (25), other forms of stationary signal information can be exploited to construct a suitable signal-adapted spectral transformation, with example measures recently extended to the graph setting given in [35, 36, 37]. Finally, we also note that, depending on the dataset, it can be beneficial to slightly smooth $T_{\mathcal{F}}(\lambda)$, in particular important at spectral regions where adjacent eigenvalues are minutely different in value and the ensemble energy significantly changes across them. A smooth $T_{\mathcal{F}}(\lambda)$, in turn, comes in favour of obtaining smoother spectral kernels.

4 Vertex Localization of Spectral Kernels

As in classical signal processing where the uncertainty principle determines the trade-off between fine localization in time (spatial) and frequency domain, a similar notion naturally extends to the graph setting, with example proposals given in [38, 23, 39, 40, 41]. As the present proposal of constructing frames is defined in the spectral domain, it is interesting to consider the theoretical constraints in the vertex localization of the resulting atoms. In particular, we first consider the bound on the vertex localization of

atoms provided through polynomial approximation [23]. For a polynomial spectral kernel of degree D, defined as

$$\mathcal{P}_D(\lambda_l) = \sum_{k=0}^{D} \alpha_k \lambda_l^k \tag{38}$$

for some coefficients $\{\alpha_k\}_{k=0}^{D}$, it can be shown that its associated atoms satisfy the localization constraint [23]

$$\forall n \in \mathcal{V}, \quad \psi_{\mathcal{P}_D,n}[m] = 0 \quad \text{if} \quad d_{\mathcal{G}}(n,m) > D, \tag{39}$$

where $d_{\mathcal{G}}(\cdot,\cdot)$ is a distance metric. As suggested in [38], the geodesic distance is one metric that can be used, in which case, $d_{\mathcal{G}}(i,j)$ is the length of the shortest path connecting vertices i and j. For a generic spectral kernel $\mathcal{K}(\lambda)$, the localization of its associated atoms can be quantified as [23]

$$|\psi_{\mathcal{K},n}[m]| \leq \sqrt{N_g} \inf_{\mathcal{P}_{D'}} \{||\mathcal{K} - \mathcal{P}_{D'}||_\infty\}, \tag{40}$$

where the infimum is taken over all polynomial kernels of degree D', as defined in (38), with $D' = d_{\mathcal{G}}(n,m) - 1$. An upper bound can be determined for the minimax polynomial approximation error of the infimum term. We refer to [23] for further details and a proof of (39) and (40).

Based on (39) and (40), if a given spectral kernel can be perfectly represented as a polynomial of degree M, its realization at a given vertex n will be localized in a sphere of radius M edges around vertex n; i.e., the lower the degree, the finer the localization in the vertex domain. If the approximation is not perfect, the vertices that fall outside the sphere will not necessarily be zero, but constrained by the bound in (40). This can be seen as the trade-off of vertex-spectral localization: the smoother the given spectral kernel $\mathcal{K}(\lambda)$ and the wider its transitions bands, the lower is its approximation error to a polynomial, and thus, the finer is the localization of its associated atoms in the vertex domain. Compared to the HCUT spectral kernels, the proposed UMT spectral kernels provide narrower transition bands (cf. Fig. 2), and therefore, the resulting atoms are expected to be less localized. As signal-adapted kernels result from incorporating the energy-equalizing transformation into the UMT design, cf. (30), the specific bound depends on the signal set used.

For an alternative description, the localization of realizations of graph atoms can be quantified using the graph spread measure [38]; the graph spread of a signal $\boldsymbol{f} \in \mathbb{R}(\mathcal{V})$ around vertex $k \in \mathcal{V}$ is defined as

$$\Delta_{\mathcal{G},k}^2(\boldsymbol{f}) = \frac{1}{||\boldsymbol{f}||_2^2} \sum_{v \in \mathcal{V}} d_{\mathcal{G}}^2(k,v) \boldsymbol{f}^2[v], \tag{41}$$

where $d_{\mathcal{G}}(\cdot,\cdot)$ is the same distance metric as that used in (39) and (40). The smaller is $\Delta^2_{\mathcal{G},k}(\boldsymbol{f})$, the more localized is $\boldsymbol{f}$ around vertex k, and vice versa. A global spread measure can also be obtained as

$$\Delta^2_{\mathcal{G}}(\boldsymbol{f}) = \min_{k\in\mathcal{V}}\left\{\Delta^2_{\mathcal{G},k}(\boldsymbol{f})\right\}. \tag{42}$$

By substituting an atom $\boldsymbol{\psi}_{\mathcal{K},n}$ for $\boldsymbol{f}$ in (41) and (42), its vertex localization can be quantified. In Section 5.2, these two measures are used to quantify vertex localization of the different frames.

5 Results

5.1 Signal-Adapted Tight Frame Constructions

We present constructions of the proposed frames for signal sets realized on the Minnesota road graph [42] and the Alameda graph [26]. The Minnesota road graph is chosen as it is considered as a benchmark in many recent studies, e.g., [17, 18, 23, 25, 24, 15, 16, 21, 19, 20, 22]. The choice of the Alameda graph is to highlight the fact that, although the proposed method is developed based on spectral energy characteristics of a signal set, it is also implicitly adapted to the graph's spectrum.

Data Realized on the Minnesota Road Graph

The Minnesota road graph is considered as a benchmark in many recent studies, e.g., [17, 18, 23, 25, 24, 15, 16, 21, 19, 20, 22]. The edges represent major roads and the vertices their intersection points, which often correspond to towns or cities. We consider a general model for realizing signals on this graph as

$$\boldsymbol{y}_{\eta,n} = \boldsymbol{x}_{\eta,n} + \boldsymbol{e}, \tag{43}$$

where $\boldsymbol{x}_{\eta,n} \in \mathbb{R}(\mathcal{V})$ denotes the graph signal of interest with density $\eta \in\,]0,1]$ and smoothness $n \in \mathbb{Z}^+$, and $\boldsymbol{e} \in \mathbb{R}(\mathcal{V})$ denotes additive white Gaussian noise of variance σ_e^2. In particular, $\boldsymbol{x}_{\eta,n}$ is constructed as

$$\boldsymbol{x}_{\eta,n} = A^n \boldsymbol{p}_{\eta}, \tag{44}$$

where $\boldsymbol{p}_{\eta} \in \mathbb{R}(\mathcal{V})$ denotes a random realization of a spike signal as $\boldsymbol{p}_{\eta}[i] \in \{0,1\}$, $i = 1,\ldots,N_g$ such that $\sum_i \boldsymbol{p}_{\eta}[i] = \eta N_g$, A^n incorporates the intrinsic structure of the graph into the signal, and the power n controls the extent of signal smoothness. Fig. 3 shows two signals realized on the Minnesota road graph using this scheme.
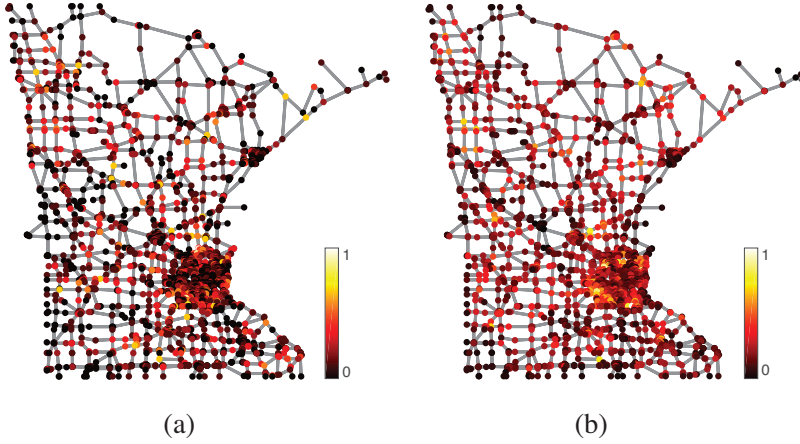
(a)   (b)

Figure 3: Sample signal realizations on the Minnesota road graph, (a) $\boldsymbol{x}_{0.2,2}$ and (b) $\boldsymbol{x}_{0.5,4}$. The plots are normalized as $\boldsymbol{x}_{\eta,n}/||\boldsymbol{x}_{\eta,n}||_\infty$.

By setting $\sigma_e^2 = 0$, two sets of clean graph signals with different smoothness were constructed as

$$\mathcal{F}_1 = \left\{\boldsymbol{y}_{\eta,2}^{[i]}\right\}_{\eta=0.2,0.5}, \quad i = 1,\ldots,10,$$

and

$$\mathcal{F}_2 = \left\{\boldsymbol{y}_{\eta,4}^{[i]}\right\}_{\eta=0.2,0.5}, \quad i = 1,\ldots,10,$$

where i denotes random realizations of $\boldsymbol{p}_\eta$, leading to 20 signals in each set.

While the distribution of the eigenvalues of this graph is rather uniform, see Fig. 4(a), the ensemble energy is concentrated towards the two ends of the spectrum for both $\mathcal{F}_1$ and $\mathcal{F}_2$, see Fig. 4(b). Fig. 4(c) shows the resulting energy-equalizing transformation functions. By incorporating $T_{\mathcal{F}_1}(\lambda)$ and $T_{\mathcal{F}_2}(\lambda)$ into the UMT system of spectral kernels, the desired signal-adapted systems of spectral kernels are obtained, see Fig. 4(d). A comparison of Figs. 4(d) and (b) highlights the energy-wise optimality of the proposed signal-adapted frame construction; i.e., more filters are allocated to spectral ranges that have higher ensemble energy. The support of the filters in the two sets vary relative to the difference in the distribution of the ensemble energy of the two signal sets, with more filters allocated to the lower end of the spectrum for the $\mathcal{F}_2$ frame than for the $\mathcal{F}_1$ frame, and vice versa at the upper end of the spectrum.

For comparison, Fig. 4(e) shows the corresponding spectrum-adapted system of spectral kernels for the Minnesota road graph, where the HCUT system of spectral
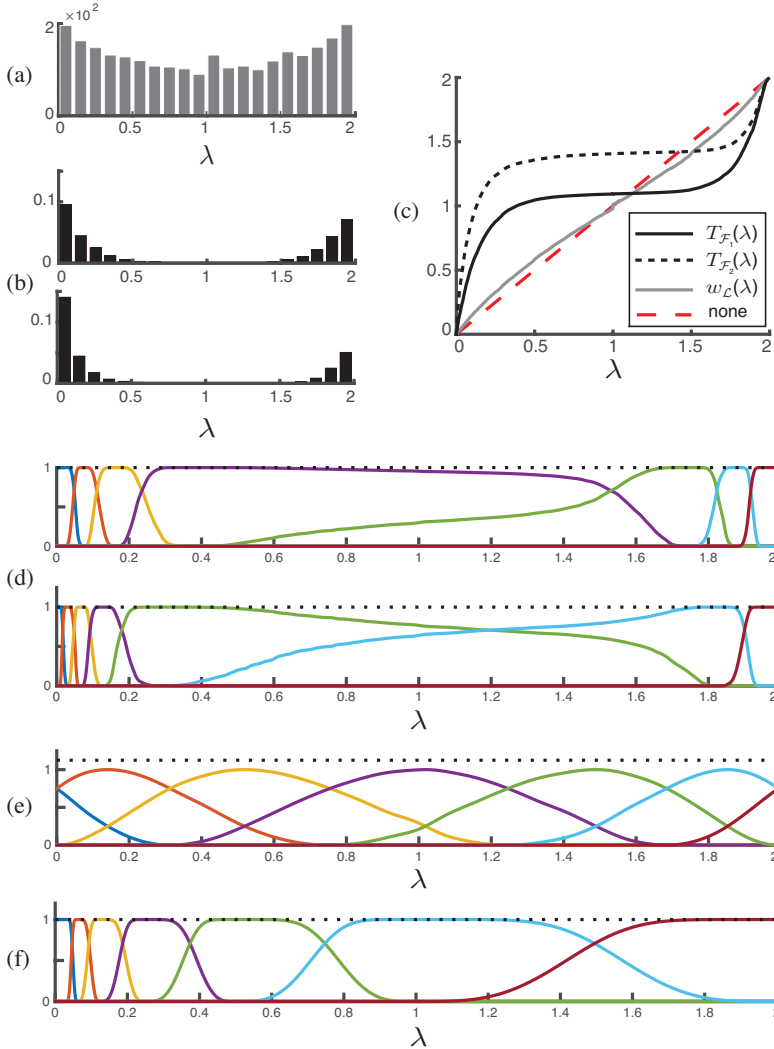
Figure 4: (a) Histograms of the eigenvalues $\Lambda_{\mathcal{L}}(\mathcal{G})$ of the Minnesota road graph. Each bar indicates the number of eigenvalues that lie in the corresponding spectral range. (b) Distribution of the ensemble energy spectral density $\bar{e}_{\mathcal{F}_1}$ (top) and $\bar{e}_{\mathcal{F}_2}$ (bottom). Each bar indicates the sum of ensemble energies of the eigenvalues lying in the corresponding spectral range. (c) Constructed energy-equalizing transformation functions, $T_{\mathcal{F}_1}(\lambda)$ and $T_{\mathcal{F}_2}(\lambda)$, and the spectrum-adapting warping function $w_{\mathcal{L}}(\lambda)$ [24]. (d) Signal-adapted system of spectral kernels constructed by warping the UMT system of spectral kernels ($J = 7$) using $T_{\mathcal{F}_1}(\lambda)$ (top) and $T_{\mathcal{F}_2}(\lambda)$ (bottom). (e) Spectrum-adapted system of spectral kernels [24] constructed by warping the HCUT system of spectral kernels ($J = 7$) using $w_{\mathcal{L}}(\lambda)$. (f) Meyer-like wavelet frame system of spectral kernels [11]. The dashed line in (d)–(f) corresponds to the function $G(\lambda)$ in (15).
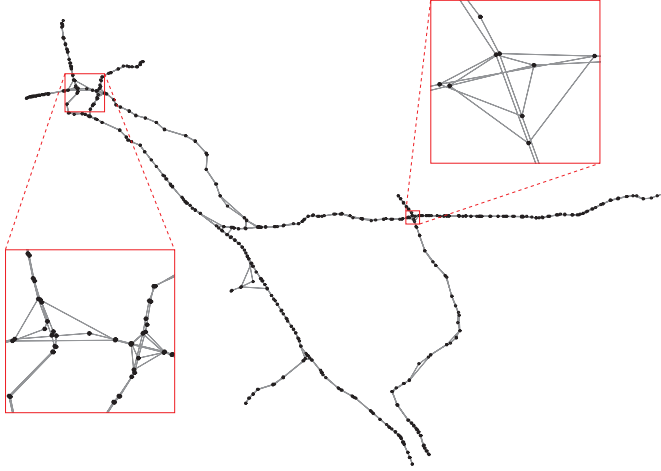
Figure 5: Illustration of the Alameda graph.

kernels [24], shown in Fig. 2(d), are warped using a spectrum-adapting warping function $w_{\mathcal{L}}(\lambda)$, shown in Fig. 4(c). $w_{\mathcal{L}}(\lambda)$ is constructed such that the distribution of eigenvalues is equalized [24]. As the distribution of the eigenvalues of this graph is almost uniform, the spectrum-adapted filters almost resemble the non-warped HCUT filters. Comparing Figs. 4(d) and (e), it can be observed that the proposed method optimizes the construction of the filters such that the energy-wise significance of the eigenvalues is taken into account, rather than only considering the distribution of the eigenvalues as in the spectrum-adapted frame.

Fig. 4(f) shows the Meyer-like wavelet frame system of spectral kernels [11], in which the kernels have the classical dyadic dilation of the wavelet scheme. The frame is neither adapted to the distribution of the eigenvalues nor to the distribution of the ensemble energy. By comparing Figs. 4(d) and (f), it is observed that the partitioning of the kernels at the lower end of the spectrum are similar, whereas a major difference is seen at the remainder of the spectrum. The similarity is more pronounced for kernels of the signal-adapted frame associated with $\mathcal{F}_1$, due to the particular initial decay pattern observed in the ensemble energy of $\mathcal{F}_1$, see Fig. 4(b), top. The benefit of the signal-adapted frame is observed when comparing the spread of the kernels in the spectral interval $[0.2, 2]$: the signal-adapted design approach allocates more subbands to the spectral interval where signal energy is expected, whereas the wavelet frame design approach, cannot allocate more subbands to spectral intervals other than the lower end.
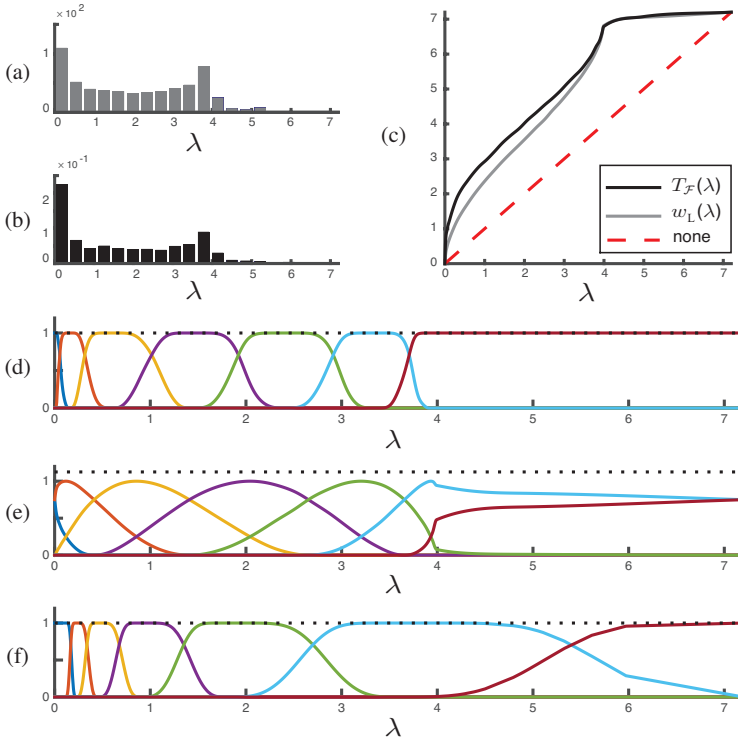
Figure 6: (a) Histogram of the eigenvalues $\Lambda_L(\mathcal{G})$ of the Alameda graph. (b) Distribution of the ensemble energy spectral density $\bar{e}_{\mathcal{F}}$ of the traffic dataset. (c) Constructed energy-equalizingtransformation functions $T_{\mathcal{F}}(\lambda)$ and the spectrum-adapting warping function $w_L(\lambda)$ [24]. (d) Signal-adapted system of spectral kernels. (e) Spectrum-adapted system of spectral kernels [24]. (f) Meyer-like wavelet frame system of spectral kernels [11].

Traffic Data on the Alameda Graph

The data are part of the Caltrans Performance Measurement System dataset[3]. The monthly bottlenecks occurring across 17 freeways in Alameda county between January 2010 and December 2015 are considered. A bottleneck could be any location where there is a persistent drop in speed, such as merges, large on-ramps and incidents. The vertices of the graph represent detector stations where bottlenecks were identified over the mentioned period, see Fig. 5. Two stations i and j are considered as connected through an edge if either 1) they are adjacent across a freeway, or 2) there is a connection at a crossing between freeways near the two stations. The latter type

---

[3]The data are publicly available at http://pems.dot.ca.gov.

of edges were defined based on satellite maps of the county available on Google Maps [43]. The signal on the graph is the average duration of bottlenecks for each specific month during three shifts (AM shift: 5am-10am, noon shift: 10am-3pm, and PM shift: 3pm-8pm), resulting in 180 signals in total.

The spectral characteristics of this signal set deviate considerably from that of the Minnesota graph. The total ensemble energy is almost uniformly spread across the eigenvalues, as observed by comparing the histogram of the eigenvalues $\Lambda_L(\mathcal{G})$ in Fig. 6(a) and the distribution of the ensemble energy spectral density in Fig. 6(b). As a result, the warping function defined for equalizing the distribution of energy across the spectrum, i.e., $T_{\mathcal{F}}(\lambda)$, closely resembles that defined for equalizing the distribution of eigenvalues; i.e., $w_L(\lambda)$, see Fig. 6(c). Consequently, almost an equal number of kernels span each part of the spectrum, with more kernels allocated to the lower half of the spectrum and vice versa, see Figs. 6(d) and (e). On the other hand, the non-adapted, Meyer-like wavelet frame has a kernel at the far end of the spectrum where there is very few eigenvalues and almost no energy, see Fig. 6(f).

Although the kernels of the proposed frame have narrower passband characteristics compared to those of the spectrum-adapted frame due to the different base set of kernels used (compare Figs. 6(d) and (e)), this example demonstrates where the proposed frame design approach and the spectrum-adapted approach coincide in terms of their respective approach to adaptivity: if the spectral energy is equally spread across the eigenvalues, the energy-equalizing transformation function $T_{\mathcal{F}}(\lambda)$ and the spectrum-adapting warping function $w_L(\lambda)$ become almost identical. Thus, although the proposed method is developed based on spectral energy characteristics of a signal set, it is optimal in the sense that it will indirectly adapt based on the graph's spectrum in the event of uniformly spread energy across the eigenvalues.

5.2   Vertex Localization

Vertex localization of atoms realized using the frames constructed on the Minnesota road graph are quantified by computing the graph spread around all graph vertices, cf. (41), for $\{\{\boldsymbol{\psi}_{\mathcal{K}_j,l}\}_{j=1,\dots,J}\}_{l=1,\dots,N_g}$. The atoms were then sorted based on their global graph spread measure, cf. (42), leading to a set of sorted indices $\{i_k\}_{k=1}^{N_g}$, such that

$$\Delta_{\mathcal{G}}^2(\boldsymbol{\psi}_{\mathcal{K}_j,i_1}) \leq \Delta_{\mathcal{G}}^2(\boldsymbol{\psi}_{\mathcal{K}_j,i_2}) \leq \cdots \leq \Delta_{\mathcal{G}}^2(\boldsymbol{\psi}_{\mathcal{K}_j,i_{N_g}}).$$

Figs. 7(a) and (b) show the global graph spread of the atoms associated to $\mathcal{K}_1$ and $\mathcal{K}_4$, respectively, for both the signal-adapted and spectrum-adapted frames of the Minnesota road graph. For $\mathcal{K}_1$, the global graph spread is greater for the atoms of the signal-adapted frame. This can be associated with the narrower spectral spread of $\mathcal{K}_1$
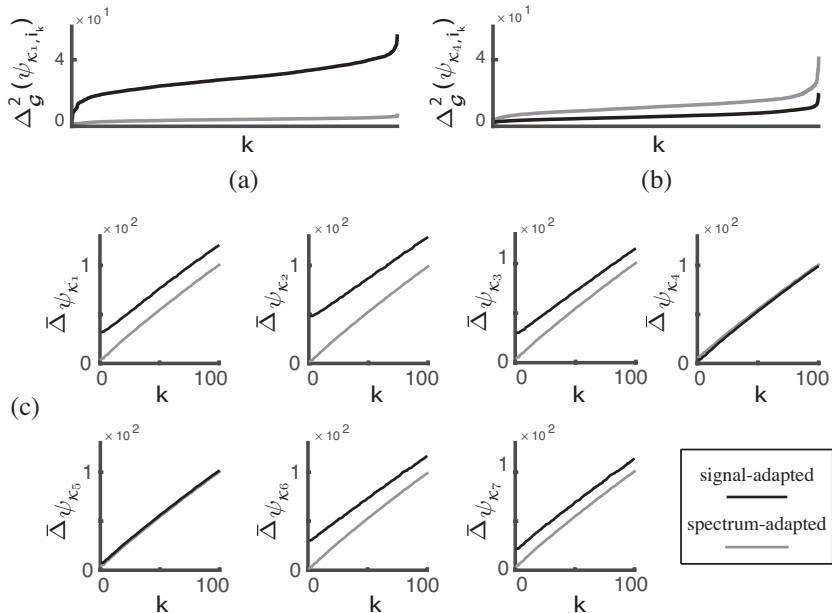
Figure 7: Global graph spread of the atoms associated with (a) $\mathcal{K}_1(\lambda)$ and (b) $\mathcal{K}_4(\lambda)$ of the signal-adapted frame (black curves) and spectrum-adapted frame (gray curves). (c) Ensemble graph spread measure for the seven subbands of the signal-adapted and spectrum-adapted frames.

of the signal adapted frame compared to that of the spectrum-adapted frame, see blue kernel in Fig. 4(d), top, and that in Fig. 4(e). On the other hand, for $\mathcal{K}_4$, the global graph spread of the atoms of the two frames become almost identical, which can be linked to the fact that $\mathcal{K}_4$ is approximately equally spread for both the signal-adapted and the spectrum-adapted frames, see purple kernel in Fig. 4(d), top, and that in Fig. 4(e).

To express the behaviour of the atoms in the vicinity of their central vertex, an ensemble measure of the change in graph spread as a function of geodesic distance from their central vertex can be obtained as

$$\bar{\Delta}_{\psi_{\mathcal{K}_j}}[k] = \frac{1}{N_g} \sum_{l=1}^{N_g} \Delta_{\mathcal{G}, v_k^{(l)}}^2 (\boldsymbol{\psi}_{\mathcal{K}_j, l}), \quad k = 1, \ldots, N_g. \tag{45}$$

where $v_k^{(l)} \in \{1, \ldots, N_g\}$ denotes the index of the kth closest vertex to the vertex

where atom $\psi_{\mathcal{K}_{j,l}}$ is centered at, based on the the geodesic distance measure; i.e.,

$$d_{\mathcal{G}}(l, v_1^{(l)} = l) = 0 < d_{\mathcal{G}}(l, v_2^{(l)}) \leq \cdots \leq d_{\mathcal{G}}(l, v_{N_g}^{(l)}).$$

Fig. 7(c) shows $\{\bar{\Delta}_{\psi_j}\}_{j=1}^{7}$ associated with the spectral kernels of the signal-adapted and spectrum-adapted frames of the Minnesota road graph, for geodesic distances of up to 100 vertices. For all subbands, and for both frames, the ensemble graph spread monotonically increases as the geodesic distance increases. As expected, for subbands $j = \{1, 2, 3, 6, 7\}$, where the kernels of the spectrum-adapted frame are more spectrally spread compared to that of the signal-adapted frame (see Fig. 4(d), top, and Fig. 4(e)), $\bar{\Delta}_{\psi_j}[k]$ is lower, whereas for subbands $j = \{4, 5\}$ the values are almost identical since the corresponding kernels of both frames are widely spread across the spectrum. These results are in line with the theoretical insight provided by (39) and (40).

5.3   Efficient Decomposition of Brain fMRI Data

Functional magnetic resonance imaging (fMRI) is a key bioimaging modality used for performing non-invasive studies of the brain. The principle behind fMRI is the detection of a signal known as the blood-oxygen-level-dependent (BOLD) signal, which arises as a result of increased blood flow to activated regions of the brain. As high temporal resolution data is required to correlate brain activity with the experimental paradigm, the resulting fMRI data are generally corrupted with an extensive amount of noise, requiring denoising.

Filters and wavelets in the most classical form used in image processing share several basic properties: they are (i) defined within Euclidean spaces (a square in 2-D or a cube in 3-D), (ii) isotropic in structure and (iii) stationary and quasi shift-invariant, meaning that their structure does not vary when applied to different regions within a volume. However, the BOLD signal is expected only within the thin convoluted layer of gray matter of the brain, but not within the white matter or cerebrospinal fluid [44]. At the spatial resolution of fMRI, isotropically shaped basis functions will cross boundaries of gray matter, even at the finest scale. Thus, it is advantageous to construct filters that adapt to this intricately convoluted domain rather than to assume that the spatial characteristics of the underlying signal is independent of its location. To this aim, many approaches have been proposed (see for example, [45, 46, 47, 48]), in particular, the construction of anatomically-adapted graph wavelets [31]. The deficiency of a fixed graph frame design and the lack of a systematic approach in determining the spectral coverage of spectral bands for analyzing fMRI data have been pointed out in [31, 30, 29]. In fact, these findings motivated us to pursue the idea of designing the proposed signal-adapted frames.
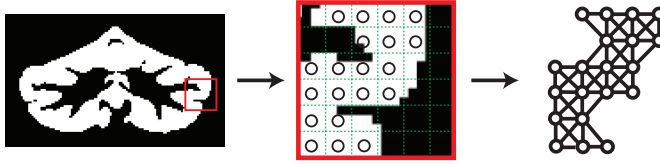
Figure 8: Illustration of the cerebellum graph.

Here, we consider the cerebellum region of the brain. The graph, as designed in [31], encodes the 3-D geometry of the cerebellar gray matter, and its construction is based on an atlas template of the cerebellum [49]. The vertices of the graph represent voxels within the cerebellar structure that correspond to gray matter, and the edges are assigned by computing connections between adjacent voxels in 3-D neighbourhood, see Fig. 8. The fMRI data were acquired from 26 healthy subjects while performing a slow event-related Eriksen flanker task [50].[4] Whole-brain functional volumes were acquired throughout the task, one every two seconds, with a total of 292 volumes per subject. An anatomical scan of each subject's brain was also collected. By registering each subject's anatomical scan to the template cerebellum, and accordingly mapping the functional volumes, cerebellar graph signals were constructed by extracting functional voxels matching the defined graph vertices. This resulted in one signal set for each subject, $\{\mathcal{F}_k\}_{k=1}^{26}$, each including 292 signals. A set including the signals from all subjects was also constructed as

$$\mathcal{F} = \mathcal{F}_1 \cup \mathcal{F}_2 \cup \cdots \cup \mathcal{F}_{26}.$$

The histogram of the eigenvalues $\Lambda_{\mathcal{L}}(\mathcal{G})$ of the cerebellum gray matter graph and the distribution of the ensemble energy spectral density of $\mathcal{F}$ are shown in Figs. 9(a) and (b), respectively. Unlike the Alameda traffic graph and data, a major difference is observed between the two distributions: most eigenvalues are located at the upper end of the spectrum, whereas the ensemble energy is significantly concentrated at the lower end of the spectrum. This leads to a major discrepancy between $T_{\mathcal{F}}(\lambda)$ and $w_{\mathcal{L}}(\lambda)$, see Fig. 9(c), and consequently, the resulting spectral kernels, see Figs. 9(d)-(g): the kernels of the signal-adapted frames are localized at the lower end of the spectrum, whereas those of the spectrum-adapted frame are localized at the higher end of the spectrum. As a result, the signal-adapting scheme leads to an optimal configuration of filters in the sense that more filters are allocated to spectral regions where higher ensemble signal energy is present rather than being allocated to part of the spectrum where more eigenvalues are located.

---

[4]The data are publicly available at https://openfmri.org/dataset/ds000102.
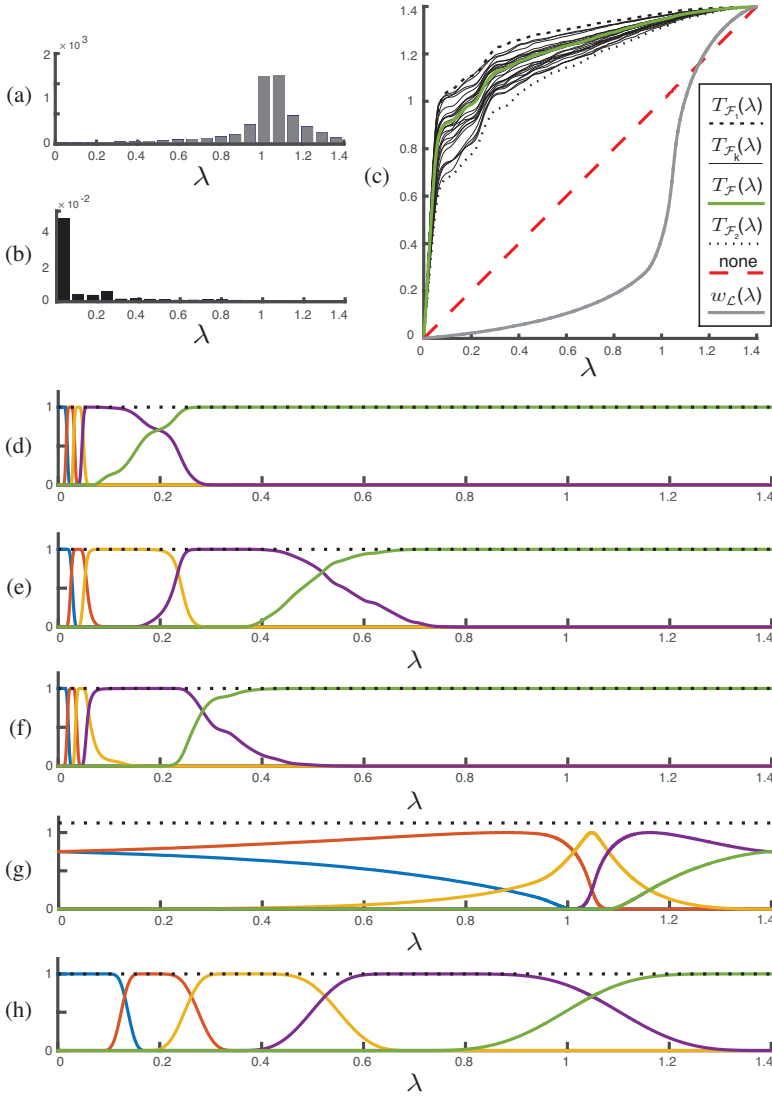
Figure 9: (a) Histogram of the eigenvalues $\Lambda_{\mathcal{L}}(\mathcal{G})$ of the cerebellum graph. (b) Distribution of the ensemble energy spectral density $\bar{e}_{\mathcal{F}}$ of $\mathcal{F}$. (c) Constructed energy-equalizing transformation functions $\{T_{\mathcal{F}_k}(\lambda)\}_{k=1}^{26}$, $T_{\mathcal{F}}(\lambda)$ and the spectrum-adapting warping function $w_{\mathcal{L}}(\lambda)$ [24]. Note that the black curves correspond to the transformation for each subjects signal set, with the transformation at the two extremes presented as dashed curves. (d)-(f) Signal-adapted system of spectral kernels based on $\mathcal{F}_1$, $\mathcal{F}_2$ and $\mathcal{F}$, respectively. (g) Spectrum-adapted system of spectral kernels [24]. (h) Meyer-like wavelet frame system of spectral kernels [11].
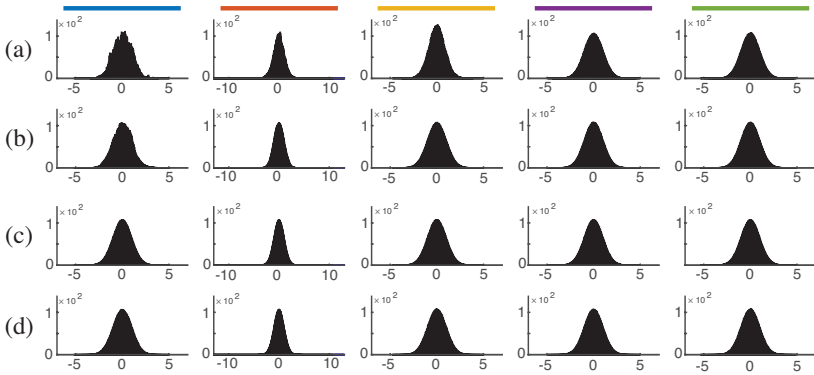
Figure 10: (a)-(d) The mean distribution of coefficients resulting from decomposing the set of signal in $\mathcal{F}_{\text{noise}}$ using the system of spectral kernels shown in Figs. 9(e)-(h), respectively. Each plot shows the mean distribution of coefficients in one subband, with the order from left to right corresponding to the blue, red, yellow, purple and green spectral kernels, respectively. Note that the distributions are shown for the same range of coefficient values for each subband across the frames, whereas the counts (y axis) are adjusted for each distribution.
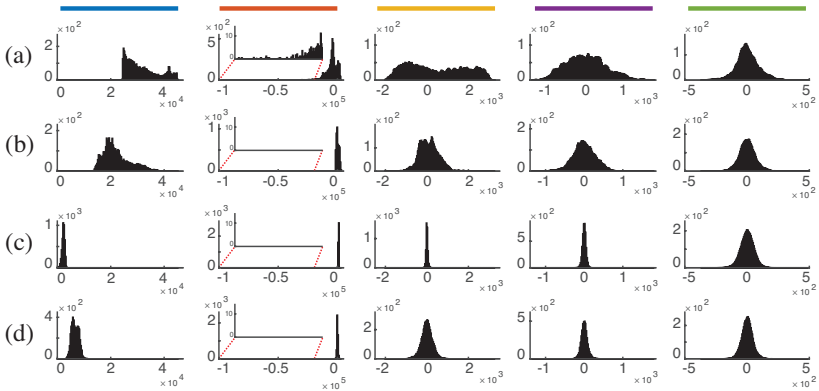
Figure 11: (a)-(e) The same as in Fig. 10 but for $\mathcal{F}_2$. For clarity, the lower end of the distributions in the second subbands are vertically magnified.

The concentration of the ensemble energy at the lower end of the spectrum makes the non-adapted tight Meyer-like wavelet design a relatively suitable design, see Fig. 9(h). However, comparing Figs. 9(f) and (h) demonstrates the efficiency of the proposed construction: the spectral range lying in the support of the first kernel of the Meyer-like wavelet frame (blue kernel) is spanned by approximately three kernels in the signal-adapted frame (blue, red and orange kernels). This suggests the superiority of the signal-adapted frame in providing a more efficient multi-scale representation of the data compared to the dyadically scaled wavelet design. Interestingly, the narrowband configuration of the proposed signal-adapted frame closely resembles that found to be optimal for analyzing cerebellar data by tunning the Meyer-like wavelet frame in [31, 30].[5]

To provide further insight than that provided by visual comparison of the frames, the set of cerebellar signals in $\mathcal{F}_2$ as well as a set of 292 white Gaussian noise signals ($\sigma^2 = 1$), denoted $\mathcal{F}_{\text{noise}}$, were decomposed using the frames shown in Figs. 9(e)-(h). The resulting coefficients $c_{\mathcal{K}_j,m}$ (cf. (18)) were normalized as $c_{\mathcal{K}_j,m}/||\psi_{\mathcal{K}_j,m}||_2$ to account for the difference in the norm of their associated atoms. Figs. 10 and 11 show the mean distribution of the normalized decomposition coefficients of $\mathcal{F}_{\text{noise}}$ and $\mathcal{F}$, respectively. For $\mathcal{F}_{\text{noise}}$, the distributions of the coefficients in all five subbands of all four frames are Gaussian-like as expected, see Fig. 10. For $\mathcal{F}_2$, the distributions of the coefficients of the last subband of all four frames closely resembles a Gaussian (see the 4 plots at the right end of Figs. 11(a)-(d)), similar to the distributions obtained on $\mathcal{F}_{\text{noise}}$, cf. Figs. 11. This suggests that the corresponding atoms of this subband have captured noise. A similar observation is made for the distributions associated with the third and fourth subbands of the spectrum-adapted and Meyer-like wavelet frame (Figs. 11(c)-(d)) as well as the fourth subband of the signal-adapted frame constructed based on $\mathcal{F}$ (Fig. 11(b)). On the other hand, the coefficients of the first four subbands of the signal-adapted frame constructed based on $\mathcal{F}_2$ significantly deviate from zero, cf. first four plots in Fig. 11(a), and have distributions unlike that expected to result from decomposing noise (cf. Fig. 10). This suggests the efficiency of the signal-adapted frame in resulting in atoms that capture signal components.

Although the coefficients of the first three subbands of the signal-adapted frame constructed based on $\mathcal{F}$ (Fig. 11(b)) also provide more information than those of the spectrum-adapted and Meyer-like wavelet frame (Figs. 11(c)-(d)), the coefficients of the signal-adapted frame constructed based on $\mathcal{F}_2$ (Fig. 11(a)) show yet greater significance. This suggests the superiority of the subject-based frame, shown in Fig. 9(e), over the frame constructed based on the energy content of the signals from the group of subjects, shown in Fig. 9(f), for decomposing $\mathcal{F}_2$. Despite this fact, if a compar-

---

[5]The similarity can be observed by comparing the spectral coverage of the first two kernels in Fig. 9(f) with that in figure 3(d) in [31] and figure 1(b) in [30].

ison between decomposition of the signals from different subjects is required, as for instance performed in [31], the group-based frame constructed based on $\mathcal{F}$ is the suitable choice.

5.4 Signal Denoising

To illustrate one application of the proposed frames, we denoise a set of signals realized on the Minnesota road graph. For different σ_e^2, noise corrupted signal sets were created using (43) as

$$\mathcal{F}_{\sigma_e} = \left\{ \boldsymbol{y}_{\eta,2}^{[i]} \right\}_{\eta=0.2,0.5}, \quad i = 1, \ldots, 10,$$

where i denotes different random realizations of $\boldsymbol{p}_\eta$ and $\boldsymbol{e}$. Denoising was performed through soft thresholding of the decomposition coefficients. In particular, the denoised signal $\tilde{\boldsymbol{x}}^{(\vartheta)}$, where ϑ denotes the global threshold, were obtained from the coefficients $c_{\mathcal{K},m}$ (cf. (18)) as

$$\tilde{\boldsymbol{x}}^{(\vartheta)} = \sum_{j,m} H(|c_{\mathcal{K}_j,m}| - \tau_{\mathcal{K}_j,m}^{(\vartheta)}) c_{\mathcal{K}_j,m} \boldsymbol{\psi}_{\mathcal{K}_j,m}, \tag{46}$$

where $H(\cdot)$ denotes the Heaviside step function and $\tau_{\mathcal{K}_j,m}^{(\vartheta)}$ denote element-adapted thresholds. In order to account for that the frame elements generally have different norms, element-adapted thresholds of the form [12]

$$\tau_{\mathcal{K}_j,m}^{(\vartheta)} = \sigma_e ||\boldsymbol{\psi}_{\mathcal{K}_j,m}||_2 \vartheta, \tag{47}$$

were used that are also adjusted with respect to the noise level.

To evaluate performance, the average mean square error reduction (ΔMSE) was computed for each ϑ as

$$\Delta\text{MSE}^{(\vartheta)} = \frac{1}{|\mathcal{F}|} \sum_{k=1}^{|\mathcal{F}|} 10 \log_{10}\left(\frac{||\boldsymbol{x}_k - \tilde{\boldsymbol{x}}_k^{(\vartheta)}||_2^2}{||\boldsymbol{x}_k - \boldsymbol{y}_k||_2^2}\right), \tag{48}$$

where k runs over the signals in the signal set, and $|\mathcal{F}|$ denotes the cardinality of the set. To compare the denoising performance across different σ_e^2 and J, the minimum MSE reduction is considered

$$\Delta\text{MSE}^{(\text{min})} = \min_\vartheta \Delta\text{MSE}^{(\vartheta)}, \tag{49}$$

where ϑ is varied within the interval $[1,5]$ with a step size of 0.25.
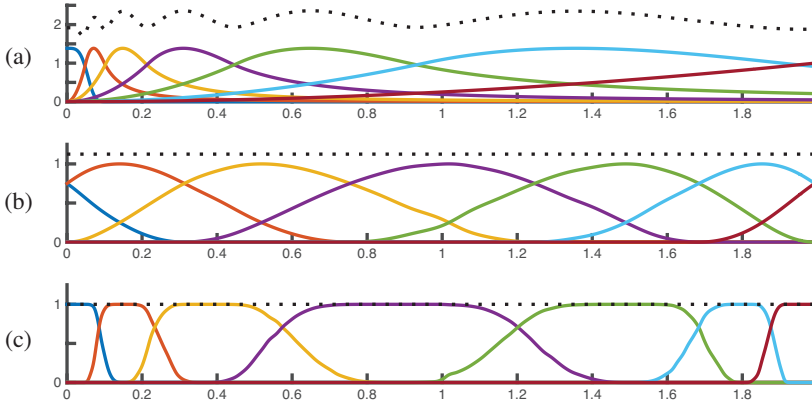
Figure 12: Systems of spectral kernels of the (a) SGWT frame [10], (b) spectrum-adapted frame and (c) the signal-adapted frame, used for denoising.

The signals in the sets $\mathcal{F}_{\sigma_e}$ were denoised using: 1) the SGWT frame [10], neither adapted to the spectrum nor to the graph signals, 2) the spectrum-adapted frame [24] and 3) the proposed frame, using up to 10 spectral scales. Fig. 12 illustrates an example of the used frames for $J = 7$ scales and $\sigma_e^2 = \sigma_x^2$. By comparing the signal-adapted frame constructed based on the noisy signals, shown in Fig. 12(c), with its respective counterpart constructed based on the clean signals, shown in the top of Fig. 4(d), it is observed that although the addition of noise has affected the support of the filters, the overall distribution of the support of the kernels across the spectrum is still consistent between the two cases. As white Gaussian noise exhibits a uniform energy spectral density, its influence on the overall distribution of ensemble energy is negligable.

Fig. 13 presents a comparison of denoising performances of the different types of frames. Fig. 13(a) presents ΔMSE measures when using $J = 7$ scales. Compared to the spectrum-adapted frame, the proposed frames show better performance across ϑ. Compared to the SGWT frame, the difference in performance is generally better for ϑ values close to the minimum ΔMSE. Fig. 13(b) presents the ΔMSE$^{(\mathrm{min})}$ measures as a function of the SNR $= \sigma_x^2/\sigma_e^2$, when using $J = 7$. The relative performance of the signal-adapted frame and SGWT frame is consistent across different SNRs, with the proposed frame offering, in general, better noise reduction. However, the spectrum-adapted frame shows better noise reduction at higher SNRs.

It is advantageous to also compare the denoising performance for frames with different number of subbands. Fig. 13(c) shows plots of the ΔMSE$^{(\mathrm{min})}$ in denoising the signals using the different frames as a function of J. Using the signal-adapted frames leads to a lower ΔMSE$^{(\mathrm{min})}$ than for the SGWT and spectrum-adapted frames. It is

also observed that the difference in performance between the proposed frame and the spectrum-adapted frame is more pronounced when using up to eight scales. In recent studies that use the SGWT [51, 31, 52, 53, 54, 55], typically, up to six scales are used, which can be explained by observing that the performance for this frame saturates at $J = 5$. In contrast, the proposed frames show a monotonic increase in performance also for larger number of scales. This suggests that the proposed signal-adapted frames have the potential to provide a more meaningful multi-scale representation of graph signals.
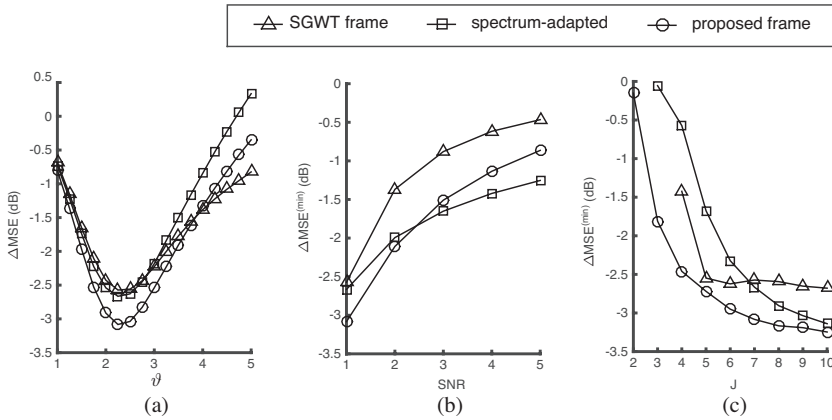
Figure 13: Comparison of denoising performance using different frames on signal set $\mathcal{F}_{\sigma_e}$. (a) ΔMSE as a function of threshold level ϑ using $J = 7$ spectral scales, where $\sigma_e^2 = \sigma_x^2$ in signal realization for all cases. (b) $\Delta\text{MSE}^{(\min)}$ as a function of noise level, $\text{SNR} = \sigma_x^2/\sigma_e^2$, using frames with (b) $J = 7$ spectral scales. (c) $\Delta\text{MSE}^{(\min)}$ as a function of the number of scales J, where $\sigma_e^2 = \sigma_x^2$ in signal realization for all cases. Note that in (c) some sample points are not displayed for the spectrum-adated and the SGWT frame; this is due to that the former is only defined for $J \geq 3$, and that the latter is not optimally designed for small J and leads to $\Delta\text{MSE}^{(\min)} > 0$.

6 Conclusion

We have presented a construction of signal-adapted tight frames for graph signals. The adaptivity of the approach is introduced by exploiting the ensemble energy spectral density, which describes the second-order statistics of the signal class at hand. It should be noted that wavelet-type decompositions are optimal for non-stationary signals, such as the ones considered in our experimental results. From this point-of-

view, the design only uses the stationary information, and its flexibility to represent non-stationary features comes with the width and smoothness of the bandpass characteristics. Conceptually, this approach is similar to optimal pyramid designs that were proposed for image processing in the 90's [56]. A MATLAB implementation of the proposed approach and the datasets used in this paper are available online at miplab.epfl.ch/software/.

Appendix A. Proof of Proposition 1

In order to ensure that the spectral kernels cover the full spectrum, a must be chosen such that

$$\lambda_{\max} \overset{(35c)}{=} \lambda_{\mathrm{II}} + a \overset{(j=J)}{=} \gamma a + (J-2)\Delta + a,$$

which using (13) leads to $a = \frac{\lambda_{\max}}{J\gamma - J - \gamma + 3}$.

To prove that the UMT system of spectral kernels form a tight frame, (17) needs to be fulfilled. Since, for all j, the supports of $\mathcal{K}'_{j-1}(\lambda)$ and $\mathcal{K}'_{j+1}(\lambda)$ are disjoint, $G(\lambda)$ can be determined as

$$
\begin{aligned}
G(\lambda) = \sum_{j=1}^{J} |\mathcal{K}'_j(\lambda)|^2 & \\
\overset{(48)}{=} &
\begin{cases}
|\mathcal{K}'_1(\lambda)|^2 \overset{(35a)}{=} 1 & \forall \lambda \in [0, a] \\
|\mathcal{K}'_1(\lambda)|^2 + |\mathcal{K}'_2(\lambda)|^2 & \forall \lambda \in]a, \gamma a] \\
|\mathcal{K}'_2(\lambda)|^2 + |\mathcal{K}'_3(\lambda)|^2 & \forall \lambda \in]\gamma a, \gamma a + \Delta] \\
\vdots & \vdots \\
|\mathcal{K}'_J(\lambda)|^2 \overset{(35c)}{=} 1 & \forall \lambda \in]\lambda_{\max} - a, \lambda_{\max}]
\end{cases} \\
\overset{(35b)}{=} &
\begin{cases}
1 & \forall \lambda \in [0, a] \\
\cos^2(x_{\mathrm{I}}) + \sin^2(x_{\mathrm{I}}) & \forall \lambda \in]a, \gamma a] \\
\cos^2(x_{\mathrm{II}}) + \sin^2(x_{\mathrm{II}}) & \forall \lambda \in]\gamma a, \gamma a + \Delta] \\
\vdots & \vdots \\
1 & \forall \lambda \in]\lambda_{\max} - a, \lambda_{\max}]
\end{cases} \\
= 1 \quad \forall \lambda \in [0, \lambda_{\max}] & \quad (50)
\end{aligned}
$$

where $x_{\mathrm{I}} = \frac{\pi}{2}\nu(\frac{1}{\gamma-1}(\frac{\lambda}{a} - 1))$ and $x_{\mathrm{II}} = \frac{\pi}{2}\nu(\frac{1}{\gamma-1}(\frac{\lambda - \Delta}{a} - 1))$.

For any given γ, the constructed set of spectral kernels form a tight frame. However, in order for the frame to satisfy the uniformity constraint given in (28), the

appropriate γ needs to be determined. From (35b), we have $\forall j \in \{2, \ldots, J-2\}$

$$\mathcal{K}'_j(\lambda) = \mathcal{K}'_{j+1}(\lambda + \Delta) \quad \forall \lambda \in]\lambda_{\mathrm{I}}, \lambda_{\mathrm{II}} + \Delta]. \tag{51}$$

By considering an inverse linear mapping of the spectral support where $\mathcal{K}'_1(\lambda) \neq 0$, i.e. $[0, \gamma a]$, to the spectral support where $\mathcal{K}'_J(\lambda) \neq 0$, i.e. $[\lambda_{\mathrm{max}} - \gamma a, \lambda_{\mathrm{max}}]$, we have

$$\mathcal{K}'_1(\lambda) = \mathcal{K}'_J(-\lambda + 2a + J\Delta) \quad \forall \lambda \in [0, \gamma a]. \tag{52}$$

Thus, from (51) and (52) we have

$$\int_0^{\lambda_{\mathrm{max}}} \mathcal{K}'_j(\lambda)\, \mathrm{d}\lambda = C_2, \quad j = 2, \ldots, J-1 \tag{53a}$$

$$\int_0^{\lambda_{\mathrm{max}}} \mathcal{K}'_1(\lambda)\, \mathrm{d}\lambda = \int_0^{\lambda_{\mathrm{max}}} \mathcal{K}'_J(\lambda)\, \mathrm{d}\lambda = C_1, \tag{53b}$$

respectively, where $C_1, C_2 \in \mathbb{R}^+$. Thus, in order to satisfy (28), γ should be chosen such that

$$C_1 = C_2$$

$$\boxtimes \int_0^{\lambda_{\mathrm{max}}} \mathcal{K}'_1(\lambda)\, \mathrm{d}\lambda = \int_0^{\lambda_{\mathrm{max}}} \mathcal{K}'_2(\lambda)\, \mathrm{d}\lambda$$

$$a + \int_a^{\gamma a} \mathcal{K}'_1(\lambda)\, \mathrm{d}\lambda = \int_a^{\gamma a} \sin\left(\frac{\pi}{2}\nu\left(\frac{1}{\gamma-1}\left(\frac{\lambda}{a}-1\right)\right)\right) \mathrm{d}\lambda$$

$$+ \int_{\gamma a}^{\gamma a + \Delta} \mathcal{K}'_2(\lambda)\, \mathrm{d}\lambda$$

$$a \stackrel{(51)}{=} \int_a^{\gamma a} \sin\left(\frac{\pi}{2}\nu\left(\frac{1}{\gamma-1}\left(\frac{\lambda}{a}-1\right)\right)\right) \mathrm{d}\lambda. \tag{54}$$

The optimal γ that satisfies (54) was obtained numerically by defining

$$Q(\gamma) = \int_a^{\gamma a} \sin\left(\frac{\pi}{2}\nu\left(\frac{1}{\gamma-1}\left(\frac{\lambda}{a}-1\right)\right)\right) \mathrm{d}\lambda - a, \tag{55}$$

and discretizing $Q(\gamma)$ within the range $(a, \gamma a]$, with a sampling factor of 1×10^{-4}. Testing for $\gamma \geq 1$, with a step size of 1×10^{-2}, the optimal value, which is independent of λ_{max} and J, was found to be $\gamma = 2.73$.
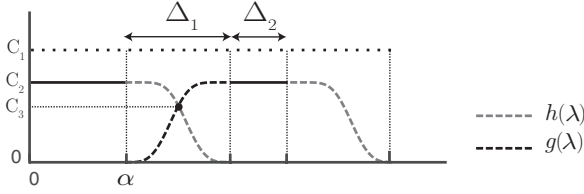
Figure 14: Design of a uniform system of spectral kernels satisfying (28) and (29). The displayed function $h(\lambda)$ and $g(\lambda)$ correspond to the ones used in the UMT design. However, any two functions passing through $(\alpha + \Delta_1/2, C_3)$ and satisfying (56) and (57) can be used to design a desired prototype system of uniform spectral kernels.

7 Uniform System of Kernels -- General Case

The UMT system of spectral kernels (cf. Proposition 1) is one prototype design that can be used as the basis for the proposed frame design approach. For the general case, other prototype system of kernels can be designed, with their design essentially breaking down to (see Fig. 14 for notations):

(i) the proper design of the pair of functions $h(\lambda)$ and $g(\lambda)$ such that they lead to smooth quadrature mirror style filters that satisfy

$$|h(\lambda)|^2 + |g(\lambda)|^2 = C_1 \in \mathbb{R}^+, \quad \forall \lambda \in [\alpha, \alpha + \Delta_1], \tag{56}$$

where $\alpha, \Delta_1 \in]0, \lambda_{\max}[$, $C_2 = \sqrt{C_1}$, $C_3 = \sqrt{C_1/2}$,

(ii) determination of α, Δ_1 and Δ_2 such that

$$\alpha C_2 = \Delta_2 C_2 + \int_\alpha^{\alpha + \Delta_1} h(\lambda)\, d\lambda. \tag{57}$$

Observe that α, Δ_1, Δ_2, $h(\lambda)$ and $g(\lambda)$ all depend on J and $\lambda_{\max}$. Fig. 14 shows an illustration of the non-zero segments of the resulting $\mathcal{K}'_1(\lambda)$ and $\mathcal{K}'_2(\lambda)$. $\{\mathcal{K}'_j(\lambda)\}_{j=3}^{J-1}$ can be obtained by translating the non-zero segments of $\mathcal{K}'_2(\lambda)$ by $(j-2)\Delta_3$, and $\mathcal{K}'_J(\lambda)$ by mirroring the non-zero segment of $\mathcal{K}'_1(\lambda)$ and translating it such that it spans the upper end of the spectrum.

References

[1] D. I. Shuman, S. K. Narang, P. Frossard, A. Ortega, and P. Vandergheynst, "The emerging field of signal processing on graphs: Extending high-dimensional data

analysis to networks and other irregular domains," *IEEE Signal Process. Mag.*, vol. 30, no. 3, pp. 83–98, 2013.

[2] A. Sandryhaila and J. Moura, "Discrete signal processing on graphs.," *IEEE Trans. Signal Process.*, vol. 61, pp. 1644–1656, 2013.

[3] S. Chen, R. Varma, A. Sandryhaila, and J. Kovačević, "Discrete signal processing on graphs: sampling theory," *IEEE Trans. Signal Process.*, vol. 63, no. 24, pp. 6510–6523, 2015.

[4] M. Jansen, G. P. Nason, and B. W. Silverman, "Multiscale methods for data on graphs and irregular multidimensional situations," *J. Roy. Statistical Soc.: Series B (Statistical Methodology)*, vol. 71, no. 1, pp. 97–125, 2009.

[5] S. K. Narang and A. Ortega, "Lifting based wavelet transforms on graphs," in *Proc. APSIPA ASC*, pp. pp. 441–444, 2009.

[6] R. Rustamov and L. Guibas, "Wavelets on graphs via deep learning," in *Proc. Adv. Neural Info. Proces. Syst.*, pp. 998–1006, 2013.

[7] I. Ram, M. Elad, and I. Cohen, "Generalized tree-based wavelet transform," *IEEE Trans. Signal Process.*, vol. 59, no. 9, pp. 4199–4209, 2011.

[8] I. Ram, M. Elad, and I. Cohen, "Redundant wavelets on graphs and high dimensional data clouds," *IEEE Signal Process. Lett.*, vol. 19, no. 5, pp. 291–294, 2012.

[9] M. Gavish, B. Nadler, and R. R. Coifman, "Multiscale wavelets on trees, graphs and high dimensional data: Theory and applications to semi supervised learning.," in *Proc. Int. Conf. Mach. Learn.*, pp. 367–374, 2010.

[10] D. Hammond, P. Vandergheynst, and R. Gribonval, "Wavelets on graphs via spectral graph theory," *Appl. Comput. Harmon. Anal.*, vol. 30, no. 2, pp. 129–150, 2011.

[11] N. Leonardi and D. Van De Ville, "Tight wavelet frames on multislice graphs," *IEEE Trans. Signal Process.*, vol. 61, no. 13, pp. 3357–3367, 2013.

[12] F. Göbel, G. Blanchard, and U. von Luxburg, "Construction of tight frames on graphs and application to denoising." Aug. 2014 [online]. Available: http://arXiv.org/abs/1408.4012.

[13] B. Dong, "Sparse representation on graphs by tight wavelet frames and applications," *Appl. Comput. Harmon. Anal.*, 2015. doi:10.1016/j.acha.2015.09.005.

[14] R. R. Coifman and M. Maggioni, "Diffusion wavelets," *Appl. Comput. Harmon. Anal.*, vol. 21, no. 1, pp. 53–94, 2006.

[15] S. K. Narang and A. Ortega, "Perfect reconstruction two-channel wavelet filter banks for graph structured data," *IEEE Trans. Signal Process.*, vol. 60, no. 6, pp. 2786–2799, 2012.

[16] S. K. Narang and A. Ortega, "Compact support biorthogonal wavelet filterbanks for arbitrary undirected graphs," *IEEE Trans. Signal Process.*, vol. 61, no. 19, pp. 4673–4685, 2013.

[17] Y. Tanaka and A. Sakiyama, "M-channel oversampled graph filter banks," *IEEE Trans. Signal Process.*, vol. 62, no. 14, pp. 3578–3590, 2014.

[18] A. Sakiyama and Y. Tanaka, "Oversampled graph Laplacian matrix for graph filter banks," *IEEE Trans. Signal Process.*, vol. 62, no. 24, pp. 6425–6437, 2014.

[19] D. B. H. Tay and J. Zhang, "Techniques for constructing biorthogonal bipartite graph filter banks," *IEEE Trans. Signal Process.*, vol. 63, no. 21, pp. 5772–5783, 2015. doi: 10.1109/TSP.2015.2460216.

[20] D. B. Tay and Z. Lin, "Design of near orthogonal graph filter banks," *IEEE Signal Process. Lett.*, vol. 22, no. 6, pp. 701–704, 2015.

[21] N. Tremblay and P. Borgnat, "Subgraph-based filterbanks for graph signals," *IEEE Trans. Signal Process.*, vol. 64, no. 15, pp. 3827–3840, 2016.

[22] H. Q. Nguyen and M. N. Do, "Downsampling of signals on graphs via maximum spanning trees," *IEEE Trans. Signal Process.*, vol. 63, no. 1, pp. 182–191, 2015.

[23] D. I. Shuman, B. Ricaud, and P. Vandergheynst, "Vertex-frequency analysis on graphs," *Appl. Comput. Harmon. Anal.*, 2015. doi: 10.1016/j.acha.2015.02.005.

[24] D. I. Shuman, C. Wiesmeyr, N. Holighaus, and P. Vandergheynst, "Spectrum-adapted tight graph wavelet and vertex-frequency frames," *IEEE Trans. Signal Process.*, vol. 63, no. 16, pp. 4223–4235, 2015.

[25] D. I. Shuman, M. J. Faraji, and P. Vandergheynst, "A multiscale pyramid transform for graph signals," *IEEE Trans. Signal Process.*, vol. 64, no. 8, pp. 2119–2134, 2016.

[26] D. Thanou, D. I. Shuman, and P. Frossard, "Learning parametric dictionaries for signals on graphs," *IEEE Trans. Signal Process.*, vol. 62, no. 15, pp. 3849–3862, 2014.

[27] D. Thanou and P. Frossard, "Multi-graph learning of spectral graph dictionaries.," in *Proc. IEEE Int. Conf. Acoust. Speech and Signal Process.*, 2015.

[28] J. Benedetto and M. Fickus, "Finite normalized tight frames," *Adv. Comput. Math.*, vol. 18, no. 2, pp. 357–385, 2003.

[29] H. Behjat, N. Leonardi, and D. Van De Ville, "Statistical parametric mapping of functional MRI data using wavelets adapted to the cerebral cortex," in *Proc. IEEE Int. Symp. Biomed. Imaging*, pp. 1070–1073, 2013.

[30] H. Behjat, N. Leonardi, L. Sörnmo, and D. Van De Ville, "Canonical cerebellar graph wavelets and their application to fMRI activation mapping," in *Proc. IEEE Int. Conf. Eng. Med. Biol. Soc.*, pp. 1039–1042, 2014.

[31] H. Behjat, N. Leonardi, L. Sörnmo, and D. Van De Ville, "Anatomically-adapted graph wavelets for improved group-level fMRI activation mapping," *NeuroImage*, vol. 123, pp. 185–199, 2015.

[32] F. Chung, *Spectral graph theory.* Providence, RI: AMS, 1997.

[33] Y. Meyer, "Principe d'incertitude, bases hilbertiennes et algebres d'operateurs," *Seminaire Bourbaki (in French)*, vol. 662, pp. 209–223, 1986.

[34] F. N. Fritsch and R. E. Carlson, "Monotone piecewise cubic interpolation," *SIAM J. Numer. Anal.*, vol. 17, no. 2, pp. 238–246, 1980.

[35] A. G. Marques, S. Segarra, G. Leus, and A. Ribeiro, "Stationary graph processes and spectral estimation." arXiv preprint arXiv:1603.04667 (2016).

[36] N. Perraudin and P. Vandergheynst, "Stationary signal processing on graphs." arXiv preprint arXiv:1601.02522 (2016).

[37] S. Chepuri and G. Leus, "Subsampling for graph power spectrum estimation." arXiv preprint arXiv:1603.03697 (2016).

[38] A. Agaskar and Y. M. Lu, "A spectral graph uncertainty principle," *IEEE Trans. Inf. Theory*, vol. 59, no. 7, pp. 4338–4356, 2013.

[39] M. Tsitsvero, S. Barbarossa, and P. Di Lorenzo, "Signals on graphs: uncertainty principle and sampling," *IEEE Trans. Signal Process.*, 2016. DOI 10.1109/TSP.2016.2573748.

[40] P. Koprowski, "Graph theoretic uncertainty and feasibility." arXiv preprint arXiv:1603.02059 (2016).

[41] N. Perraudin, B. Ricaud, D. Shuman, and P. Vandergheynst, "Global and local uncertainty principles for signals on graphs." arXiv preprint arXiv:1603.03030 (2016).

[42] D. Gleich, "The MatlabBGL matlab library [online]."

[43] "Google, [google maps for alameda county.]." Retrieved March, 2016.

[44] N. Logothetis and B. Wandell, "Interpreting the BOLD signal.," *Annu. Rev. Physiol.*, vol. 66, pp. 735–769, 2004.

[45] S. J. Kiebel, R. Goebel, and K. J. Friston, "Anatomically informed basis functions," *NeuroImage*, vol. 11, no. 6, pp. 656–667, 2000.

[46] M. K. Chung, S. M. Robbins, K. M. Dalton, R. J. Davidson, A. L. Alexander, and A. C. Evans, "Cortical thickness analysis in autism with heat kernel smoothing," *NeuroImage*, vol. 25, no. 4, pp. 1256–1265, 2005.

[47] D. J. Hagler Jr, A. P. Saygin, and M. I. Sereno, "Smoothing and cluster thresholding for cortical surface-based group analysis of fMRI data," *NeuroImage*, vol. 33, no. 4, pp. 1093–1103, 2006.

[48] S. Ozkaya and D. Van De Ville, "Anatomically adapted wavelets for integrated statistical analysis of fMRI data," in *Proc. IEEE Int. Symp. Biomed. Imaging*, (Chicago, IL), pp. 469–472, 2011.

[49] J. Diedrichsen, J. H. Balsters, J. Flavell, E. Cussans, and N. Ramnani, "A probabilistic MR atlas of the human cerebellum," *NeuroImage*, vol. 46, no. 1, pp. 39–46, 2009.

[50] A. M. C. Kelly, L. Q. Uddin, B. B. Biswal, F. X. Castellanos, and M. P. Milham, "Competition between functional brain networks mediates behavioral variability," *NeuroImage*, vol. 39, no. 1, pp. 527–537, 2008.

[51] W. H. Kim, V. Singh, M. K. Chung, C. Hinrichs, D. Pachauri, O. C. Okonkwo, and S. C. Johnson, "Multi-resolutional shape features via non-Euclidean wavelets: Applications to statistical analysis of cortical thickness," *NeuroImage*, vol. 93, pp. 107–123, 2014.

[52] W. H. Kim, N. Adluru, M. K. Chung, O. C. Okonkwo, S. C. Johnson, B. Bendlin, and V. Singh, "Multi-resolution statistical analysis of brain connectivity graphs in preclinical Alzheimer's disease.," *NeuroImage*, vol. 118, pp. 103–117, 2015.

[53] C. Li and A. B. Hamza, "A multiresolution descriptor for deformable 3D shape retrieval," *Vis. Comput.*, vol. 29, no. 6, pp. 513–524, 2013.

[54] M. Zhong and H. Qin, "Sparse approximation of 3D shapes via spectral graph wavelets," *Vis. Comput.*, vol. 30, no. 6, pp. 751–761, 2014.

[55] X. Yan, H. Qin, J. Li, H. Zhou, and J. G. Zong, "Infrared and visible image fusion with spectral graph wavelet transform," *J. Opt. Soc. Am. A*, vol. 32, no. 9, pp. 1643–1652, 2015.

[56] M. Unser, "On the optimality of ideal filters for pyramid and wavelet signal approximation," *IEEE Trans. Signal Process.*, vol. 41, no. 12, pp. 3591–3596, 1993.

Paper III

Interpolation in the Presence of Domain Inhomogeneity

Abstract

Standard interpolation techniques are implicitly based on the assumption that the signal lies on a homogeneous domain. In this article, the proposed interpolation method instead exploits prior information about domain inhomogeneity, characterized by different, potentially overlapping, subdomains. By introducing a domain-similarity metric for each sample, the interpolation process is then based on a domain-informed consistency principle. We illustrate and demonstrate the feasibility of domain-informed linear interpolation in 1D, and also, on a real fMRI image in 2-D. The results show the benefit of incorporating domain knowledge so that, for example, sharp domain boundaries can be recovered by the interpolation, if such information is available.

1 Introduction

Interpolation has been studied extensively in various settings. The main frameworks are based on concepts such as smoothness for spline-generating spaces [1], underlying Gaussian distributions for "kriging" [2], and spatial relationship for inverse-distance-weighted interpolation [3]. Yet, while advanced concepts have been developed for describing these signal spaces, the underlying domain is always assumed to be homogeneous. In a sub-category of super-resolution image processing techniques [4], such as in [5, 6, 7, 8, 9, 10, 11, 12], the interpolation phase is adapted based on the context of the signal; such adaptation schemes are based on the characteristics of either the image itself [5, 6, 7] or another high resolution image that is of the same nature as that of the low resolution image to be interpolated [9, 8, 10, 11, 12]. Here, we consider a different scenario in which signals are sampled over a known inhomogeneous domain; i.e., a domain characterized by a set of subdomains, that can be overlapping, available as supplementary data. This supplementary information is of a completely different nature than that of the samples to be interpolated; it describes the signal domain, rather than the signal itself.

1.1 Problem Formulation

Assume that the following set of information is given:

1. A sequence of samples $s[k]$ obtained as

$$s[k] = \langle s(x), \delta(x - k) \rangle, \quad \text{for all } k \in \mathbb{Z}, \tag{1}$$

   where $s(\cdot) \in L_2$ (denoting the Hilbert space of all continuous, real-valued functions that are square integrable in Lebesgue sense) and $s[\cdot] \in \ell_2$ (denoting the Hilbert space of all discrete signals that are square summable).

2. Domain knowledge[6] described by J different subdomain indicator functions $\tilde{d}_j(x)$, $j = 1, \ldots, J$, presented in normalized form as

$$d_j(x) = \frac{\tilde{d}_j(x)}{\sum_{l=1}^{J} \tilde{d}_l(x)}, \quad \text{such that } \sum_{j=1}^{J} d_j(x) = 1. \tag{2}$$

---

[6]We assume that every point belongs to at least one subdomain, and that the domain information can be specified by a continuous function.

Using $\tilde{d}_j(x)$, $j = 1, \ldots, J$, space-dependent index sets of maximal and minimal association to the underlying subdomains can be derived as

$$\mathcal{H}_x = \{i | d_i(x) = \max_j d_j(x)\}, \quad \text{for all } x \in \mathbb{R}, \tag{3}$$

$$\mathcal{L}_x = \{i | d_i(x) = \min_j d_j(x)\}, \quad \text{for all } x \in \mathbb{R}. \tag{4}$$

Given prior knowledge on domain inhomogeneity under the form (2)–(4), the objective is to adapt conventional interpolation methods such that they accommodate this information. To reach this objective, we start from shift-invariant generating kernels such as splines [13, 1, 14], and then transform them into shift-variant kernels based on the domain knowledge.

The remainder of this letter is organized as follows. In Section II, the basis for obtaining a domain-informed interpolated signal is formulated. In Section III, as a proof-of-concept, standard linear interpolation is extended to the proposed domain-informed setting, and an illustrative example is presented. In Section IV, the proposed interpolation scheme is applied to a real fMRI image.

2   Theory for Domain-Informed Interpolation

The proposed domain-informed interpolation scheme is based on two fundamental concepts: (i) deriving a domain-informed shift-variant basis, based on a shift-invariant basis of the integer shifts of a generating function φ; (ii) fulfilling the "domain-informed consistency principle"—a principle that we define as an extension of the consistency principle [15].

2.1   Domain-Informed Shift-Variant Basis

Consider a compactly-supported generator $\varphi(x)$ (i.e., $\varphi(x) = 0$, $\forall |x| \geq \Delta^{(\varphi)} \in \mathbb{R}^+$) of a shift-invariant space

$$\mathcal{V}(\varphi) = \left\{ \hat{s}(x) = \sum_{k \in \mathbb{Z}} c[k] \cdot \varphi(x - k) : c[\cdot] \in \ell_2 \right\}, \tag{5}$$

where $c[\cdot]$ are the weights of the integer-shifted basis functions. The generating function $\varphi(x)$ can be any of compact-support kernels used in standard interpolation. In the presence of domain inhomogeneity, the idea is to transform $\varphi(\cdot - k)$ into $\varphi_{\xi_k}(\cdot - k)$: a modulated version of $\varphi(\cdot - k)$ that is defined based on a domain

similarity metric ξ_k that describes the domain in the adjacency of k. With this construction, a shift-variant space

$$\mathcal{V}_\xi(\varphi) = \left\{ \hat{s}(x) = \sum_{k \in \mathbb{Z}} c[k] \cdot \varphi_{\xi_k}(x - k) : c[\cdot] \in \ell_2 \right\}, \tag{6}$$

is obtained. We propose the following definition of ξ_k, which will subsequently guide the design of φ_{ξ_k}.

Definition (Domain Similarity Metric)

Given a description of an inhomogeneous domain under the form (2)–(4), a domain similarity metric $\xi_k(x) \in [0, 1]$ can be defined in the Δ neighbourhood of each $k \in \mathbb{Z}$ as

$$\xi_k(x) = \begin{cases} W_{k,x}\, \mathcal{S}\left(d_{h_k}(k + x) - 0.5\right), & |x| < \Delta, |\mathcal{H}_k| = 1, \\ W_{k,x}\, \mathcal{S}\left(d_{l_{k+x}}(k + x) - 0.5\right), & |x| < \Delta, |\mathcal{H}_k| > 1, \\ 0, & |x| \geq \Delta, \end{cases} \tag{7}$$

where $|\mathcal{H}_.|$ denotes the cardinality of set $\mathcal{H}_.$, $\mathcal{S}(\cdot)$ denotes the logistic function, $\mathcal{S}(n) = (1 + e^{-\gamma\, n})^{-1} \in [0, 1]$ with $\gamma > 0$, $h_. \in \mathcal{H}_.$, $l_. \in \mathcal{L}_.$, and $W_{k,x}$ denotes a weight factor

$$W_{k,x} = 1 - \frac{1}{J} \sum_{j=1}^{J} |d_j(k + x) - d_j(k)|, \tag{8}$$

which increases the adaptation to domain knowledge. For minimal adaptation, $W_{k,x}$ can be set to 1.

In (7), if $k \in \mathbb{Z}$ and $(k + x) \in \mathbb{R}$ are (i) maximally associated to the same subdomain, and (ii) the maximal association of $(k + x) \in \mathbb{R}$ has a probability greater than 0.5, $\xi_k(x) \to 1$, otherwise, $\xi_k(x) \to 0$. The parameter γ of $\mathcal{S}(\cdot)$ tunes both the smoothness and strength of this adaptation; a greater γ, up to a suitable degree, leads to a stronger as well as smoother adaption to changes in domain inhomogeneity.

The metrics $\{\xi_k(x)\}_{k \in \mathbb{Z}}$ are defined as local functions in the neighbourhood of each $k \in \mathbb{Z}$. On the global domain support, a domain similarity function, denoted

$$\rho(x, k) : x \in \mathbb{R} \setminus \mathbb{Z}, k \in \mathcal{K}_x^{(\Delta)} : \{k \in \mathbb{Z} \mid |x - k| < \Delta\} \to [0, 1],$$

can be defined as

$$\rho(x, k) = \frac{\xi_k(x - k)}{\sum_{k' \in \mathcal{K}_x^{(\Delta)}} \xi_{k'}(x - k')}, \tag{9}$$

which satisfies the following three properties:

1. $\rho(x, i) = \rho(x, j)$ implies perfect similarity of the domains at x, i and j.

2. $\rho(x, i) > \rho(x, j)$ implies greater similarity of the domains at x and i than the similarity of the domains at x and j, and vice versa.

3. for $x \in \mathbb{R} \setminus \mathbb{Z}$, we have $\sum_{k \in \mathbb{Z}} \rho(x, k) = 1$, since

$$\sum_{k \in \mathbb{Z}} \rho(x, k) \stackrel{(7)}{=} \cdots + 0 + \frac{\sum_{i \in \mathcal{K}_x^{(\Delta)}} \xi_i(x - i)}{\sum_{k' \in \mathcal{K}_x^{(\Delta)}} \xi_{k'}(x - k')} + 0 + \cdots = 1. \quad (10)$$

2.2 DICP: Domain-Informed Consistency Principle

There are different ways to define φ_{ξ_k}. In this letter, we consider the construction of a particular class of domain-informed, shift-variant basis that leads to interpolation satisfying the following principle.

Definition (Domain-Informed Consistency Principle)

Given a sequence of samples, as in (4), and a properly defined domain similarity function, as in (9), the interpolated signal $\hat{s}(\cdot)$ must satisfy the following conditions:

(i) perfect fit at integers; i.e.

$$\hat{s}(k) = s[k], \quad \text{for all } k \in \mathbb{Z}. \quad (11)$$

(ii) for any $x \in \{\mathbb{R} \setminus \mathbb{Z}\}$ and the set $\mathcal{K}_x^{(\Delta)} = \{k \in \mathbb{Z} \mid |x - k| < \Delta\}$, if for all $i, j \in \mathcal{K}_x^{(\Delta)}$ we have $\rho(x, i) \neq \rho(x, j)$,

$$\underset{k \in \mathcal{K}_x^{(\Delta)}}{\arg \max} \left\{ \rho(x, k) \right\} = \underset{k \in \mathcal{K}_x^{(\Delta)}}{\arg \min} \left\{ \left| \hat{s}(x) - s[k] \right| \right\}. \quad (12)$$

Criterion (i) is the consistency principle [15]. Criterion (ii) is based on the assumption that the underlying signal $s(x)$, at any position $x \in \mathbb{R} \setminus \mathbb{Z}$, is more likely to be similar to those sample in its Δ neighbourhood that have a "similar domain" as x. As such, the DICP ensures that the interpolated signal is consistent not only at the given sample points, but also at intermediate points between samples.

3   DILI: Domain-Informed Linear Interpolation

We propose a specific scheme to adapt standard linear interpolation (SLI) to incorporate domain knowledge. A definition of a shift-variant basis for this particular setting is presented, such that the interpolated signal is ensured to satisfy the DICP. In particular, the basis is a domain-informed version of the linear B-spline basis function [1], the "hat" function with support 2 ($\Delta = 1$) defined as

$$\Lambda(x) = \begin{cases} 1 - |x|, & |x| < 1 \\ 0, & |x| \geq 1. \end{cases} \tag{13}$$

Proposition 2. *(Domain-Informed Linear Interpolation) For a given set of samples (4) and constraints (2), the domain-informed linear interpolated signal satisfying the DICP is given by*

$$\forall x \in \mathbb{R}, \quad \hat{s}(x) = \sum_{k \in \mathbb{Z}} s[k] \varphi_{\xi_k}(x - k), \tag{14}$$

where

$$\varphi_{\xi_k}(x) = \begin{cases} 0 & |x| \geq 1 \\ \Lambda(x) & |x| < 1, \ D(x_k) = 0, \ x_k \notin \mathcal{D} \\ \tilde{\xi}_k(x) & \text{otherwise}, \end{cases} \tag{15}$$

where $x_k = (k + x) \in \mathbb{R}$, and

$$\tilde{\xi}_k(x) = \frac{\xi_k(x)}{\xi_{\lfloor x_k \rfloor}(x) + \xi_{\lceil x_k \rceil}(x)}, \text{ for } |x| < 1, \tag{16}$$

$$D(x) = \tilde{\xi}_{\lfloor x \rfloor}(x - \lfloor x \rfloor) - \tilde{\xi}_{\lceil x \rceil}(x - \lceil x \rceil), \text{ for } x \in \mathbb{R},$$

$$\mathcal{D} = \left\{ x \in \mathbb{R} \mid D(x) = 0, \ \lim_{\varepsilon \to 0} \int_{x-\varepsilon}^{x+\varepsilon} D(x) dx = 0 \right\},$$

Proof. See Appendix II. □

DILI has the property that in any domain interval $[\alpha, \beta]$, $\alpha, \beta \in \mathbb{R}$, that is either homogeneous, i.e.,

$$\forall x \in [\alpha, \beta] : d_l(x) = 1, \ d_j(x) = 0, \ j \in \{\{1, \ldots, J\} - l\},$$

or uniformly inhomogeneous, i.e.,

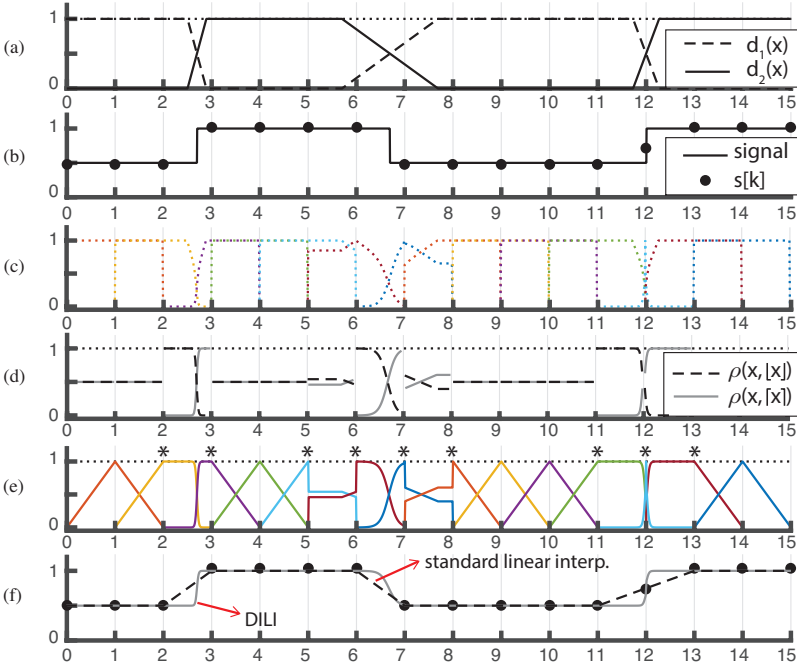$$\forall x \in [\alpha, \beta] : d_1(x) = d_2(x) = \cdots = d_J(x),$$

Figure 1: DILI. (a) Signal domain. (b) Signal samples. (c) $\{\xi_k(x)\}_{k=1,\ldots 14}$, for $|x| <= 1$. (d) $\{\rho(x,k)\}_{k\in\{\lfloor x\rfloor,\lceil x\rceil\}}$, for $\Delta = 1$. (e) $\{\varphi_{\xi_k}(x)\}_{k=1,\ldots,14}$. In (a), (d)-(e), the black dotted lines show partition of unity constraints. (f) DILI vs. SLI.

it exploits basis functions that are identical to those used in SLI, i.e., $\forall x \in [\alpha,\beta], k \in \mathbb{Z} : \varphi_k(x) = \Lambda(x-k)$; thus, the DILI and SLI signals are identical within the interval $[\alpha,\beta]$.

An example setting for constructing DILI is presented in Fig. 1. The signal domain consists of two subdomains, see Fig. 1(a), that satisfy (2). The domain has several homogeneous intervals, such as $[0, 2.5]$ or $[8, 11]$, as well as inhomogeneous intervals. In particular, three types of inhomogeneous domain intervals are observed at the transition between the two subdomains: a fast transition that falls between two samples, i.e., interval $[2, 3]$, a slow transition, i.e. interval $[5, 8]$, and a transition that occurs symmetrically around a sample point, $k = 12$. The signal samples and the underlying continuous signal are displayed in Fig. 1(b).

Fig. 1(c) illustrates the set of domain similarity metrics $\{\xi_k(x)\}_{k\in\mathbb{Z}}$, in $\Delta = 1$ neighbourhood of each $k \in Z$. Fig. 1(d) illustrates the corresponding domain similarity function $\{\rho(x,k)\}_{k\in\mathcal{K}_x^{(1)}}$, defined over the global support; the function is displayed in two parts, defining the left-hand and right-hand local neighbourhood of
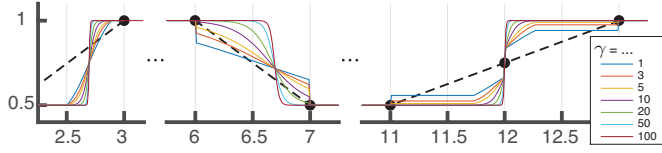
Figure 2: DILI using a range of different γ. The dashed line corresponds to SLI as shown in Figure 1(f).

each $k \in \mathbb{Z}$. Fig. 1(e) illustrates the resulting set of domain-informed splines, cf. (15); only those that reside in the adjacency of the domain transition boundaries, marked with asterisks, deviate from $\Lambda(x)$. A greater number deviate from their standard counterpart at the slower subdomain transition interval. As sample $s[12]$ lies at the exact intersection of the two subdomains, $\xi_{12}(x)$ as well as $\varphi_k(x)$ are strongly suppressed; i.e., $s[12]$ will have minimal effect in the interpolated values in its neighbourhood.

The resulting SLI and DILI are shown in Fig. 1(f). SLI and DILI are identical in regions associated to only a single subdomain. However, DILI better matches the underlying signal in the subdomain transition bands, satisfying the DICP. In Fig. 1(c)-(f), the logistic function $\mathcal{S}(\cdot)$ in (7) was used with parameter $\gamma = 20$. Fig. 2 illustrates the effect of varying γ; the DILI signals are illustrated only in the adjacency of the three subdomain transition regions, since they are, elsewhere, identical to SLI. In essence, γ determines the strength of associating the point to be interpolated, to the similarity of its domain and that of nearby samples; a greater γ results in a greater strength of this relationship.

4 Experimental Results

Using tensor products, a direct, separable extension of DILI to Euclidean m-D space can be formulated. In particular, the 2-D extension, denoted domain-informed bi-linear interpolation (DIBLI), is obtained as

$$\forall x, y \in \mathbb{R}, \quad \hat{s}(x, y) = \sum_{i=1}^{I} \sum_{j=1}^{J} s[i, j] \varphi_{\xi_{i,j}}^{(1)}(x - i) \varphi_{\xi_{i,j}}^{(2)}(y - j),$$

where $s[i, j]$ denotes the sample at position (i, j) in the $I \times J$ 2-D space and $\varphi_{\xi_{i,j}}^{(k)}(\cdot)$ denotes the domain-informed kernel at (i, j) along the k-th dimension. The properties of DILI directly extend to the 2-D setting.

To show the practicality of the proposed approach in an application, we present interpolation results using the proposed scheme on an fMRI dataset. In brain studies

using fMRI, a sequence of whole-brain functional data is acquired. To track brain activity at high temporal resolution, fMRI data are recorded at a relatively low spatial resolution. The fMRI data is commonly accompanied with a three to four fold higher resolution anatomical MRI scan, which provides information about the convoluted brain tissue delineating gray matter (GM) and white matter (WM), each of which have different functional properties [16], and cerebrospinal fluid (CSF); the topology also varies across subjects [17, 18]. Hence, the goal is to exploit the richness of anatomical data to improve the quality of interpolation and resampling of fMRI data, in the same spirit as approaches that aim to enhance denoising of such data [19].

Fig. 3 illustrates the setting for applying DIBLI on a 2-D slice of an fMRI volume, see Fig. 3(a), that accompanies a 3-fold higher resolution structural MRI scan, see Fig. 3(b). Segmenting the structural scan, one obtains GM, WM, and CSF probability maps, see Figs. 3(d)-(f). These maps are treated as normalized subdomain functions that satisfy (2) across any column/row in the plane, see Figs. 3(h)-(i). Figs. 3(j) and (k) show standard bilinear interpolation (SBLI) and DIBLI of the functional pixels shown in Fig. 3(g), respectively. The SBLI and DIBLI images are identical at homogeneous parts of the domain (see black arrows), whereas at the inhomogeneous parts (see white arrows), DIBLI presents finer details. Sharp signal boundaries at the intersection of subdomains can be recovered by DIBLI. The accuracy of this representation is limited by the level of discrepancy observed in the domain description. For example, see the circled region in Fig. 3(k) and the corresponding domain description in Figs. 3(d)-(f). In the red circled region, the underlying domain is very convoluted, whereas in the green circled region, a large amount of uncertainty is observed in the description of the subdomains. It should also be noted that the brain domain is intrinsically a 3-D representation, and that the functional data are recorded in 3-D. Therefore, extending the interpolation to 3-D and incorporating the association of the samples to the 3-D subdomain description can further enhance the results. As an alternative, the level of adaptation to domain knowledge can be reduced by setting the weight factor of the domain similarity metric to 1; cf. $W_{k,x}$ in (8). The resulting DIBLI interpolation is shown in Fig. 3(l), which may seem more visually appealing than Fig. 3(k), and yet, it presents significant subtle details that are missing in Fig. 3(j). This suggests the benefit of tuning the adaptation extent of the domain similarity metric relative to the quality and smoothness of available domain data.
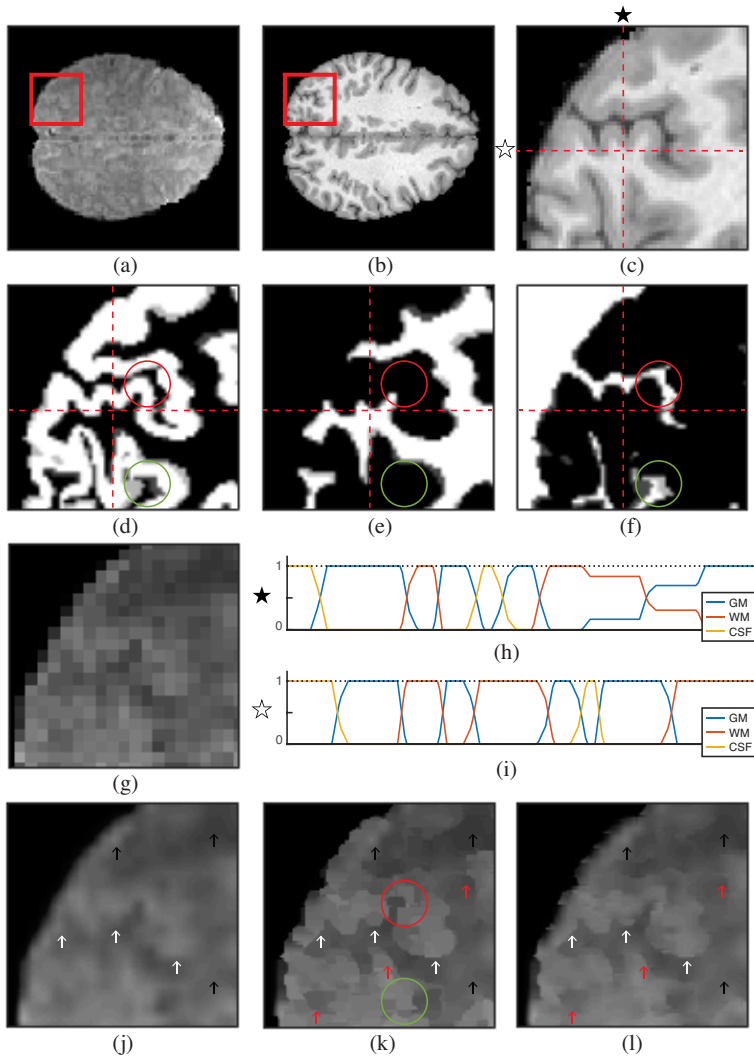
Figure 3: DIBLI. (a) A 2-D slice of an fMRI volume, (b) The structural scan. (c) Close-up of an ROI. (d) GM, (e) WM, and (f) CSF of the ROI. (g) fMRI data in the ROI. (h)-(i) Column and row domain data for the marked position in (c). (j) SBLI. (k) DIBLI with $W_{k,x}$ as in (8). (l) DIBLI with $W_{k,x} = 1$.

5   Conclusion and Outlook

We have proposed an interpolation scheme that incorporates a-priori knowledge of the signal domain, such that the interpolated signal is consistent not only at sample points, with respect to the given samples, but also at intermediate points between samples, with respect to the given domain knowledge. As a proof-of-concept, domain-informed linear interpolation has been presented as an extension of standard linear interpolation. Interpolation approaches that use higher order B-splines may also be extended based on the proposed domain-informed consistency principle, by defining suitable domain similarity metrics matching the support of the generating kernel. Results from applying the proposed approach on fMRI data demonstrated its potential to reveal subtle details. Our future research will focus on further evaluating the properties of domain-informed interpolation and its extension to incorporate higher order B-spline generating functions.

Appendix

Proof. (Proposition 1) We prove that the proposed interpolation satisfies both conditions of the DICP, cf. Definition 1.

Condition (i)
Perfect fit at integers is satisfied since

$$
\begin{aligned}
\forall k \in \mathbb{Z}, \quad \hat{s}(k) &= \langle \hat{s}(x), \delta(x-k) \rangle \\
&\stackrel{(14)}{=} \sum_{n \in \mathbb{Z}} s[k] \underbrace{\langle \varphi_{\xi,n}(x-n), \delta(x-k) \rangle}_{\varphi_{\xi,n}(k-n)} \\
&= s[k] \underbrace{\varphi_{\xi,k}(0)}_{\stackrel{(15),(7)}{=} 1} \\
&= s[k].
\end{aligned}
\tag{17}
$$

Condition (ii)
Define $\forall x \in \{\mathbb{R} \setminus \mathbb{Z}\}$, $f_{\lfloor x \rfloor}(x) = |\hat{s}(x) - s[\lfloor x \rfloor]|$ and $f_{\lceil x \rceil}(x) = |\hat{s}(x) - s[\lceil x \rceil]|$. The second condition of the principle, cf. (12), is satisfied if it can be shown that:

$$
\rho(x, \lfloor x \rfloor) > \rho(x, \lceil x \rceil) \to f_{\lfloor x \rfloor}(x) < f_{\lceil x \rceil}(x),
\tag{18}
$$
$$
\rho(x, \lfloor x \rfloor) < \rho(x, \lceil x \rceil) \to f_{\lfloor x \rfloor}(x) > f_{\lceil x \rceil}(x).
\tag{19}
$$

Define $\forall x \in \mathbb{R}, x^+ = x - \lfloor x \rfloor$ and $x^- = x - \lceil x \rceil$. Integer-shifted $\Lambda(x)$ form a partition of unity, $\forall x \in \mathbb{R}$, as

$$\sum_{k \in \mathbb{Z}} \Lambda(x - k) = \Lambda(x^+) + \Lambda(x^-) = 1, \tag{20}$$

and so do integer-shifted $\{\tilde{\xi}_k(x)\}_{k \in \mathbb{Z}}$, cf. (16), as

$$\sum_{k \in \mathbb{Z}} \tilde{\xi}_k(x - k) \overset{(10)}{=} \tilde{\xi}_{\lfloor x \rfloor}(x^+) + \tilde{\xi}_{\lceil x \rceil}(x^-) = 1. \tag{21}$$

Thus, integer-shifted, domain-informed first degree spline basis form a partition of unity, since $\forall x \in \mathbb{R}$

$$\sum_{k \in \mathbb{Z}} \varphi_{\xi,k}(x - k) \overset{(15)}{=} \varphi_{\xi,\lfloor x \rfloor}(x^+) + \varphi_{\xi,\lceil x \rceil}(x^-) \overset{(21),(20)}{=} 1. \tag{22}$$

The function $f_{\lfloor x \rfloor}(x)$ in (18) can be expanded as

$$
\begin{aligned}
f_{\lfloor x \rfloor}(x) &\overset{(14)}{=} \left| \sum_{k=\lfloor x \rfloor}^{\lceil x \rceil} s[k]\varphi_{\xi,k}(x - k) - s[\lfloor x \rfloor] \right| \\
&= \left| s[\lfloor x \rfloor] \underbrace{\left(\varphi_{\xi,\lfloor x \rfloor}(x^+) - 1\right)}_{\overset{(22)}{=} -\varphi_{\xi,\lceil x \rceil}(x^-)} + s[\lceil x \rceil] \varphi_{\xi,\lceil x \rceil}(x^-) \right| \\
&= \left| (s[\lceil x \rceil] - s[\lfloor x \rfloor]) \underbrace{\varphi_{\xi,\lceil x \rceil}(x^-)}_{\overset{(15),(7)}{\longrightarrow} \geq 0} \right| \\
&= \left| s[\lceil x \rceil] - s[\lfloor x \rfloor] \right| \cdot \varphi_{\xi,\lceil x \rceil}(x^-).
\end{aligned}
\tag{23}
$$

Similarly, $f_{\lceil x \rceil}(x)$ in (18) can be written as

$$f_{\lceil x \rceil}(x) = \left| s[\lfloor x \rfloor] - s[\lceil x \rceil] \right| \cdot \varphi_{\xi,\lfloor x \rfloor}(x^+). \tag{24}$$

From the left hand relation in (18) we have

$$\rho(x, \lfloor x \rfloor) > \rho(x, \lceil x \rceil) \overset{(9),(15)}{\longrightarrow} \varphi_{\xi,\lfloor x \rfloor}(x^+) > \varphi_{\xi,\lceil x \rceil}(x^-) \overset{(23),(24)}{\longrightarrow} f_{\lceil x \rceil}(x) > f_{\lfloor x \rfloor}(x).$$

(19) can be proved in the same way as done for (18). $\qquad\square$

References

[1] M. Unser, "Splines: A perfect fit for signal and image processing.," *IEEE Signal Process. Mag.*, vol. 16, no. 6, pp. 22–38, 1999.

[2] M. Oliver and R. Webster, "Kriging: a method of interpolation for geographical information systems," *Int. J. Geograph. Inform. Sys.*, vol. 4, no. 3, pp. 313–332, 1990.

[3] G. Lu and D. Wong, "An adaptive inverse-distance weighting spatial interpolation technique," *Comput. Geosci.*, vol. 34, no. 9, pp. 1044–1055, 2008.

[4] S. Park, M. Park, and M. Kang, "Super-resolution image reconstruction: a technical overview.," *IEEE Signal Process. Mag.*, vol. 20, no. 3, pp. 21–36, 2003.

[5] S. Alipour, X. Wu, and S. Shirani, "Context-based interpolation of 3-D medical images.," in *Proc. IEEE Int. Conf. Eng. Med. Biol. Soc.*, pp. 4112–4115, 2010.

[6] L. Cordero-Grande, G. Vegas-Sanchez-Ferrero, P. Casaseca-de-la-Higuera, and C. Alberola-Lopez, "A Markov random field approach for topology-preserving registration: Application to object-based tomographic image interpolation.," *IEEE Trans. Image Process.*, vol. 21, no. 4, pp. 2047–2061, 2012.

[7] A. Neubert, O. Salvado, O. Acosta, P. Bourgeat, and J. Fripp, "Constrained reverse diffusion for thick slice interpolation of 3D volumetric MRI images," *Comput. Med. Imag. Graph.*, vol. 36, no. 2, pp. 130–138, 2012.

[8] J. Manjón, P. Coupé, A. Buades, V. Fonov, D. Collins, and M. Robles, "Non-local MRI upsampling," *Med. Image Anal.*, vol. 14, no. 6, pp. 784–792, 2010.

[9] F. Rousseau and Alzheimer's Disease Neuroimaging Initiative, "A non-local approach for image superresolution using intermodality priors," *Med. Image Anal.*, vol. 14, no. 4, pp. 594–605, 2010.

[10] K. Jafari-Khouzani, "MRI upsampling using feature-based nonlocal means approach," *IEEE Trans. Med. Imag.*, vol. 33, no. 10, pp. 1969–1985, 2014.

[11] K. Jafari-Khouzani, "MRI upsampling using feature-based nonlocal means approach," *IEEE Trans. Med. Imag.*, vol. 33, no. 10, pp. 1969–1985, 2014.

[12] A. Rueda, N. Malpica, and E. Romero, "Single-image super-resolution of brain MR images using overcomplete dictionaries.," *Med. Image Anal.*, vol. 17, no. 1, pp. 113–132, 2013.

[13] C. de Boor, *A practical guide to splines.* New York: Springer-Verlag, 1978.

[14] M. Unser and T. Blu, "Fractional splines and wavelets," *SIAM review*, vol. 42, no. 1, pp. 43–67, 2000.

[15] M. Unser and A. Aldroubi, "A general sampling theory for nonideal acquisition devices.," *IEEE Trans. Signal Process.*, vol. 42, no. 11, pp. 2915–2925, 1994.

[16] N. Logothetis and B. Wandell, "Interpreting the BOLD signal.," *Annu. Rev. Physiol.*, vol. 66, pp. 735–769, 2004.

[17] J. F. Mangin, D. Riviere, A. Cachia, E. Duchesnay, Y. Cointepas, D. Papadopoulos-Orfanos, P. Scifo, T. Ochiai, F. Brunelle, and J. Regis, "A framework to study the cortical folding patterns.," *NeuroImage*, vol. 23, pp. S129–S138, 2004.

[18] M. de Schotten, A. Bizzi, F. Dell'Acqua, M. Allin, M. Walshe, R. Murray, S. Williams, D. Murphy, and M. Catani, "Atlasing location, asymmetry and inter-subject variability of white matter tracts in the human brain with MR diffusion tractography," *NeuroImage*, vol. 54, no. 1, pp. 49–59, 2011.

[19] H. Behjat, N. Leonardi, L. Sörnmo, and D. Van De Ville, "Anatomically-adapted graph wavelets for improved group-level fMRI activation mapping," *NeuroImage*, vol. 123, pp. 185–199, 2015.

Paper IV

Domain-Informed Spline Interpolation

Abstract

Standard interpolation techniques are implicitly based on the assumption that the signal lies on a single homogeneous domain. In contrast, many naturally occurring signals lie on a mixed (inhomogeneous) domain, such as brain activity associated to different brain tissue. We propose an interpolation method that instead exploits prior information about domain inhomogeneity, characterized by different, potentially overlapping, subdomains. As proof of concept, the focus is put on extending conventional shift-invariant B-spline interpolation. Given a known inhomogeneous domain, B-spline interpolation of a given order is extended to a domain-informed, shift-variant interpolation. This is done by constructing a domain-informed generating basis that satisfies stability properties. We illustrate example constructions of domain-informed generating basis, and show their property in increasing the coherence between the generating basis and the given inhomogeneous domain. By advantageously exploiting domain knowledge, we demonstrate the benefit of domain-informed interpolation over standard B-spline interpolation through Monte Carlo simulations across a range of B-spline orders. We also demonstrate the feasibility of domain-informed interpolation in a neuroimaging application where the domain information is available by a complementary image contrast. The results demonstrate the benefit of incorporating domain knowledge so that an interpolant consistent to the anatomy of the brain can be recovered by the proposed interpolation.

Interpolation has been extensively studied in various settings. The main frameworks are based on concepts such as smoothness for spline-generating spaces [1], underlying Gaussian distributions for "kriging" [2], and spatial relationship for inverse-distance-weighted interpolation [3]. Yet, while advanced concepts have been developed for describing these signal spaces, the underlying domain is always assumed to be homogeneous. Here, we consider a different scenario in which signals are sampled over a known "inhomogeneous" domain; i.e., a domain characterized by a set of subdomains with their description available as supplementary data. In a sub-catagory of super-resolution image processing techniques, the interpolation phase is adapted such that the scheme becomes close, in spirit, to the interpolation scenario that we consider here. In particular, they adapt the interpolation such that information from a high resolution signal is exploited to enhance interpolation on a set of samples acquired at low resolution. For example, an iterative, patch-based non-local reconstruction scheme was introduced in [4]; the use of inter-modality priors to regularize the similarity between the up-sampled image and a secondary high resolution image was proposed in [5]; a non-local means feature-based technique that uses structural information of a high resolution image with a different contrast was presented in [6]; sparsity promoting priors using overcomplete dictionaries learned from the data were exploited in [7]. Yet, such schemes do not fall within the problem that we formulate in this paper. The low resolution data samples and the supplementary high resolution information considered in these proposals are both of the same nature and, in essence, both describe the signal. In the scheme proposed in this article, the supplementary high resolution information instead describes the *domain* of the signal, which has a completely different temporal/spatial characteristic than that of the signal (samples) defined on the domain. Moreover, rather than being a learning scheme, our proposal is formulated as a shift-variant extension of conventional shift-invariant interpolation schemes [8, 9], such as linear, cubic or higher order B-spline interpolations.

Problem Formulation

Assume that the following set of information is given:

1. Domain knowledge described by a set of non-negative subdomain functions

$$\mathcal{D} : \left\{ d_j \in \mathrm{L}_2, \ j \in \mathcal{J} : \{1, \ldots, J\} \right\}, \tag{1}$$

which form a partition of unity as

$$\sum_{j=1}^{J} d_j(x) = 1, \quad \forall x \in \mathbb{R}. \tag{2}$$

Remark: We denote a segment $[a, b], a, b \in \mathbb{R}$, of the domain as *homogeneous* if there exists an $l \in \mathcal{J}$ such that

$$d_l(x) = 1, \quad \forall x \in [a, b], \tag{3}$$

and *inhomogeneous* if (3) does not hold for any $l \in \mathcal{J}$.

2. A uniform sequence of samples $s[k]$ taken from a continuous function $s(x)$ as

$$s[k] = \langle s(x), \delta(x - kT) \rangle, \tag{4}$$

where $T \in \mathbb{R}^+$ denotes the sampling step.

The objective is to recover $s(x)$ using the given set of samples $s[k]$. The approach is to extend any conventional interpolation method that employs a shift-invariant basis to an interpolation that employs a shift-variant basis, such that prior information on the domain inhomogenuity is accommodated. In particular, consider a compactly-supported generator $\varphi(x)$ (i.e., $\varphi(x) = 0, \forall |x| \geq \Delta^{(\varphi)} \in \mathbb{R}^+$) of a shift-invariant space

$$\mathcal{V}_\varphi = \left\{ \tilde{s}_T(x) = \sum_{k \in \mathbb{Z}} c[k] \cdot \varphi \left(\frac{x}{T} - k \right) : c \in \ell_2 \right\}. \tag{5}$$

The generating function $\varphi(x)$ can be any of compact-support kernels used in standard interpolation. In the presence of domain inhomogeneity, the idea is to transform $\varphi(\cdot - k)$ into $\varphi_k(\cdot - k)$: a tailored version of $\varphi(\cdot - k)$ whose definition is based on the domain structure in the adjacency of k. With this construction, a shift-variant, domain-informed space

$$\mathcal{V}_\varphi^{(\mathcal{D})} = \left\{ \tilde{s}_T(x) = \sum_{k \in \mathbb{Z}} c[k] \cdot \varphi_k \left(\frac{x}{T} - k \right) : c \in \ell_2 \right\}, \tag{6}$$

is obtained.

In this article, we focus on formulating the domain-informed interpolation theory for B-spline generating functions [1].

Different application areas can be envisioned for domain-informed interpolation. Earth sciences is one application area, where a spatially continuous representation of earth surface parameters, such as precipitation, land vegetation and atmospheric methane is desired to be computed from a discrete set of rain gauge measurements [10, 3], fossil pollen measurements [11, 12] and satellite estimates of methane

[13, 14], respectively. In these scenarios, the well-defined geographical structure of the earth, anthropogenic land-cover models [15] and geophysical models of the earth's surrounding atmosphere may be exploited as descriptors of the inhomogeneous domain to improve the standard approach to interpolation.

Neuroimaging is another area where domain-informed interpolation can be beneficial. In brain studies using functional magnetic resonance imaging (fMRI), a sequence of whole-brain brain functional data is acquired at relatively low spatial resolution to enable tracking brain function at high temporal resolution. An anatomical MRI scan is also commonly acquired, providing information about the convoluted brain tissue delineating gray and white matter, each of which have different functional properties [16]. Unlike functional data, anatomical data can be recorded at high spatial resolution, with resolutions three- to fourfold higher than the functional data. Hence, the goal would be to exploit the richness of anatomical data to define the domain of the acquired functional data and, in turn, to improve the quality of interpolation/resampling of the data[17, 18, 19]. In this article, we will demonstrate the feasibility of domain-informed interpolation in providing a high resolution representation of brain functional data such that the representation is consistent with the underlying brain anatomy.

The article is organized as follows. Section II, defines the properties of domain-informed generating basis. Section III, introduces the scheme for designing a domain-informed B-spline generating basis, and presents an illustrative example construction of such a basis. Section IV, presents domain-informed B-spline interpolation. In Section V, we show the benefit of domain-informed interpolation over standard B-spline interpolation through Monte Carlo simulations across a range of B-spline orders. In Section VI, we conclude by demonstrating the feasibility of domain-informed interpolation in a neuroimaging application.

1   Domain-Informed Generating Basis

Let L_2 denote the Hilbert space of all continuous, real-valued functions that are square integrable in Lebesgue's sense, with the L_2 inner-product defined as

$$\forall f, g \in L_2, \quad \langle f, g \rangle_{L_2} = \int_{-\infty}^{+\infty} f(x) g(x) \, dx < \infty, \tag{7}$$

and L_2-norm is defined for all $f \in L_2$ as $\|f\|_{L_2}^2 = \langle f, f \rangle_{L_2}$. Let ℓ_2 denote the Hilbert space of all discrete signals that are square summable, with the ℓ_2 inner product de-

fined as

$$\forall p, q \in \ell_2, \quad \langle p, q \rangle_{\ell_2} = \sum_{k \in \mathbb{Z}} p[k] q[k] < \infty, \tag{8}$$

and the ℓ_2-norm is defined for all $p \in \ell_2$ as $\|p\|_{\ell_2}^2 = \langle p, p \rangle_{\ell_2}$. In the following, we use the convention $\langle \cdot, \cdot \rangle = \langle \cdot, \cdot \rangle_{\ell_2}$ and $\| \cdot \| = \| \cdot \|_{\ell_2}$ to simplify the notation.

For a given compactly-supported generator $\varphi(x)$, let $\Phi^* = \{\varphi(x/T - k)\}_{k \in \mathbb{Z}}$ denote the standard shift-invariant basis of $\varphi(x)$ and $\Phi = \{\varphi_k(x/T - k)\}_{k \in \mathbb{Z}}$ denote a shift-variant basis of $\varphi(x)$; i.e., for all $k \in \mathbb{Z}$, $\varphi_k(\cdot - k)$ denotes a tailored version of $\varphi(\cdot - k)$, which may potentially be identical to $\varphi(\cdot - k)$ for a subset of $k \in \mathbb{Z}$.

Definition (Domain-Informed Generating Basis)

For a given domain definition as in (1), a basis Φ forms a domain-informed generating basis if and only if the following three conditions are met:

1. Φ forms a Riesz basis, which is ensured if there exists constants $0 < A < B < \infty$ such that [20]

$$\forall c \in \ell_2, \quad 0 \le A\|c\|_{\ell_2}^2 \le \left\| \sum_{k \in \mathbb{Z}} c[k] \varphi_k(\frac{x}{T} - k) \right\|_{L_2}^2$$
$$\le B\|c\|_{\ell_2}^2 \le \infty. \tag{9}$$

   This condition in necessary in order for (6) to be a stable, unambiguous representation model.

2. Φ forms a partition of unity, i.e.,

$$\forall x \in \mathbb{R}, \quad \sum_{k \in \mathbb{Z}} \varphi_k(\frac{x}{T} - k) = 1. \tag{10}$$

   This condition is necessary in order to have the approximation error vanish, see [9, Appendix B] for proof.

3. Any element of Φ whose compact support lies entirely within a homogeneous segment of the domain becomes identical to its corresponding element in Φ^*; i.e., $\varphi_k(x/T - k) = \varphi(x/T - k)$ if the domain is homogeneous at interval $[(k - \Delta^{(\varphi)})T, (k + \Delta^{(\varphi)})T]$.

We denote a basis satisfying only the first two conditions as a *generating basis*.

2 Domain-Informed B-spline Generating Basis

This section presents the scheme to construct domain-informed generating basis based on a B-spline generator function $\beta^{(n)}(x)$ of a desired order n. Domain-informed generating basis using generating functions other than B-splines may also be designed based on the same scheme.

2.1 B-spline Generating Basis

The central B-spline $\beta^{(n)}(x)$ is obtained recursively as

$$\beta^{(n)}(x) = (\beta^{(0)} * \beta^{(n-1)})(x), \tag{11}$$

where $(\cdot * \cdot)(x)$ denotes continuous-domain convolution and

$$\beta^{(0)}(x) = \begin{cases} 1, & -\frac{1}{2} < x < \frac{1}{2} \\ \frac{1}{2}, & |x| = \frac{1}{2} \\ 0, & \text{otherwise.} \end{cases} \tag{12}$$

$\beta^{(n)}(x)$ is supported in the interval $[-\Delta^{(n)}, \Delta^{(n)}]$, where $\Delta^{(n)} = (n+1)/2$. We define $\Delta^{(n)}$-neighbourhood sets in the vicinity of each point x, denoted $\Delta_x^{(n)}$, as

$$\Delta_x^{(n)} : \left\{ k \in \mathbb{Z} \ \middle| \ \left| \frac{x}{T} - k \right| < \Delta^{(n)} \right\}; \tag{13}$$

the set specifies the indices of sample points that fall within the $\Delta^{(n)}$-neighbourhood of a given point x. The scaled, integer-shifted set $\{\beta^{(n)}(x/T - k)\}_{k \in \mathbb{Z}}$ forms a B-spline generating basis spanning the space of piecewise polynomial functions of order $n - 1$.

2.2 Domain-Informed B-spline Generating Basis

We construct a domain-informed B-spline associated to each sample point as the superposition of two B-spline based kernels as given in the following definition.

Definition (Domain-Informed B-splines)

For a given set of subdomain functions ([1]), a set of samples $s[k], k \in \mathbb{Z}$ and a B-spline generating function $\beta^{(n)}(x)$, a domain-informed B-spline associated to each sample

point $k \in \mathbb{Z}$ can be defined as

$$
\beta_k^{(n)}(x) = \begin{cases} \dot{\beta}_k^{(n)}(x) + \ddot{\beta}_k^{(n)}(x), & |x| \le \Delta^{(n)} \\ 0, & \text{otherwise,} \end{cases} \tag{14}
$$

where $\dot{\beta}_k^{(n)}(x)$ denotes a dominant kernel that characterises the overall shape and $\ddot{\beta}_k^{(n)}(x)$ a residual kernel that tunes the shape to the given domain knowledge in the adjacency of sample point k.

In the following, we formulate the construction of $\dot{\beta}_k^{(n)}(x)$ and $\ddot{\beta}_k^{(n)}(x)$. Firstly, using the subdomain functions, a set of subdomain-informed B-splines associated to each $k \in \mathbb{Z}$ and $j \in \mathcal{J}$ are obtained as

$$
\beta_{k,j}^{(n)}(x) = \begin{cases} d_j((x+k)T)\beta^{(n)}(x), & |x| \le \Delta^{(n)} \\ 0, & \text{otherwise.} \end{cases} \tag{15}
$$

It is straight forward to verify that subdomain-informed B-splines satisfy

$$
\sum_{k \in \mathbb{Z}} \beta_{k,j}^{(n)}(\frac{x}{T} - k) = d_j(x), \quad \forall x \in \mathbb{R}, \tag{16}
$$

and

$$
\sum_{j \in \mathcal{J}} \beta_{k,j}^{(n)}(x) = \beta^{(n)}(x), \quad \forall k \in \mathbb{Z}. \tag{17}
$$

Let $\mathcal{I}_k$ denote the set of indices of the subdomains maximally associated to sample k, i.e.,

$$
\mathcal{I}_k : \left\{ i \in \mathcal{J} \,\middle|\, i = \arg\max_{j \in \mathcal{J}} \{d_j(kT)\} \right\}, \tag{18}
$$

and $\mathcal{R}_k$ denote the set of the remaining subdomain indices, i.e.,

$$
\mathcal{R}_k = \mathcal{J} \setminus \mathcal{I}_k, \tag{19}
$$

where $\setminus$ denotes set difference. $|\mathcal{I}_k| > 1$ infers that more than one subdomain is maximally associated with sample point k. The dominant kernel $\dot{\beta}_k^{(n)}(x)$ is defined as

$$
\dot{\beta}_k^{(n)}(x) = \sum_{i \in \mathcal{I}_k} \beta_{k,i}^{(n)}(x). \tag{20}
$$

By cumulating the non-dominant subdomain-informed B-splines, a residual function $\Omega(x) : x \in \mathbb{R} \to [0, 1]$ can be defined as

$$\Omega(x) = \sum_{l \in \Delta_x^{(n)}} \sum_{j \in \mathcal{R}_l} \beta_{l,j}^{(n)}(\frac{x}{T} - l) \tag{21}$$

$$= 1 - \sum_{l \in \Delta_x^{(n)}} \dot{\beta}_l^{(n)}(\frac{x}{T} - l). \tag{22}$$

In particular, $\Omega(x) = 0$ at any homogeneous part of the domain. Using $\Omega(x)$, the residual kernel $\ddot{\beta}_k^{(n)}(x)$ is defined as

$$\ddot{\beta}_k^{(n)}(x) = \begin{cases} \theta_k(x) \cdot \Omega((x + k)T), & |x| \leq \Delta^{(n)} \\ 0, & \text{otherwise,} \end{cases} \tag{23}$$

where $\theta_k(x)$, in its simplest form, equals a weighting function $w_k(x)$ defined as

$$w_k(x) = \begin{cases} \dfrac{\dot{\beta}_k^{(n)}(x)}{\sum_{l \in \Delta_{x_k T}^{(n)}} \dot{\beta}_l^{(n)}(x_k - l)}, & |x| \leq \Delta^{(n)} \\ 0, & \text{otherwise} \end{cases} \tag{24}$$

where $x_k = x + k$. The values of $\{d_j(x)\}_{j \in \mathcal{J}}$ are incorporated in $\dot{\beta}_k^{(n)}(x)$ and thus implicitly reflected in $w_k(x)$. To control changes in $\ddot{\beta}_k^{(n)}(x)$ relative to changes in the subdomains, $\theta_k(x)$ can be adaptively defined as

$$\theta_k(x) := \frac{\Theta\left(w_k(x)\right)}{\sum_{l \in \Delta_{x_k T}^{(n)}} \Theta\left(w_l(x_k - l)\right)} \in [0, 1], \tag{25}$$

where $\Theta(\cdot) : [0, 1] \to [0, 1]$ denotes a desired smooth, monotonically increasing function satisfying $\Theta(x) = x$ for $x \in \{0, 0.5, 1\}$, $\Theta(x) \leq x$ for $x < 0.5$ and $\Theta(x) \geq x$ for $x > 0.5$. Note that by setting $\Theta(x) = x$, we have $\theta_k(x) = w_k(x)$ since $\sum_{l \in \Delta_{x_k T}^{(n)}} w_l(x_k - l) = 1$.

Proposition 3. *(Domain-Informed B-spline Generating Basis) For a given sequence of samples $\{s[k]\}_{k \in \mathbb{Z}}$ as in (4), a given set of subdomain functions as in (1) and a given B-spline generating function $\beta^{(n)}(x)$, the set of functions $\{\beta_k^{(n)}(x/T - k)\}_{k \in \mathbb{Z}}$ form a domain-informed generating basis, satisfying the three properties of a domain-informed generating basis.*

Proof. See Appendix II. □

2.3 Illustrative Example Realization of Domain-informed B-spline Generating Bases

We present two example realizations of domain-informed B-spline generating bases to illustrate the construction scheme. Before presenting the constructions, we formulate a scheme to randomly realize inhomogeneous domains with a desired number of subbands, varying patterns of transition between subbands and satisfying (2). To enable varying the extent of adaptation of the bases to the domain knowledge, we also define a tunable $\Theta(x)$, cf. (25).

2.4 Realization of inhomogeneous domains

An inhomogeneous domain consisting of J subdomains can be realized through the following scheme. Let $L \in \mathbb{R}^+$ and $U \in \mathbb{R}^+$ denote the domain's lower and upper range, respectively. A system of $K \in \mathbb{Z}^+$ Meyer-type kernels $\{m_k(x), \forall x \in [L, U]\}_{k=1,\dots,K}$ is constructed, see Figure 1(a). The details of the construction is given in Appendix II. The benefit of using a Meyer-type system of kernels is that they provide smooth, compactly-supported kernels with minimal overlap only between adjacent kernels. A random, monotonically increasing function, $w(x) : [L, U] \to [L, U]$ is then constructed. By incorporating $w(x)$ in $\{m_k(x)\}_{k=1,\dots,K}$, a warped version of the Meyer-type system is obtained as: $\{m'_k(x) = m_k(w(x))\}_{k=1,\dots,K}$, see Figure 1(b). The warped kernels exhibit varying patterns of transition between adjacent kernels, with different orders of smoothness.

A set of J subdomain functions satisfying (1) are then realized as

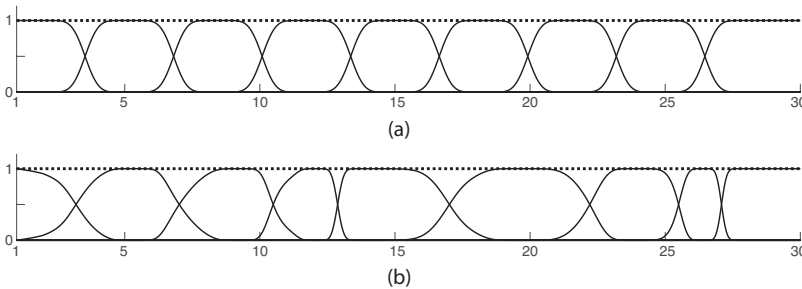$$\forall x \in [L, U], \quad d_j(x) = \sum_{k \in \mathcal{K}_j} m_k(x), \quad j = 1, \dots, J,$$

(a)

(b)

Figure 1: (a) A Meyer-type system of kernels; $K = 9$, $L = 1$ and $U = 30$. (b) A warped version of the system of kernels in (a).

where $\mathcal{K}_j \subset \{1, \cdots, K\}$ such that $\cup_{j=1}^{J} \mathcal{K}_j = \{1, \cdots, K\}$ and $\cap_{j=1}^{J} \mathcal{K}_j = \emptyset$. Figure 2(a) shows an example inhomogeneous domain, consisting of two subdomains, constructed using this scheme. The domain has several homogeneous intervals, such as $[1, 6]$ and $[19, 21]$, as well as varying inhomogeneous intervals present at the transition regions between the two subdomains.

2.5 Defining a tunable $\Theta(\cdot)$ function

By incorporating a suitable $\Theta(\cdot)$ in (25), the extent of adaptation to variation in proximity of subdomain transitions can be increased in the design of domain-informed B-splines. In particular, we exploit the logistic function to define $\Theta(\cdot)$ as

$$\Theta(x) = (1 + e^{-\gamma/2})/(1 + e^{-\gamma(x-1/2)}), \tag{26}$$

where $\gamma \geq 1$ is a free parameter.

2.6 Realizations of B-spline Generating Bases

Figures 2 and 3 show an example construction of domain-informed B-spline generating basis using first and third order B-spline kernels, respectively. Domain-informed B-splines whose support lie at a homogeneous part of the domain are identical to their standard counterpart; for example, see domain-informed B-splines centered at sample points 5, 15 and 20 in Figures 2(e) and 3(e). On the other hand, domain-informed B-splines that reside in the adjacency of domain transition boundaries deviate from their standard counterpart. Domain-informed B-splines have their peak amplitude close to the sample point where they are localized and have declining tails as in standard B-splines. This property is due to the employed construction scheme that enables adapting to domain inhomogeneities relative to the amplitude of the generating function along its support; i.e., the central parts of the kernels are more affected by domain inhomogeneities than their tails.
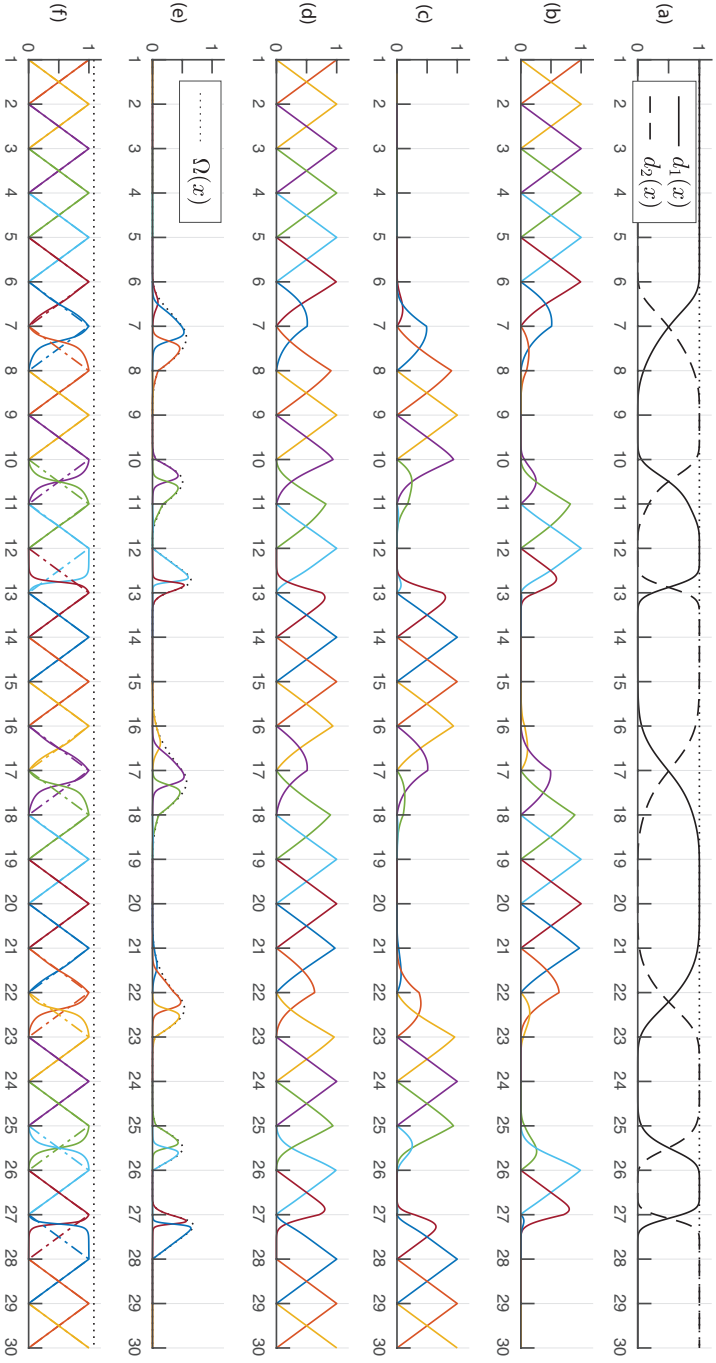
Figure 2: (a) An inhomogeneous domain consisting of two subdomains. (b)-(c) Subdomain-informed B-splines $\beta_{k,1}^{(1)}(x-k)$ and $\beta_{k,2}^{(1)}(x-k)$, respectively. (d) Dominant kernels $\dot{\beta}_k^{(1)}(x-k)$. (e) Residual kernels $\ddot{\beta}_k^{(1)}(x-k)$. (f) Domain-informed B-splines $\beta_k^{(1)}(x-k)$ (solid lines) overlaid on standard B-splines $\beta^{(1)}(x-k)$ (dashed lines).
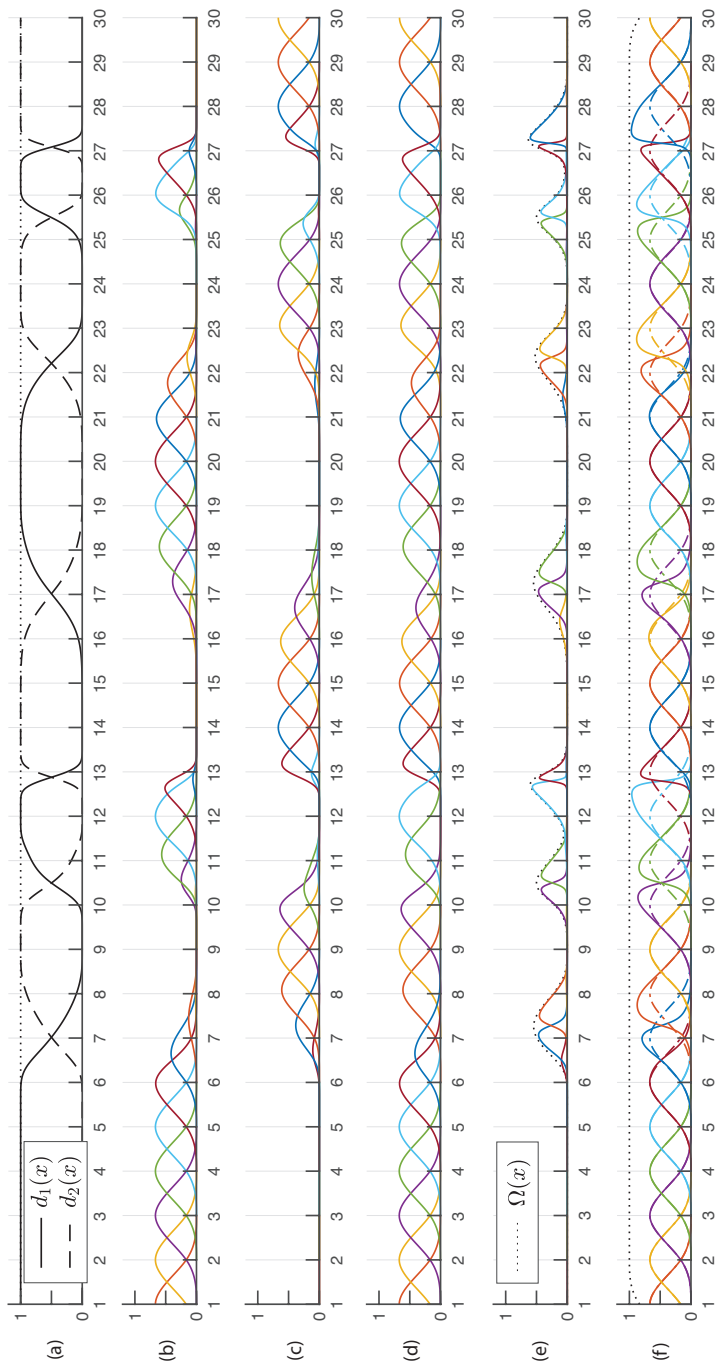
Figure 3: Construction of domain-informed B-splines of order three. (a)–(f) The same as in , but for B-splines of order three.

2.7   Domain-Basis Coherence

It is insightful to quantify the coherence between a given inhomogeneous domain and a basis defined on the domain. To this aim, we first define a domain similarity metric.

Definition (Domain Similarity Metric)

Given a description of an inhomogeneous domain as in ([1]), a domain similarity metric can be defined in the Δ-neighborhood of each $k \in \mathbb{Z}$ as

$$
\xi_k(x) = \begin{cases} \Theta\left(1 - \dfrac{1}{J}\sum_{j=1}^{J}|d_j(x_kT) - d_j(kT)|\right), & |x| < \Delta \\ 0, & |x| \geq \Delta, \end{cases}
\tag{27}
$$

where $x_k = x + k$, $\Theta(\cdot)$ is defined as in ([25]); $\xi_k(x) \in [0, 1]$.

The domain similarity metric can be used to quantify the relative difference in coherence between a domain and a domain-informed generating basis relative to that between the domain and the corresponding shift-invariant, generating basis.

Definition (Domain-Basis Coherence Factor)

Given a description of an inhomogeneous domain as in ([1]), a domain-basis coherence factor associated to domain-informed basis Φ can be defined as

$$
\mathcal{R}_\Phi = \frac{\sum_{k\in\mathbb{Z}}\langle\xi_k(x), \varphi_k(x)\rangle_{L_2}}{\sum_{k\in\mathbb{Z}}\langle\xi_k(x), \varphi(x)\rangle_{L_2}}.
\tag{28}
$$

In Figure [4], the dashed curves show the change in $\mathcal{R}_\Phi$ for the domain shown in Figure [2](a) as a function of the free parameter γ in constructing domain-informed B-spline basis; the two marked positions on the dashed curves show $\mathcal{R}_\Phi$ associated to the domain-informed B-spline basis shown in Figures [2](e) and [3](e). $\mathcal{R}_\Phi$ is greater than one across γ, ranging from 1 to 50 with steps of 1, reflecting a greater domain-basis coherence of the domain-informed B-spline basis relative to the standard B-spline basis. The coherence factor is greater for the third order domain-informed B-spline basis than that of first order domain-informed B-spline basis. Moreover, $\mathcal{R}_\Phi$ increases with the increase in γ, up to a point that it almost saturates. Thus, the parameter γ can be used to tune the level of adaptation of the design to the domain info relative to the extent of certainty we assume on the domain data. The lower the adopted value of γ, the lower is the domain adaptation.
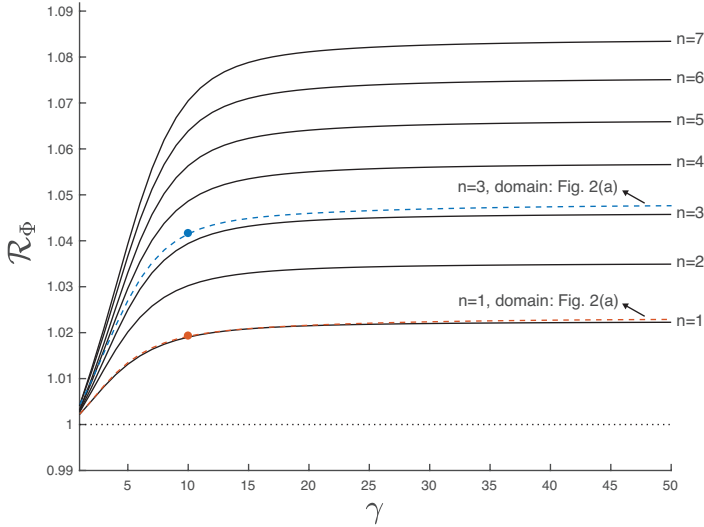
Figure 4: Domain-basis coherence factor, for domain-informed B-splines of orders 1-7. The solid lines show ensemble values over 1000 inhomogeneous domain realizations. The dashed lines show the domain-basis coherence factor associated to the domain shown in Figure 2(a); the two marked points show the domain-basis coherence factor for the particular DIBSI basis shown in Figures 2(e) and 3(e), i.e., using $\gamma = 10$.

To provide a more general picture of the coherence behavior, we generated 1000 realizations of inhomogeneous domains using the same scheme as that used to construct the domain shown in Figure 2(a). Domain-informed B-spline basis of orders from 1 to 7 were constructed for each realization of inhomogeneous domain, over the range of γ. Figure 4 shows the resulting ensemble $\mathcal{R}_\Phi$, i.e., each point being the average of 1000 $\mathcal{R}_\Phi$ values, one associated to each domain realization. For each domain-informed B-spline basis order n, the ensemble coherence factor increases with the increase in γ, and gradually saturates. Moreover, for a given γ, the ensemble coherence factor associated to a higher order basis is greater than that associated to a lower order basis.

3   Domain-Informed B-spline Interpolation

We propose domain-informed B-spline interpolation (DIBSI) with the following assumption about the underlying signal: at inhomogeneous intervals of the domain, the signal is expected to be consistent with the given domain description, whereas

at homogeneous intervals of the domain, the signal is expected to have smoothness characteristics provided by the chosen spline order n.

Proposition 4. *(Domain-Informed B-spline Interpolation) For a given domain description as in (1)–(2), a sequence of samples $\{s[k]\}_{k\in\mathbb{Z}}$ as in (4) and a B-spline generating function $\beta^{(n)}(x)$, the n-th order domain-informed B-spline interpolant of the set of samples is obtained as*

$$\forall x \in \mathbb{R}, \quad \tilde{s}(x) = \sum_{k\in\mathbb{Z}} c[k]\beta_k^{(n)}(\frac{x}{T} - k), \tag{29}$$

where $\beta_k^{(n)}(\cdot)$ is given as in (14) and the coefficients $c[k]$ are obtained through solving the set of equations

$$\forall k \in \mathbb{Z}, \quad \sum_{l=k-\lfloor n/2 \rfloor}^{k+\lfloor n/2 \rfloor} c[l]\beta_l^{(n)}(k - l) = s[k]. \tag{30}$$

The resulting interpolant $\tilde{s}(x)$ has the following properties:

1. *$\tilde{s}(x)$ satisfies the consistency principle [21]*

$$\tilde{s}_T(kT) = s[k], \forall k \in \mathbb{Z}. \tag{31}$$

2. *At homogeneous parts of the domain, $\tilde{s}(x)$ is equal to the n-th order spline interpolant obtained using standard spline interpolation, i.e., a piecewise polynomial of order $n - 1$.*

Proof. (Property 1) Domain-informed B-spline interpolation leads to perfect fit at sample points $k \in \mathbb{Z}$ since

$$\begin{aligned}
\tilde{s}(k) &= \langle \tilde{s}(x), \delta(x - kT) \rangle \\
&\overset{(29)}{=} \sum_{l\in\mathcal{K}} c[k] \underbrace{\left\langle \beta_l^{(n)}(\frac{x}{T} - l), \delta(x - kT) \right\rangle}_{\beta_l^{(n)}(k-l)} \\
&\overset{(14)}{=} \sum_{l=k-\lfloor n/2 \rfloor}^{k+\lfloor n/2 \rfloor} c[k]\beta_l^{(n)}(k - l) \\
&\overset{(30)}{=} s[k].
\end{aligned} \tag{32}$$

(Property 2) In any homogeneous domain interval $[a, b]$, domain-informed B-spline basis functions are identical to their standard B-spline basis function (property 3 of domain-informed B-spline generating basis). Therefore, the domain-informed and standard B-spline interpolants become identical within the interval $[a, b]$.

$\square$

Remark: For domain-informed B-splines of order $n = 0$ and 1, the coefficients $c[k]$ are identical to the signal samples, i.e. $\forall k \in \mathcal{K}$, $c[k] = s[k]$. For higher order domain-informed B-splines, using matrix formulation, the solution to (30) is obtained by solving a $2\lfloor n/2 \rfloor + 1$ band-diagonal matrix of linear equations; for cubic B-splines, i.e., $n = 3$, the formulation leads to solving a tridiagonal matrix equation.

4 DIBSI vs BSI on simulated data

To enable validation of the proposed interpolation scheme, a set of synthetic random signals are required. Due to the assumption of inhomogeneity of the signal domain, realizing such signals is not straight forward. We present a scheme for realizing random signals of a desired piecewise smoothness characteristic on an inhomogeneous domain, such that the signals respect the inhomogeneity of the domain. Assume given an inhomogeneous domain as in (1), consisting of J subdomains. First, a set of J signals of a desired smoothness characteristic are realized; in particular, each of the J signals are constructed by realizing (i) a randomly jittered, uniform knot sequence $[k + \epsilon_k]$ where $k \in \mathbb{Z}$, $\epsilon_k \in [-\alpha, \alpha]$ and $\alpha \in [0, 0.5)$, and (ii) J random sequences of control values $\{v_j[k] \in [0, 1]\}_{j=1}^{J}$. Using (i) and (ii), J random spline signals of order n, denoted $f_{t,v_j}(x)$, are constructed such that [22]

$$\forall k \in \mathbb{Z}, \quad f_{t,v_j}(t[k]) = v_j[k], \quad j = 1, \ldots, J.$$

Signals $\{f_{t,v_j}(x)\}_{j=1}^{J}$ are then transformed to signals associated to each subdomain as

$$s_j(x) = H\left(d_j(x) - \frac{1}{J}\right) f_{t,v_j}(x), \quad j = 1, \ldots, J,$$

where $H(\cdot)$ denotes the Heaviside step function. With this model, we make a minimal assumption on the nature of the signals at the transition between subdomains. By superimposing the subdomain signals, a signal defined on the given inhomogeneous domain is obtained as

$$s(x) = \sum_{j \in \mathcal{J}} s_j(x). \tag{33}$$

Using this signal construction scheme and the domain construction scheme presented in Section 2.3, a set of D domains, and on each domain a set of S signals were

randomly realized. B-spline interpolation (BSI) and DIBSI was then implemented on samples derived from each signal across a range of sampling steps $T \in [0.1, 1]$ (step size = 0.1) and B-spline orders $n = 1, \cdots, 6$. For $\tilde{s}_T(x)$ to be a good approximation of $s(x)$, the quality of interpolation needs to improve proportionally to the decrease in T. The interpolation error can be quantified using the distance metric $\|\tilde{s}_T(x) - s(x)\|_{L_2}$. The ensemble interpolation error associated with DIBSI can be quantified as

$$\varepsilon_{\mathcal{V}_\varphi^{(\mathcal{D})}}(T) = \frac{1}{DS} \sum_{i=1}^{D} \sum_{j=1}^{S} \frac{\|\tilde{s}_T^{(i,j)}(x) - s^{(i,j)}(x)\|_{L_2}}{\|s^{(i,j)}(x)\|_{L_2}}, \qquad (34)$$

where $s^{(i,j)}(x)$ denotes the j-th realized signal on the i-th realized domain and $\tilde{s}_T^{(i,j)}(x) \in \mathcal{V}_\varphi^{(\mathcal{D})}$ denotes the domain-informed B-spline interpolant obtained based on samples extracted from $s^{(i,j)}(x)$ at a sampling step T. For BSI where $\tilde{s}_T^{(i,j)}(x) \in \mathcal{V}_\varphi$, the ensemble interpolation error, denoted $\varepsilon_{\mathcal{V}_\varphi}(T)$, can be quantified in the same way as in (34).

Figure 5 shows ensemble interpolation errors $\varepsilon_{\mathcal{V}_\varphi}(T)$ and $\varepsilon_{\mathcal{V}_\varphi^{\mathcal{D}}}(T)$ on a randomly realized set of 10,000 signals ($D = 100$ and $S = 100$) for $\varphi = \{\beta^{(n)}(x)\}_{n=1,\cdots,6}$. DIBSI outperforms BSI across the range of B-spline orders. For each B-spline order, both $\varepsilon_{\mathcal{V}_\varphi}(T)$ and $\varepsilon_{\mathcal{V}_\varphi^{\mathcal{D}}}(T)$ decrease proportional to the decrease in T. The difference between $\varepsilon_{\mathcal{V}_\varphi}(T)$ and $\varepsilon_{\mathcal{V}_\varphi^{\mathcal{D}}}(T)$ increases with the increase in the order of the B-splines.

Aside from the comparisons showing the enhanced performance of DIBSI over BSI across the range of B-spline orders, it is insightful to compare the performance of DIBSI itself across different B-spline orders to that of BSI. Figures 6(b) and (c) show the approximation errors of BSI and DIBSI, respectively; the signal set used is the same as the one used for Figure 5, and thus, the plots are essentially a rearrangement of those shown in Figure 5. BSI using higher order B-splines does not consistently lead to greater reduction in the interpolation error, see Figure 6(a), whereas DIBSI shows better consistency, see Figure 6(b).
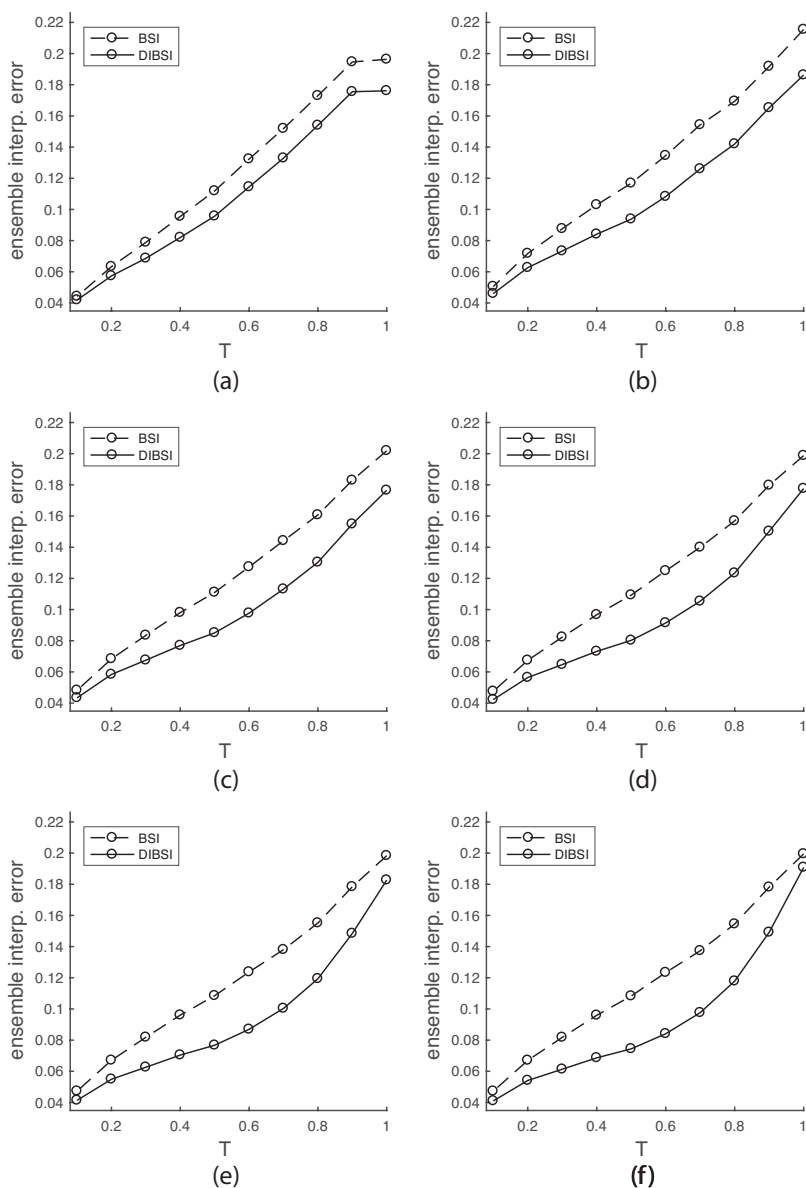
Figure 5: (a)-(f) Ensemble interpolation errors of BSI and DIBSI, with generating basis constructed using $\beta^{(n)}(x)$ for $n = 1, \ldots, 6$, respectively.
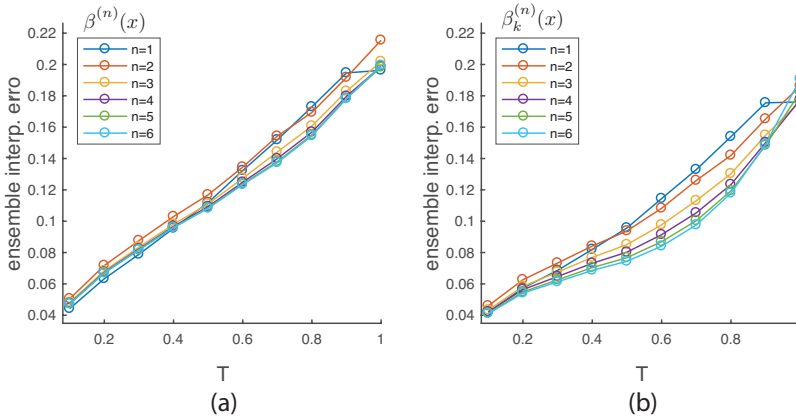
Figure 6: Ensemble interpolation errors over signals realized on inhomogeneous domains ($D = 100, S = 100$) using (a) BSI and (b) DIBSI.

5   DIBSI vs BSI on neuroimaging data

To show the practicality of the proposed approach, we present interpolation results using the proposed scheme on an fMRI dataset. In brain studies using fMRI, a sequence of whole-brain functional data is acquired. To track brain activity at high temporal resolution, fMRI data are recorded at a relatively low spatial resolution. The data is commonly accompanied with a three- to fourfold higher resolution anatomical MRI scan, which provides information about the convoluted brain tissue delineating gray matter (GM) and white matter (WM), each of which have different functional properties [16], and cerebrospinal fluid (CSF); the topology also varies across subjects [23]. Hence, the goal is to exploit the richness of subject-specific anatomical data, which define the domain of the acquired fMRI data, to improve the quality of interpolation and resampling of fMRI data. Such an interpolation scheme functions in the same spirit as signal processing techniques that aim to enhance linear [24] and non-linear [25, 26] denoising, deconvolution [27] and multi-scale decomposition [28] of fMRI data through exploiting anatomical constraints. Interpolation approaches that aim to map volumetric fMRI data on to the cortical surface [29, 30] are also related in the sense that they aim to enhance surface interpolation by accounting for the irregularity of the domain. Yet, such interpolation schemes are different from that we propose here since they adapt to the irregularity of the domain rather than to its inhomogeneity; i.e., they obtain an interpolant on a homogenous, irregular domain rather than one on an inhomogeneous domain.

Figure 7 illustrates the setting for applying domain-informed B-spline interpolation on an fMRI dataset. We use data of a subject from the Human Connectome

Project [31]. Figure 7(a) shows a 2-D slice of fMRI data, extracted from a 3-D fMRI volume of the subject. The resolution of the image is 2×2 mm^2. Figure 7(b) shows the structural scan of the brain of the same subject, which has an almost 3 fold higher resolution, 0.7×0.7 mm^2. Both slices are extracted such that they are aligned to the same neurological coordinate. By segmenting the anatomical scan, gray matter, white matter and cerebrospinal fluid probability maps, which determine the probability of each voxel being of either tissue, are obtained; Figures 7(b)-(d) show these probability maps, upsampled to a resolution of 0.2×0.2 mm^2. We treat the region outside the brain mask also as part of the cerebrospinal fluid map. Bilinear interpolation of these maps are used to define normalized subdomain functions that satisfy (1) along any column/row in the plane. Figure 7(f) shows the subdomain function set along the marked line shown in Figures 7(b)-(e). The domain is very inhomogeneous, build of a convoluted mix of the two tissue types and CSF.

Figure 7(g) shows DIBSI basis of order three constructed for the inhomogeneous domain given in Figure 7(f). The basis is adapted to the convoluted description of the domain, and shows to be robust to complex delineation patterns between subdomains, for instance see interval [14, 17]. Figure 7(h) shows the fMRI samples along the marked line shown in Figures 7(a), as well as the resulting BSI and DIBSI interpolants. At any homogeneous parts of the domain DIBSI results in an interpolant that is identical to BSI; for instance see the DIBSI and BSI interpolants within the interval [24, 27] in Figure 7(g). At the inhomogeneous parts of the domain, DIBSI presents finer details than the SBLI image. For instance, see the domain description within the interval [7, 15], cf. Figure 7(f). Within this interval samples from gray matter (samples 8 and 10), white matter (samples 7 and 11) and cerebrospinal fluid (sample 9) are given, cf. Figure 7(h). On one hand, both BSI and DIBSI satisfy the consistency principle at the sample points. On the other hand, in between the samples, BSI maintains the smoothness characteristic enforced by using third order B-splines whereas DIBSI leads to a signal that is consistent with the description of the domain. For example, consider sample point 3 that is purely associated to CSF. Its adjacent samples, i.e., sample points 2 and 4, are both associated to gray matter. In such cases, the domain-informed B-splines realized at the sample point extensively adapt to the associated domain, and as such, minimize the mixing of sample points associated to different subdomains. In other words, the best sample to use to obtain the interpolant within the range [2.5,4] is sample point 3, and therefore, the contribution of $\beta_2^{(3)}(x-2)$ and $\beta_4^{(3)}(x-4)$ is minimized within this range. Similar scenarios are observed at sample points 8 and 13. As another example, consider samples 6 and 7 that are both purely associated to white matter. Their adjacent samples, i.e., samples 5 and 8, lie within gray matter. In such a scenario, domain-informed B-splines exhibit a 'crossing' behavior. Although both $\beta_6^{(3)}(x-6)$ and $\beta_8^{(3)}(x-8)$ have part
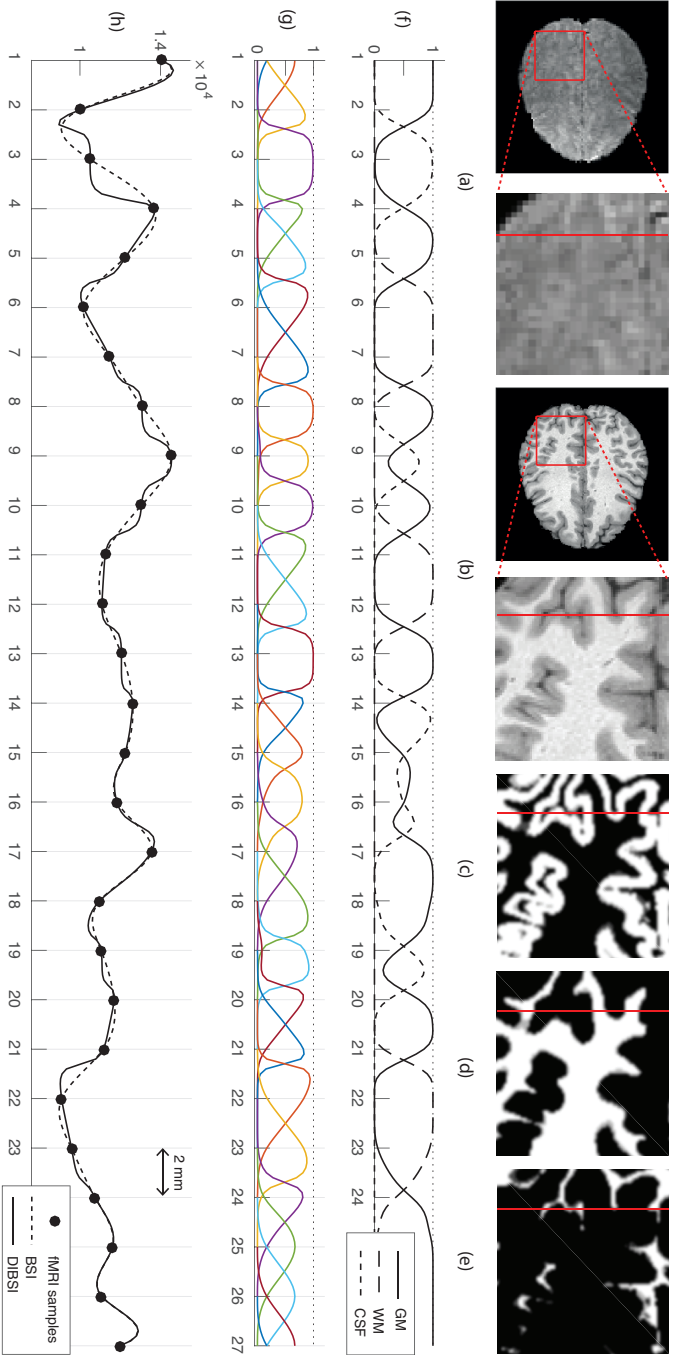
Figure 7: (a) A slice of fMRI data of a subject, including a close-up of an ROI. (b) The subject's brain anatomy at the same neurological coordinate as in (a). (c) Gray matter, (d) white matter and (e) cerebrospinal fluid segmented probability maps of the ROI shown in (b). (f) Description of the inhomogeneous domain along the marked line within the ROI in (b). (g) DIBSI basis, of order three, associated to the domain shown in (f). (h) B-spline interpolation and domain-informed B-spline interpolation of the functional samples along the marked line within the ROI in (a).

of their support within the interval $[5.5, 7.5]$, their amplitude within this interval is significantly suppressed to prevent mixing of gray matter samples with white matter samples in obtaining an interpolant within white matter. Similar scenarios can be observed along the domain.

It should be noted that the brain domain is intrinsically a 3-D representation, and that the functional data are acquired in 3-D. Therefore, extending the interpolation to 3-D and incorporating the association of the samples to the 3-D subdomain description can further enhance the results. A separable extension of the proposed approach to 2-D and 3-D using tensor products is straightforward. However, such an extension can only incorporate domain knowledge along the Euclidean axis. As such, inconsistent interpolation patterns may be obtained if the domain description is convoluted. Moreover, the results may vary depending on the axis that is chosen for initial interpolation. A non-separable higher dimensional extension is likely necessary to efficiently encode a convoluted domain description such as that presented here for the fMRI setting.

6 Conclusion

We have proposed an interpolation scheme that incorporates a priori knowledge of the signal domain, such that the interpolant is consistent not only at sample points, with respect to the given samples, but also at intermediate points between samples, with respect to the given domain knowledge. The interpolation was formulated as an extension of B-spline interpolation. Shift invariant interpolation approaches that use generating functions other than B-splines may also be extended based on the same scheme presented here. Validation on simulated data showed reduced interpolation errors on a range of B-spline orders and sampling steps. Results from applying the proposed approach on fMRI data demonstrated the potential of domain-informed interpolation in up-sampling low resolution functional brain data to obtain subtle activation patterns consistent to the anatomy of the brain.

Appendix I

In the following, we prove that the proposed domain-informed B-spline basis satisfies the three properties of a domain-informed generating basis.

Proof of property 1

Let $\widehat{c}(e^{j\Omega})$ denote the discrete-domain Fourier transform of $c \in \ell_2$, i.e., $\widehat{c}(e^{j\Omega}) = \sum_{k \in \mathbb{Z}} c[k] e^{-j\Omega k}$ with its inverse given as

$$c[k] = \frac{1}{2\pi} \int_0^{2\pi} \widehat{c}(e^{j\Omega}) e^{j\Omega k} d\Omega. \tag{35}$$

Let $\varphi_k(x) = \beta_k^{(n)}(x)$, $\Phi = \{\varphi_k(x)\}_{k \in \mathbb{Z}}$ and $s(x)$ denote the central term in (9), i.e.,

$$s(x) = \sum_{k \in \mathbb{Z}} c[k] \varphi_k(x - k). \tag{36}$$

which can be formulated in the Fourier domain as

$$\begin{aligned}
\widehat{s}(\omega) &\overset{(36)}{=} \int_{-\infty}^{+\infty} \sum_{k \in \mathbb{Z}} c[k] \varphi_k(x - k) e^{-j\omega x} dx \\
&\overset{(35)}{=} \sum_{k \in \mathbb{Z}} \int_0^{2\pi} \widehat{c}(e^{j\Omega}) e^{j\Omega k} \frac{d\Omega}{2\pi} \int_{-\infty}^{\infty} \varphi_k(x - k) e^{-j\omega x} dx \\
&= \int_0^{2\pi} \widehat{c}(e^{j\Omega}) \sum_{k \in \mathbb{Z}} \left(\int_{-\infty}^{\infty} \varphi_k(x - k) e^{-j\omega x} dx \right) e^{j\Omega k} \frac{d\Omega}{2\pi}.
\end{aligned} \tag{37}$$

Incorporating the change of variable $l = x - k$ and $dl = dx$, (37) can be rewritten as

$$\begin{aligned}
\widehat{s}(\omega) &= \int_0^{2\pi} \widehat{c}(e^{j\Omega}) \sum_{k \in \mathbb{Z}} \left(\int_{-\infty}^{\infty} \varphi_k(l) e^{-j\omega l} dl \right) e^{-j(\omega - \Omega)k} \frac{d\Omega}{2\pi} \\
&= \int_0^{2\pi} \widehat{c}(e^{j\Omega}) \widehat{\Phi}(\omega, e^{j(\omega - \Omega)}) \frac{d\Omega}{2\pi},
\end{aligned} \tag{38}$$

where

$$\begin{aligned}
\widehat{\Phi}(\omega, e^{j\Omega}) &:= \sum_{v \in \mathbb{Z}} \left(\int_{-\infty}^{\infty} \varphi_v(u) e^{-j\omega u} du \right) e^{-j\Omega v} \\
&= \sum_{v \in \mathbb{Z}} \widehat{\varphi}_v(\omega) e^{-j\Omega v}.
\end{aligned} \tag{39}$$

By invoking the L_2 space Parseval identity $\|s\|_{L_2}^2 = \frac{1}{2\pi} \int_{-\infty}^{\infty} |\widehat{s}(\omega)|^2 d\omega$, we have

$$\|s\|_{L_2}^2 \overset{(38)}{=} \frac{1}{(2\pi)^3} \int_{-\infty}^{\infty} \left| \int_0^{2\pi} \widehat{c}(e^{j\Omega}) \widehat{\Phi}(\omega, e^{j(\omega-\Omega)}) d\Omega \right|^2 d\omega$$

$$= \frac{1}{(2\pi)^3} \sum_{n\in\mathbb{Z}} \int_0^{2\pi} \left| \int_0^{2\pi} \widehat{c}(e^{j\Omega}) \Gamma(n, \omega, \Omega) d\Omega \right|^2 d\omega, \qquad (40)$$

where $\Gamma(\cdot, \cdot, \cdot)$ is defined as

$$\Gamma(n, \omega, \Omega) := \widehat{\Phi}(\omega + 2\pi n, e^{j(\omega + 2\pi n - \Omega)}). \qquad (41)$$

Using the mean value theorem, the inner integral in (40) can be bounded as

$$\frac{1}{2\pi} \int_0^{2\pi} \widehat{c}(e^{j\Omega}) \, d\Omega \inf_{\Omega \in [0, 2\pi]} \Gamma(n, \omega, \Omega)$$

$$\leq \int_0^{2\pi} \widehat{c}(e^{j\Omega}) \Gamma(n, \omega, \Omega) \, d\Omega$$

$$\leq \frac{1}{2\pi} \int_0^{2\pi} \widehat{c}(e^{j\Omega}) \, d\Omega \sup_{\Omega \in [0, 2\pi]} \Gamma(n, \omega, \Omega). \qquad (42)$$

Sequentially extending inequality (42) by i) incorporating the second power in (40), ii) invoking the ℓ_2 space Parseval identity $\|c\|_{\ell_2}^2 = \frac{1}{2\pi} \int_0^{2\pi} |\widehat{c}(e^{j(\Omega)})|^2 d\Omega$, and iii) incorporating the outer integration and the outer summation of (42), lower and upper bounds on $\|s\|_{L_2}^2$ are obtained as

$$\overbrace{\frac{1}{(2\pi)^2} \sum_{n\in\mathbb{Z}} \int_0^{2\pi} \inf_{\Omega \in [0, 2\pi]} \Gamma(n, \omega, \Omega) \, d\omega}^{A} \cdot \|c\|_{\ell_2}^2$$

$$\leq \|s\|_{L_2}^2$$

$$\leq \underbrace{\frac{1}{(2\pi)^2} \sum_{n\in\mathbb{Z}} \int_0^{2\pi} \sup_{\Omega \in [0, 2\pi]} \Gamma(n, \omega, \Omega) \, d\omega}_{B} \cdot \|c\|_{\ell_2}^2, \qquad (43)$$

where A and B denote the required constants for declaring that Φ forms a Riesz basis, cf. (9).

Proof of property 2

We have, for all $x \in \mathbb{R}$

$$\sum_{k \in \mathbb{Z}} \beta_k^{(n)}(x - k)$$

$$\overset{(14),(23)}{=} \sum_{k \in \Delta_x^{(n)}} \dot{\beta}_k^{(n)}(x - k) + \sum_{k \in \Delta_x^{(n)}} \theta_k(x - k)\Omega(x)$$

$$\overset{(21)}{=} \sum_{k \in \Delta_x^{(n)}} \sum_{i \in \mathcal{I}_k} \beta_{k,i}^{(n)}(x - k)$$

$$+ \sum_{k \in \Delta_x^{(n)}} \theta_k(x - k) \sum_{l \in \Delta_x^{(n)}} \sum_{i \in \mathcal{R}_k} \beta_{l,i}^{(n)}(x - l)$$

$$= \sum_{k \in \Delta_x^{(n)}} \sum_{i \in \mathcal{I}_k} \beta_{k,i}^{(n)}(x - k)$$

$$+ \sum_{k \in \Delta_x^{(n)}} \sum_{i \in \mathcal{R}_k} \beta_{k,i}^{(n)}(x - k) \underbrace{\sum_{k \in \Delta_x^{(n)}} \theta_k(x - k)}_{=1}, \tag{44}$$

$$= \sum_{k \in \Delta_x^{(n)}} \sum_{i \in \mathcal{J}} \beta_{k,i}^{(n)}(x - k) \overset{(16),(17)}{=} 1 \tag{45}$$

where the partition of unity in (44) follows from

$$\sum_{k \in \Delta_x^{(n)}} \theta_k(x - k) = \sum_{k \in \Delta_x^{(n)}} \frac{\Theta\left(w_k(x - k)\right)}{\sum_{l \in \Delta_{k+x-k}^{(n)}} \Theta\left(w_l(k + x - k - l)\right)}$$

$$= 1.$$

Proof of property 3

For any $k \in \mathbb{Z}$, if the domain is homogeneous within the support $[k - \Delta^{(n)}, k + \Delta^{(n)}]$, i.e., there exists an $l \in \mathcal{J}$ such that for all $|x - k| \leq \Delta^{(n)}$ we have $d_l(x) = 1$ and

$\{d_j(x) = 0\}_{j \in \mathcal{J} \backslash l}$, then

$$\beta_k^{(n)}(x) = \dot{\beta}_k^{(n)}(x) + \ddot{\beta}_k^{(n)}(x)$$

$$= \overbrace{d_l((x+k)T)}^{=1} \cdot \beta^{(n)}(x) + \theta_k(x) \cdot \Omega(\overbrace{(x+k)}^{:=x_k} T),$$

$$\overset{(22)}{=} \beta^{(n)}(x) + \theta_k(x) \left(1 - \sum_{i \in \Delta_{x_k T}^{(n)}} \dot{\beta}_i^{(n)}(x_k - i) \right)$$

$$= \beta^{(n)}(x) + \theta_k(x) \left(1 - \sum_{i \in \Delta_{x_k T}^{(n)}} \overbrace{\beta^{(n)}(x_k - i)}^{=1} \right)$$

$$= \beta^{(n)}(x) \tag{46}$$

7 Appendix II

We define a Meyer-type system of $K \in \mathbb{Z}^+$ kernels

$$m'_k(x) : [L, U] \to [0, 1], \quad k = 1, \dots, K,$$

where $L, U \in \mathbb{R}^+$ and $L < U/(2K)$, in a way similar to that given in [28], with the difference that i) we enforce the kernels to form a partition of unity as

$$\sum_{k=1}^{K} |m'_k(x)| = 1, \quad \forall x \in [L, U], \tag{47}$$

as opposed to over their second power as in [28], and ii) we skip enforcing the first and last kernels having L_2 norms equal to that of $\{m'_k(x)\}_{k=2}^{K-1}$.

Using the auxiliary function of the Meyer wavelet [32]
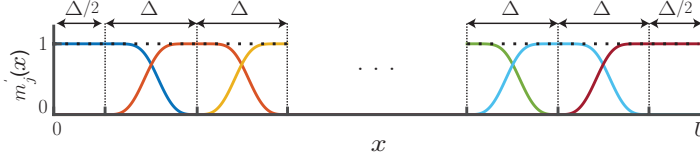
$$\nu(x) = x^4(35 - 84x + 70x^2 - 20x^3),$$

Figure 8: Meyer-type system of spectral kernels.

a system $K \geq 2$ kernels $\{m_k'(x)\}_{k=1}^K$ that span the range $[0, U]$ can be defined as

$$m_1'(x) = \begin{cases} 1 & \forall x \in [L, \Delta/2] \\ \cos^2(\frac{\pi}{2}\nu(\frac{x}{\Delta} - \frac{1}{2}))) & \forall x \in (\Delta/2, 3\Delta/2] \\ 0 & \text{elsewhere} \end{cases} \tag{48a}$$

$$m_k'(x) = \begin{cases} \sin^2(\frac{\pi}{2}\nu(\frac{x}{\Delta} - k + \frac{3}{2})) & \forall x \in (\alpha, \alpha + \Delta] \\ \cos^2(\frac{\pi}{2}\nu(\frac{x}{\Delta} - k + \frac{1}{2})) & \forall x \in (\alpha + \Delta, \alpha + 2\Delta] \\ 0 & \text{elsewhere} \end{cases} \tag{48b}$$

$$m_K'(x) = \begin{cases} \sin^2(\frac{\pi}{2}\nu(\frac{x}{\Delta} - K + \frac{3}{2})) & \forall x \in (\kappa, \kappa + \Delta] \\ 1 & \forall x \in (\kappa + \Delta, U] \\ 0 & \text{elsewhere} \end{cases} \tag{48c}$$

where $\Delta = U/K$ (see Figure 8 for notation), $\alpha = (k-3/2)\Delta$ and $\kappa = (K-3/2)\Delta$. The set of kernels (48) satisfy (47) since

$$\sum_{k=1}^K |m_k'(\lambda)| = \begin{cases} m_1'(x) \stackrel{(48a)}{=} 1 & \forall x \in [L, \Delta/2] \\ m_1'(x) + m_2'(x) & \forall x \in (\Delta/2, 3\Delta/2] \\ m_2'(x) + m_3'(x) & \forall x \in (3\Delta/2, 5\Delta/2] \\ \vdots & \vdots \\ m_J'(x) \stackrel{(48c)}{=} 1 & \forall x \in (U - \Delta/2, U] \end{cases}$$

$$\stackrel{(48b)}{=} \begin{cases} 1 & \forall x \in [L, \Delta/2] \\ \cos^2(x_{\text{I}}) + \sin^2(x_{\text{I}}) & \forall x \in (\Delta/2, 3\Delta/2] \\ \cos^2(x_{\text{II}}) + \sin^2(x_{\text{II}}) & \forall x \in (3\Delta/2, 5\Delta/2] \\ \vdots & \vdots \\ 1 & \forall x \in (U - \Delta/2, U] \end{cases}$$

$$= 1 \quad \forall x \in [0, U]$$

where $x_{\mathrm{I}} = \frac{\pi}{2}\nu(\frac{x}{\Delta} - 1/2)$ and $x_{\mathrm{II}} = \frac{\pi}{2}\nu(\frac{x}{\Delta} - 3/2)$; in the first equality we use the property that for all $k \in \{2, \dots, K-1\}$ the supports of $m'_{k-1}(x)$ and $m'_{k+1}(x)$ are disjoint.

References

[1] M. Unser, "Splines: A perfect fit for signal and image processing.," *IEEE Signal Process. Mag.*, vol. 16, no. 6, pp. 22–38, 1999.

[2] M. Oliver and R. Webster, "Kriging: a method of interpolation for geographical information systems," *Int. J. Geograph. Inform. Sys.*, vol. 4, no. 3, pp. 313–332, 1990.

[3] G. Lu and D. Wong, "An adaptive inverse-distance weighting spatial interpolation technique," *Comput. Geosci.*, vol. 34, no. 9, pp. 1044–1055, 2008.

[4] J. Manjón, P. Coupé, A. Buades, V. Fonov, D. Collins, and M. Robles, "Non-local MRI upsampling," *Med. Image Anal.*, vol. 14, no. 6, pp. 784–792, 2010.

[5] F. Rousseau and Alzheimer's Disease Neuroimaging Initiative, "A non-local approach for image superresolution using intermodality priors," *Med. Image Anal.*, vol. 14, no. 4, pp. 594–605, 2010.

[6] K. Jafari-Khouzani, "MRI upsampling using feature-based nonlocal means approach," *IEEE Trans. Med. Imag.*, vol. 33, no. 10, pp. 1969–1985, 2014.

[7] A. Rueda, N. Malpica, and E. Romero, "Single-image super-resolution of brain MR images using overcomplete dictionaries.," *Med. Image Anal.*, vol. 17, no. 1, pp. 113–132, 2013.

[8] M. Unser, A. Aldroubi, and M. Eden, "B-spline signal processing: part I – theory," *IEEE Trans. Signal Process.*, vol. 41, no. 2, pp. 821–833, 1993.

[9] M. Unser, "Sampling—50 years after Shannon," *Proc. IEEE*, vol. 88, no. 4, pp. 569–587, 2000.

[10] M. Borga and A. Vizzaccaro, "On the interpolation of hydrologic variables: formal equivalence of multiquadratic surface fitting and kriging," *J. Hydrol.*, vol. 195, no. 1, pp. 160–171, 1997.

[11] M. Gaillard, S. Sugita, F. Mazier, A. Trondman, A. Brostrom, T. Hickler, J. Kaplan, E. Kjellström, U. Kokfelt, P. Kunes, and C. Lemmen, "Holocene land-cover reconstructions for studies on land cover-climate feedbacks," *Clim. Past*, vol. 6, pp. 483–499, 2010.

[12] B. Pirzamanbein, J. Lindström, A. Poska, S. Sugita, A. Trondman, R. Fyfe, F. Mazier, A. Nielsen, J. Kaplan, A. Bjune, and H. Birks, "Creating spatially continuous maps of past land cover from point estimates: a new statistical approach applied to pollen data," *Ecol. Complex.*, vol. 20, pp. 127–141, 2014.

[13] C. Frankenberg, J. F. Meirink, M. van Weele, U. Platt, and T. Wagner, "Assessing methane emissions from global space-borne observations," *Sci.*, vol. 308, no. 5724, pp. 1010–1014, 2005.

[14] F. Keppler, J. Hamilton, M. Braβ, and T. Röckmann, "Methane emissions from terrestrial plants under aerobic conditions," *Nat.*, vol. 439, no. 7073, pp. 187–191, 2006.

[15] J. Kaplan, K. Krumhardt, and N. Zimmermann, "The prehistoric and preindustrial deforestation of europe," *Quaternary Sci. Rev.*, vol. 28, no. 27, pp. 3016–3034, 2009.

[16] N. Logothetis and B. Wandell, "Interpreting the BOLD signal.," *Annu. Rev. Physiol.*, vol. 66, pp. 735–769, 2004.

[17] M. Brett, A. Leff, C. Rorden, and J. Ashburner, "Spatial normalization of brain images with focal lesions using cost function masking," *NeuroImage*, vol. 14, no. 2, pp. 486–500, 2001.

[18] A. Andrade, F. Kherif, J. Mangin, K. J. Worsley, O. Paradis, A. Simon, S. Dehaene, D. L. Bihan, and J. Poline, "Detection of fMRI activation using cortical surface mapping," *Hum. Brain Mapp.*, vol. 12, no. 2, pp. 79–93, 2001.

[19] J. Ashburner, "A fast diffeomorphic image registration algorithm," *NeuroImage*, vol. 38, pp. 95–113, 2007.

[20] O. Christensen, *An introduction to frames and Riesz bases*, vol. 7 of *Applied and Numerical Harmonic Analysis*. Boston: Birkhaüser, 2003.

[21] M. Unser and A. Aldroubi, "A general sampling theory for nonideal acquisition devices.," *IEEE Trans. Signal Process.*, vol. 42, no. 11, pp. 2915–2925, 1994.

[22] C. de Boor, *A practical guide to splines.* New York: Springer-Verlag, 1978.

[23] J. F. Mangin, D. Riviere, A. Cachia, E. Duchesnay, Y. Cointepas, D. Papadopoulos-Orfanos, P. Scifo, T. Ochiai, F. Brunelle, and J. Regis, "A framework to study the cortical folding patterns.," *NeuroImage*, vol. 23, pp. S129–S138, 2004.

[24] S. J. Kiebel, R. Goebel, and K. J. Friston, "Anatomically informed basis functions," *NeuroImage*, vol. 11, no. 6, pp. 656–667, 2000.

[25] S. Ozkaya and D. Van De Ville, "Anatomically adapted wavelets for integrated statistical analysis of fMRI data," in *Proc. IEEE Int. Symp. Biomed. Imaging*, (Chicago, IL), pp. 469–472, 2011.

[26] H. Behjat, N. Leonardi, L. Sörnmo, and D. Van De Ville, "Anatomically-adapted graph wavelets for improved group-level fMRI activation mapping," *NeuroImage*, vol. 123, pp. 185–199, 2015.

[27] Y. Farouj, F. I. Karahanoğlu, and D. Van De Ville, "Regularized spatiotemporal deconvolution of fMRI data using gray-matter constrained total variation," in *Proc. IEEE Int. Symp. Biomed. Imaging*, pp. 472–475, Ieee, 2017.

[28] H. Behjat, U. Richter, D. Van De Ville, and L. Sörnmo, "Signal-adapted tight frames on graphs.," *IEEE Trans. Signal Process.*, vol. 64, no. 22, pp. 6017–6029, 2016.

[29] C. Grova, S. Makni, G. Flandin, P. Ciuciu, J. Gotman, and J. Poline, "Anatomically informed interpolation of fMRI data on the cortical surface," *NeuroImage*, vol. 31, no. 4, pp. 1475–1486, 2006.

[30] G. Operto, R. Bulot, J. L. Anton, and O. Coulon, "Projection of fMRI data onto the cortical surface using anatomically-informed convolution kernels," *NeuroImage*, vol. 39, no. 1, pp. 127–135, 2008.

[31] D. Van Essen, S. Smith, D. Barch, T. Behrens, E. Yacoub, K. Ugurbil, and WU-Minn HCP Consortium, "The WU-Minn human connectome project: an overview," *NeuroImage*, vol. 80, pp. 62–79, 2013.

[32] Y. Meyer, "Principe d'incertitude, bases hilbertiennes et algebres d'operateurs," *Seminaire Bourbaki (in French)*, vol. 662, pp. 209–223, 1986.

LUND
UNIVERSITY